AN EXPERIMENTAL AND THEORETICAL INVESTIGATION

OF

[illegible] FOLD DEVELOPMENT

(A thesis submitted for the degree of Doctor of Philosophy
of the University of London)

by

John Morris Summers

Department of Geology
Imperial College

May, 1979.

ABSTRACT

This thesis is concerned with the development of fold structures in uniform, well laminated or foliated geological systems. Such structures include monoclinic and conjugate kink bands, 'box' folds and chevron folds. These types of structure occur over a wide range of geological scales in materials or layered systems with a well developed planar anisotropy.

The thesis is divided into two distinct sections. The first section (Chapters 1, 2 and 3) is concerned with mechanical models of fold development in uniform multilayers. Chapter 1 contains a review of previous work in this field and particular emphasis is placed on the work of M. Biot. The role of mechanical anisotropy in producing active amplification of folds in uniform, finely laminated multilayers is discussed.

A mathematical analysis is derived and discussed in Chapters 2 and 3. This model is concerned with the role of mechanical anisotropy in the incremental and finite development of localised, tabular zones of layer or foliation rotation. The analysis is relevant to the development of localised kink bands or monoclines. This model is based on the mathematical relationship between the response to stress of a finely laminated system and that of a mechanically equivalent, transversely isotropic, homogeneous anistropic continuum. By using stress-strain rate relationships which apply to such a continuum, a finite fold development model is obtained which allows one to explain many of the features seen in natural kink-like asymmetric folds. A number of important predictions concerning the variation in the orientation and magnitude of stresses within such structures are discussed.

In the second part of the thesis a series of scale model experiments which were designed to simulate the development of large scale décollement folds (500m - 5km wavelength) in uniform sedimentary sequences are described and illustrated. The experiments were carried out using paraffin wax as the principal model material. The models were deformed at temperatures of 35^0 - 45^0C in order to reduce the "strength" of the wax to the levels required by the theory of scale modelling. The validity of the models as simulations of natural large scale fold development is discussed.

Acknowledgements

I am endebted to Dr. N.J.Price and Dr. J.W.Cosgrove for their constant help and encouragement throughout the course of this work and wish to thank Dr. Price for providing the initial opportunity to carry out the research. I also gratefully acknowledge the financial support provided by Royal Dutch/Shell Exploration and Production Laboratories, Rijswijk, Netherlands and the help given by Dr. G.Mandl of this organisation.

I have benefited from many discussions with colleagues particularly Chris Spiers, Nick Shaw, John-Paul Latham and Dr. Ken McClay at Imperial College and with Dr.'Pete' Cobbold of the University of Rennes. Chris Spiers is thanked for his introduction to the world of computer graphics and for his help with computing. Thanks are also due to Miss Juliet Hornsby for typing.

Finally, it is not possible to express, sufficiently, my gratitude for the understanding, help and encouragement given by my wife, Julie, and my parents during the last four years.

TABLE OF CONTENTS

Abstract			i
Acknowledgements			ii
Table of Contents			iii
CHAPTER 1		Discussion of published mechanical models of fold development, fold mechanisms.	1
1.1		Introduction.	1
1.2		Mechanical analyses of fold development.	9
	1.2.1	Analytical models for the initial stages of fold development in single layer and multilayer systems.	11
	1.2.2	Analyses of the finite development of folds in multilayers.	40
CHAPTER 2		Rotation domain analysis for the incremental and finite development of localised kink-like structures in foliated and layered materials.	54
2.1		Introduction.	54
	2.1.1	Constraints placed on the initial and finite geometry of the structure.	54
	2.1.2	Symmetry of applied stresses with respect to the structure.	56
	2.1.3	The concept of local macroscopic strain, variation in the stress and strain tensors.	58
2.2		Construction of equations describing the incremental deformation of the structure.	61
	2.2.1	Incremental strain rate tensor.	61
	2.2.2	Relationship between incremental strain and foliation rotation.	70
	2.2.3	Incremental stress tensor.	79
2.3		Predictions of the analysis.	85
	2.3.1	Incremental foliation rotation as a function of foliation attitude.	87
	2.3.2	Finite rotation of foliation within an individual foliation element.	97
	2.3.3	Finite deformation of specific low amplitude foliation perturbations.	105

2.3.4	Variation in stress across a foliatio domain.	139
2.3.5	Variation in mean stress as a function of foliation attitude.	139
2.3.6	Variation in the orientation of principal stress trajectories as a foliation attitude.	149
2.3.7	Change in the state of stress within specific structures during finite deformation.	158
Chapter 3	Discussion of the assumptions of the rotation domain analysis; the effect of volumetric strain on the predictions of the analysis.	188
3.1	Introduction	188
3.2	The use of a homogeneous anisotropic continuum as a model for a foliated or layered geological system.	188
3.2.1	Statistical homogeneity	188
3.2.2	Effect of bending resistance within locally defined foliation elements.	189
3.2.3	Effect of change in the volume of locally defined foliation elements.	190
Chapter 4	Large scale fold simulation experiments.	234
4.1	Introduction	234
4.2	Relationship between the deformation of a model and a prototype system - the principles of scale modelling.	238
4.3	Rheological tests on model materials used in the fold simulation experiments	247
4.4	Relationship between the significant properties of paraffin wax multilayers and the equivalent properties of scaled tectonic prototypes.	265
4.5	Results of the model experiments.	277
4.5.1	Effect of boundary shear stresses on the development of structures.	277
4.5.2	Effect of the strength of competent units the multilayer sequence on fold development	279

4.53	Development of structures in individual experiments.	288
	Appendices	302
	Bibliography	310

CHAPTER 1

1.1 INTRODUCTION

This thesis reports the results of an investigation into the finite development of fold structures in multilayered and foliated materials. The investigation was concerned, principally, with physical processes which contribute to the development of folds styles which are characteristic of materials or systems with a pronounced planar anisotropy. Such materials would include rocks with a technically induced planar fabric (Slaty cleavage, schistosity) and certain types of uniform, well-bedded sedimentary rock sequences. Folds developed in such materials often have a distinctly angular finite fold geometry. The folds may be single hinged or multiple hinged and the hinge zones characteristically mark a distinct and rapid change in the attitude of foliation planes or bedding. Various terms have been used to describe such structures depending on the symmetry of the structural elements contained within a fold and, to a certain extent, on the scale on which the fold is developed. One class of structures which develop in materials with a well developed foliation are angular folds with a monoclinic symmetry. Such structures have been called kink bands, knick zones, joint drags (Dewey, 1965), monoclinic folds or monoclines. These structures are generally made up of a localised zone of rotated bedding or foliation contained within a uniform body of foliated or bedded material. Characteristically, the bounding surfaces or axial planes defining the kinked domain are inclined at an oblique angle to the general trend of the foliation outside the domain. Under certain circumstances, the kink domains may be arranged in pairs with axial surfaces inclined toward one another. The general symmetry of these paired structures is orthorhombic and the structures may be classed as a set of conjugate kink bands, a conjugate fold or a box fold.

A second type of angular structure which is typical of well-bedded or foliated materials is the chevron fold (zig-zag, concertina or accordian fold). Chevron folds are characterised by straight limbs

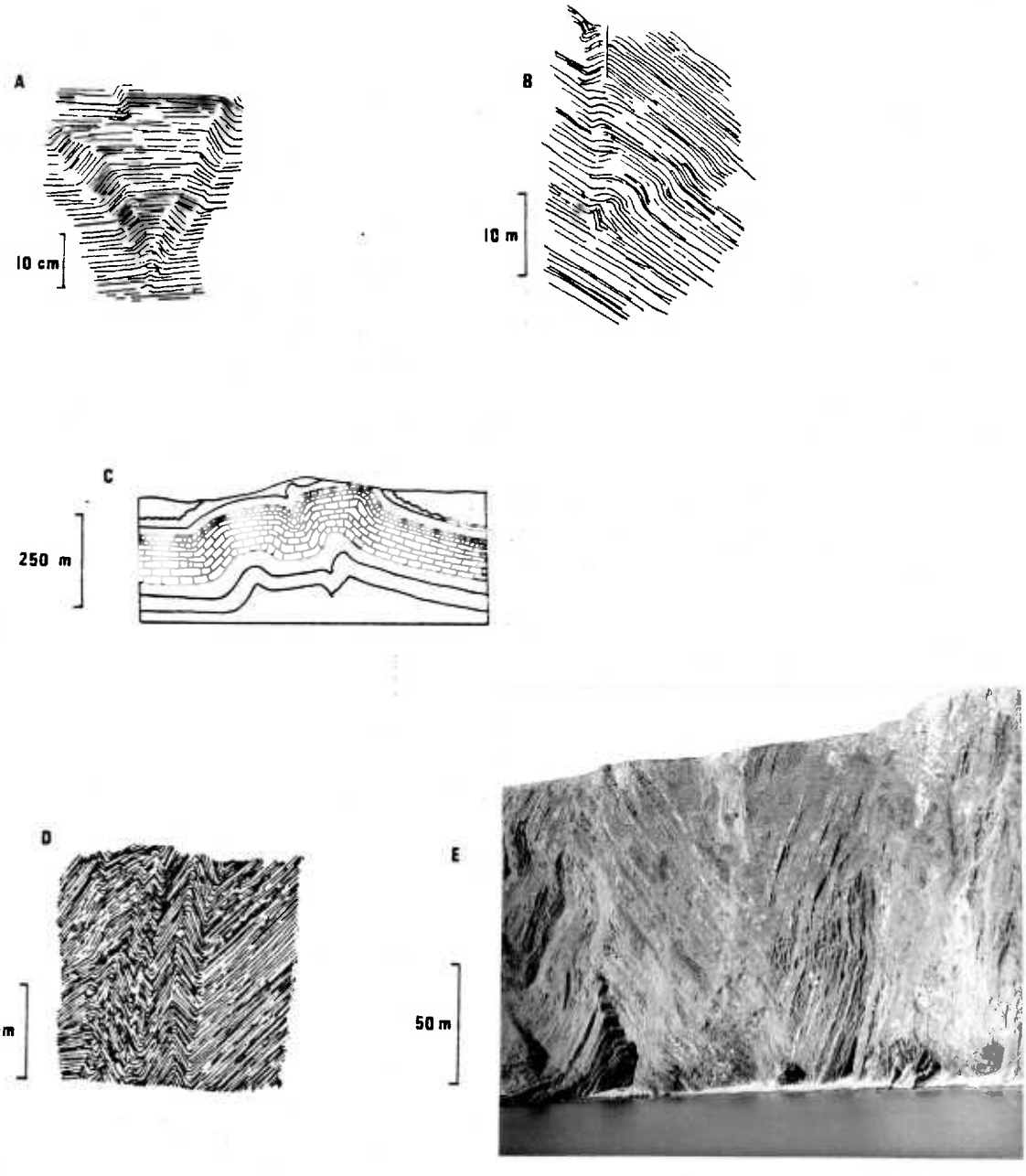


Fig. 1.1 Natural examples of natural angular conjugate folds (A,B,C) and chevrons (D,E) taken from a wide range of geological scales.

A) Conjugate kink bands in slate, Ards Peninsula, Northern Ireland. (after Anderson, 1968)

B) Conjugate kink bands / box fold in an inclined sequence of fine grained limestones interbedded with shales, Indonesian Timor. (sketched from photo by Dr. M. Audley-Charles)

C) Large scale conjugate kink bands / box folds, Hauensteinbasis rail tunnel, Jura Mountains, S.W.France. (after Buxtorf,1916, Laubscher,1976b)

D) Chevron folds in phyllite, Rhoscolyn, Anglesey, N. Wales. (sketched from photo-micrograph by Dr. J. Cosgrove)

E) Chevron folds in a greywacke/shale turbite sequence, Hartland Quay, North Devon.

and a relatively narrow hinge. The axial plane of the fold is a plane of mirror symmetry.

An examination of published descriptions of natural structures indicates that folds with the general geometrical characteristics of conjugate and monoclinic kinks and chevron folds can develop over a very wide range of geological scales, under a wide range of environmental conditions and in foliated of layered materials with very different lithologies. A series of line diagrams taken from natural examples of conjugate folds and chevron folds have been included in fig. 1.1 to illustrate this point.

Structures with the general geometrical characteristics of small scale kink bands developed in foliated metamorphic rocks can also form, for example, in well bedded sedimentary sequences where they occur as both isolated, large scale asymmetric folds and conjugate box folds with amplitudes and limb lengths of the order of kilometers. One problem which has tended to limit the extent to which such structures have been recognised in the past is that of scale of observation. Weiss (1968) has stated: "Such folds are easily recognised in platy rocks if they are developed on a small scale and can be studied directly. Large (macroscopic) folds are less easily recognised unless the hinge regions are properly exposed and the narrowness of the zone of curvature seen". He continued: ".... Another factor of the same kind is the difficulty of recognising such folds in coarsely or massively bedded rocks such as thick sedimentary sequences. The 'slip surfaces' may be shaly partings between massive, isotropic layers of limestone, sandstone or quartzite, and can be spaced hundreds of feet apart. 'Kink' or 'conjugate' kink folds' forming in such sequences may have amplitudes of many thousands of feet and hinge zones which are only kink surfaces with respect to the dimensions of the whole fold" A similar opinion is expressed by Beloussov (1965) : ".... box folds are often overlooked by geologists .... and we could cite numerous examples where such structures are shown more rounded than they actually are."

The views expressed in these quotations are confirmed by descriptions of natural large scale fold structures published by Faill (1969, 1973) and Laubscher (1976b). Faill has demonstrated that large scale

flexural folds in the Valley and Ridge Province of the Appalachian region of North America are characterised by localised rotation of bedding within well defined kink-like domains. Geometrically similar structures (monoclinic and conjugate kinks) are developed, in the Valley and Ridge Province, on scales ranging from a few centrimetres to 18 kilometres. The upper limit on the span of folds which can be observed directly is approximately 150 m and the kink geometry of the larger structures was deduced by detailed mapping.

The most well documented examples of large scale monoclinic and conjugate folds with the general geometrical characteristics of monoclinic and conjugate kinks are provided by structures developed in the sedimentary cover rocks of the Jura region of S. W. France. Laubscher (1975, 1976a, 1976b) has interpreted the development of specific fold structures in this region in terms of a kink mechanism (e.g. fig. 1.2). In his description of these structures, Laubscher (1976b) states "Jura folds do not resemble models of continuously distributed buckling, rather than can be approximated by discrete, externally rotated kink bands with rounded hinges."

Similarities between the finite geometry of fold structures developed on different scales does not, necessarily, imply a similarity in the processes by which the structures developed. Paterson and Weiss (1966) and Cobbold et al. (1971) have demonstrated, for example, that even such geometrically simple structures as symmetric chevron folds may be produced by contrasting mechanisms which involve either the convergence and coalescence of conjugate kink bands or the progressive straightening of initially sinusoidal buckles during fold amplification. In either case the relative simplicity of the finite fold geometry masks a more complex history of progressive deformation and associated change in fold style.

Kink bands or kink like asymmetric folds with similar finite geometric characteristics may also evolve with contrasting histories of progressive deformation. Model experiments with ductile materials such as plasticene and modelling clays (Summers, 1970; Ghosh, 1968) have shown, for example, that angular conjugate kink domains can develop as a result of a gradual, progressive increase in the angularity of the limbs of an initially rounded or sinusoidal fold. In contrast kink domains developed in the card deck model experiments described by Weiss (1968) are distinct and angular immediately they appear within

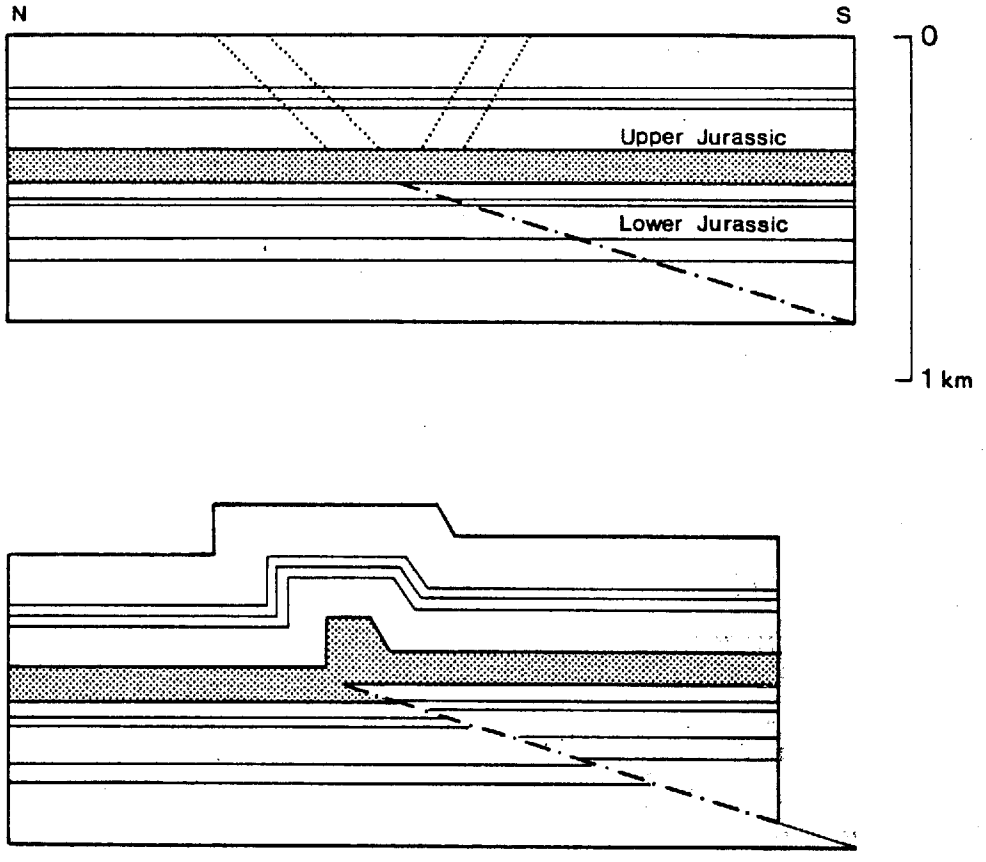


Figure 1.2 Kinematic interpretation of the initial stages of development of the Gaumois-S anticline, Jura fold belt by H.P. Laubscher, 1976 b. The structure is interpreted as a large scale set of complimentary kinks developed as localised zones of bed rotation. Laubscher's interpretation of this and other structures in the Jura region demonstrates the probable importance of monoclinic and conjugate kinking as a mechanism of large scale fold development in well bedded sedimentary sequences.

the card deck. The structures, which are generated by a layer parallel compression, tend to initiate and propagate so rapidly in these experiments that the processes involved in the initiation of the kink instability are obscure even when viewed in successive frames of a cine film.

In spite of the possible differences in mechanisms of deformation and in the detailed geometrical and structural characteristics of angular folds of the types discussed above, the degree of angularity of these structures appears to be closely related to the presence of a marked mechanical anisotropy in the materials which contain such structures. The presence of slickensides on bedding planes, evidence for high shear strain developed within weak interbeds, etc., indicate that the total deformation of the structures is dominated by shear along the direction of the planar anisotropy.

There are a number of approaches that can be used to investigate the processes involved in progressive deformations such as the development of multilayer folds. One obvious method is to study, in detail, the evidence provided by natural examples of the structures of interest. Since this evidence is almost invariably limited to the appearance of the structure at the final stage of deformation, any conclusions, based on this evidence, about the mechanisms of deformation or the stages of development involved in the growth of the structures are the result of informed guesswork or deduction. In many cases, lack of sufficient evidence or the complexity of the structure and its relationship to adjacent structures may restrict the extent to which the deformation history can be deduced.

Additional methods of study are available, however, which can provide independent evidence for the mechanisms by which natural structures develop and can be used to refine, or to test, the deductions made from a study of natural structures. In the field of tectonic folding, these methods are (i) the use of theoretical analysis to investigate the parameters which control the development of fold instabilities in layered or foliated materials, (ii) the use of physical models to simulate, in the laboratory, the development of particular types of fold structures. Each of these methods has certain advantages and certain disadvantages. Theoretical analysis, for example, provides essential evidence about the mechanics of the development of fold instabilities in layered systems. However, the

technique is restricted to a description of the behaviour of relatively simple systems and materials with idealised and rheologically simple mechanical properties. Until the last decade, mathematical analyses could be applied, with confidence, only to incremental deformations. Recently, however, the use of the finite element method has made it possible to simulate large finite fold deformations by numerical analysis. The application of this technique to the problem of tectonic folding is still in its infancy and the majority of published analyses are concerned with fold growth in simple, single layer systems.

The method of physically modelling fold processes has a long history stretching back to the demonstration experiments of Hall (1815) and the simulations of large scale folding in the Appalachian Mountain belt carried out by Willis (1891). This technique has one clear advantage; using model experiments one can observe the complete deformation history of an experimental structure and the deformation is obviously not subject to computational errors which may accumulate in a numerical finite element analysis and effect the accuracy of this method of simulation (see Casey, 1976). Model experiments can lead to the recognition of previously unsuspected mechanisms of folding or unsuspected changes in fold style with finite deformation (Cobbold et al., 1971) and the technique can produce a tangible and stimulating demonstration of particular fold deformation processes. The design and interpretation of model experiments should, however, be approached with due caution. The accuracy of any deductions which are made on the basis of experiments depends upon the accuracy with which the significant physical properties of the experiment are known. This knowledge should include an understanding of the rheolological properties of the model materials used in the experiment, and the nature and likely influence of the boundary conditions which are applied to the model. In the case of experiments designed to study fold development, for example, the presence of unwanted boundary stress concentrations and of unknown, localised initial foliation or layer disturbances within the model may significantly affect the course of finite fold development. These problems apply, particularly, to experiments using well laminated, highly anisotropic models which may be subject to the development of localised folds associated with a significant degree of instability.

This thesis presents the results of an investigation into multilayer fold development using both the techniques of mechanical analysis and physical modelling. This thesis is divided into two distinct sections which consider, separately, the results of the two approaches. In the first section (chapter 2 and 3), the construction and predictions of a mathematical model of finite fold development in uniform materials with a pronounced planar anisotropy is described. The analysis is concerned principally with the contribution of mechanical anisotropy to the development and geometry of multilayer folds and, particularly, with processes which may contribute to the development and characteristic geometry of natural kink bands and kink like asymmetric folds. The analysis is based on an important approximation whereby the bulk response to stress of a discretely layered or foliated material is analysed in terms of the response of an equivalent homogeneous, anisotropic continuum. The method is based on the pioneering work of Biot and has been recently used by Casey (1976) and Cobbold (1976) to investigate the finite amplification of symmetric fold instabilities. The significance of this approach to multilayer folding and its relationship to other methods of theoretical analysis, are considered in section 1.2, along with a review of previous work in this field.

The final section of the thesis (Chapter 4) reports the results of physical model experiments which were designed to investigate the specific problem of large scale fold development in uniform, well bedded sedimentary sequences. The choice of model materials in these experiments were governed both by the need to simulate the deformational properties of such a natural system and to model the role of gravitational body forces in the development of natural large scale folds.

The theoretical analysis, described in this thesis was not designed specifically to investigate the development of structures in the model experiments. (The analysis does not, for example, take into account the influence of gravitational body forces). However, a number of features of the experimental structures can be related to the predictions of the theoretical model and, in combination, the analysis and the experiments illustrate the role of bedding anisotropy in the development of large scale angular structures such as isolated monoclines and conjugate or box folds.

1.2 MECHANICAL ANALYSIS OF FOLD DEVELOPMENT

A substantial body of literature has accumulated over the past two decades containing reports of the results of theoretical studies into the cause and effects of fold development in layered and foliated materials. In this section, emphasis is placed on models of fold initiation and amplification which are based on a consideration of the mechanical stability of layered systems under simple boundary loading conditions. Other types of mathematical models of fold development derived from empirical arguments based on the finite geometry and strain distribution within natural folds will not be considered in any detail.

The discussion of published theoretical analyses of fold development contained within this section is not presented as a comprehensive historical review of work in this field. The number of publications and the variety of approaches used would make this a forbidding task. Reviews of the literature are given by Huddleston (1973), Huddleston and Stephenson (1973), Johnson (1970, 1976) and Hobbs et al., (1977). In this section, the writer is principally concerned with the relevance of previous publications to the problem of the mechanisms of fold initiation and amplification in multilayers. Particular emphasis will be placed on the work of Maurice Biot.

It is convenient to divide published theoretical analysis of fold development into:

(i) Those analyses which are concerned with the initial stability of a layered system and involve the construction of stability equations for the system. These equations are then solved (assuming particular boundary conditions, material properties, etc) to obtain analytical expressions for the displacements associated with the initial development of fold instabilities. In general, this approach gives rise to displacement solutions and associated fold instabilities which are sinusoidal and continuous along the initial trend of the layering. Solutions are restricted to the initial stages of amplification of layer disturbances which are, themselves, sinusoidal or made up of discrete, sinusoidal components. Some of the most significant results of such analyses will be considered in Section 1.2.1.

(ii) Those analyses which are concerned with the finite development of folds. Significant progress has been made in the last decade on the specific problem of the finite growth of folds in single, confined layers using the method of finite element analysis. Using this method, large time-dependent deformations can be numerically modelled by integrating successive incremental deformations of a representative network of locally defined material elements. The reader is referred to Casey (1976) for a comprehensive discussion of the application of this method to the study of fold development in viscous materials and for a critique of the previous work in this field. Diettrich and Carter (1969), Huddleston and Stephanson (1973) and Casey (1976) have used this method to simulate the finite amplification of simple sinusoidal buckles in a uniform isotropic plate, contained within an effectively infinite matrix. Cobbold (1973) and Williams et al (1977) have studied the particular problem of finite fold growth from a localised deflection of a single plate and Parrish (1973) used a finite element method in an attempt to simulate single layer fold development in materials with a power law stress-strain rate relationship. Casey (1976) repeated some of the earlier work of Dietrich and Carter (1969) using a more accurate method of numerically integrating the displacement rate solutions obtained for successive stages in the amplification of a sinusoidal single layer buckle (viscous layer and matrix). It is sobering to note that the simulations of Casey and of Dietrich and Carter disagree by a difference in predicted amplitude of 44% after 0.23 bulk natural strain (assuming the same initial perturbation geometry in rheologically equivalent systems).

At present, the application of finite element analysis to the important problems of multilayer folding is limited and those analyses which have been published are considered in section 1.2.2.

1.2.1 ANALYTICAL MODELS FOR THE INITIAL STAGES OF FOLD AMPLIFICATION IN SINGLE LAYER AND MULTILAYER SYSTEMS

A wide range of analyses have been presented in the literature which are concerned with the stability of layered system of various degrees of complexity under a state of layer parallel compression. The majority of these analyses are limited to a description of two dimensional deformation in the profile plane of folding (normal to fold axes). In addition, authors assume idealised rheological properties for the individual components of the multilayer system such as linear elastic, linear viscous or linear visco-elastic. In general it is assumed that deformation occurs at constant volume. In this thesis, emphasis will be placed on the behaviour of materials with a linear viscous rheology.

The simplest type of problem which has been analysed is that of a single, uniform isotropic plate confined on either side by an effectively infinite, rheologically weaker matrix (fig. 1.3A). The most important early analyses of this system are those of Ramberg (1959) and Biot (1957, 1959, 1961). In the analyses of both Ramberg and Biot, the formulation of the stability equations for the stressed plate is, in essence, identical to that adopted in engineering science to quantify the stability and collapse or buckling of stressed elastic beams and plates, i.e. the development of fold instabilities is viewed as a process of buckling in the engineering sense. (As will be shown later in this section, this is not the only mechanism that can produce an active amplification of folds in layered systems). The manipulation of elastic plate buckling equations to deal with the case of incompressible viscous material properties is based on the formal correspondence between the stress-strain and stress-strain rate relationships for linear elastic and linear viscous materials respectively.

Biot (1965a, 1965d) recognized that there are important similarities between the relatively simple problem of the stability of a confined isotropic plate (fig. 1.3A) and the more complex problem of the stability of a confined multilayered plate. (fig. 1.3.B). He has described a method of analysis which can be applied to the buckling behaviour of both systems.

The most significant feature of Biot's approach is the use of an approximation whereby the response of a discretely layered or foliated material to stress is analysed in terms of the response of

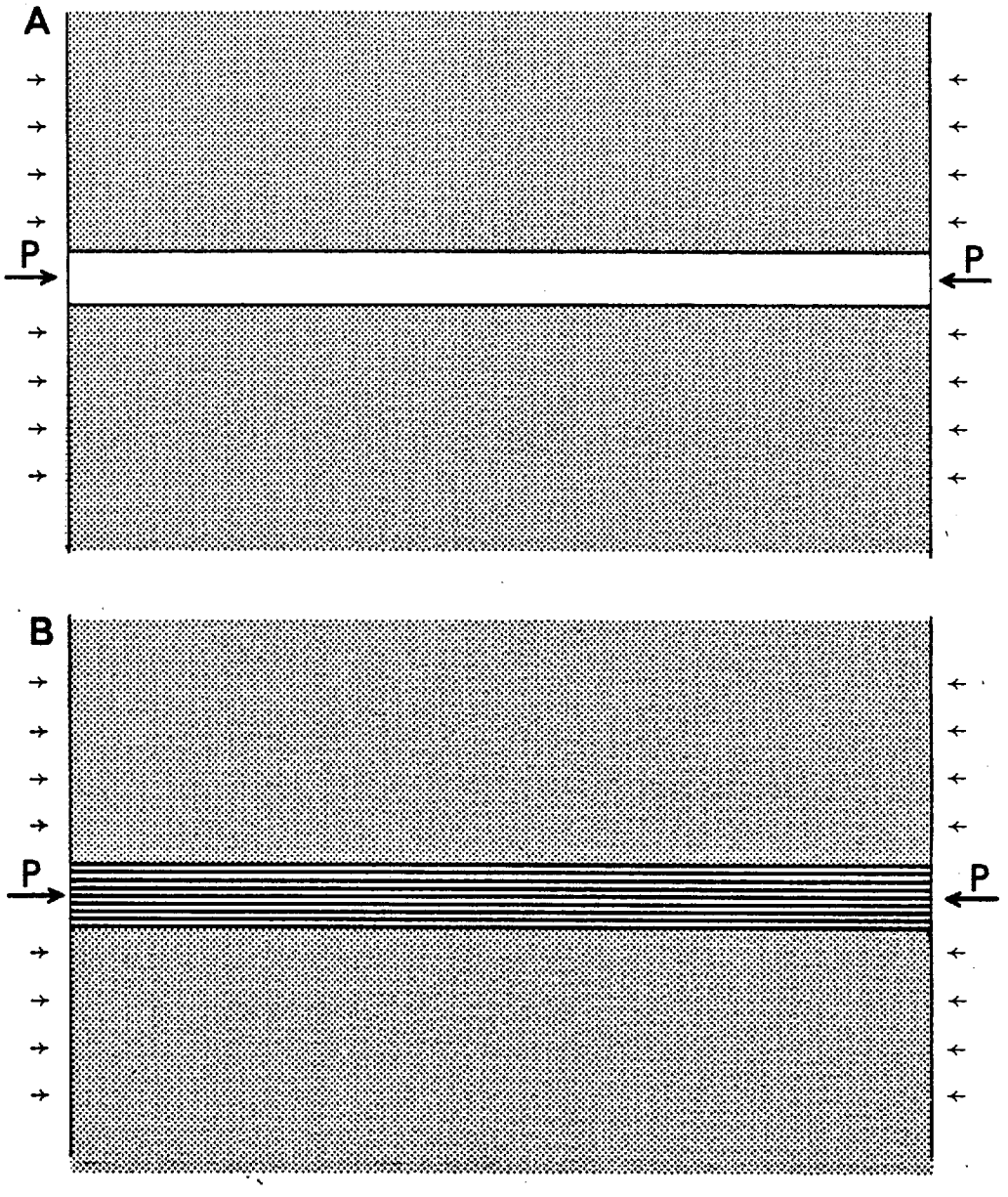


Figure 1.3

Plate/matrix systems.

A) Homogeneous isotropic plate in homogeneous, isotropic matrix.

B) Heterogeneous multilayered plate (anisotropic in homogeneous isotropic matrix.

an equivalent homogeneous continuum with anisotropic mechanical properties. This mechanical anistropy represents the "bulk" mechanical anisotropy of the equivalent discretely layered continuum. If this approximation is applied to the case of a confined, multilayered plate, for example, then a stability analysis of this system is simplified to an analysis of the buckling behaviour of a confined, homogeneous plate with anisotropic properties. The formulation of this stability analysis is then identical to that of a confined isotropic plate except that the deformational behaviour of the plate is quantified in terms of anisotropic rather than isotropic material properties.

This approximation introduces a number of important simplifications into the analysis. An alternative, and more complex, method of analysing the behaviour of a multilayer system under layer parallel compression is to obtain stress and displacement solutions for individual components of the multilayer sequence. An attempt is then made to match these stress and displacement solutions at the interfaces between adjacent laminae and therefore obtain a solution for the buckling response of the whole multilayer. This method was used by Ramberg (1961, 1970). The macroscopic approach used by Biot will be followed in this discussion because it brings to light the underlying mechanics of single layer and multilayer folding.

In order to model the contribution of layer anisotropy to the overall buckling behaviour of a discretely layered plate, Biot obtained two viscous coefficients η_n and η_t which are a measure of the bulk (i.e. macroscopic) resistance of the plate to layer parallel compression and layer parallel shear respectively. In a simple, uniform multilayer sequence made up of alternating competent units and incompetent units (fig. 1.4) the bulk stiffness coefficients η_n and η_t are given by:

$$\eta_n = \alpha_1 \eta_1 + \alpha_2 \eta_2 \qquad \ldots\ldots \quad 1.1$$

$$\eta_t = \frac{\eta_1 \eta_2}{\alpha_1 \eta_1 + \alpha_2 \eta_2} \qquad \ldots\ldots \quad 1.2$$

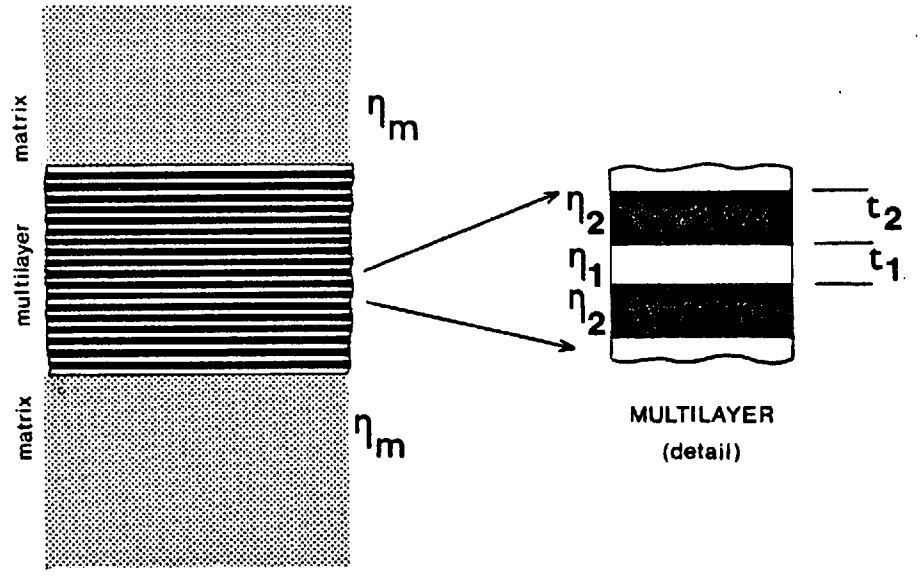


Figure 1.4

Figure 1.5 A

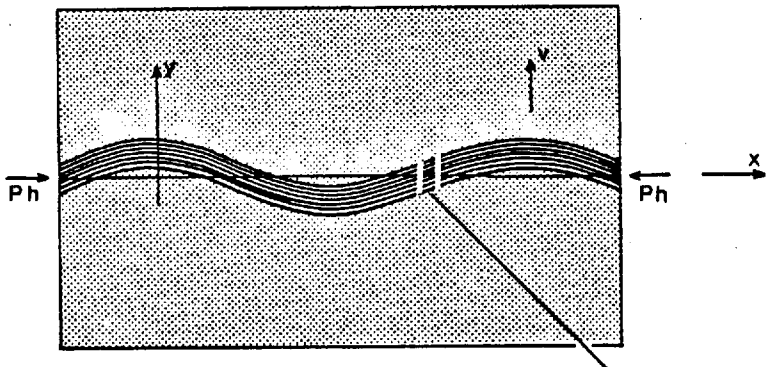
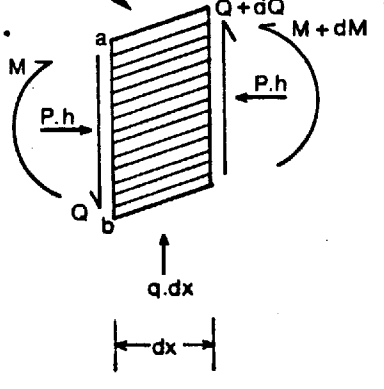


Figure 1.5 B.



η_1 = viscosity coefficient of the competent units

η_2 = viscosity coefficient of the incompetent units

$\alpha_1 = \frac{t_1}{t_1 + t_2}$ = fractional thickness of competent units

$\alpha_2 = \frac{t_2}{t_1 + t_2}$ = fractional thickness of incompetent units

The formulation of the stability equations for the buckling of a confined plate is based on a consideration of the equilibrium of a representative sectional element of the plate (fig. 1.5A, B). The derivation of these equilibrium conditions can be found in any standard treatment of plate buckling (e.g. Timoschenko, 1961; Biot, 1959; Johnson 1970, 1977). For equilibrium of moments and forces acting on such an element (fig. 1. 5 B) it can be shown that:

$$\frac{dM}{dx} = Q \qquad \ldots\ldots 1.3$$

$$\frac{dQ}{dx} + q = P\,h\,\frac{d^2 v}{dx^2} \qquad \ldots\ldots 1.4$$

... where M is the total moment acting on a sectional face (ab); P is the stress acting parallel to the trend of the plate; Q is the shear stress acting on a sectional face; q is a normal stress resulting from the resistance of the confining matrix to lateral deflection, v, of the plate and h is the total thickness of the plate. (All forces and moments are calculated for a unit depth into the x,y profile plane of fig. 1.5).

Equations 1.3 and 1.4 form the basis of the majority of analyses which are concerned with the initial development of buckling instabilities in a confined plate. The application of these equations to the particular case of a confined viscous multilayer is discussed by

Biot (1965d). Biot was concerned with the stability of sinusoidal deflections of the multilayered plate during the low amplitude phase of fold development. He showed that, under a constant applied load P, any initial sinusoidal deflection of the plate of the form $v = \bar{v} \cos \ell x$ (wavelength $\lambda = 2\pi/\ell$) will amplify as an exponential function of time. The increase in amplitude of a sinusoidal perturbation with time has the form:

$$\bar{v}(t) = \bar{v}(0)\, e^{pt} \qquad \ldots\ldots 1.6$$

where: $\bar{v}(0)$ is the initial amplitude

The incremental rate of amplification of a particular perturbation wavelength can be expressed as the ratio $(d\bar{v}(t)/dt)/\bar{v}(t)$ where:

$$\frac{d\bar{v}(t)}{dt} \cdot \frac{1}{\bar{v}(t)} = \frac{p\, \bar{v}(0)\, e^{pt}}{\bar{v}(0)\, e^{pt}} = p \qquad \ldots\ldots 1.7$$

For a plate/matrix system with specific rheological properties, the rate of amplification of a given perturbation wavelength ($\lambda = 2\pi/\ell$) can be expressed as a function of that wavelength. Since the rate of amplification, p, depends also on the applied load, P, it is convenient to express this dependence in terms of the ratio P/p. For the particular case of a uniform multilayered plate (fig. 1.5) Biot obtained the following relationship (Biot, 1968d, p. 254):

$$\frac{P}{\eta_t p} = 4\eta_m \cdot \frac{1}{\ell h} + \frac{A\ell^2}{A\ell^2 + 1} \qquad \ldots\ldots 1.8$$

where η_m = viscosity of the matrix

$\eta_n = \alpha_1 \eta_1 + \alpha_2 \eta_2$

$\eta_t = \eta_1 \eta_2 / (\alpha_1 \eta_2 + \alpha_2 \eta_1)$

$\ell = 2\pi / \lambda$

h = total thickness of the plate

where: $$A = \frac{1}{3} \cdot \frac{\eta_n}{\eta_t} \cdot h^3$$

The reader is referred to Biot (1965d) for a description of the derivation of equation 1.8 and of the assumptions adopted in the analysis. The equation is restricted to a description the rate of amplification of particular perturbation wavelengths during the low amplitude stages of buckling. (It is assumed, for example, that the wavelength and plate thickness are not functions of time).

The form of equation 1.8 leads to the prediction of a dominant wavelength. Equation 1.8 can be used to graph the relationship between amplification rate (P/p) and the wavelength of the plate perturbation. The minimum in this relationship corresponds to that wavelength which will amplify at the fastest rate (p maximum) - the dominant wavelength. The dominant wavelength can be found, for any given plate/matrix system, by differentiating equation 1.8 with respect to ℓ and solving the resultant expression for the maximum growth rate condition $d(P/p)/d\ell = 0$. A discussion of the concept of a dominant wavelength and the associated phenomenon of wavelength selection is given in Biot (1961).

The significance of the analysis described in the preceeding paragraphs lies in Biot's discussion of the buckling behaviour of the confined plate and the influence of mechanical anisotropy of the plate on this behaviour. (Biot, 1965d, pp. 254-258). Biot showed that the form of internal deformation which characterises this buckling behaviour is a function of the collective or bulk anisotropy of the plate as expressed by the ratio of viscosity coefficients η_n η_t. Consider, for example, the extreme case in which the layering indicated in fig. 1.4 is mechanically passive ($\eta_1 = \eta_2 = \eta$) and the plate is isotropic.

For this case, the compressional and shear stiffness coefficients η_n and η_t are equal and given by $\eta_n = \eta_t = \eta$, and equation 1.8 becomes:

$$\frac{P}{p} = \frac{4\eta_m}{\ell h} + \frac{1/3.\ell^2.h^2}{1/3.\ell^2.h^2 + 1} \cdot \eta$$

If this equation is applied only to systems with a relatively large contrast in the viscosities of plate and matrix then it can be shown (Biot, 1961) that $\ell^2 h^2 \ll 1$ and:

$$\frac{P}{p} \simeq \frac{4\eta_m}{\ell h} + \frac{1}{3}\ell^2 h^2 \eta \qquad \ldots\ldots 1.9$$

The dominant wavelength, λ_d, can be obtained from the condition:

$$\frac{d(\frac{P}{p})}{d\ell} = -\frac{4\eta_m}{\ell h} + \frac{2}{3}\ell h^2 \eta = 0 \qquad \ldots\ldots 1.9a$$

Solving equation 1.10 for λ_d:

$$\frac{\lambda}{h}_d = \frac{2\pi}{\ell_d h} = 2\pi\sqrt[3]{(\eta/6\eta_m)} \qquad \ldots\ldots 1.10$$

This equation is the familiar Biot-Ramberg expansion for the dominant wavelength of a confined, isotropic plate.

The form of internal deformation which characterises the buckling of an isotropic plate or of a multilayered plate with a low contrast between the viscosity coefficients of the alternating competent and incompetent laminae is illustrated in fig. 1.6A. Deformation marker lines drawn initially perpendicular to the plate boundaries remain perpendicular to these boundaries during the initial stages of buckling. The overall deformation of the plate has the form called tangential longitudinal strain by Ramsay (1967). This type of folding is associated with fold wavelengths which are large in comparison with the total thickness of the multilayer.

If the collective anisotropy of a multilayer is relatively high ($\eta_n \gg \eta_t$) then the internal deformation of the anisotropic plate will

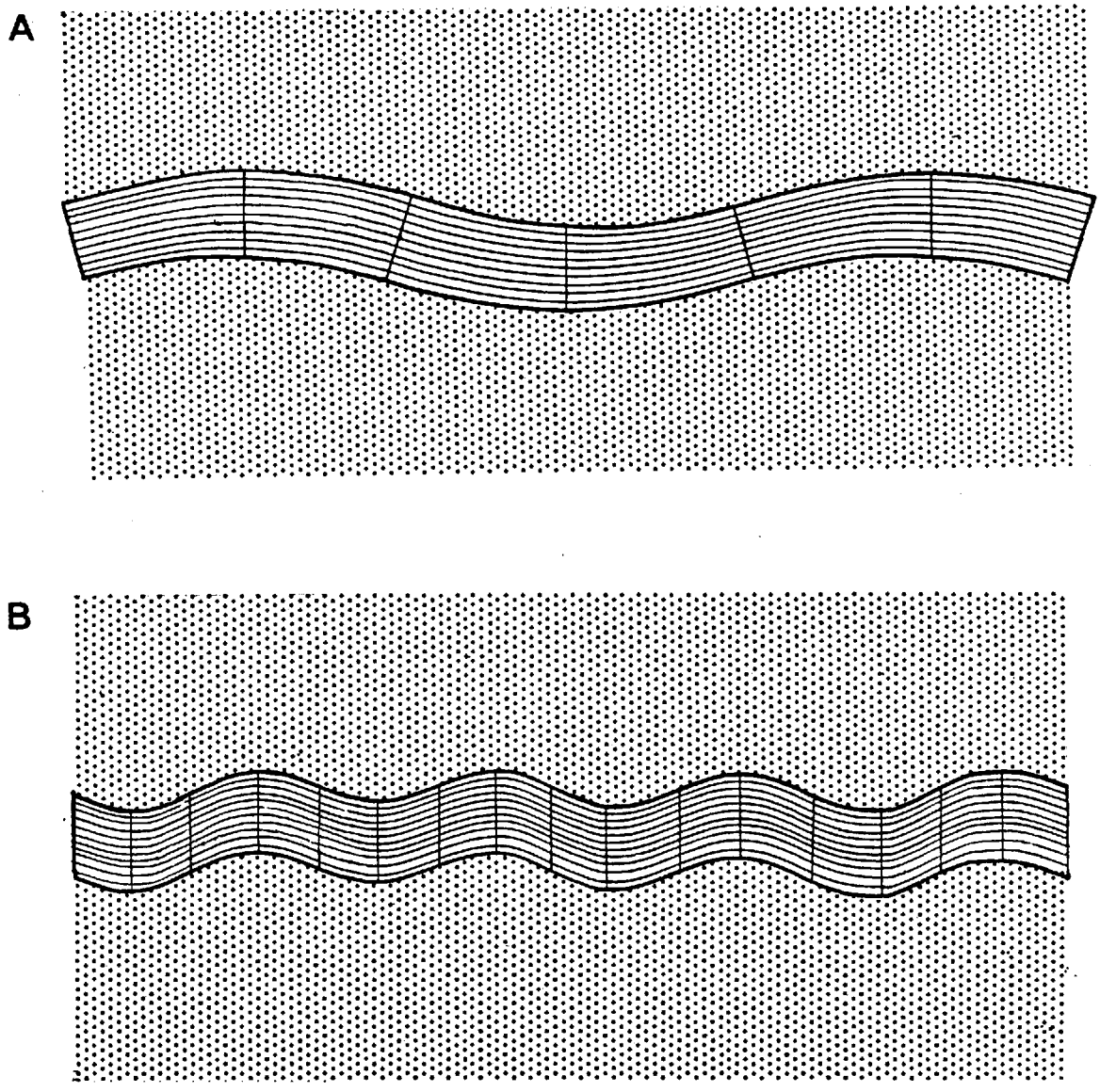


Figure 1.6 Effect of the types of multilayer instability which Biot (1965 d) has called "similar folding of the first kind" (1.6 A) and "similar folding of the second kind" (1.6 B) on the macroscopic defomation of a series of passive marker lines drawn initially normal to the plane of the multilayer.

tend toward the form shown in fig. 1.6B. In this case, a series of marker lines drawn normal to plate boundaries remain parallel, and do not rotate during the initial stages of fold amplification. The total deformation of the plate resembles the deformation which would be produced by heterogeneous simple shear parallel to the fold axial planes. This type of behaviour is associated with fold wavelengths which are small and of the same order as the total thickness of the multilayer ($\lambda_d/h \rightarrow 1$).

The contrasting styles of deformation illustrated in figs. 1.6A and 1.6B have been called "similar folding of the first kind" and "similar folding of the second kind" by Biot (1965d, pp. 254-255). They represent end members of a complete range of internal deformation styles with 'second kind' folding being associated with multilayers with a high degree of mechanical anisotropy. The transition from 'first kind' to 'second kind' similar folding involves not only a change in geometry of internal displacements within a layered plate, however, but also a significant change in the mechanism which underlies the development of the fold instability. The underlying mechanism of similar folding of the first kind is an overall flexing or buckling of the total thickness of the plate which is equivalent to the simple buckling of an isolated elastic beam or plate under an end load. This type of behaviour matches the classic engineering concepts of buckling. In contrast, the mechanism which underlies the amplification of fold instabilities by second kind similar folding is related to the phenomenon of non-coaxial deformation in an anisotropic continuum.

This important point can be clarified by considering the mechanical significance of the property of bulk anisotropy which Biot assigned to the multilayered plate in the analysis described in the preceeding paragraphs. As has been indicated, Biot investigated the deformational behaviour of the multilayered plate, not in terms of the response to stress of individual components of the multilayer, but in terms of the total deformation of an equivalent homogeneous plate with anisotropic properties. These properties represent, statistically, the influence of the fine structure of the multilayer.

In the analysis, the directional mechanical properties of a simple two component multilayer are expressed in terms of two contrasting bulk viscosities η_n and η_t. The coefficients are equivalent

to the principal stiffness coefficents of the layered material. Cobbold (1976) has presented a more general method of describing the bulk mechanical properties of multilayered or foliated material which he has used as the basis for an analytical model of the incremental and finite amplification of symmetric similar folds in such materials. The approach used by Cobbold will be considered in some detail because it clarifies the nature of the fold mechanism which is associated with the development of second kind similar fold instabilities and can also be used to demonstrate the mechanical significance of layer or foliation anisotropy and the important role which this factor can play in the active amplification of a wide range of natural multilayer folds.

In order to represent the bulk mechanical properties of a uniform, layered or foliated material in terms of the properties of an eqivalent homogeneous continuum it is necessary to obtain an expression for the relationship between stress and incremental strain in that continuum. The most general relationship between components of the three dimensional stress (σ_{ij}) and strain (e_{mn}) tensors in an anisotropic continuum has the form (Nye, 1957) :

$$\sigma_{ij} = C^{ij}_{mn} \cdot e_{mn}$$

..... where the superscript and subscript notation implies the usual summation convention.*

For a continuum with viscous properties, the components of the stiffness matrix C^{ij}_{mn} are linear viscous operators. It is convenient to express the deformational characteristics of such a material in terms of a general eqation relating components of stress to components of incremental strain rate ($\dot{e}_{mn}$).

$$\sigma_{ij} = V^{ij}_{mn} \cdot \dot{e}_{mn}$$

..... where $C^{ij}_{mn} = V^{ij}_{mn} \cdot \left(\frac{d}{dt}\right)$

* *The sign conventions adopted in this thesis for stress and strain / strain rate are given in appendix 2.1*

In the most general type of anisotropic deformation the stiffness matrix, V^{ij}_{mn}, has 81 independent coefficients relating the 9 components of the stress tensor to the 9 components of the incremental strain rate tensor. However, the problem of specifying the form of the stiffness matrix can be considerably simplified by examining the form of symmetry of the matrix that is required to model the incremental response to stress of a discretely layered or foliated body of material and by placing certain restrictions on the type of deformation to be considered.

For the purpose of this discussion, it is necessary to obtain a relationship between stress and incremental strain rate for an element of a homogeneous continuum (fig. 1.7 B) whose deformational characteristics represent those of an equivalent element of a discretely layered material (fig. 1.7 A). The symmetry of the mechanical properties of the layered element can be described with reference to a set of orthogonal axes a, b and c. The ab plane represents the plane of layering. If the individual components of the layered element are isotropic then the properties of the element identified in fig. 1.7 A will be constant along any direction within the ab plane with c as an axis of radial symmetry. The representative continuum element (fig. 1.7 B) has an eqivalent anisotropic symmetry with symmetry axes which are directionally equivalent to the axes a, b and c. The ab symmetry plane is represented by the dashed planes shown in fig. 1.7 B.

The following restrictions are placed on the type of deformation to be considered :

(i) The deformation is referred to a set of orthogonal reference axes x, y and z. The axes are oriented with z lying within the ab symmetry plane of the material elements.

(ii) Deformation is plane strain within the x,y plane.i.e. $e_{zz} = 0$.

(iii) Deformation of the layered element and, by analogy, the homogeneous continuum element, occurs at constant volume. i.e. $e_{xx} + e_{yy} = 0$.

(iv) σ_{zz} is a principal stress. This implies $e_{xy} = e_{yx} = 0$.

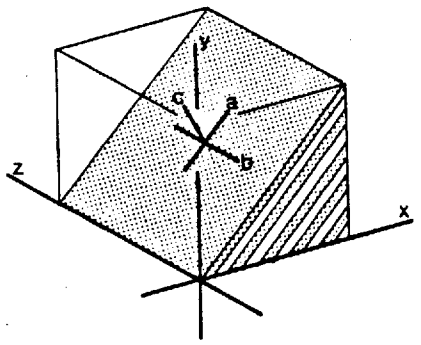


Figure 1.7 A

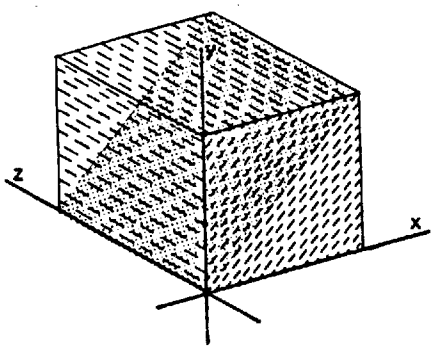


Figure 1.7 B

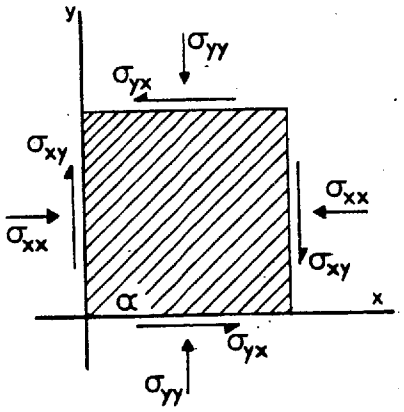


Figure 1.7 C

Cobbold (1976) has shown that, under these conditions, the bulk deformation of the multilayer element can be represented by the following, relatively simple relationship between the stress and incremental strain rate tensors of the representative homogeneous anisotropic continuum (Cobbold, 1976, equation 16).

$$\sigma'_{xx} = 2N_\alpha \dot{e}_{xx} + 2T_\alpha \dot{e}_{xy}$$

$$\sigma_{xy} = 2T_\alpha \dot{e}_{xx} + 2Q_\alpha \dot{e}_{xy}$$

..... where the prime notation indicates deviatoric stress $\sigma'_{xx} = (\sigma_{xx} - \sigma_{yy})/2$

These equations can be re-arranged to express the components of incremental strain rate in terms of the components of stress acting in the x,y coordinate plane :

$$\dot{e}_{xx} = \frac{1}{4(N_\alpha Q_\alpha - T_\alpha^2)} \left[2Q_\alpha \sigma'_{xx} - 2T_\alpha \sigma_{xy} \right] \quad \ldots\ldots 1.13$$

$$\dot{e}_{xy} = \frac{1}{4(N_\alpha Q_\alpha - T_\alpha^2)} \left[-2T_\alpha \sigma'_{xx} + 2T_\alpha \sigma_{xy} \right] \quad \ldots\ldots 1.14$$

The three stiffness coefficients N_α, Q_α and T_α are sufficient to quantify the plane strain response of the continuum element shown in fig. 1.7 B (and, by mechanical analogy, that of the multilayered element shown in fig. 1.7 A) to the plane stress system σ_{xx}, σ_{yy} and σ_{xy} (fig. 1.7 C) under the conditions listed above. The three components of the stiffness matrix, N_α, Q_α and T_α are not, however, invariant properties of the continuum element and the magnitude of these coefficients depends on the orientation of the analysis reference coordinates x and y with respect to the material symmetry planes of the continuum. Cobbold has shown that the magnitude of the coefficients can be expressed in terms of two principal stiffness coefficients N and Q whose product $N.Q = 1/(N_\alpha Q_\alpha - T_\alpha^2)$ is an invariant of the stiffness matrix. (see also Casey, 1976, pp. 193-195). The physical significance of N and Q has been discussed by Cobbold et al. (1971). The orientation of the material symmetry planes can be defined by the angle α shown in fig. 1.7 C.

The following relationships can be obtained for the orientation dependence of the coefficients N_α, Q_α and T_α (Cobbold, 1976, equation 13)*:

$$N_\alpha = -\left(\frac{1}{2}(N + Q) + \frac{1}{2}(N - Q)\cos 4\alpha\right) \quad \ldots\ldots 1.15a$$

$$Q_\alpha = +\left(\frac{1}{2}(N + Q) - \frac{1}{2}(N - Q)\cos 4\alpha\right) \quad \ldots\ldots 1.15b$$

$$T_\alpha = -\left(\frac{1}{2}(N - Q)\sin 4\alpha\right) \quad \ldots\ldots 1.15c$$

Introducing equations 1.15 into equations 1.13 and 1.14 gives:

$$\dot{e}_{xx} = -\dot{e}_{yy} = \frac{1}{4NQ}\left[-\left((N + Q) - (N - Q).\cos 4\alpha\right)\sigma'_{xx} + (N - Q).\sin 4\alpha.\sigma_{xy}\right] \quad \ldots. 1.1$$

$$\dot{e}_{xy} = \frac{1}{4NQ}\left[-(N - Q).\sin 4\alpha.\ \sigma'_{xx} + \left((N + Q) + (N - Q).\cos 4\alpha\right)\sigma_{xy}\right] \quad \ldots. 1.1/$$

These equations can be used to calculate the finite strain tensor (plane strain, constant volume deformation) for the body of material defined in fig. 1.7C given the orientation α of the ab material symmetry plane.

The physical significance of the principal stiffness coefficients N and Q can be demonstrated by examining the incremental response of a continuum element for three special values of α ($\alpha = 0^\circ, 90^\circ, 45^\circ$).

(A) $\underline{\alpha = 0^\circ}$

For this orientation:

$$N_\alpha = N$$

$$Q_\alpha = Q$$

$$T_\alpha = 0$$

Introducing these identities into equations 1.13 and 1.14 :

Note the sign conventions adopted in this thesis (see appendix 2.1)

$$\dot{e}_{xx} = -\frac{1}{4NQ} \cdot 2Q \cdot \sigma'_{xx} \qquad \ldots\ldots 1.18$$

$$\dot{e}_{xy} = +\frac{1}{4NQ} \cdot 2N \cdot \sigma_{xy} \qquad \ldots\ldots 1.18a$$

For the special case where σ_{xx} and σ_{yy} are principal stresses σ_1 and σ_3, respectively :

$$\dot{e}_{xx} = -\frac{(\sigma_1 - \sigma_3)}{4\ N} \qquad \ldots\ldots 1.19$$

$$\dot{e}_{xy} = 0 \qquad \ldots\ldots 1.19a$$

Inspection of equations 1.19 and 1.19a shows:

(i) The continuum is incrementally isotropic for a principal compression, σ_1, directed within the ab plane (i.e. $\sigma_{xy} = 0 \rightarrow \dot{e}_{xy} = 0$ when $\alpha = 0$).

(ii) The stiffness coefficient N is a measure of the resistance the continuum to direct compression along the plane of transverse isotropy.

The coefficient N is equivalent to the bulk viscosity of a multi-layered material with respect compression along the direction of the layering ($N \equiv \eta_n$).

(B) $\underline{\alpha = 90^\circ}$

For this orientation :

$$N_\alpha = N$$

$$Q_\alpha = Q$$

$$T_\alpha = 0$$

Introducing these identities into equations 1.13 and 1.14 :

$$\dot{e}_{xx} = -\frac{1}{4NQ} \cdot 2Q \cdot \sigma'_{xx} = -\frac{\sigma'_{xx}}{2N} \qquad \ldots\ldots 1.21$$

$$\dot{e}_{xy} = -\frac{1}{4NQ} \cdot 2Q \cdot \sigma_{xy} = -\frac{\sigma'_{xy}}{2Q} \qquad \ldots\ldots 1.22$$

A comparison of equations 1.21 and 1.22 with equations 1.18 and 1.18a shows that the orientations $\alpha = 0$ and $\alpha = 90^{o}$ are mechanically equivalent. Thus the continuum is incrementally isotropic under a principal compression, σ_1, acting normal to the ab plane. Inspection of equation 1.22 shows that the principal stiffness coefficient Q is a measure of the resistance of the anisotropic continuum to shear along the plane of transverse isotropy. Q is equivalent to the bulk viscosity of a multilayered material with respect to shear parallel to the layering ($Q \equiv \eta_t$).

(C) $\underline{\alpha = 45^{o}}$

For this orientation :

$$N_\alpha = Q$$
$$Q_\alpha = N$$
$$T_\alpha = 0$$

Introducing these identities into equations 1.13 and 1.14 :

$$\dot{e}_{xx} = -\frac{1}{4NQ} \cdot 2N \cdot \sigma'_{xx} = -\frac{\sigma'_{xx}}{2Q} \qquad \ldots\ldots 1.23$$

$$\dot{e}_{xy} = -\frac{1}{4NQ} \cdot 2Q \cdot \sigma'_{xy} = -\frac{\sigma_{xy}}{2N} \qquad \ldots\ldots 1.24$$

Inspection of equations 1.23 and 1.24 shows that a rotation of the plane of transverse isotropy from $\alpha = 0^o$ to $\alpha = 45^o$ effectively inverts the material stiffness N , with respect to compression along x, from $N_\alpha = N(\alpha = 0^o)$ to $N_\alpha = Q$ $(\alpha = 45^o)$ and the material stiffness Q_α, with respect to shear along x, from $Q_\alpha = Q$ $(\alpha = 0^o)$ to $Q_\alpha = N$ $(\alpha = 45^o)$. This inversion will produce a significant decrease in effective compressional stiffness, N_α, if the continuum has a degree of mechanical anisotropy ($N \gg Q$). Some of the implications of this modulus inversion have been discussed by Cobbold et al (1971). (See Section 1.2.2). Inspection of equations 1.23 and 1.24 also shows that the continuum is incrementally isotropic under a principal compression, σ_1, applied at 45° to the ab plane (i.e. $\sigma_{xy} = 0 \rightarrow \dot{e}_{xy} = 0$ for $\alpha = 45^o$).

If the maximum principal compression, σ_1, is applied at any other orientation to the plane of transverse isotropy (i.e. $0^o < \alpha < 45^o$ or $45^o < \alpha < 90^o$) then the principal axes of stress and incremental strain rate do not coincide and the material is incrementally anisotropic. Consider, for example, the general response of an element of the anisotropic continuum to principal stresses σ_1 $(= \sigma_{xx})$ and σ_3 $(= \sigma_{xy})$ - fig. 1.8A. For the special case where σ_{xx} is a principal stress and $\sigma_{xy} = 0$, equations 1.16 and 1.17 become:

$$\dot{e}_{xx} = \frac{1}{4NQ}\left[-\left[(N + Q) - (N - Q)\cos 4\alpha\right]\sigma'_{xx}\right] \qquad \ldots\ldots 1.25$$

$$\dot{e}_{xy} = \frac{1}{4NQ}\left[-(N - Q)\sin 4\alpha \cdot \sigma'_{xx}\right] \qquad \ldots\ldots 1.26$$

It is convenient to express the influence of material anisotropy in these equations in terms of the ratio of principal stiffness coefficients N/Q:

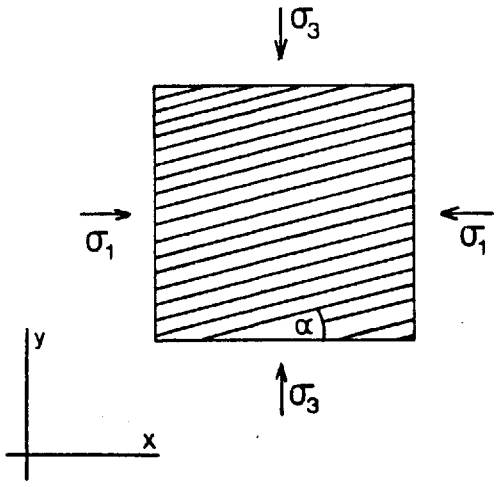


Figure 1.8 A

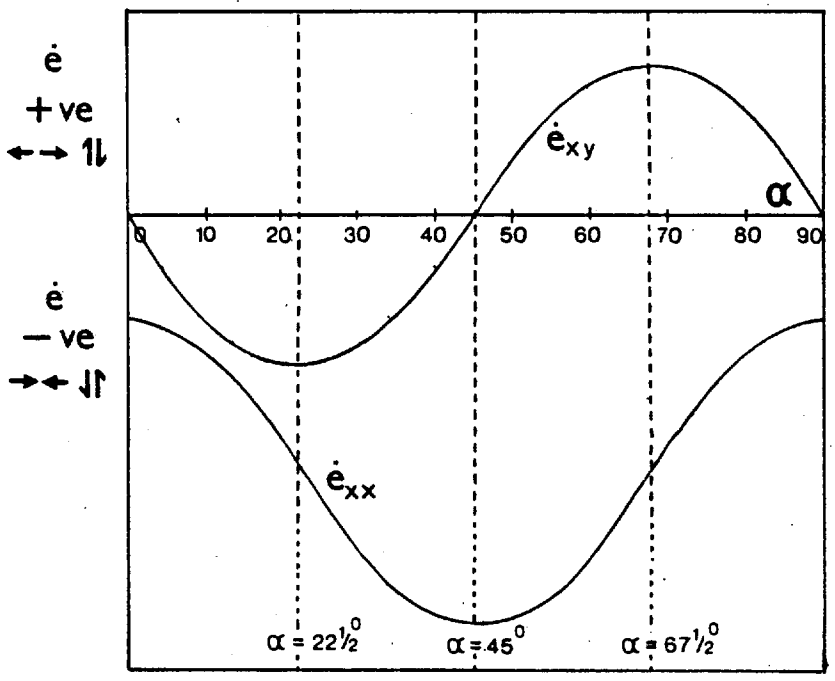


Figure 1.8 B Variation in $\dot{e}_{xx}$ and $\dot{e}_{xy}$ with variation in α for the plane stress system shown in fig. 1.8 A.

$$\dot{e}_{xx} = \frac{\sigma'_{xx}}{4N}\left[-\left[(N/Q + 1) - (N/Q - 1)\cos 4\alpha\right]\right] \quad \ldots\ldots 1.27$$

$$\dot{e}_{xy} = \frac{\sigma'_{xx}}{4N}\left[-(N/Q - 1)\sin 4\alpha\right] \quad \ldots\ldots 1.28$$

The ratio N/Q is equivalent to the ratio of the bulk compressional stiffness coefficient, η_n, to the bulk shear stiffness, η_t, measured along the plane of layering in a discretely layered material .

$$\frac{N}{Q} \equiv \frac{\eta_n}{\eta_t} = \alpha_1^2 + \alpha_2^2 + \alpha_1\alpha_2\left(\frac{\eta_1}{\eta_2} + \frac{\eta_2}{\eta_1}\right)$$

..... where η_1, η_2, η_1 and η_2 have been defined with reference to fig.1.5.

Note, if $\eta_1 >> \eta_2$, then :

$$\frac{N}{Q} \equiv \frac{\eta_n}{\eta_t} \simeq \frac{\eta_1}{\eta_2}$$

The variation in the magnitudes of the incremental strain rate components $\dot{e}_{xx}$ and $\dot{e}_{yy}$ with the angle of inclination α, implied by equations 1.27 and 1.28 is shown diagramatically in fig. 1.8B. α is considered positive in these equations for an anticlockwise rotation of the plane of transverse isotropy with respect to the x reference axis.

The graphical expression of equations 1.27 and 1.28 in fig.1.8B can be used to demonstrate, qualitatively, an important mechanism of fold amplification which is directly related to the mechanical anisotropy of a multilayer or foliated material. This mechanism is invol-

ved in the development of the type of fold instability which Biot has called second kind similar folding (fig. 1.6B).

Consider the implications of equations 1.27 and 1.28 for the low amplitude deformation of the fold illustrated in fig.1.8C. The fold is assumed to be developed in a finely laminated, uniform multilayer with a high degree of bulk anisotropy ($N/Q \equiv \eta_n/\eta_t \gg 1$) and has the low wavelength to total multilayer thickness ratio which is characteristic of similar folding of the second kind. The state of stress within the multilayer is assumed to be uniform with σ_{xx} ($\equiv P$, fig. 1.3) as the maximum principal compressive stress. (σ_1, fig. 1.8C).

If the response of the multilayer to this stress is considered only in terms of the bulk mechanical anisotropy of the multilayer, then a qualitative estimate of this response can be obtained from the stress-strain rate relationships indicated in fig. 1.8C In the hinge region, $\alpha = 0$ and incremental deformation will be coaxial with the applied stress ($\dot{e}_{xy} = 0$). In the limb regions of the structure, however, the principal compression, σ_{xy} acts at a small inclincation, $\alpha > 0$, to the mechanical layering. Consequently this applied stress will produce not only a shortening along its line of action, but also a shear, e_{xy}, expressed as a shear directed parallel to the axial surfaces of the fold. This effect is related to the general non-coaxiality of incremental stress and strain axes in a material possessing a mechanical anisotropy. The sense of shear will be opposite on either side of fold axial plane and the macroscopic expression of resulting variation in deformation across the fold is heterogeneous simple shear. Cobbold (1976) has shown that this mechanism will produce significant rates of layer rotation and of mechanically active fold amplification during the initial stages of amplification of symmetric, similar folds in materials with a mechanically effective planar anisotropy. In the ensuing discussion the mechanism will be referring to as rotational instability.

The equations which form the basis of the homogeneous anisotropic continuum analogy for the deformational behaviour of a discretely layered material do not contain terms which reflect the internal resistance of that material to bending deformation. (i.e. these equations neglect the individual and combined resistance of competent laminae within a uniform multilayer to flexing and can be applied with confidence only to a material in which the thickness of individual laminae is insignificant composed with the total dimensions of the

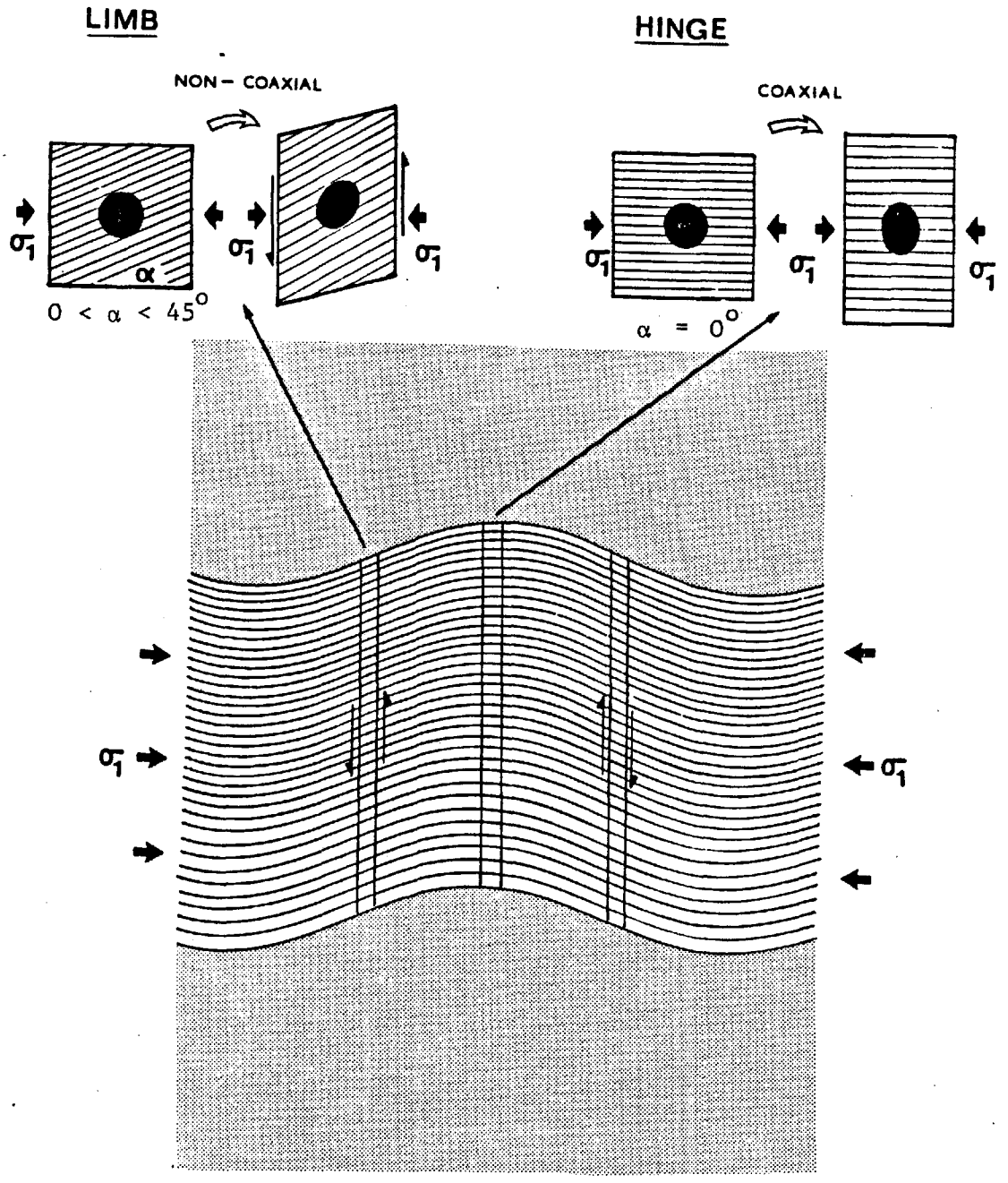


Figure 1.8 C Relationship between the phenomenon of of non-coaxial deformation in an anisotropic material and the development of macroscopic heterogeous simple shear parallel to the axial plane of a "second kind similar fold" . During the low amplitude phase of fold development the degree of non coaxiality and the rate of axial plane parallel shear ($\dot{e}_{xy}$) is maximum for a limb dip α of $22\frac{1}{2}^o$ - see fig. 1.8 B.

material under investigation.

This neglect has important consequences for any analysis in which the response to stress of a multilayer is considered solely in terms of the mechanical effects of layer anisotropy. In Biot's analysis of a multilayer/matrix system, for example, this neglect is not serious if the multilayer has a low degree of mechanical anisotropy ($\eta_n/\eta_t \rightarrow 1$). As has been indicated, for this case the multilayer flexes effectively as a uniform plate and the relatively ineffective mechanical anisotropy assigned to the plate merely produces a slight modification of this flexural deformation (first kind similar folding). The analysis must be modified, however, if it is to be applied to significantly anisotropic multilayers. In this case, where the analysis leads to the prediction of short wavelength folding (second kind similar folding) through the mechanism of rotational instability, the flexural stiffness of individual laminae may be significant. Indeed, if it is neglected, as it is in the derivation of equation 1.8, the stability analysis leads to the prediction of a dominant wavelength along the length of the plate which is zero. The physical significance of this result has been discussed, briefly, by Biot (1965d, pp. 256-257) and he resolved the problem by introducing an additional term into equation 1.8 to account for the effect of the individual and combined bending resistance of competent laminae. With the modification equation 1.8 becomes:

$$\frac{P}{\eta_t p} = \frac{4\eta}{\ell h} + \frac{A\ell^2}{A\ell^2 + 1} + \frac{1}{3} \cdot n_c \cdot \frac{\eta_1}{\eta_t} \cdot \ell^2 \cdot \frac{h_1^3}{h} \quad \ldots\ldots 1.29$$

where : h_1 is the thickness of the individual competent laminae.

n_c is the total number of the competent laminae.

This equation leads to the modified prediction of a finite, dominant wavelength in highly anisotropic multilayers.

In the author's opinion, Biot's macroscopic approach to the analysis of a multilayered or foliated material has a number of advantages. As has been indicated, it leads to a recognition of the importance of rotational instability as a mechanism of fold

amplification in well laminated, highly anisotropic multilayers. This mechanism is distinct from the classic concept of plate buckling in layered systems subject to layer parallel compression. This approach can also be used as a basis for investigating the complex problem of finite fold development in multilayered materials. Before considering the importance of the homogeneous anisotropic continuum analogy in finite deformation analyses some remarks will be made about a type of deformation called internal buckling.

Biot (1964, 1965a, 1965c) indentified internal buckling as a mode of fold deformation which can develop either within a multilayer which is contained within an effectively rigid confining medium or as localised, self-confined "packets" of folds within a multilayer of effectively infinite thickness (see Summers, 1970; Cobbold et al. 1971). The existence of internal buckling was first recognised by Biot (1963a) in a rigorous analysis of the stability of a rigidly confined homogeneous continuum with anisotropic mechanical properties. In subsequent papers (Biot, 1964, 1965c), he extended the analysis to investigate internal buckling within a uniform, anisotropic multilayer by taking into account the influence of the bending resistance of competent laminae within such a multilayer. As with similar folding of the second kind, the primary mechanism which underlies the development of internal buckling in a layered material is related to the mechanical anisotropy of that material and the phenomenon of rotational instability.

The theory of internal instability can be applied to an anisotropic continuum only for the special cases in which the principal compression is applied parallel to the ab plane, at 45° to the plane or normal to the plane (fig. 1.9). The particular case of interest in this discussion is that of compression parallel to the plane of transverse isotropy, equivalent to compression applied parallel to the layering in an equivalent, discretely layered material.

A detailed discussion of internal buckling will not be given in this section and, for this, the reader is referred to Biot (1963a, 1964 , 1965a), Cobbold et al (1971), Johnson (1970), Cosgrove (1972) and Casey (1976). The most significant results of the analysis are summarised below:

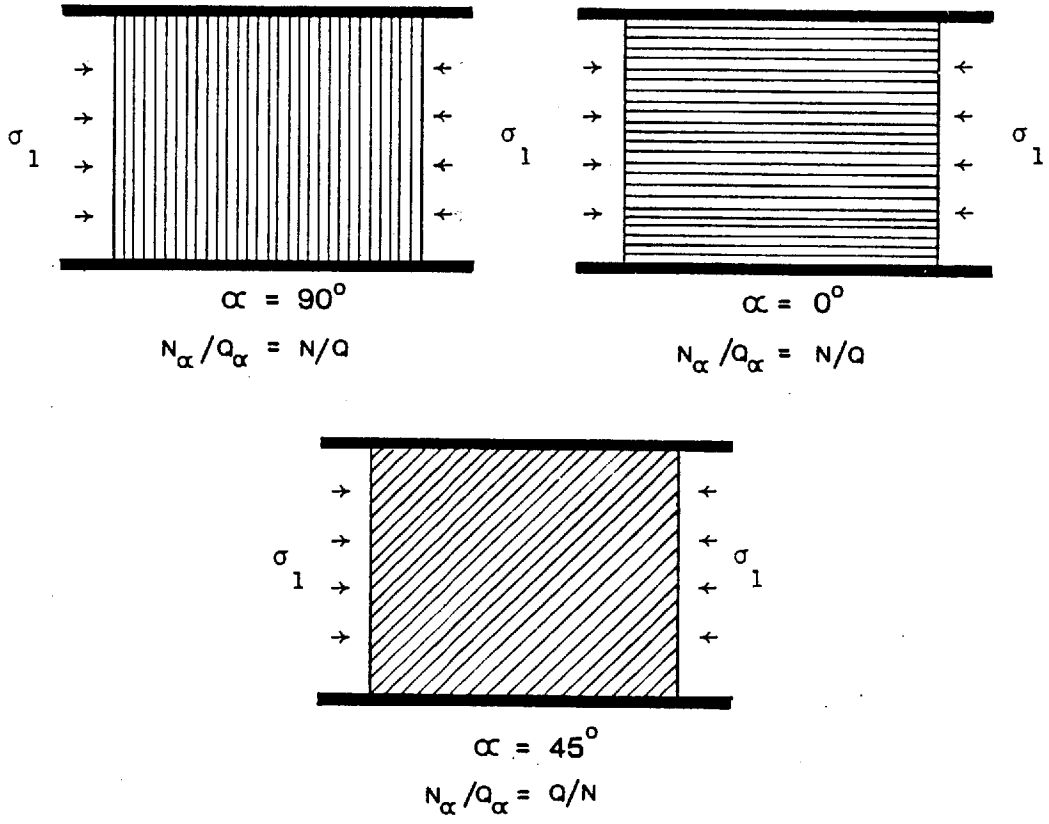


Figure 1.9

(i) Under rigid confinement, a purely viscous anisotropic continuum will be subject to the development of a flow instability which is expressed as an ordered pattern of displacement within the body of the continuum.

(ii) The geometry of the flow instability is a function of the ratio of direct to shear stiffness of the material measured along the direction of applied compression (along x - fig.1.9). This ratio is given by the ratio N_α/Q_α of the continuum where α is inclination of the transverse isotropy plane to the direction of applied compression ($\alpha = 0^\circ$, 45° or 90°).

(iii) For the case corresponding to layer parallel compression within a mechanically equivalent multilayer it is necessary to specify that $\alpha = 0^\circ$ and N_α (= N) > Q_α (= Q). Biot has shown that for $N_\alpha > Q_\alpha/2$, the internal instability analysis leads to the prediction of sinusoidal displacement pattern of the form (fig.1.10):

$$u = - C \ell \xi \cos\ell x \sin\xi\ell y \qquad \ldots\ldots 1.30$$

$$v = C \ell \sin\ell x \cos\xi\ell y \qquad \ldots\ldots 1.31$$

The effect of this displacement pattern on a series of marker lines drawn initially parallel to the direction of applied compression is shown in fig. 1.10. A corresponding pattern of displacement affecting a discretely layered material will produce a continuous train of folds which are sinusoidal along x, with an amplitude (A_y) which is maximum along the central plane of the multilayer ($A_y = 0$) and decreases, as a cosine function, to zero at the confining boundaries according to:

$$A_y = A_{y=0} \cos\xi\ell y$$

The parameter ξ is equal to the ratio of the fold wavelegth along x the wavelength of the amplitude function along y ($\lambda_y = 2h$). In addition, $\tan^{-1}(\xi)$ is equal to slope of a line joining points of inflection along the fold limbs. With respect to the y coordinate axis

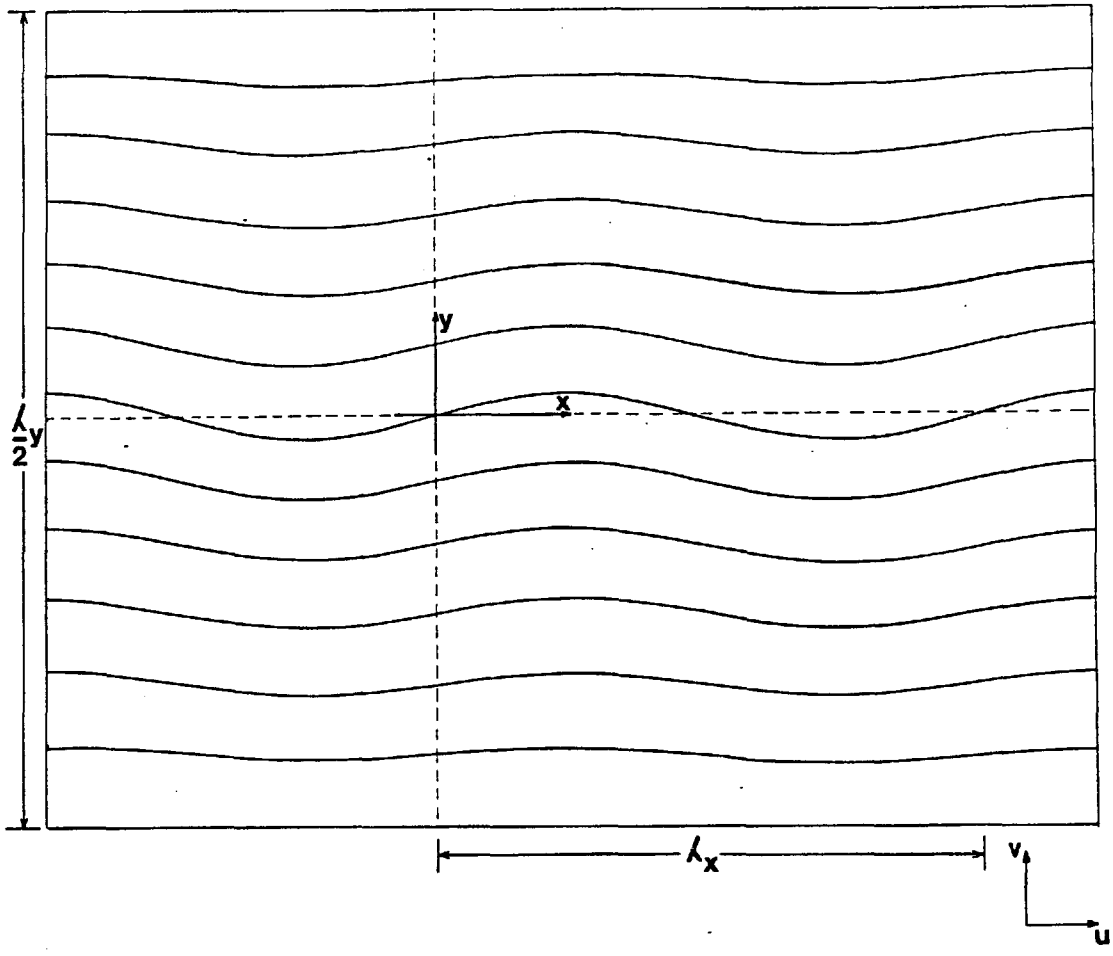


Figure 1.10 Effect of the displacement functions,

$$u = - C \ell \xi \cos\ell x \sin\ell\xi y$$

$$v = C \ell \sin\ell x \cos\ell\xi y$$

on a series of marker lines drawn parallel to the x coordinate before deformation.

This displacement pattern illustrates the low amplitude form of an internal buckling instability (type 1) generated within a uniform, confined multilayer. The wavelengths of this displacement pattern in the x (λ_x) and y (λ_y) coordinate directions are given by :

$$\lambda_x = 2\pi/\ell \ , \ \lambda_y = 2\pi/\ell\xi$$

and

$$\lambda_x/\lambda_y = \xi$$

(iv) The stability analysis gives rise to the following expression for the rate of amplification of sinusoidal displacements of the form given by equations 1.30 and 1.31 :

$$\frac{P}{Q_p} = 1 + 2(N/Q - 1)\xi^2 + \xi^4 \qquad \ldots\ldots 1.32$$

This equation can be compared directly with the equivalent expression (equation 1.8) derived for an anisotropic viscous plate confined by an isotropic viscous matrix. The same method is used to determine the perturbation geometry corresponding to the maximum rate of instability growth i.e. the equation is solved for the perturbation geometry corresponding to the minimum value of P/p. For the case of internal instability, equation 1.32 is solved for the most unstable wavelength ratio ξ. Inspection of equation 1.32 indicates that P/p is minimum for $\xi = 0$. This implies that the most unstable perturbation geometry is associated with a sinusoidal wavelength along x which is zero. The cause of this paradox is the same as that which underlies the prediction of a zero wavelength for similar folding of the second kind, i.e. by analysing the behaviour of a layered material solely in terms of mechanical anisotropy, no account is taken of the flexural resistance of competent laminae. As with the case of second kind similar folding, Biot has shown that it is necessary to add a correction term to the stability equation 1.32 to take this factor into account. (see Biot, 1964, pp. 564-565).

On the basis of Biot's work on multilayer folding it is possible to recognise a continuous sequence of deformation styles associated with the initial stages of fold amplification of a confined multilayer. The type of folding which occurs is primarily a function of the relative magnitudes of the rheological moduli of the multilayer components and matrix. In a viscous system the relevant moduli are η_1 (viscosity coefficient of the competent laminae within the multilayer), η_2 (viscosity coefficient of the incompetent laminae and η_3 (viscosity coefficient of the matrix. The sequence of fold behaviour expressed by the stressed multilayer can be summarised as follows:

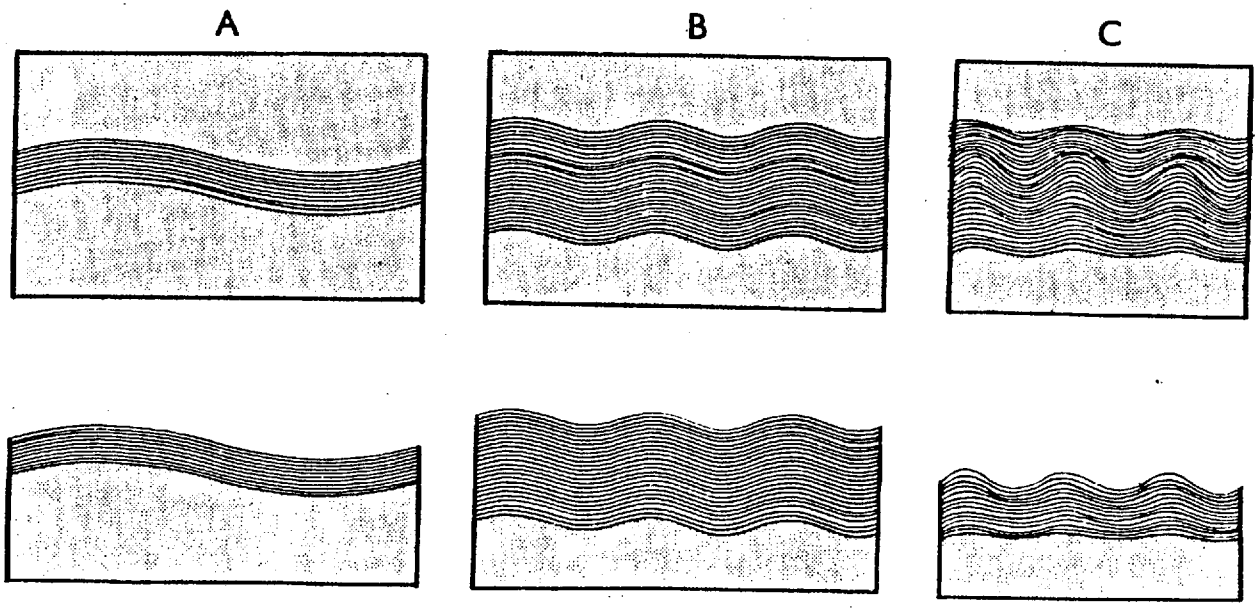


Figure 1.11 Representation of the transition from similar folding of the first kind (1.11 A) through similar folding of the second kind (1.11 B) to internal buckling (1.11 C) shown for a totally confined multilayer (upper sequence) and a partially confined multilayer (lower sequence) - see text for details of the parameters which control the transitions illustrated in this figure.

(a) $\eta_1 \simeq \eta_2$; $\eta_1, \eta_2 > \eta_m$. The multilayer flexes effectively as a single plate and the wavelength of the fold instability is large in comparison with the total thickness of the multilayer (similar folding of the first kind - fig. 1.11A).

(b) $\eta_1 \gg \eta_2$; $\eta_2 < \eta_m$; $\eta_1 \gg \eta_m$. The multilayer fold instability will approach the deformation style which Biot has called similar folding of the second kind. Viewed macroscopically, the internal deformation of the multilayer resembles heterogeneous simple shear parallel to the fold axial planes. This behaviour is associated with a high degree of mechanical instability within the multilayer ($\eta_1 \gg \eta_2 \rightarrow \eta_n \gg \eta_t$) and the development of rotational instability (fig. 1.11B).

(c) $\eta_1 \gg \eta_2$; $\eta_1 \leqslant \eta_n$. The multilayer fold instability will approach the deformation mode which Biot has called internal buckling. The relatively high resistance of the confining matrix inhibits the development of differential displacements of the multilayer boundaries and folding is characterised by a variation in fold amplitude across the thickness of the multilayer (fig. 1.11C).

Biot has shown that the deformation modes illustrated in fig.1.11 can develop either within a totally confined multilayer or in a multilayer, with a free surface, which rests on a uniform, semi-infinite matrix. The latter case is relevant to the problem of the development of fold instabilities in a uniform sedimentary sequence overlying a uniform substrate. The principal effect of a gravitational body forces on the development of fold instabilities, in such a system is to provide an additional constraint on differential displacements of the multilayer boundaries (Biot, 1966). This effectively reduces the magnitude of the dominant wavelength predicted for a given multilayer/matrix system.

1.2.2 THEORETICAL ANALYSES OF THE FINITE DEVELOPMENT OF MULTILAYER FOLDS

Although the work of Biot and others is fundamental to the present understanding of the factors which control the development of fold instabilities in simple multilayer systems, the work is of somewhat limited practical use in the interpretation of natural multilayer folds. Analytical solutions to stability analyses of the type discussed in the preceeding section are generally restricted to a description of the growth of multilayer fold instabilities from

initial layer perturbations which are sinusoidal and extend indefinitely along the plane of layering. In addition, the analyses can be applied, strictly, only to the low amplitude stages of fold development. The geologist is principally interested in natural multilayer folds which have significant finite amplitudes. These structures may develop from initial layer perturbations which are localised rather than periodic and the geometry of both the initial layer perturbation and the associated finite fold structure may be distinctly non-sinusoidal.

At present, the application of techniques of finite deformation analysis, such as finite element analysis, to the problem of multilayer fold development, is somewhat limited. Two approaches have been presented in the literature which can be compared directly with the contrasting methods of analysing the initial stability of multilayers discussed in the preceeding section. The first method is to examine the finite deformation of multilayer folds in terms of the deformation and inter-reaction of individual layer components within the multilayer. This approach has been used by
in finite element analyses of the growth of multilayer folds from a low amplitude, sinusoidal perturbation of the layering. The method is expensive in computer time and, at present, has only been used to study the deformation of very simple multilayers. , for example, applied a finite element analysis to the growth of an initial sinusoidal perturbation in a multilayer "sandwich" made up of three competent viscouslayers separated by incompetent viscous layers. The multilayer is confined within an extensive viscous matrix with the same strength as the incompetent components of the multilayer.

The alternative approach, which involves the representation of the bulk deformational properties of a discretely layered material by those of an equivalent homogeneous anisotropic continuum, has been used by Casey (1976) and Cobbold (1976). These finite deformation analyses are concerned solely with the contribution of layer or foliation anisotropy to the finite growth of particular types of initial layer perturbations, (i.e. active fold amplification by the mechanism of rotational instability). The method used by Casey and Cobbold was to model the incremental response to stress of representative elements of a layered or foliated material within a fold structure in terms of the response of equivalent elements of a transversely isotropic, homogeneous continuum with anisotropic mechanical properties. The

equivalence between the mechanical properties of these two types of materials and the significance of layer anisotropy in the incremental response to stress of a transversely isotropic material element has been outlined in section 2.2.1. It should be noted that the equations used by Casey and Cobbold do not contain terms which would reflect the flexural resistance of competent laminae within a representative element of layered material.

Casey (1976) used the homogeneous anisotropic continuum analogy to simulate the finite development of an initial layer perturbation with the geometry predicted by Biot's theory of internal instability (see fig. 1.10). The boundary conditions assumed in Casey's model are identical to those adopted by Biot in his incremental analysis. The analysis carried out by Casey is therefore relevant to the problem of the finite development of folds in a uniform, statistically homogeneous multilayer confined by effectively rigid boundaries. Because of the neglect of competent laminae bending resistance, Casey's analysis is most accurate for a multilayer in which the thickness of individual laminae is negligable in comparison with the total thickness of the confined multilayer.

Biot obtained an expression (equation 1.32) for the rate of amplification of sinusoidal perturbations as a function of the wavelength ratio ($\lambda_x/\lambda_y = \xi$). Casey chose an arbitrary value for this wavelength ratio in defining the geometry of the initial layer perturbation. The finite amplification of this initial perturbation was then studied by using a sophisticated finite element analysis to integrate successive stages in the deformation of a network of mutually defined material elements. The most significant results of this analysis are summarised briefly below.

(i) During the initial stages of amplification of the perturbation (up to a maximum limb dip of approximately 15°) the rate of amplification is an exponential function of time as predicted by Biot's incremental analysis. For a given value of anisotropy ratio (N/Q) and a given initial wavelength ratio, ξ, the magnitude of this amplification rate is also close to that predicted by Biot's analysis.

(ii) The predictions of Biot's analytical model appear to break down beyond a maximum limb rotation of approximately 15°, and subsequently, the amplification rate becomes an approximately linear

function of time. This decelleration in the fold growth rate first affects the central region of the confined multilayer. The amplitude of the fold profiles toward the boundaries of the multilayer then "catches up" with that of the central zone and this results in the finite development of a zone of approximately constant fold amplitude across a substantial proportion of the confined multilayer. Casey also demonstrated that once the amplitude of the fold profiles within the central region begin to stabilise, after the initial stage of exponential growth, the folds become increasingly angular (i.e. chevron) in geometry. In these respects, the results of the numerical fold simulation compare very favourably with the results of physical model experiments designed to simulate internal buckling in uniform multilayers (see Summers, 1970; Cobbold et al., 1971, Latham, in press).

Cobbold (1976) has described an important analysis in which the homogeneous continuum analogy is applied to the problem of the finite amplification of symmetric similar folds. This finite deformation analysis is used to investigate the growth of an initial foliation disturbance with the geometry shown in fig. 1.12. An important assumption in the analysis is that the profile geometry of successive foliation surfaces is constant along the axial trace of the fold (along the y axis of fig. 1.12) throughout deformation. Thus the fold structure remains similar in the definition of Ramsay (1967) and is assumed to extend indefinitely through a multilayer of effectively infinite thickness. (It should be noted that the type of structure investigated by Cobbold is formally equivalent to an internal instability with a wavelength ratio λ_x/λ_y which is effectively zero, i.e. the total thickness of the confined multilayer is given by $h \to \infty$ and $\lambda_x/\lambda_y = \lambda_x/2h \to 0$.)

The assumption of an invariant amplitude along y introduces a number of important simplifications into the finite deformation analysis. Cobbold obtained a series of analytical expressions which define, completely, the incremental and finite deformation of symmetric, similar folds through the mechanism of rotational instability. On the basis of these analytic expressions, Cobbold discussed the role of mechanical anisotropy in the growth of symmetric similar folds and the influence of mechanical anisotropy on the finite geometry of such structures.

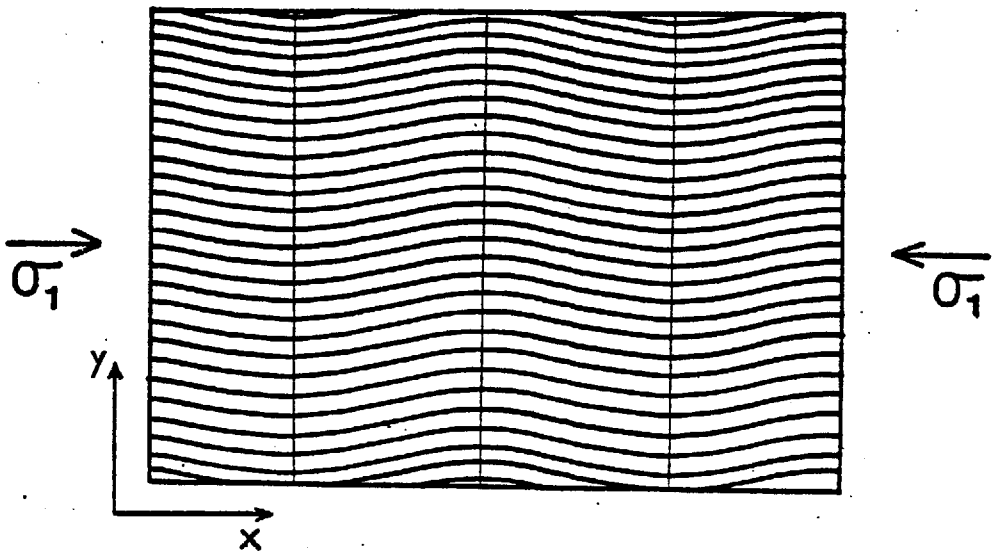


Figure 1.12 Form of initial foliation perturbation assumed by Cobbold (1976) in a finite deformation analysis based on the anisotropic continuum analogy.

The writer has developed a finite deformation analysis, based on the anisotropic continuum analogy, which is logical extension of the approach used by Cobbold. This analysis was designed to simulate the finite deformation of a low amplitude layer or foliation perturbation of the form shown in fig. 1.13. The structure has the geometry of a low amplitude kink band or monocline and is defined as a tabular zone of rotated layering or foliation which lies oblique to the general trend of the foliation outside the domain.

A detailed discussion of the assumptions adopted in the analysis, the method of construction of the analysis and the results are presented in chapters 2 and 3. Before considering the model in detail, however, some remarks should be made on the present understanding of the factors which may favour the development of conjugate kink instabilities rather than any other fold style in a confined multilayer subjected to layer parallel compression.

Two contrasting types of mechanical analysis have been presented in the literature which are relevant to this problem:

(i) COBBOLD ET AL (1971)

Cobbold et al. presented an analysis in which an attempt is made to determine the properties of a multilayer or foliated material which control whether folds develop as symmetric structures of the type shown in fig. 1.14A or as conjugate kinks as in fig. 1.14C. A similar, though less detailed analysis, is given by Johnson (1970).

The analysis is based on an extension of Biot's discussion of the development of internal instabilities in confined anisotropic materials (Biot, 1965a). In using Biot's analysis, Cobbold et al. concentrated on the role of layer or foliation anisotropy as the principal parameter which controls structural style in a well laminated or foliated materials. They recognised in Biot's discussion of the physical expression of internal instability a possible explanation for the development of fold structures with axial surfaces oblique to the direction of applied maximum compression (e.g. conjugate kinks or conjugate folds). Biot has shown that the form of internal instability which develops within a confined anisotropic continuum is a function of the ratio of direct to shear modulus measured along the direction of applied compression. In a viscous anisotropic continuum, this ratio is given by N/Q (see section 1.2.1) The physical expression of internal instability

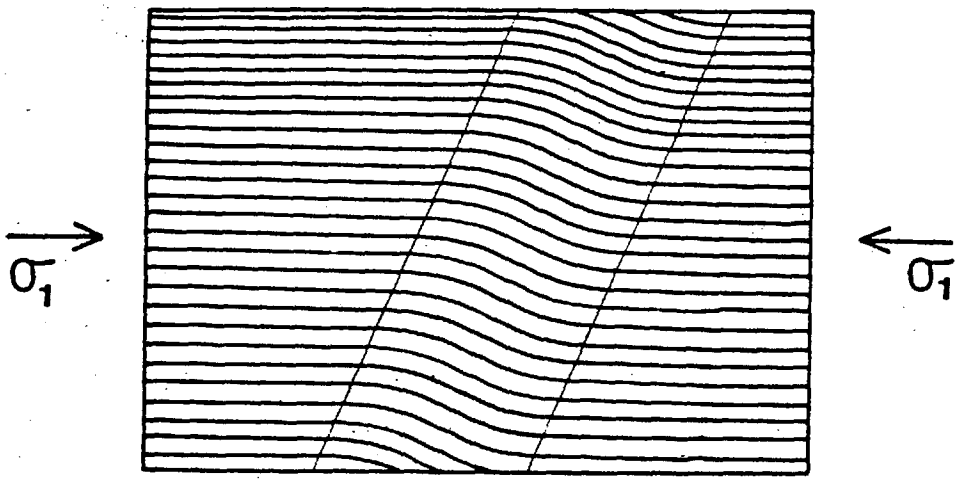


Figure 1.13 Form of initial foliation perturbation assumed in the rotation domain analysis described in chapters 2 and 3.

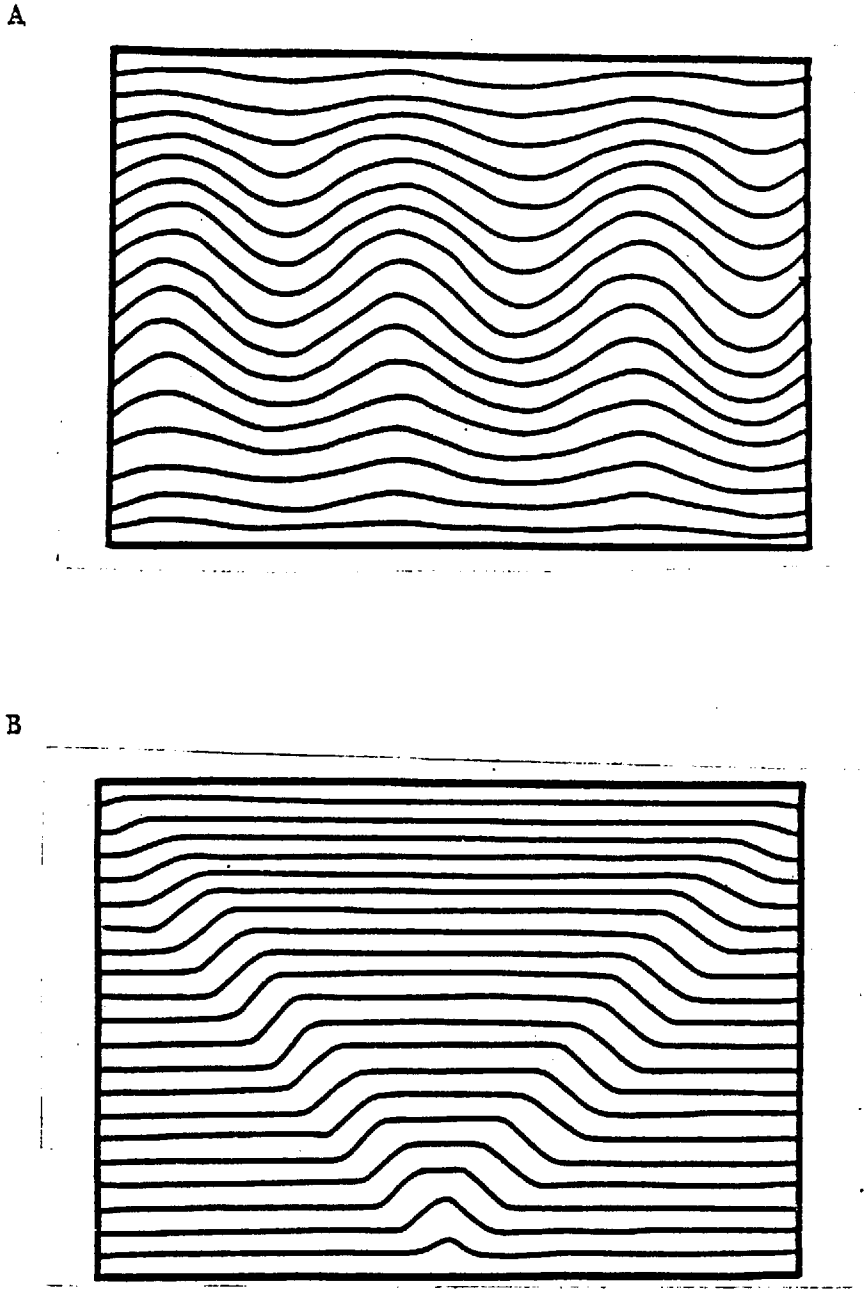


Figure 1.14 Contrasting fold styles developed within a confined mulilayer under a maximum compression acting initially, parallel to the plane of layering.

can take two forms which Biot has called type 1 and type 2 instabilities. Type 1 instabilities are predicted for a ratio of direct to shear modulus, N_α/Q_α, which is greater than 0.5. This will be the case for compression applied along the plane of layering in a discretely layered viscous continuum. The physical expression of type 1 instabilities has previously been discussed in section 1.2. with reference to fig. 1.10. The instability is associated with the development of internal buckles, characterised by axial surfaces which are normal to the direction of applied compression and to the initial orientation of the layering.

Cobbold et al were particularly interested in the relevance of the second type of internal instability (type 2) to the problem of conjugate kinking. Type 2 instabilities are predicted in a viscous anisotropic continuum where the direct stiffness N_α measured along the direction of applied compression is less than the shear modulus Q_α (specifically, $N_\alpha/Q_\alpha < 0.5$). Following Biot, Cobbold et al recognised that this condition applies to a discretely layered material in which the compression is applied at 45° to the plane of layering. It has been shown in section 1.2. that the modulus ratio N_α/Q_α is given by:

$$\frac{N_\alpha}{Q_\alpha} = \frac{Q}{N}$$

... for $\alpha = 45^\circ$, where N and Q are the stiffness coefficients of the layered material with respect to layer parallel compression and layer parallel shear respectively.

Biot illustrated the physical expression of type 2 instabilities by the effect of these instabilities on a confined layered material. This diagram is reproduced in fig. 1.15A. An important concept Biot's discussion of the form of type 1 and type 2 instabilities is the mathematical concept of characteristic directions. The physical significance of characteristic directions in the context of Biot's analysis has been discussed in detail by Cobbold (1972) and has been applied, somewhat speculatively, to a wide range of geological structures by Johnson and Ellen (1974). The theory of internal stability leads a prediction of the orientation of characteristic directions as

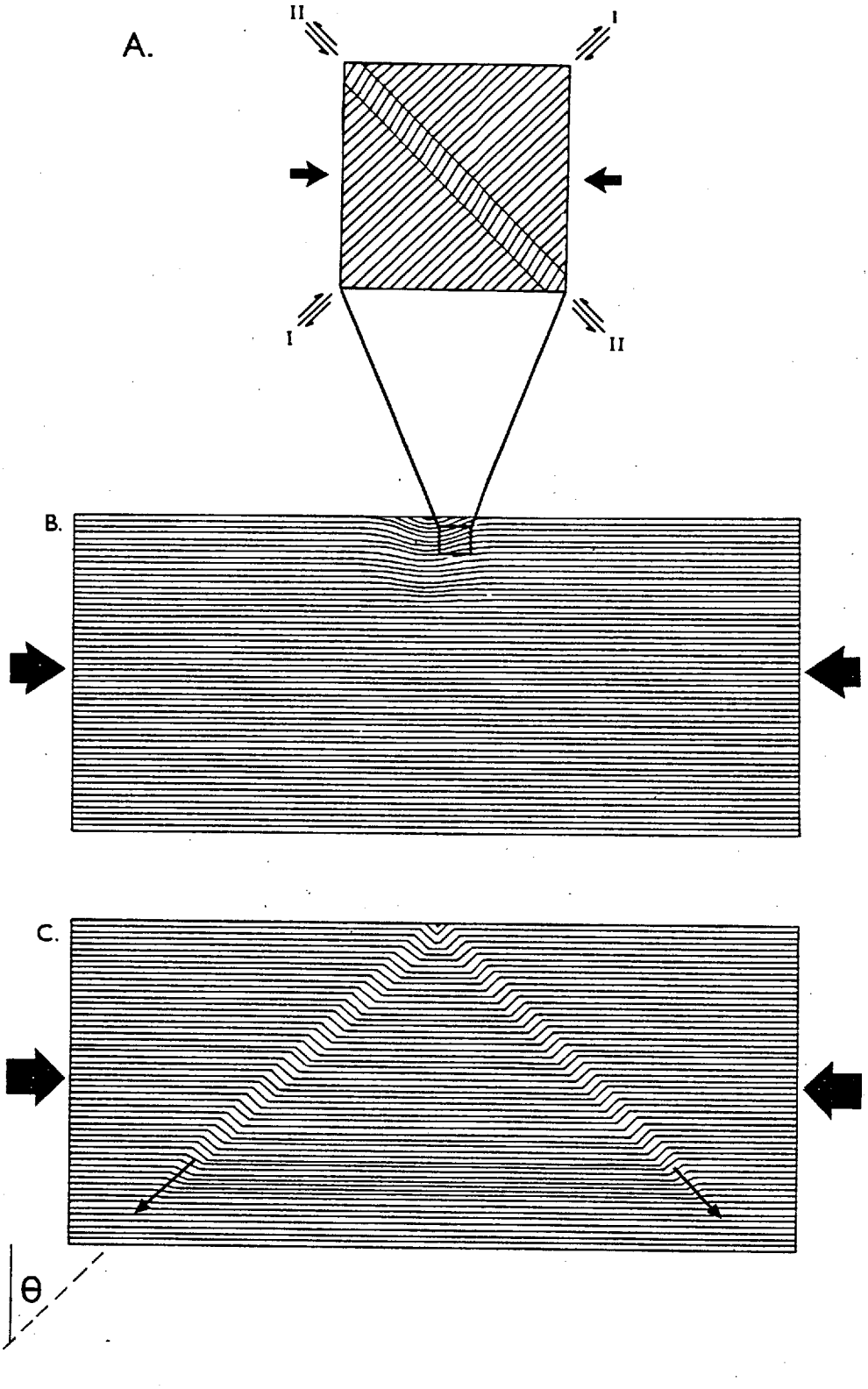


Figure 1.1 Mechanism of kink initiation proposed by Cobbold, Cosgrove and Summers, 1971. See text for details

a function of the modulus ratio N_α/Q_α. Specifically, type 1 instabilities tend to propagate along characteristic directions which are normal to the direction of applied compression. Cobbold et al relate this to the development of upright symmetric structures with axial surfaces normal to the compression direction. Type 2 instabilities are predicted to develop about characteristic directions which are symmetrically disposed, in orientations oblique to the compression direction. Biot illustrates the physical expression of type 2 characteristic directions in a layered material (fig. 1.15A) as (I) slip parallel to the plane of layering and (II) a complimentary band of layer rotation in the form of a kink.

Biot's suggestion that type 2 internal instabilities could take the form of kink-like rotation domains was taken up by Cobbold et al. There is an obvious problem, however, in applying this suggestion directly to the development of conjugate kink structures in a confused multilayer under layer *parallel* compression. As has been indicated, the ratio N_α/Q_α for layer parallel compression will be greater than 0.5 and the theory indicates that this situation will be characterised by the initiation of upright sinusoidal folds (type 1). In order to resolve this paradox, Cobbold et al suggested that kink initiation may result from the development of type 2 instabilities in a locally confined element of a multilayered material rather than through the response of the whole multilayer. The situation envisaged by Cobbold et al is summarised, diagrammatically, in fig. 1.15B. A locally defined element of layered material on the flank of a zone of layer perturbation is examined for the development of internal instability as if it were a rigidly confined anisotropic continuum. On the basis of this reasoning, the authors imply that the locally developed internal instability would be associated with the locally reduced modulus ratio N_α/Q_α. Thus the local instability would be type 2 if the inclination, α, of the layering with respect to the compression direction is sufficient to reduce the effective modulus ratio N_α/Q_α below the threshold $N_\alpha/Q_\alpha < 0.5$. Instabilities would develop along characteristic directions oblique to the applied compression and propagation along one characteristic could take the form of a kink band. (fig. 1.15C).

Cobbold et al. qualified this suggestion by examining the only case of inclined layering to which Biot's internal instability analysis

can be applied i.e. a local element in which the foliation inclination is given by $\alpha = 45^{o}$. The local modulus ratio N_{α}/Q_{α} for such an orientation is given by Q/N. Thus, if the principal stiffness coefficients, N and Q, of a layered or foliated material are defined, the locally effective modulus $N_{\alpha}/Q_{\alpha} = Q/N$ can be substituted into the stability equations derived by Biot and an expression obtained for the orientation of the local type 2 characteristic direction. This direction is then used to specify the orientation of the associated kink domain with respect to the overall trend of the layering and applied compression direction (the angle θ in fig.1.15C).

Cobbold et al argued that local modulus inversion will be sufficient to reduce the locally effective modulus ratio N_{α}/Q_{α} well below the type 2 threshold if the ratio of the principal stiffness coefficients N/Q is relatively high i.e. the material has a high degree of anisotropy. For this reason, they suggested that kink style deformation associated with the local development of type 2 internal instability would be favoured in such materials and that folds developed in layered materials with a low degree of mechanical anisotropy would tend to be rounded and sinusoidal with axial planes oriented normal to the compression direction. Cobbold et al conclude that sinusoidal buckles (formed in materials with a low degree of anisotropy) and conjugate kink bands (formed in materials with a high degree of anisotropy) are not isolated structural types, formed by different mechanisms, but are end members of a range of possible fold structures corresponding to a continuous range in the possible values of the bulk anisotropy of a layered or foliated material.

Closer examination of the model proposed by Cobbold et al indicates, however, that this model may need to be significantly modified. In particular, the concept of the local development of a type 2 internal instability and the subsequent development of a propagating kink is open to serious question. Even if a perfect modulus inversion ($N_{\alpha}/Q_{\alpha} \rightarrow Q/N$) occurs within a locally defined foliation element, the response of this element to compression cannot be examined by using the theory of internal instability. The boundary conditions which would exist on the orthogonal faces of this element will be entirely different from those required by the very specific conditions of Biot's analysis. For this reason alone, any attempt to investigate the

incremental response of this element in terms of the predictions of this analysis is unjustified. This implies that it is not possible to specify a locally developed "characteristic direction" and the correlation of this phenomenon with the subsequent propagation of a kink is questionable. Therefore, there is some doubt about the conclusion that kink folding is simply related to a high degree of material anisotropy.

(ii) HONEA AND JOHNSON (1976)

Honea and Johnson have also presented a mechanical analysis of the conditions which favour kink folding in a uniform multilayer under layer parallel compression. However, the models of Cobbold et al. and Honea and Johnson differ, significantly, in both the methods of analysis that are used and in the conclusions which are reached. In complete contrast to the macroscopic, continuum approach adopted by Cobbold et al, Honea and Johnson attempted to analyse kink folding by isolating a single representative layer from a uniform multilayer sequence and examining the elastic buckling profiles which would be produced within this isolated plate under various idealised conditions of shear stress applied to the surface of the plate. In the writer's opinion the analysis can be criticised on a number of grounds and the construction of the analysis and the conclusions reached will not be considered in any detail. The analysis is an extreme simplification of what is a complex process. It is difficult to justify an analysis of kink initiation which is based on an approximate investigation of the elastic stability of a single plate under very simple boundary conditions. Those boundary conditions are almost certainly not representative of the surface stresses which would exist on individual laminae within even a simple multilayer.

The main conclusion reached by Honea and Johnson is that kink initiation will occur within zones of a stressed multilayer in which the cohesion and frictional resistance between adjacent laminae is overcome. They suggest that these zones of kink initiation may develop on the limbs of initially formed internal buckles or in local zones of initial layer disturbance. Thus the principal parameter which, they suggest, will favour conjugate kinking is the existence of a "contact strength" between individual laminae and the fact that "...layers can slip in some places rather than others."

Honea and Johnson's suggestion that conjugate kinks can develop on and propagate from the kinks of low amplitude, type 1 fold instabilities in a confined multilayer is similar to that of Cobbold et al. However, they insist that this will only occur if local loss of interlayer cohesion occurs in the limb regions. In their view, it is this, and not the development of local modulus inversion and subsequent rotational instability, which is the criterion for kinking. Honea and Johnson present an analysis to estimate conditions and multilayer characteristics favourable to the development of local "zones of failure", and subsequent kinking, on the limbs of internal buckles. They obtain, using somewhat dubious arguments, two quantitative parameters, K_1 and K_2, which they call the indices of kink folding and indicate how these parameters can be used to determine whether sinusoidal buckles or kinks will develop in a multilayer with particular mineral properties. From calculations based on these indices, Honea and Johnson conclude "... the criterion developed by Cobbold et al is in direct contradiction to the criteria presented above. Cobbold et al conclude that high anisotropy favours kink folding but our conclusion is opposite".

In the writer's opinion, a satisfactory mechanical model has yet to be formulated which explains the conditions and multilayer characteristics which might favour the initiation of conjugate folds or conjugate kinks, rather than any other than any other fold style. The very fact that the contrasting analyses of Cobbold et al. and Honea and Johnson are based on fundamentally different mechanisms of deformation within a layered system (rotational instability associated with bulk mechanical anisotropy in the former case; the elastic buckling of discrete plates in the latter case) serves to illustrate the probable complexity of the problem. In constructing a finite deformation analysis of kink or kink like folds, the writer has made the *a priori* assumption that the structure develops from an initial foliation perturbation (fig. 1.13) which itself has the geometrical characteristics of a low amplitude kink band or monocline. This assumption effectively ignores the problem of kink fold or monocline initiation. In the description of the analysis, the rotated limb of the structure is referred to as a foliation rotation domain rather than as a kink band. The term foliation rotation domain has been adopted in order to avoid the implication that the analysis is restricted to structures which are distinctly angular throughout deformation.

CHAPTER 2

2.1 INTRODUCTION

It has been indicated in Chapter 1 that one method of approaching the complex problem of the deformation of layered or foliated materials is to study the response to stress of such materials in terms of the response to stress of an equivalent homogeneous anisotropic continuum. The work of Biot (e.g. 1965, 1965a) on the development of fold instabilities in layered systems and the subsequent work of Cobbold et al. (1971), Casey (1976) and Cobbold (1976) on the finite development of fold instabilities has shown that the homogeneous continuum analogy can be used to explain many of the features seen in natural structures developed in well bedded or foliated geological materials.

The finite deformation analysis which is described in this section uses the homogeneous continuum analogy in order to model the incremental and finite response to stress of the type of structure shown in fig. 1.13. Equations 1.13 and 1.14 form the basis of this deformation analysis. These equations are used to calculate the local incremental response to stress of material elements contained within a structure. It will be shown that the incremental deformation of a kink-like domain of rotated layering or foliation can be analysed in terms of the response to stress of a series of locally representative, domain parallel material elements. The configuration of these elements is illustrated in fig. 2.1. In order to use this method, it is necessary to place certain constraints on the geometry of a structure and on the variation in displacements which occur within the structure during incremental and finite deformation. It is also necessary to make certain assumptions about the symmetry of applied stresses with respect to a structure. These assumptions and implications of these assumptions are considered in the following subsections.

2.1.1. CONSTRAINTS PLACED ON THE INITIAL AND FINITE GEOMETRY OF THE STRUCTURE

These constraints can be described with reference to fig. 2.1. and the set of orthogonal axes x, y and z which are indicated in this figure.

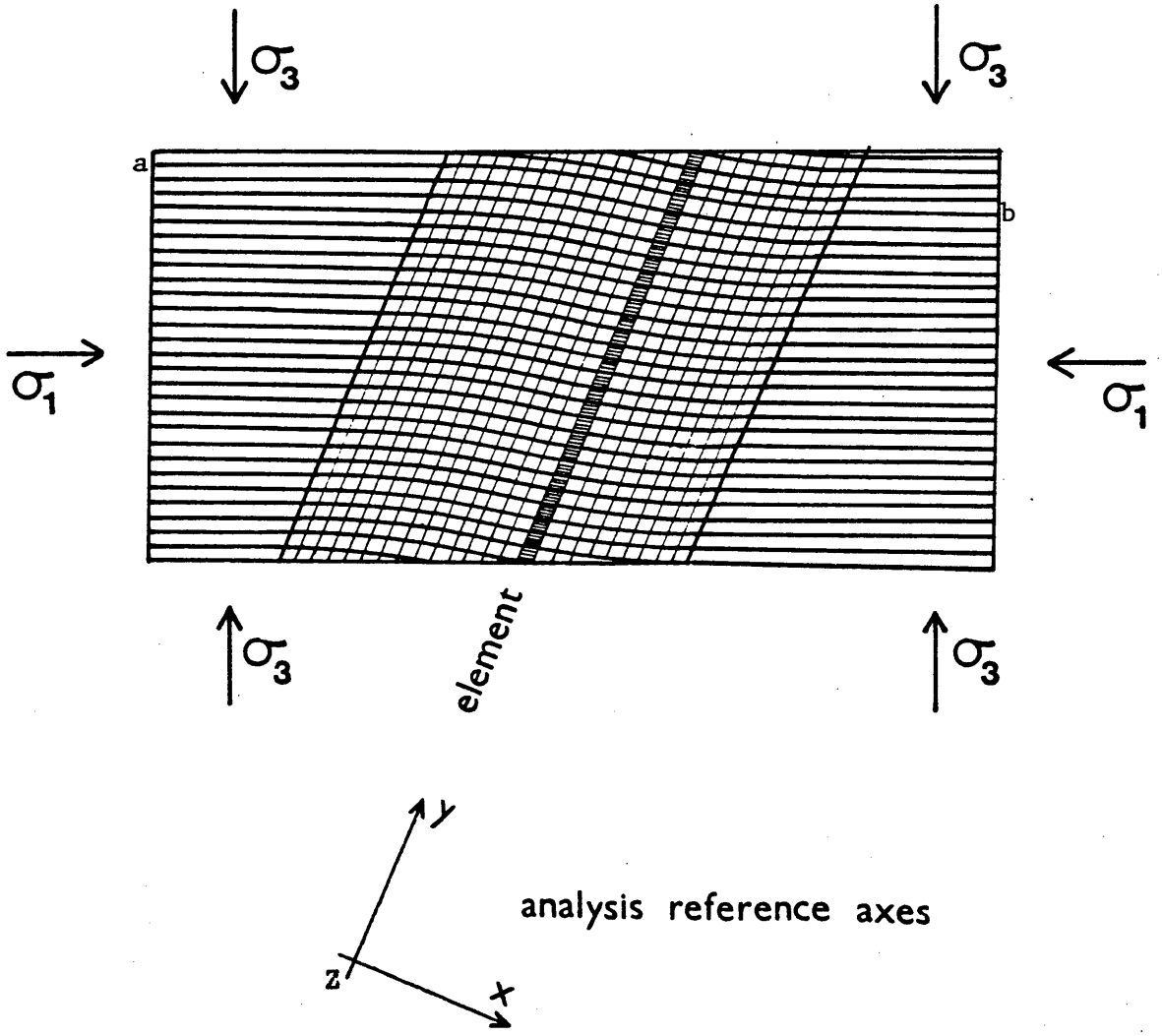


Figure 2.1 Type of structure analysed in the rotation domain analysis. The successive profile planes (eg. ab) shown in this figure do not represent the boundaries between discrete isotropic laminae within a multilayered material. Strictly they represent the trend of a plane of transverse isotropy within an orthotropic, anisotropic material which is equivalent to the trend of the layer plane within an equivalent, discretely layered material. The effect of a finite layer thickness is not taken into account in the response equations which form the basis of the analysis and the analysis can be applied, with confidence, only to structures in which the thickness of individual laminae is small incomparison with the width of the rotation domain.

The plane containing x and y is a profile plane and rotation of the foliation occurs about axes orientated normal to this plane (z). In the description which follows the zone of rotated foliation will be referred to as the rotation domain and the foliation contained within this domain as the "internal foliation". The foliation in the zones surrounding the rotation domain will be referred to as the "external foliation". The initial structure has the following properties:

(i) The boundaries of the rotation domain are plane and parallel.

(ii) The profile geometry of successive foliation planes is constant, i.e. there is no change in profile geometry along the direction of the y coordinate axis and the structure is assumed to extend indefinitely along this direction. The fold is a 'similar' fold with respect to y coordinate axis (see: Ramsay, 1967, p.427).

The following conditions are maintained during incremental and finite deformation of the initial foliation perturbation:

(i) The opposing boundaries of the rotation domain remain plane and parallel throughout deformation although, as will be shown, these boundaries may rotate with respect to the plane of the external foliation.

(ii) The initial condition of similarity of successive foliation surfaces is maintained throughout deformation.

2.1.2 SYMMETRY OF APPLIED STRESSES WITH RESPECT TO THE STRUCTURE

A particularly important condition which is applied to the analysis is that the maximum principal compressive stress, σ_1, in the external foliation zones, is oriented parallel with the trace of the external foliation and acts normal to the rotation (or fold) axis of the structure (fig.2.2). The minimum principal compressive stress, σ_3, acts normal to foliation within this zone and σ_2 acts normal to the profile plane x, y. These stress orientations are maintained throughout deformation. It should be noted that the stress symmetry illustrated in fig. 2.2 applies only to stresses within the external folation. It will be shown during the course of the analysis that rotation of principal stress trajectories must occur within the boundaries of the rotation domain.

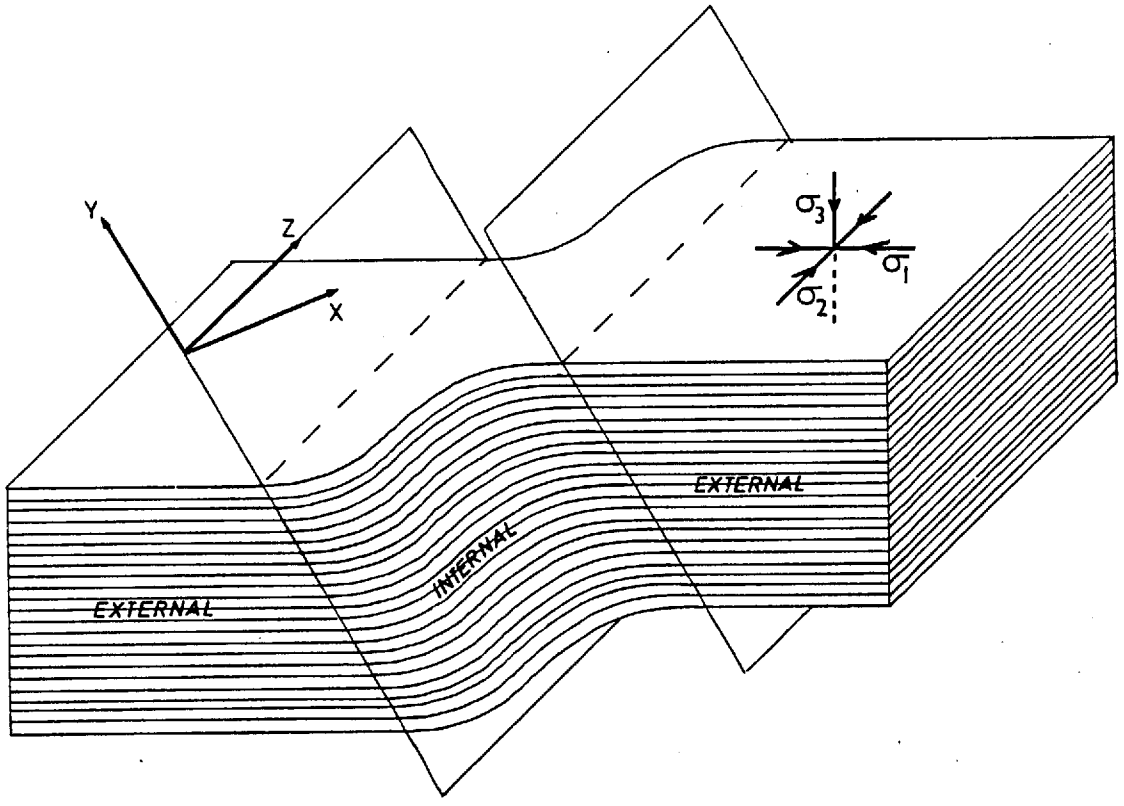


Figure 2.2 Three dimensional representation of the orientation of a structure with respect to the analysis reference coordinates x, y and z. Deformation is assumed to be plane strain in the x,y profile plane. z is parallel to the foliation rotation axis. The orientation of principal stresses σ_1, σ_2 and σ_3 shown this figure applie only to stresses within the unrotated external foliation. σ_1 and σ_3 may rotate within the boundaries of the rotation domain (internal foliation) although, under the conditions of the analysis, σ_2 will remain parallel to z throughout the structure.

2.1.3. THE CONCEPT OF LOCAL MACROSCOPIC STRAIN; VARIATION IN THE INCREMENTAL STRESS AND STRAIN TENSORS

By considering the deformation of individual foliation elements in terms of the deformation of equivalent elements of a homogeneous anisotropic continuum it is possible to investigate the incremental response to stress of these elements in terms of *macroscopic* strains induced in each element. (These strains are a macroscopic representation of the complex variation in strain which will be present at the level of individual layer components within an element of discretely layered material). The magnitudes of these macroscopic strains can be expressed in terms of macroscopic incremental displacements u and v measured parallel to the x and y coordinates directions respectively. During an increment of deformation, the x, y coordinate axes are oriented with x normal to rotation domain boundaries and y parallel to these boundaries. The total incremental deformation of individual, domain parallel foliation elements can be resolved into three strain components referred to the x, y coordinate frame - (i) incremental direct strains e_{xx} and e_{yy}, (ii) incremental shear strains e_{xy} and e_{yx} and (iii) a rigid body rotation, Ω. These strain components can be expressed in terms of displacement gradients :*

$$e_{xx} = \frac{\partial u}{\partial x}$$

$$e_{yy} = \frac{\partial v}{\partial y}$$

$$e_{xy} = -\frac{1}{2}\left(\frac{\partial u}{\partial y} + \frac{\partial v}{\partial x}\right)$$

$$\Omega = -\frac{1}{2}\left(\frac{\partial v}{\partial x} - \frac{\partial u}{\partial y}\right)$$

By taking into account the constraints imposed on the initial and finite geometry of a structure (Section 2.1.1), it is possible to place certain limitations on the allowable variation of these macroscopic strain components within the profile plane of a structure. If the structure is to remain similar with respect to the y coordinate

* *The sign conventions adopted for strain is given in appendix 2.1*

axis and opposing rotation domain boundaries remain plane and parallel throughout deformation then there can be no variation in any of the strain or rotation components along the length of an element.

Thus :

$$\frac{\partial e_{xx}}{\partial y} = \frac{\partial^2 u}{\partial x \partial y} = 0 \qquad \ldots\ldots 2.5$$

$$\frac{\partial e_{xy}}{\partial y} = \frac{\partial^2 v}{\partial y^2} = 0 \qquad \ldots\ldots 2.6$$

$$\frac{\partial e_{xy}}{\partial y} = -\frac{1}{2}\left(\frac{\partial^2 u}{\partial y^2} + \frac{\partial^2 v}{\partial x \partial y}\right) = 0 \qquad \ldots. 2.7$$

$$\frac{\partial \Omega}{\partial y} = -\frac{1}{2}\left(\frac{\partial^2 v}{\partial x \partial y} + \frac{\partial^2 u}{\partial y^2}\right) = 0 \qquad \ldots. 2.8$$

These conditions also imply that the boundaries of individual foliation elements remain plane and mutually parallel throughout deformation.

Adding equations 2.7 and 2.8 :

$$\frac{\partial e_{xy}}{\partial y} + \frac{\partial \Omega}{\partial y} = \frac{\partial^2 v}{\partial x \partial y} = 0$$

Now :

$$\frac{\partial^2 v}{\partial x \partial y} = \frac{\partial^2 v}{\partial y \partial x} = \frac{\partial \left(\frac{\partial v}{\partial y}\right)}{\partial x} = 0$$

Therefore :

$$\frac{\partial e_{yy}}{\partial x} = 0 \qquad \ldots\ldots 2.9$$

Thus, in any increment of deformation the induced incremental direct strain e_{yy} must be constant throughout the structure (i.e. constant from element to element within the rotation domain and equal to the incremental direct strain e_{yy} induced within the external foliation). Since the strains which are considered are incremental,

the conditions which apply to strain also apply to incremental strain *rates* and, in particular:

$$\frac{\partial \dot{e}_{yy}}{\partial x} = 0 \qquad \ldots\ldots 2.10$$

Variation in the stress tensor

If the structure shown in fig. 2.1 is to remain similar with respect to the y coordinate axis throughout deformation, and material properties are constant along y within an individual foliation element, then there can be no variation in any of the components of the local stress tensor along the y direction, during a deformation increment. This implies:

$$\frac{\partial \sigma_{xx}}{\partial y} = 0 \qquad \ldots\ldots 2.11$$

$$\frac{\partial \sigma_{yy}}{\partial y} = 0 \qquad \ldots\ldots 2.12$$

$$\frac{\partial \sigma_{xy}}{\partial y} = 0 \qquad \ldots\ldots 2.13$$

.... where σ_{xx}, etc. are stresses resolved along the x and y coordinates of the analysis.

These stress components are 'macroscopic stresses' acting within individual foliation elements. They are essentially a statistical average of the complex variation of local stress at the level of individual layer components which would be present in an element of discretely layered material. Because the structure is considered in terms of the behaviour of a macroscopically homogeneous continuum, these stress components are subject to the conditions of stress equilibrium within a continuum. For equilibrium, in the absence of body stresses:

$$\frac{\partial \sigma_{xx}}{\partial x} + \frac{\partial \sigma_{xy}}{\partial y} = 0 \qquad \ldots\ldots 2.14$$

$$\frac{\partial \sigma_{yx}}{\partial x} + \frac{\partial \sigma_{yy}}{\partial y} = 0 \qquad \ldots\ldots 2.15$$

Combining equations 2.11 - 2.13 with equations 2.14 and 2.15:

$$\frac{\partial \sigma_{xy}}{\partial x} = 0 \qquad \ldots\ldots 2.16$$

$$\frac{\partial \sigma_{xx}}{\partial x} = 0 \qquad \ldots\ldots 2.17$$

These conditions are fundamental to the analysis. They imply that:

(i) The direct stress, σ_{xx}, acting normal to the rotation domain boundaries must be constant throughout the structure. Thus the total normal stress σ_{xx} acting within each foliation element must be equal to resolved stress, σ_{xx}, acting on the rotation domain boundaries in the external foliation.

(ii) The shear stress, σ_{xy}, acting parallel to the boundaries of each internal foliation element must be constant throughout the structure and equal to the resolved shear stress, σ_{xy}, acting on the rotation domain boundaries in the external foliation.

It should be noted that at this stage in the analysis it is not possible to define the magnitude of σ_{yy} acting within individual foliation elements within the rotation domain. Although σ_{yy} is defined in the external foliation, a gradient in σ_{yy} can exist across the rotation domain without violating the conditions of stress equilibrium. The problem is resolved in the next section in which the equations describing the macroscopic response of an element of foliated material to stress (equations 1.13 and 1.14) are combined with

conditions of stress equilibrium and strain rate compatibility to quantify the total incremental response to stress of the type of structure shown in fig. 2.1.

2.2 CONSTRUCTION OF THE EQUATIONS DESCRIBING THE INCREMENTAL DEFORMATION OF A STRUCTURE

2.2.1 INCREMENTAL STRAIN RATE TENSOR

In order to quantify the local incremental response of any foliation element to externally applied, foliation parallel compression the stress-strain rate relationships given by equations 1.13 and 1.14 are used.

$$\dot{e}_{xx} = \frac{1}{4NQ}\left\{-\left[(N+Q)-(N-Q)\cos 4\alpha\right]\sigma'_{xx} + \left[(N-Q)\sin 4\alpha\right]\sigma_{xy}\right\} \quad \ldots\ldots 1.13$$

$$\dot{e}_{xy} = \frac{1}{4NQ}\left\{-\left[(N-Q)\sin 4\alpha\right]\sigma'_{xx} + \left[(N+Q)+(N-Q)\cos 4\alpha\right]\sigma_{xy}\right\} \quad \ldots\ldots 1.14$$

The angle α contained within these equations represents the angle between the x coordinate axis of the chosen stress/strain coordinate frame and the plane of the foliation (see fig. 1.8A).

In the context of the analysis described in this section, the angle α is equivalent to the local inclination of the foliation, within a foliation element, to the domain boundary normal (x coordinate axis of the rotation domain analysis). This is illustrated in the simplified diagram shown in fig. 2.3. The angle α has a simple relationship to the important angular parameters θ and ω which are defined in fig. 2.3. θ is the orientation of the boundaries of the rotation domain with respect to a line drawn normal to the external folation. ω is angle of inclination of the internal foliation to the plane of the external and expresses the magnitude internal of foliation rotation with respect to the external foliation. It should be noted that, for clarity, the structure shown in fig. 2.3 is drawn with a uniform internal foliation orientation. Obviously the angle ω will vary continuously through a rotation domain with a non-uniform internal foliation orientation such as the structure shown in fig.2.1.

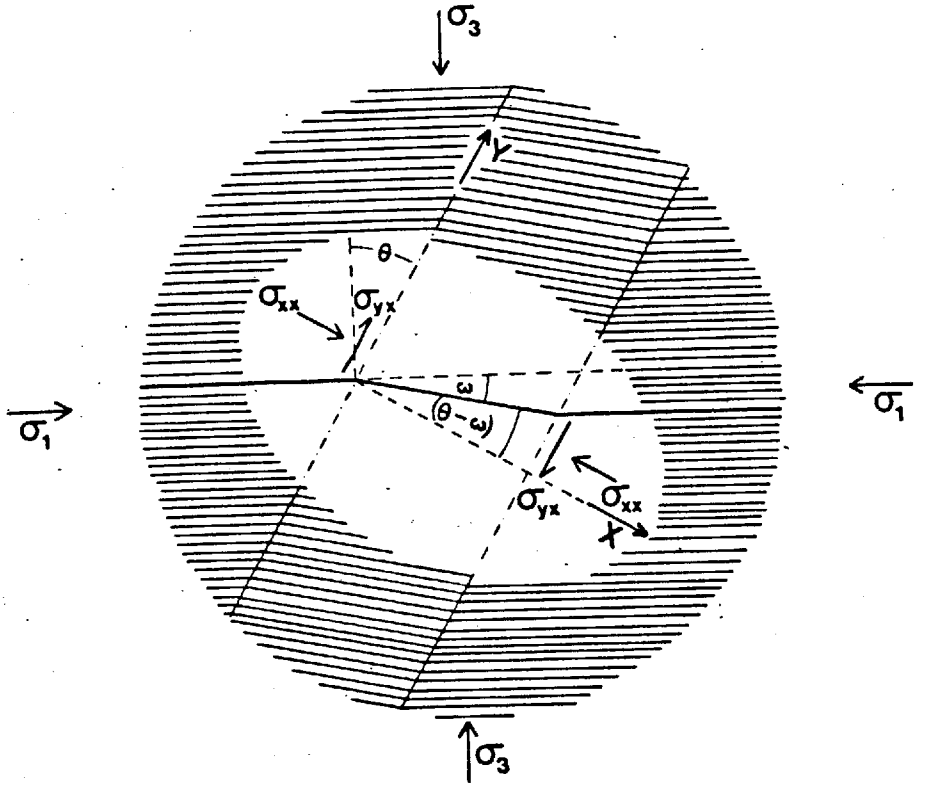


Figure 2.3 Definition of the angular parameters θ and ω. For simplicity, the angle ω is shown for a rotation domain with a uniform internal foliation orientation (ω constant). ω will vary continuosly through a rotation domain with a non-uniform internal foliation orientation.

Inspection of fig. 2.3 shows that α is given, in terms of θ and ω, by:

$$\alpha = \theta - \omega \qquad \ldots\ldots 2.18$$

This identity is introduced into equations 1.13 and 1.14 to obtain expressions for the local direct strain and shear strain rate developed within individual foliation elements of a rotation domain.

$$\dot{e}_{xx} = \frac{1}{4NQ}\left\{ - \left[(N+Q) - (N-Q)\cos 4(\theta-\omega)\right]\sigma'_{xx} + \left[(N-Q)\sin 4(\theta-\omega)\right]\sigma_{xy} \right\} \qquad \ldots\ldots 2.19$$

$$\dot{e}_{xy} = \frac{1}{4NQ}\left\{ -\left[(N-Q)\sin 4(\theta-\omega)\right]\sigma'_{xx} + \left[(N+Q) + (N-Q)\cos 4(\theta-\omega)\right]\sigma_{xy} \right\} \qquad \ldots\ldots 2.19a$$

There are certain advantages in expressing these equations in terms of anisotropy ratio , N/Q, rather than in terms of absolute values of the principal stiffness coefficients N and Q.

$$\dot{e}_{xx} = \frac{1}{4N}\left\{ - \left[(N/Q+1) - (N/Q-1)\cos 4(\theta-\omega)\right]\sigma'_{xx} + \left[(N/Q-1)\sin 4(\theta-\omega)\right]\sigma_{xy} \right\} \qquad \ldots\ldots 2.20$$

$$\dot{e}_{xy} = \frac{1}{4N}\left\{ -\left[(N/Q-1)\sin 4(\theta-\omega)\right]\sigma'_{xx} + \left[(N/Q+1) + (N/Q-1)\cos 4(\theta-\omega)\right]\sigma_{xy} \right\} \qquad \ldots\ldots 2.21$$

In any defined structure, each of the terms contained in the right hand side of equations 2.20 and 2.21 are known except the magnitude of the band normal deviatoric stress component σ'_{xx}. It has been shown in subsection 2.1.3. that the magnitude of the shear stress σ_{xy} within each foliation element is given by the resolved shear stress acting on the rotation domain boundaries ($\partial\sigma_{xy}/\partial x = 0$). Therefore:

$$\sigma_{xy} = \frac{\sigma_1 - \sigma_3}{2} \sin 2\theta$$

$$\sigma_{xy} = \tau_m^e \sin 2\theta$$

where τ_m^e is the maximum shear stress in the external foliation.

Equations 2.20 and 2.21 become :

$$\dot{e}_{xx} = \frac{1}{4N} \left\{ - \left[(N/Q+1) - (N/Q-1) \cos 4(\theta-\omega)\right] \sigma'_{xx} + \left[(N/Q-1) \sin 4(\theta-\omega)\right] \tau_m^e \right\} \quad \ldots\ldots 2.22$$

$$\dot{e}_{xy} = \frac{1}{4N} \left\{ \left[(N/Q-1) \sin 4(\theta-\omega)\right] \sigma'_{xx} + \left[(N/Q+1) + (N/Q-1) \cos 4(\theta-\omega)\right] \tau_m^e \right\} \quad \ldots\ldots 2.23$$

The total normal stress σ_{xx} in each foliation element is given by the stress equilibrium condition $\partial\sigma_{xx}/\partial_x = 0$ and, from resolution of the principal stresses acting within the external foliation,:

$$\sigma_{xx} = \left[\frac{\sigma_1 + \sigma_3}{2}\right] + \left[\frac{\sigma_1 - \sigma_3}{2}\right] \cos 2\theta \qquad \ldots\ldots 2.24$$

The equivalent deviatoric stress competent, σ'_{xx}, cannot be defined from conditions of stress equilibrium alone because the magnitude of the stress gradient $\partial\sigma_{yy}/\partial x$ is unknown. However, this stress component can be calculated from certain necessary conditions of strain rate compatibility which are required by the analysis. It has been shown that the rate of band parallel direct strain, $\dot{e}_{yy}$, must be constant across a structure in order to maintain the geometrical conditions of the analysis.

i.e. $$\frac{\partial \dot{e}_{yy}}{\partial y} = 0 \qquad \ldots\ldots 2.10$$

The continuum equations 1.13 and 1.14 and the equivalent equations 2.22 and 2.23 for the deformation of foliation elements within a parallel sided rotation domain are valid only for deformation at constant local volume. For plane strain deformation, this implies:

$$e_{xx} + e_{yy} = 0 \qquad \ldots\ldots 2.25$$

and

$$\dot{e}_{xx} + \dot{e}_{yy} = 0 \qquad \ldots\ldots 2.26$$

Differentiating equation 2.26 with respect to x :

$$\frac{\partial \dot{e}_{xx}}{\partial x} + \frac{\partial \dot{e}_{yy}}{\partial x} = 0 \qquad \ldots\ldots 2.27$$

Combining equations 2.10 and 2.27 :

$$\frac{\partial \dot{e}_{xx}}{\partial x} = 0 \qquad \ldots\ldots 2.28$$

This condition indicates that, for deformation of foliation elements at constant volume, the incremental direct strain rate component $\dot{e}_{xx}$ must be constant from element to element of the rotation domain and equal to the rate of direct strain, resolved along x, in the external foliation.

The combined conditions:

$$\frac{\partial \dot{e}_{xx}}{\partial x} = 0 \quad \text{and} \quad \frac{\partial \dot{e}_{yy}}{\partial x} = 0$$

...indicate that the pure shear component of deformation, referred to axes x and y, must be uniform throughout a structure. The only non-zero gradient of the incremental strain rate tensor is the gradient $\partial \dot{e}_{xy}/\partial x$.

The geometrical conditions of the analysis and the condition of constant volume deformation constrain a structure to deform by a combination of :

(i) Homogeneous pure shear parallel and normal to boundaries of the defined foliation elements

(ii) Heterogeneous simple shear parallel to the boundaries of the defined foliation elements

(iii) A rotation of the boundaries of individual foliation elements which is constant across the structure.

It will be shown in chapter 3 of this thesis that certain mechanisms may operate within a natural structure to produce a change in the volume of initially defined layer or foliation elements. Such an effect would result, for example, from the migration of incompetent material, within a multilayer sequence, across a structure. The implications of this possibility will be considered in detail in chapter 3. However, the initial assumption of constant volume deformation will be used at this stage because it brings to light many of the physical properties of a parallel sided layer rotation domain in the form of a kink-like asymmetric fold.

Because of the condition $\partial \dot{e}_{xx}/\partial x = 0$, it is possible to specify the magnitude of the strain rate component, $\dot{e}_{xx}$ in any part of a defined structure. This is achieved by calculating the rate of resolved direct strain, $\dot{e}_{xx}$, in the external foliation. The total stress tensor within the external zones is known from the defined orientation of the principal stresses σ_1 and σ_3 within these zones. In addition, the orientation of the foliation planes with respect to the x coordinate axis, within the external zones, is given by the condition $\omega = 0$. If the superscripts e and i are used to indicate strain rates and stresses within the external and internal foliation zones respectively then the deviatonic stress component σ'^{e}_{xx} is given by:

$$\sigma'^{e}_{xx} = \sigma^{e}_{xx} - \bar{\sigma}^{e} \qquad \ldots\ldots 2.29$$

where $\bar{\sigma}^{e}$ is the mean stress in the external foliation

Now $$\bar{\sigma}^{e} = \frac{\sigma^{e}_{1} + \sigma^{e}_{3}}{2} \qquad \ldots\ldots 2.30$$

and : $$\sigma^{e}_{xx} = \frac{\sigma^{e}_{1} + \sigma^{e}_{3}}{2} + \frac{\sigma^{e}_{1} - \sigma^{e}_{3}}{2} \cos 2\theta \qquad \ldots\ldots 2.31$$

Therefore : $$\sigma'^{e}_{xx} = \frac{\sigma^{e}_{1} - \sigma^{e}_{3}}{2} \cos 2\theta$$

$$\sigma'^{e}_{xx} = \tau^{e}_{m} \cos 2\theta \qquad \ldots\ldots 2.32$$

Introducing this identity into equation 2.22, an expression is obtained for the resolved direct strain rate $\dot{e}^{e}_{xx}$ in the external foliation:

$$\dot{e}^{e}_{xx} = \frac{\tau^{e}_{m}}{4N} \left\{ - \left[(N/Q+1) - (N/Q-1) \cos 4(\theta-\omega) \right] \cos 2\theta + \left[(N/Q-1) \sin 4(\theta-\omega) \right] \sin 2\theta \right\}$$

Since $\omega = 0$ in the external foliation :

$$\dot{e}^{e}_{xx} = \frac{\tau^{e}_{m}}{4N} \left\{ - \left[(N/Q+1) - (N/Q-1) \cos 4\theta \right] \cos 2\theta + \left[(N/Q-1) \sin 4\theta \right] \sin 2\theta \right\}$$

Simplifying this equation :

$$\dot{e}^{e}_{xx} = \frac{\tau^{e}_{m}}{4N} \left[- 2 \cos 2\theta \right] \qquad \ldots\ldots 2.32$$

It can be seen that the magnitude of the resolved strain rate $\dot{e}^{e}_{xx}$, is not a function of the anisotropy ratio N/Q. It was shown in a previous discussion of the properties of a transversely isotropic, anisotropic continuum that such a material will respond to principal stresses σ_1 and σ_3, acting parallel with and normal to the planes of transverse isotropy, as if it were an isotropic continuum with an effective isotropic stiffness given by the layer parallel direct modulus, N. This is exactly the situation in the external foliation and the external foliation responds to the foliation symmetric applied

principal stresses as if it were an isotropic material throughout deformation. Note that, even if the foliated material is highly anisotropic ($N \gg Q$), the magnitude of the total strain rate tensor and resolved strain rate components in the external foliation will be governed only by the maximum stiffness coefficient N and are independent of the layer parallel shear modulus Q. The parameter $\tau_m^e/4N$ is a measureof the stress level within the external foliation and will appear throughout the analysis.

Now, from the condition $\partial \dot{e}_{xx}/\partial x = 0$, it is necessary that:

$$\dot{e}^i_{xx} = \dot{e}^e_{xx}$$

...where $\dot{e}^i_{xx}$ is the domain normal incremental direct strain rate in any element of the internal foliation.

This strain rate component is given by equation 3.22:

$$\dot{e}^i_{xx} = \frac{1}{4N}\left\{ - \left[(N/Q+1) - (N/Q-1)\cos 4(\theta-\omega)\right] \sigma'^i_{xx} + (N/Q-1)\sin 4(\theta-\omega)\tau^e_m \sin 2\theta \right\}$$

Equations 2.22 and 2.33 can be equated to obtain an expression for the unknown deviatonic stress component, σ'^i_{xx}, acting within elements of the internal foliation:

$$\frac{\tau^e_m}{4N}\left[-2\cos 2\theta\right] = \frac{1}{4N}\left\{ - \left[(N/Q+1) - (N/Q-1)\cos 4(\theta-\omega)\right] \sigma'^i_{xx} + (N/Q-1)\sin 4(\theta-\omega)\,\tau^e_m \sin 2\theta \right\}$$

Solving for σ'^i_{xx} :

$$\sigma'^i_{xx} = \tau^e_m \left[\frac{(N/Q-1)\sin 4(\theta-\omega)\sin 2\theta + 2\cos 2\theta}{(N/Q+1) - (N/Q-1)\cos 4(\theta-\omega)} \right] \qquad \ldots\ldots 2.34$$

This expression indicates the local magnitude of the resolved deviatonic stress, σ'^i_{xx}, which must act within individual foliation

elements in order to maintain the necessary conditions of element to element direct strain compatibility under the condition of constant volume deformation. The expression is used later in the analysis to quantify the magnitude and orientation of principal stresses within the rotation domain at successive stages in the development of particular structures. It has geological significant consequences which concern the development of principal stress rotation and mean stress variation across natural kink structures on kink-like asymmetric folds.

Equation 2.34 can be used to complete the description of the incremental response of any element of the structure shown in fig.2.1. to the externally applied stresses. The shear component of deformation of a foliation element can be calculated by introducing the derived value of σ'_{xx} into equation 2.23:

$$\dot{e}^{i}_{xy} = \frac{\tau^{e}_{m}}{4N}\left\{ - (N/Q-1)\sin 4(\theta-\omega)\left[\frac{(N/Q-1)\sin 4(\theta-\omega)\sin 2\theta + 2\cos 2\theta}{(N/Q+1) - (N/Q-1)\cos 4(\theta-\omega)}\right] - \left[(N/Q+1) - (N/Q-1)\cos 4(\theta-\omega)\right]\sin 2\theta \right\}$$

Simplifying this equation :

$$\dot{e}^{i}_{xy} = \frac{\tau^{e}_{m}}{4N}\left\{ \frac{4\,(N/Q)\sin 2\theta - 2\,(N/Q-1)\sin 4(\theta-\omega)\cos 2\theta}{(N/Q+1) - (N/Q-1)\cos 4(\theta-\omega)} \right\} \quad \cdots\cdots 2.35$$

Equations 2.33 and 2.35 are sufficient to describe the total incremental strain rate tensor with any part of a defined structure with the geometry shown in fig. 2.1. These equations contain four variables which can be specified for such a structure.

(i) N/Q - the anisotropy ratio of the layered or foliated material containing the structure.

(ii) θ - the orientation of the boundaries of the rotation domain with respect to the external foliation.

(iii) $\tau^{e}_{m}/4N$ - the maximum shear stress within the external foliation expressed as a fraction of the maximum principal stiffness coefficient, N.

(iv) ω - the local rotation of the foliation with respect to the orientation of the plane of the external foliation.

2.2.2 RELATIONSHIP BETWEEN INCREMENTAL STRAIN AND FOLIATION ROTATION

In order to use equations 2.33 and 2.35 to quantify the *finite* response of a foliation rotation domain to stress it is necessary to integrate these equations either analytically or numerically. This cannot be done directly because the equations contain angular terms, θ and ω, which are themselves functions of finite strain. In order to continue with the analysis it is necessary to quantify the relationship between incremental strain components and corresponding incremental changes in the angles θ and ω. This can be done with reference to fig. 2.4 which shows small increments in the angles $\omega(\omega \rightarrow \omega + \Delta\omega)$ and $\theta(\theta \rightarrow \theta + \Delta\theta)$ and in displacement Δu and Δv, associated with an increment in strain. For clarity, rotations and displacements have been exaggerated and are referred to a rotation domain with a uniform internal foliation orientation. The coordinate axes x, y have been positioned with x horizontal and y vertical in this figure. It is important to note that the deformation of the structure must include a small rotation $\Delta\theta$ of the rotation domain boundaries with respect to the external foliation.

From the geometry of triangles opq and op'q' :

$$\tan(\theta-\omega) = \frac{pq}{op}$$

$$\tan\left[(\theta+\Delta\theta) - (\omega+\Delta\theta)\right] = \frac{q'p'}{op}$$

i.e.

$$\tan\left[(\theta-\omega) - (\Delta\omega-\Delta\theta)\right] = \frac{q'p'}{op}$$

Let:

$$qp = D \qquad q'p' = D + \Delta D$$

$$op = A \qquad op' = A + \Delta A$$

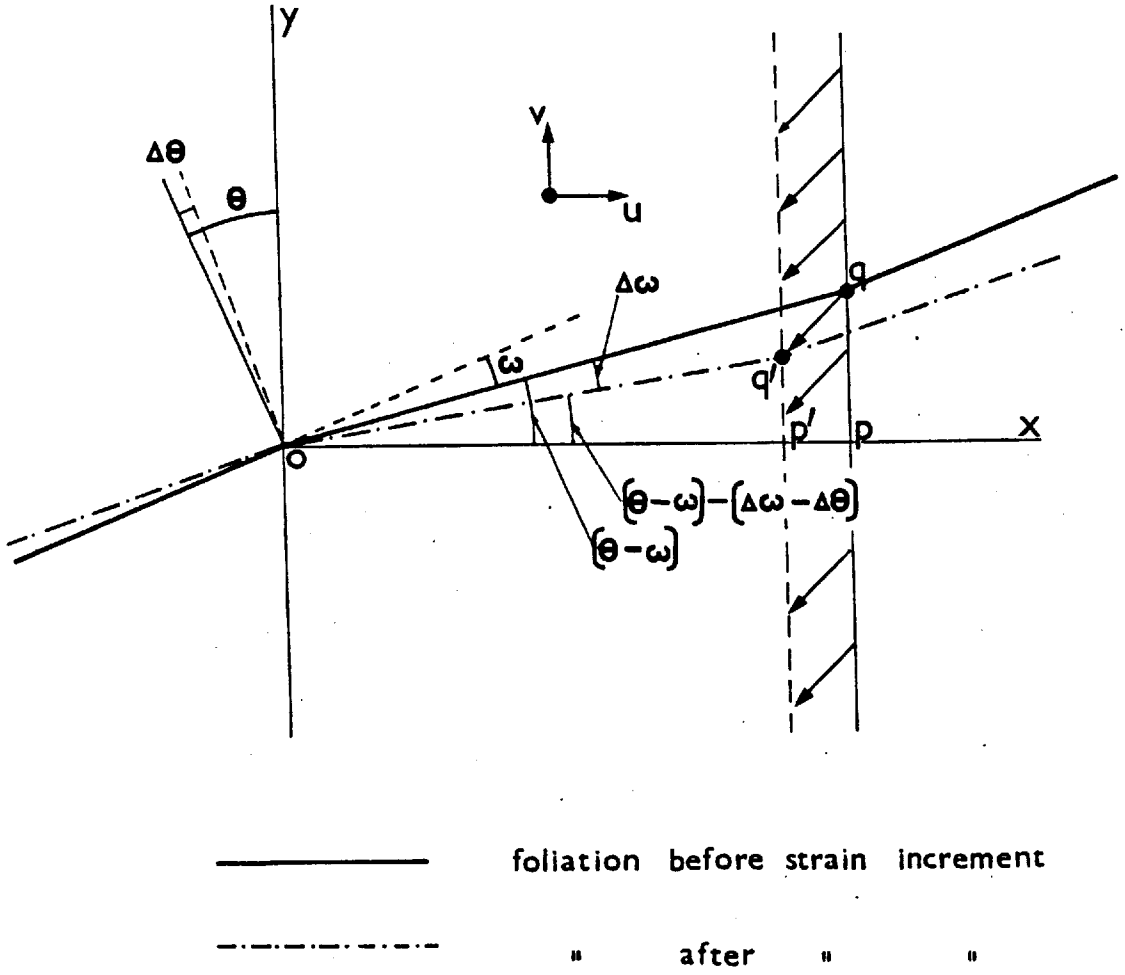


Figure 2.4 Displacements and rotations associated with an increment of deformation applied to both the internal and external foliation of a rotation domain. For diagrammatic clarity, the deformation is illustrated for a rotation domain with a uniform internal foliation orientation (ω constant within the domain). The rotation domain has been oriented, for convenience, with the domain boundaries (y axis) vertical.
(Deformation increment has been exaggerated in this figure)

Thus :
$$\frac{\tan\left[(\theta-\omega) - (\Delta\omega-\Delta\theta)\right]}{\tan\ (\theta-\omega)} = \frac{A + \Delta A}{A} \cdot \frac{D}{D + \Delta D}$$

$$\frac{\tan\left[(\theta-\omega) - (\Delta\omega-\Delta\theta)\right]}{\tan\ (\theta-\omega)} = \frac{1 + \Delta A/A}{1 + \Delta D/D} \qquad \ldots\ldots 2.36$$

The incremental changes in the lengths of ^{o}q and pq ($D \to D + \Delta D$, $A \to A + \Delta A$) can be expressed in terms of displacements u and v:

$$\Delta A = A \cdot \frac{\partial u}{\partial y} + \frac{\partial v}{\partial x}$$

$$\Delta D = D \cdot \frac{\partial u}{\partial y} + \frac{\partial u}{\partial x}$$

and

$$\Delta A = \frac{\partial v}{\partial y} + \frac{D}{A}\frac{\partial v}{\partial x} \quad ; \quad \Delta D = \frac{A}{D}\frac{\partial u}{\partial y} + \frac{\partial u}{\partial x}$$

Introducing these identities into equation 2.36:

$$\frac{\tan\left[(\theta-\omega) - (\Delta\omega-\Delta\theta)\right]}{\tan\ (\theta-\omega)} = \frac{1 + \dfrac{\partial v}{\partial y} + \dfrac{D}{A}\dfrac{\partial v}{\partial x}}{1 + \dfrac{\partial u}{\partial x} + \dfrac{A}{D}\dfrac{\partial u}{\partial y}}$$

Now :
$$\frac{D}{A} = \cot\ (\theta-\omega)$$

$$\frac{A}{D} = \tan\ (\theta-\omega)$$

$$\frac{\tan\left[(\theta - \omega) - (\Delta\omega - \Delta\theta)\right]}{\tan\ (\theta - \omega)} = \frac{1 + \dfrac{\partial v}{\partial y} + \cot\ (\theta-\omega)\dfrac{\partial v}{\partial x}}{1 + \dfrac{\partial u}{\partial x} + \tan\ (\theta-\omega)\dfrac{\partial u}{\partial y}} \qquad \ldots\ldots 2.37$$

The left hand side of equation 2.37 can be expanded and expressed in a more convenient form:

$$\text{L. H. S.} = \frac{\sin\left[(\theta-\omega) - (\Delta\omega-\Delta\theta)\right]}{\cos\left[(\theta-\omega) - (\Delta\omega-\Delta\theta)\right]} \cdot \frac{\cos(\theta-\omega)}{\sin(\theta-\omega)}$$

$$= \frac{\sin(\theta-\omega)\cos(\Delta\omega-\Delta\theta) - \cos(\theta-\omega)\sin(\Delta\omega-\Delta\theta)}{\sin(\theta-\omega)\sin(\Delta\omega-\Delta\theta) + \cos(\theta-\omega)\cos(\Delta\omega-\Delta\theta)} \cdot \frac{\cos(\theta-\omega)}{\sin(\theta-\omega)}$$

Now : $\cos(\Delta\omega-\Delta\theta) = \cos\Delta\omega\cos\Delta\theta + \sin\Delta\omega\sin\Delta\theta$

$\sin(\Delta\omega-\Delta\theta) = \sin\Delta\omega\cos\Delta\theta - \cos\Delta\omega\sin\Delta\theta$

For incremental deformation, both $\Delta\omega$ and $\Delta\theta$ are small and the following approximations can be used:

$\cos\Delta\theta \rightarrow 1$

$\cos\Delta\omega \rightarrow 1$

$\sin\Delta\theta \rightarrow 1$

$\sin\Delta\omega \rightarrow 1$

Thus : $\cos(\Delta\omega - \Delta\theta) \rightarrow 1 + \Delta\omega\cdot\Delta\theta$

$\sin(\Delta\omega - \Delta\theta) \rightarrow (\Delta\omega - \Delta\theta)$

Now : $\Delta\omega\cdot\Delta\theta \ll 1$

and : $1 + \Delta\omega\cdot\Delta\theta \simeq 1$

Thus: $\cos(\Delta\omega - \Delta\theta) \rightarrow 1$

Introducing these identities into equation 2.37 :

$$\text{L. H. S.} = \frac{\sin(\theta-\omega) - \cos(\theta-\omega).(\Delta\omega-\Delta\theta)}{\sin(\theta-\omega).(\Delta\omega-\Delta\theta) + \cos(\theta-\omega)} \cdot \frac{\cos(\theta-\omega)}{\sin(\theta-\omega)}$$

$$= \frac{1 - \cot(\theta-\omega) \cdot (\Delta\omega-\Delta\theta)}{1 + \tan(\theta-\omega) \cdot (\Delta\omega-\Delta\theta)}$$

Thus :

$$\frac{1 - \cot(\theta-\omega) \cdot (\Delta\omega-\Delta\theta)}{1 + \tan(\theta-\omega) \cdot (\Delta\omega-\Delta\theta)} = \frac{1 + \frac{\partial v}{\partial y} + \cot(\theta-\omega)\frac{\partial v}{\partial x}}{1 + \frac{\partial u}{\partial x} + \tan(\theta-\omega)\frac{\partial u}{\partial y}}$$

Cross multiplying and ignoring second order terms $\Delta\omega.\frac{\partial u}{\partial x}$, etc. :

$$-\cot(\theta-\omega).(\Delta\omega-\Delta\theta) + \partial u/\partial x + \tan(\theta-\omega).\partial u/\partial y = \tan(\theta-\omega).(\Delta\omega-\Delta\theta) + \partial v/\partial y + \cot(\theta-\omega).\partial v/\partial x$$

Rearranging this equation :

$$(\tan(\theta-\omega) + \cot(\theta-\omega)).(\Delta\omega-\Delta\theta) = \frac{\partial u}{\partial x} - \frac{\partial v}{\partial y} - \cot(\theta-\omega).\frac{\partial v}{\partial x} + \tan(\theta-\omega).\frac{\partial u}{\partial y}$$

..... 2.38

The following conditions and identities can be used to express this equation in terms of incremental strain components e_{xx} and e_{xy} rather than displacement gradients.

(i) No variation in displacement u occurs in the y direction - this condition is required to maintain parallelism of opposing rotation domain boundaries during an increment of deformation.

i.e. $\frac{\partial u}{\partial y} = 0$

(ii) $e_{xx} = \frac{\partial u}{\partial x} = -\frac{\partial v}{\partial y}$

Thus : $$\frac{\partial u}{\partial x} - \frac{\partial v}{\partial y} = 2\, e_{xx}$$

(iii) $$e_{xy} = -\frac{1}{2}\left(\frac{\partial u}{\partial y} + \frac{\partial v}{\partial x}\right)$$

$$e_{xy} = -\frac{1}{2}\left(\frac{\partial v}{\partial x}\right)$$

Thus : $$\frac{\partial v}{\partial x} = -2\, e_{xy}$$

In terms of incremental strains equation 2.38 becomes :

$$(\tan(\theta-\omega) + \cot(\theta-\omega)).(\Delta\omega-\Delta\theta) = 2\, e_{xx} + 2\cot(\theta-\omega)\, e_{xy}$$

..... 2.38a

Both incremental strain components e_{xx}, e_{xy} and incremental rotations occur over a small increment in time Δt Dividing both sides by Δt and taking the limit $\Delta t \to 0$:

$$(\tan(\theta-\omega) + \cot(\theta-\omega)).\left(\frac{d\omega}{dt} - \frac{d\theta}{dt}\right) = 2\frac{de_{xx}}{dt} + \cot(\theta-\omega)\frac{de_{xy}}{dt}$$

Now : $$\tan(\theta-\omega) + \cot(\theta-\omega) = \frac{2}{\sin 2(\theta-\omega)}$$

Thus : $$\frac{d\omega}{dt} - \frac{d\theta}{dt} = \sin 2(\theta-\omega).\frac{de_{xx}}{dt} + \sin 2(\theta-\omega).\cot(\theta-\omega).\frac{de_{xy}}{dt}$$

Also : $$\sin 2(\theta-\omega).\cot(\theta-\omega) = 2\cos^2(\theta-\omega)$$

Using the "dot" notation for a time derivative, equation 2.38b is rearranged to give an expression for the incremental rate of foliation rotation, $d\omega/dt$:

$$\dot{\omega} = \sin 2(\theta-\omega).\dot{e}_{xx} + 2\cos^2(\theta-\omega).\dot{e}_{xy} + \dot{\theta} \qquad \ldots\ldots 2.39$$

At this stage of the analysis, the only unknown term in the right hand side of equation 2.39 is $\dot{\theta}$. In order to complete this equation ., the magnitude of the incremental rate of rotation of the boundaries of the rotation domain with respect to the external foliation must be calculated.

It has been shown that the external foliation responds to the externally applied stresses as if it were an isotropic material with a uniform stiffness modulus, N. The rotation domain boundaries effectively rotate as if they were passive marker lines representing deformation in the external foliation. Consider the change in orientation of the rotation domain boundaries during a small increment in isotropic deformation in the external foliation (fig. 2.5) :

$$\theta \rightarrow \theta + \Delta\theta$$

The principal axes of the incremental strain tensor of the external foliation coincide with the principal stress axes. Ramsay (1967) has shown that the change in angle of a passive marker line, with strain, is given by:

$$\frac{\tan\theta'}{\tan\theta} = \frac{\tan(\theta+\Delta\theta)}{\tan\theta} = \frac{1+e_{11}}{1-e_{11}} \qquad \ldots\ldots 2.40$$

..... for the strain increment shown in fig. 2.14.

e_{11} is an increment in direct strain measured in the direction of the plane of the external foliation.

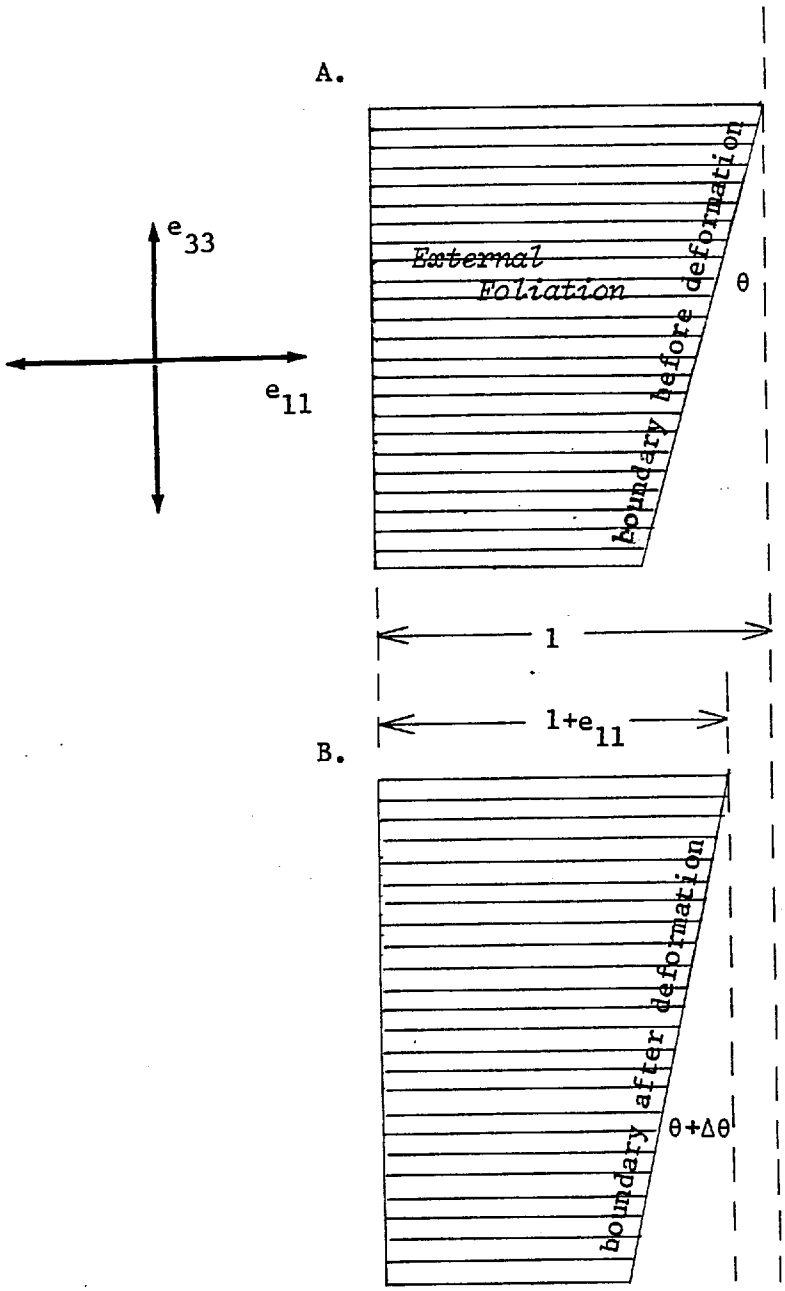


Figure 2.5 Effectively passive rotation of the boundaries of an oblique rotation domain in response to an increment of pure shear deformation in the external foliation. Deformation in the external foliation is co-axial with the applied, foliation symmetric stresses σ_1^e and σ_3^e. The incremental rotation of the domain boundaries ($\Delta\theta$) is given by (Ramsay, 1967, pp. 66-67) :

$$\tan(\theta+\Delta\theta)/\tan(\theta) = (1+e_{11})/(1-e_{11})$$

Expanding the left hand side of equation 2.40 :

$$\frac{\tan(\theta+\Delta\theta)}{\tan\theta} = \frac{\sin\theta\cos\Delta\theta + \cos\theta\sin\Delta\theta}{\cos\theta\cos\Delta\theta - \sin\theta\sin\Delta\theta} \cdot \frac{\cos\theta}{\sin\theta}$$

As $\Delta\theta \to 0$: $\sin\Delta\theta \to \Delta\theta$; $\cos\Delta\theta \to 1$

Thus :
$$\frac{\tan(\theta+\Delta\theta)}{\tan\theta} \to \frac{\sin\theta + \cos\theta\,\Delta\theta}{\cos\theta - \sin\theta\,\Delta\theta} = \frac{1 + \cot\theta.\Delta\theta}{1 - \tan\theta.\Delta\theta}$$

And :
$$\frac{1 + \cot\theta.\Delta\theta}{1 - \tan\theta.\Delta\theta} = \frac{1 + e_{11}}{1 - e_{11}}$$

Cross multiplying and ignoring second order terms $\Delta\theta.\, e_{11}$, etc:

$$(\tan\theta + \cot\theta)\,\Delta\theta = 2\, e_{11}$$

$$\Delta\theta = e_{11} \sin 2\theta$$

Dividing both sides of equation 2.41 by Δt and taking the limit $\Delta t \to 0$

$$\frac{d\theta}{dt} = \frac{de_{11}}{dt} \sin 2\theta$$

The incremental direct strain rate $\dot{e}_{11}$ in the external foliation is given by:

$$\dot{e}_{11} = \frac{de_{11}}{dt} = -\frac{\tau_m^e}{2N}$$

Thus :

$$\dot{\theta} = -\frac{\tau_m^e}{4N}\left[2\ \sin 2\theta\right] \qquad \ldots\ldots\ 2.42$$

Expressions have now been derived for each of the terms contained within equation 2.39. The incremental rate of foliation rotation within any element of the structure shown in fig. 3.1. can be quantified by introducing the values derived for $\dot{e}_{xx}$ (equation 2.33), $\dot{e}_{xy}$ (equation 2.35) and $\dot{\theta}$ (equation 2.42) into equation 2.39. The full expression for $\dot{\omega}$ becomes:

$$\dot{\omega} = \frac{\tau_m^e}{4N}\left\{ -2\cos 2\theta \cdot \sin 2(\theta-\omega) + \left[\frac{4\ (N/Q) - 2\ (N/Q-1)\ \sin 4(\theta-\omega)\ \cos 2\theta}{(N/Q+1) - (N/Q-1)\ \cos 4(\theta-\omega)}\right] \cdot 2\cos^2\theta \right\}$$

$$2\ \sin 2\theta \qquad \ldots\ldots\ 2.43$$

Before discussing the implications of this equation for the incremental and finite deformation of a kink-like foliation rotation band a further series of equations will be derived to define the stress conditions within a structure.

2.2.3 Incremental stress tensor

It has been shown that the conditions of element to element strain compatibility and so elemental volume change lead to the prediction of a necessary gradient in deviatonic stress σ'_{xx} across a structure. The local magnitude of this stress component, within a specific element of the structure, is given by equation 2.34:

$$\sigma'_{xx} = \tau_m^e \left[\frac{2\cos 2\theta + (N/Q-1)\ \sin 4(\theta-\omega)\ \sin 2\theta}{(N/Q+1) - (N/Q-1)\ \cos 4(\theta-\omega)}\right]$$

This equation can be used to quantify the local magnitude of mean stress, $\bar{\sigma}$, within individual elements of the structure as follows. The mean stress within any element of the internal foliation can be calculated from the following relationship:

$$\bar{\sigma}^{i} = \sigma^{i}_{xx} - \sigma'^{i}_{xx}$$

mean stress — total normal stress — deviatoric stress

The condition $\partial\sigma_{xx}/\partial x = 0$ implies that the total normal stress σ_{xx} is constant across the rotation domain and equal to the total normal stress, σ^{e}_{xx}, resolved along x, acting in the external foliation.

$$\sigma^{i}_{xx} = \sigma^{e}_{xx} = \frac{\sigma^{e}_{1} + \sigma^{e}_{3}}{2} + \frac{\sigma^{e}_{1} - \sigma^{e}_{3}}{2} \cos 2\theta$$

$$= \bar{\sigma}^{e} + \tau^{e}_{m} \cos 2\theta$$

Therefore :

$$\bar{\sigma}^{i} = (\bar{\sigma}^{e} + \tau^{e}_{m} \cos 2\theta) - \sigma'^{i}_{xx}$$

A convenient method of expressing the variation in mean stress across a particular structure is to calculate the difference between the local mean stress, $\bar{\sigma}^{i}$, within the rotation domain and the mean stress in the external foliation, $\bar{\sigma}^{e}$.

$$\bar{\sigma}^{i} - \bar{\sigma}^{e} = (\bar{\sigma}^{e} + \tau^{e}_{m} \cos 2\theta - \sigma'^{i}_{xx}) - \bar{\sigma}^{e}$$

$$\bar{\sigma}^{i} - \bar{\sigma}^{e} = \tau^{e}_{m} \cos 2\theta - \sigma'^{i}_{xx}$$

Substituting the derived expression, 2.34, for σ'_{xx} into this equation:

$$\bar{\sigma}^{i} - \bar{\sigma}^{e} = \tau_m^e \cos 2\theta - \tau_m^e \left[\frac{2\cos 2\theta + (N/Q-1)\sin 4(\theta-\omega)\sin 2\theta}{(N/Q+1) - (N/Q-1)\cos 4(\theta-\omega)} \right]$$

Simplifying this expression:

$$\bar{\sigma}^{i} - \bar{\sigma}^{e} = \tau_m^e \cdot \left[\frac{(N/Q-1)(\cos 2\theta - \cos 2(2\omega-\theta)}{(N/Q+1) - (N/Q-1)\cos 4(\theta-\omega)} \right] \quad \ldots\ldots 2.44$$

It will be shown that the equation leads to a number of geologically important predictions concerning the induced variation in local mean stress across structures. The equation can also be used to obtain a complete description of the orientation and magnitude of principal stresses with any element of a defined rotation band. There are a number of ways of approaching the problem but the physical significance of the results can best be illustrated by the use of a Mohrs circle representation of stress.

In figure 2.6A, a two dimensional Mohrs circle representation of the state of stress within the external foliation is shown as the heavy circle, centre O, radius OP. The point P represents the total normal stress, σ_{xx}^{e}, and the shear stress, σ_{xy}^{e}, acting on the boundaries of a rotation domain. By geometry the angle between the maximum principal compressive stress σ_1^e and the normal to the plane of stress resolution (rotation domain boundaries) is θ - fig. 2.66.

It is known, from conditions of stress equilibrium, that the total normal stress σ_{xx}^{i} and the shear stress σ_{xy}^{i} acting on each element of the rotation domain are equal in magnitude and direct to the corresponding resolved stresses in the external foliation. Therefore the Mohrs circle representation of the state of stress with any element of the rotation domain must pass through P. In addition, the equation 3.44 can be used to position the centre of this circle, Q, as follows:

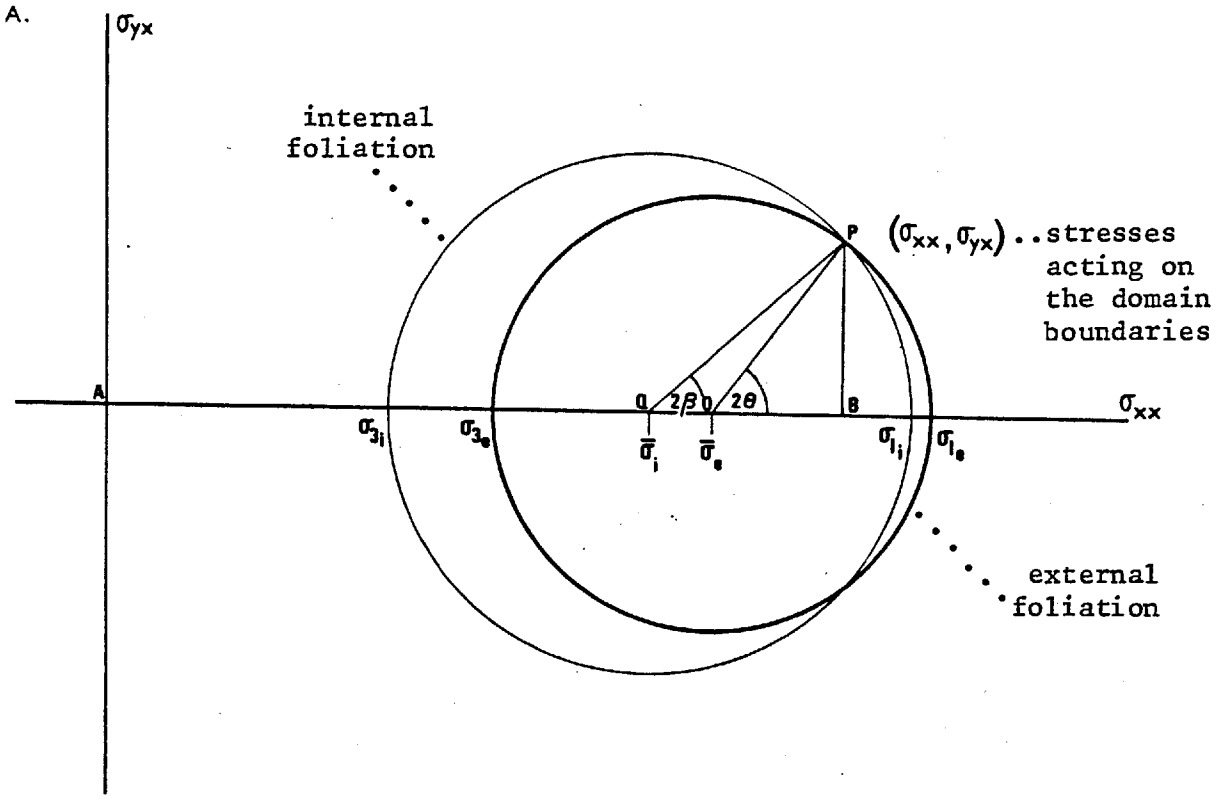


Figure 2.6 A Mohr's circle representations of the two dimensional state of stress in the external and internal foliation zones. The angles θ and β represent the local angle between the normal to the rotation domain boundaries and the line of action of σ_1 in the external (σ_1^e) and internal (σ_1^i) foliation zones respectively.

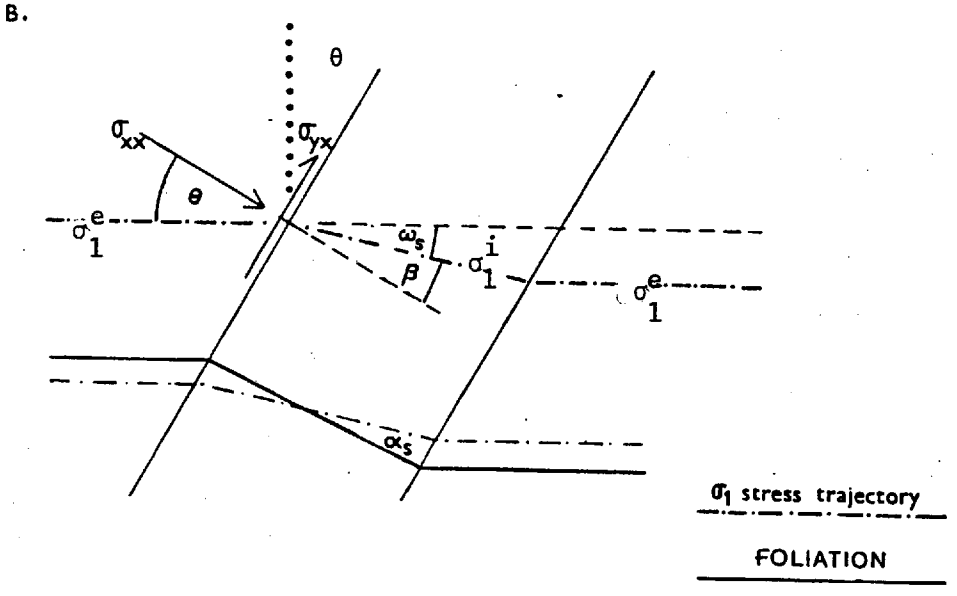


Figure 2.6 B Definition of the angles β - the inclination of σ_1^i to the rotation domain normal; ω_s - the inclination of σ_1^i with respect to the plane of the external foliation and the line of action of σ_1^e; α_s - the inclination of σ_1^i with respect to the plane of the internal foliation

(i) $\bar{\sigma}^i = AQ$

$\bar{\sigma}^e = AO$

$\bar{\sigma}^i - \bar{\sigma}^e = AQ - AO = OQ$

(ii) $\tau_m^e = OP$

$$\frac{\bar{\sigma}^i - \bar{\sigma}^e}{\tau_m^e} = \frac{OQ}{OP}$$

Thus :

$$\frac{OQ}{OP} = \frac{(N/Q - 1)\left\{\cos 2\theta - \cos 2(2\omega - \theta)\right\}}{(N/Q + 1) - (N/Q - 1)\cos 4(\theta - \omega)}$$

If the state of stress in the external foliation is defined then this equation can be used to calculate the distance OQ in fig. 2.6A and position the centre of the Mohr's circle for a specific element of the internal foliation. Thus the complete stress tensor within any element of the foliation rotation domain can be defined - tight circle, centre Q, radius QP.

The magnitude of β defines the angle between the x coordinate axis and the local orientation of the maximum principle compressive stress, σ_1^i, within specific elements of the internal foliation.

By geometry :

$BP = \tau_m^e \sin 2\theta$

$OB = \tau_m^e \cos 2\theta$

$$QB = \tau_m^e \ (\cos 2\theta - (\bar{\sigma}^i - \bar{\sigma}^e)/ \tau_m^e)$$

Thus, the angle β is given by :

$$\beta = \frac{1}{2} \arctan (BP/QB)$$

$$\beta = \frac{1}{2} \arctan \ \sin 2\theta \ / \ (\cos 2\theta - \frac{\bar{\sigma}^i - \bar{\sigma}^e}{\tau_m^e})$$

..... 2.45

The local strain rotation of the maximum principal compressive stress trajectories within the rotation domain can be more conveniently defined by the angle ω_s, fig. 3.6B. ω_s is the local rotation of σ_1^i with respect to the direction of action of σ_1^e, the maximum principal compressive stress within the external foliation. This angle is analogous to, and can be compared directly with, the local rotation of the foliation itself, ω.

By geometry (fig. 2.9B) :

$$\omega_s = \theta - \beta$$

$$\omega_s = \theta - \frac{1}{2} \arctan \left[\sin 2\theta \ / \ (\cos 2\theta - \frac{\bar{\sigma}^i - \bar{\sigma}^e}{\tau_m^e}) \right]$$

Expanding this equation :

$$\omega_s = \theta - \frac{1}{2} \arctan \left[\sin 2\theta \Big/ \cos 2\theta - \frac{(N/Q-1)(\cos 2\theta - \cos 2(2\omega-\theta)}{(N/Q+1) - (N/Q-1)\cos 4(\theta-\omega)} \right]$$

..... 2.46

The local inclination, α_s, of the σ_1^i stress trajectories with respect to the plans of foliation is given by (fig. 2.6B):

$$\alpha_s = \omega - \omega_s$$

$$\alpha_s = \omega - \theta + \frac{1}{2} \arctan \left[\sin 2\theta \Big/ \cos 2\theta - \frac{(N/Q-1)(\cos 2\theta - \cos 2(2\omega-\theta)}{(N/Q+1) - (N/Q-1)\cos 4(\theta-\omega)} \right]$$

..... 2.47

2.3 PREDICTIONS OF THE ANALYSIS

A series of analytical expressions have been derived in the preceeding sections which give a complete description of the physical response of a parallel sided domain of rotated foliation or layering to a defined state of externally applied stress. Although these expressions have been based solely on the anisotropic response of a layered or foliated material to stress, and do not contain terms which would reflect the tendency for individual competent components of such materials to buckle or flex in the classic sense, it will be shown that the analysis explains many of the features seen in folds developed in well bedded or foliated geological materials. In the author's opinion the results of the analysis illustrate the significant role played by foliation or layer anisotropy during the finite development of structures in such materials.

The analysis is particularly useful because it can be used to investigate the response of a parallel sided layer rotation domain oriented at any angle, θ, to the external foliation. If a value of $\theta = 0^\circ$ is introduced into the analysis then the analysis can be used to investigate the response of either

(a) a localised rotation domain oriented normal to the external foliation - fig. 2.7A or

(b) adjacent, parallel rotation domains in the form of the limbs of a series of symmetric, similar folds. - fig. 2.7B. In this special case the role of the "external foliation" is played by a narrow zone of unrotated foliation which straddles the hinge zones of the structures. As in the case of a localised oblique rotation domain, σ_1 must act parallel to the foliation surfaces in the external foliation - i.e. normal to axial planes of the structures shown in fig. 2.7 B.

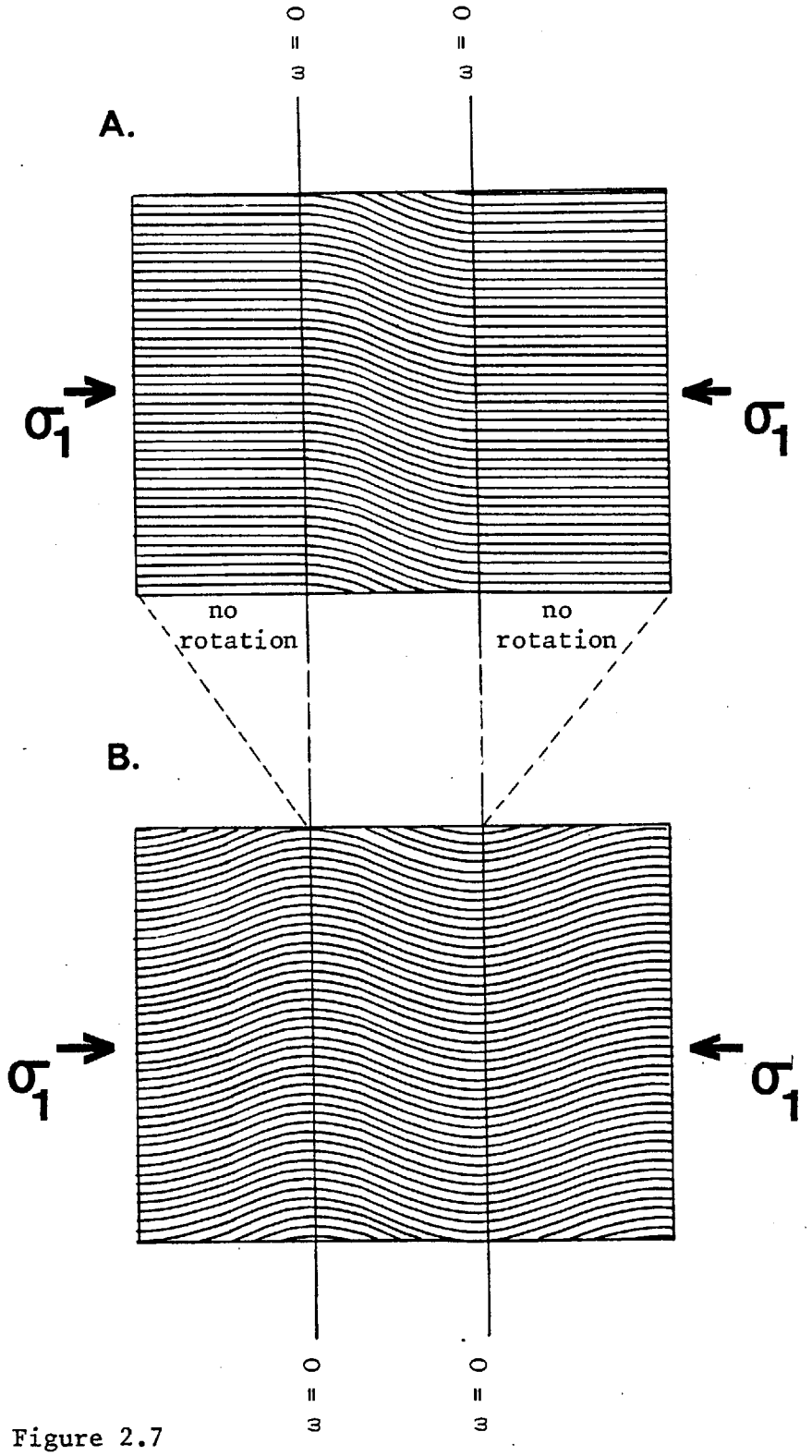


Figure 2.7

The analysis simplifies to the special case of the deformation of symmetric similar folds discussed by Cobbold (1976) if the angle θ is set at 0°.

For convenience the various analytic expressions derived in the analysis have been listed in table 2.1. Each expression involves four variables which can be defined for a particular structure and which are of obvious geological significance.

(i) $\frac{\tau_m^e}{4N}$ - the stress level in the external foliation expressed as the ratio between the maximum shear stress in the external foliation and the maximum principal stiffness coefficient N.

(ii) N/Q - the anisotropy ratio, which is fundamental property of a laminated material and can be measured or estimated.

(iii) θ - the orientation of the rotation domain with respect to the external foliation.

(iv) ω - the local finite rotation of the foliation within that element in which strain rates, foliation rotation rate, stress conditions, etc., are to be calculated.

It should be noted that in a specified structure (θ, N/Q known), under a defined level of externally applied stress ($\tau_m^e/4N$), the local incremental conditions are a function only of the local attitude, ω, of the foliation planes. Under the geometrical and displacement conditions assumed in the analysis, all components of stress, incremental strain rate, etc., are constant along the length of individual foliation elements (independent of y).

2.3.1. INCREMENTAL FOLIATION ROTATION RATE AS A FUNCTION OF FOLIATION ATTITUDE

The variation of the incremental foliation rotation rate across specific rotation domains can be described most conveniently by plotting the predicted rate, $\dot{\omega}$, as a function of the local foliation orientation, ω. This method of describing the predictions of the equations contained in table 2.1 represents a scan of local incremental conditions across a rotation band with a *specific orientation*, θ, with respect to the external foliation. The influence of anisotropy ratio, N/Q, on the variation of a particular parameter with foliation orientation, ω, can be shown by a series of curves corresponding to different values of N/Q.

TABLE 2.1

ANALYTICAL EXPRESSIONS DERIVED IN THE ROTATION DOMAIN ANALYSIS

VARIABLE	ANALYTICAL EXPRESSION FOR THIS VARIABLE	NOTES
$\dot{e}_{xx}$ (2.32)	$\dot{e}_{xx} = \frac{\tau_m^e}{4N}\left[-2\cos 2\theta\right]$	Direct strain rate resolved along a direction, x, normal to the plane of the rotation domain boundaries. $\dot{e}_{xx}$ must be constant across the rotation domain under the conditions of the analysis. (independent of ω and N/Q.)
$\dot{e}_{xy}$ (2.35)	$\dot{e}_{xy} = \frac{\tau_m^e}{4N}\left[\frac{4(N/Q) - 2(N/Q-1)\sin 4(\theta-\omega)\cos 2\theta}{(N/Q+1) - (N/Q-1)\cos 4(\theta-\omega)}\right]$	Shear strain rate resolved along a a direction, y, parallel to the plane of the rotation domain boundaries.
$\dot{\theta}$ (2.42)	$\dot{\theta} = \frac{\tau_m^e}{4N}\left[2\sin 2\theta\right]$	Rate of rotation of the rotation domain boundaries with respect to the plane of the external foliation.
$\dot{\omega}$ (2.43)	$\dot{\omega} = \frac{\tau_m^e}{4N}\left[-2\cos 2\theta \cdot \sin 2(\theta-\omega) + \frac{4(N/Q) - (N/Q-1)\sin 4(\theta-\omega)\cos 2\theta\theta}{(N/Q+1) - (N/Q-1)\cos 4(\theta-\omega)\theta} \cdot 2\cos^2(\theta-\omega) - 2\sin 2\theta\right]$	Rate of rotation of the plane of the internal foliation with respect to the plane of the external foliation.
$\bar{\sigma}^i - \bar{\sigma}^e$ (2.44)	$\bar{\sigma}^i \; \bar{\sigma}^e = \tau_m^e\left[\frac{(N/Q-1)\left\{\cos 2\theta - \cos 2(2\omega-\theta)\right\}}{(N/Q+1) - (N/Q-1)\cos 4(\theta-\omega)}\right]$	Difference between the local mean stress within the internal foliation ($\bar{\sigma}^i$) and the mean stress within the unrotated external foliation ($\bar{\sigma}^e$).
ω_s (2.46)	$\omega_s = \theta - \frac{1}{2}\arctan\left[\sin 2\theta \Big/ \left(\cos 2\theta - \frac{(N/Q-1)\left\{\cos 2\theta - \cos 2(2\theta-\omega)\right\}}{(N/Q+1)-(N/Q-1)\cos 4(\theta-\omega)}\right)\right]$	Local rotation of the σ_1 trajectories within the internal foliation (σ_1^i) with respect to the line of action of σ_1 in the external foliation (σ_1^e).
α_s (2.47)	$\alpha_s = \omega-\theta+\frac{1}{2}\arctan\left[\sin 2\theta \Big/ \left(\cos 2\theta - \frac{(N/Q-1)\left\{\cos 2\theta - \cos 2(2\theta-\omega)\right\}}{(N/Q+1)-(N/Q-1)\cos 4(\theta-\omega)}\right)\right]$	Local attitude of the σ_1 trajectories with respect to the plane of foliation.

The variation in local incremental foliation rotation rate, $\dot{\omega}$, as function of ω (equation 2.39) is illustrated in figs. 2.8A, B, C, D and E for rotation domain orientations, θ, of (A) 0°, (B) 15°, (C) 30°, (D) 45°, (E) 60°. In each figure, rotation rate profiles have been constuctive for three representative values of material anisotropy ratio (N/Q = 1.0 (isotropic), 5.0 and 100.0 (highly anisotropic)). The rate of incremental foliation rotation, $\dot{\omega}$, has been expressed in dimensionless form by expressing this rate as a fraction of the stress level in the external foliation (i.e. as $\dot{\omega}/(\tau_m^e/4N)$). (Because the maximum rate of foliation rotation achieved in a material with N/Q = 100 is significantly greater than the maximum rate developed in the less anisotropy examples the rotation rate profiles for this case are shown on separate graphs with an expanded rate axis).

The graphs show the following features:

(i) If the material is isotropic (N/Q = 1) then the foliation surfaces and rotation domain boundaries shown, for example, in fig. 2.1, have no unique mechanical significance. They represent purely passive markers drawn on the surface of a body of isotropic, linearly viscous material and the rotation domain formed by these is "apparent" rather than real. Such an apparent rotation domain will undergo homogeneous deformation (pure shear) on principal axes of strain which are co-axial with the applied principal stresses σ_1 and σ_3. If a value of N/Q = 1 is introduced into the rotation rate equation 2.39 then this equation simplifies to an expression for the passive rotation of a marker line making an angle ω to the applied principal compression, σ_1. This prediction is reflected in the rotation rate profiles shown in figs. 2.8 for N/Q = 1. The rate profiles are the same in each figure (i.e. independent of the orientation, θ, of the "apparent" rotation domain). As required, the passive rotation rate is maximum for a passive foliation inclination of 45° to the applied compression. ($\omega = 45^{\circ}$).

(ii) As would be expected, increase in the value of material anisotropy rather tends to produce an increase in the predicted rate of incremental foliation rotation. The phrase 'tends to produce' is used advisedly because over certain ranges of foliation orientation, ω, the foliation rotation rate is actually less than it would be if the material was incrementally isotropic and the foliation mechanically passive. This applies even to the highest degree of anisotropy

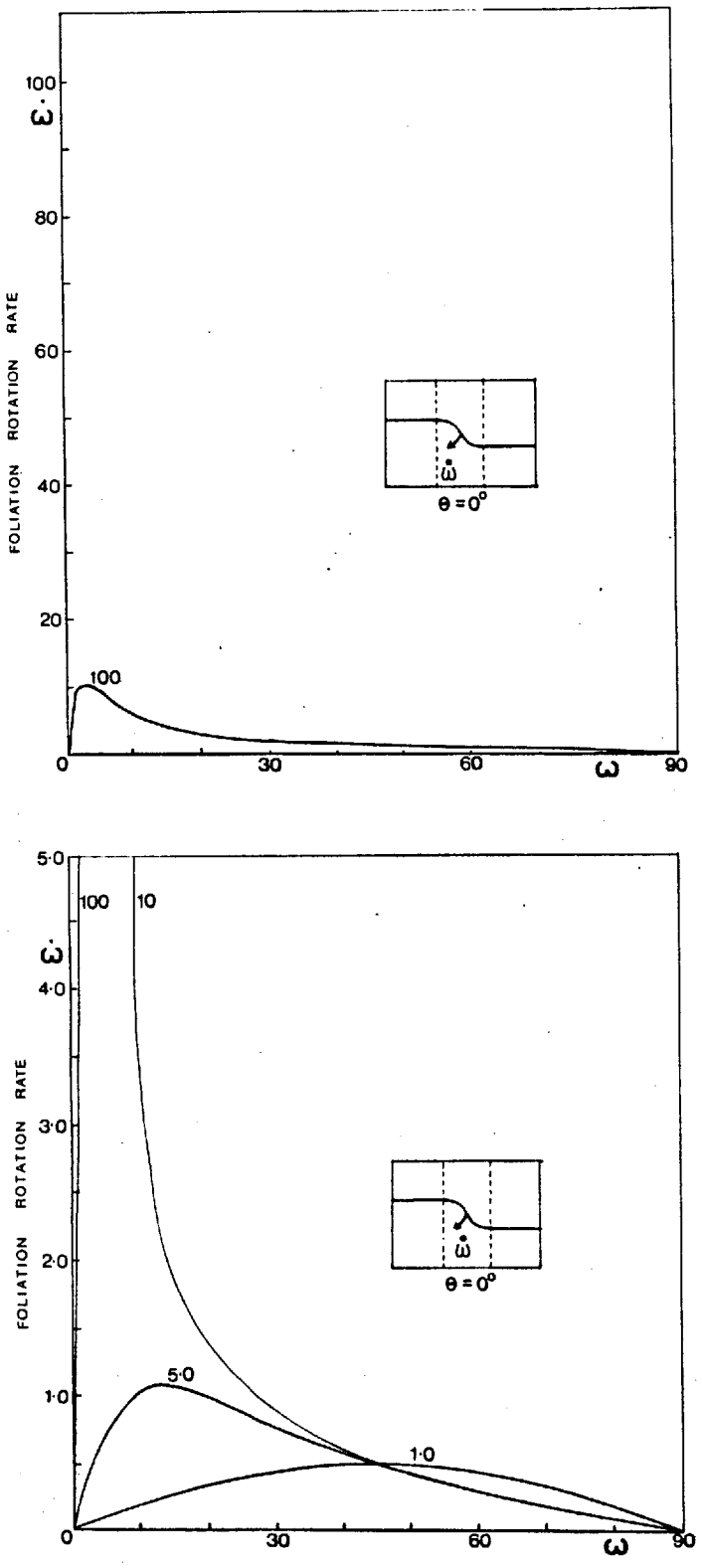


Figure 2.8 A Graphical representations of the variation in incremental foliation rotation rate $\dot{\omega}$ as a function of foliation orientation (N/Q = 1.0 (isotropic), 5.0 and 100.0) The magnitude of $\dot{\omega}$ is shown as normalised to the stress level in the external foliation (ie. $\dot{\omega}$ is expressed as $\dot{\omega}/(\dot{\tau}^{e}_{m}/4N)$.

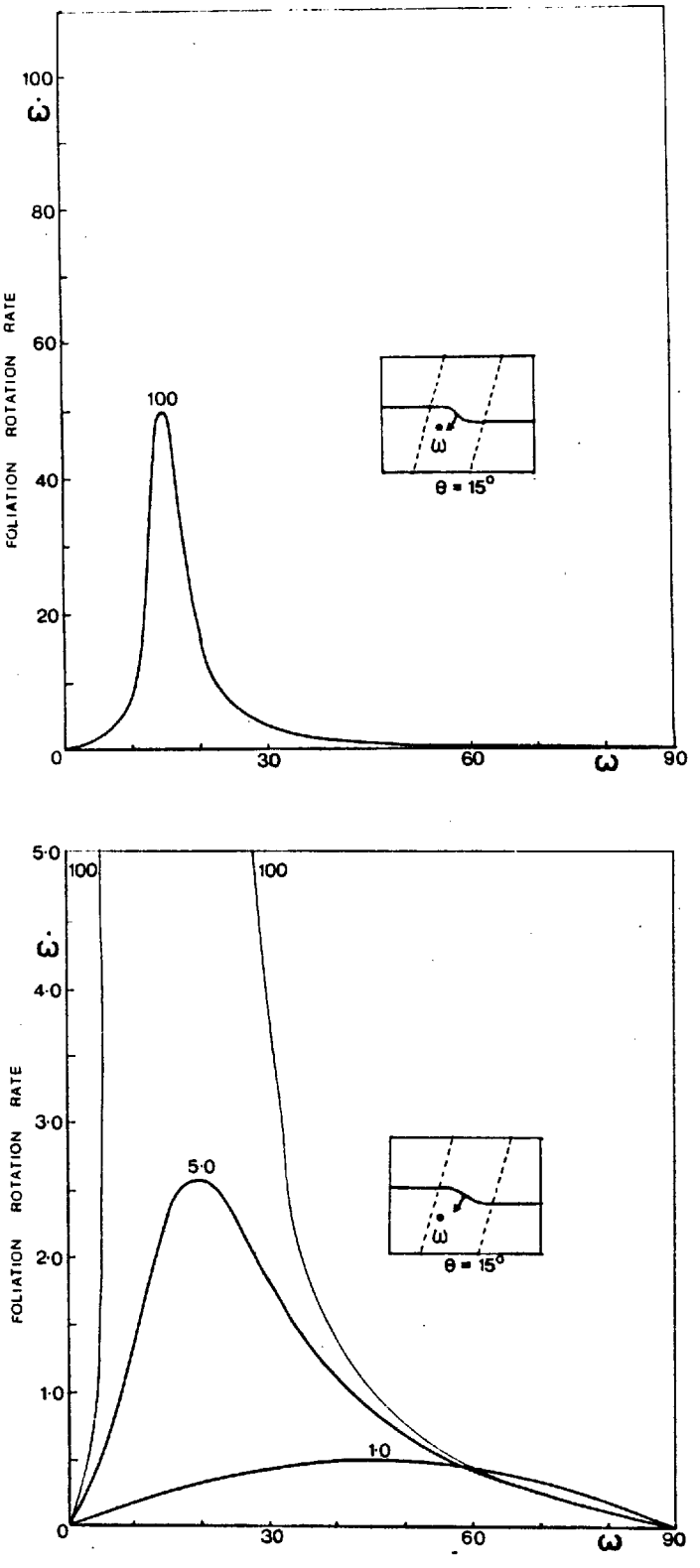


Figure 2.8 B $\dot{\omega}$ versus ω, $\theta = 15^{o}$

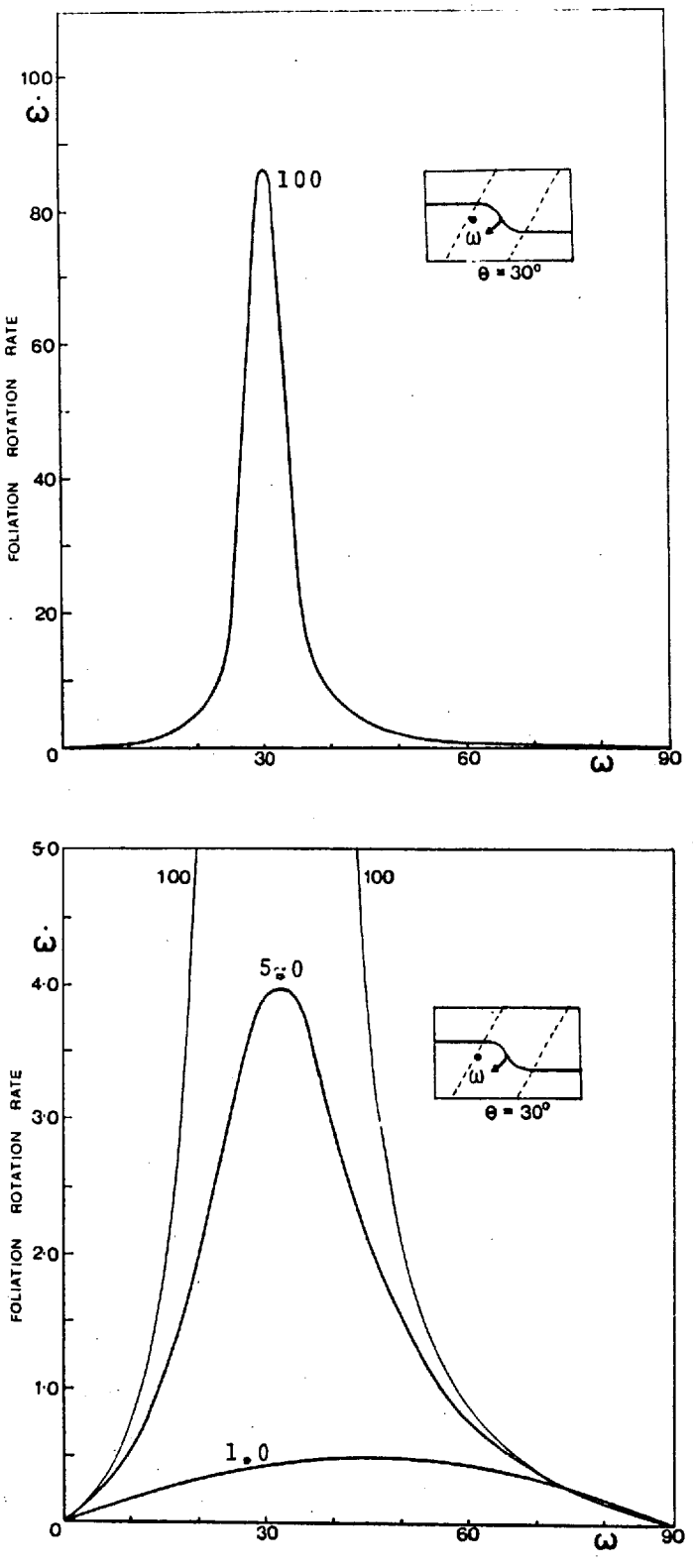


Figure 2.8 C $\dot{\omega}$ versus ω, $\Theta = 30^{o}$

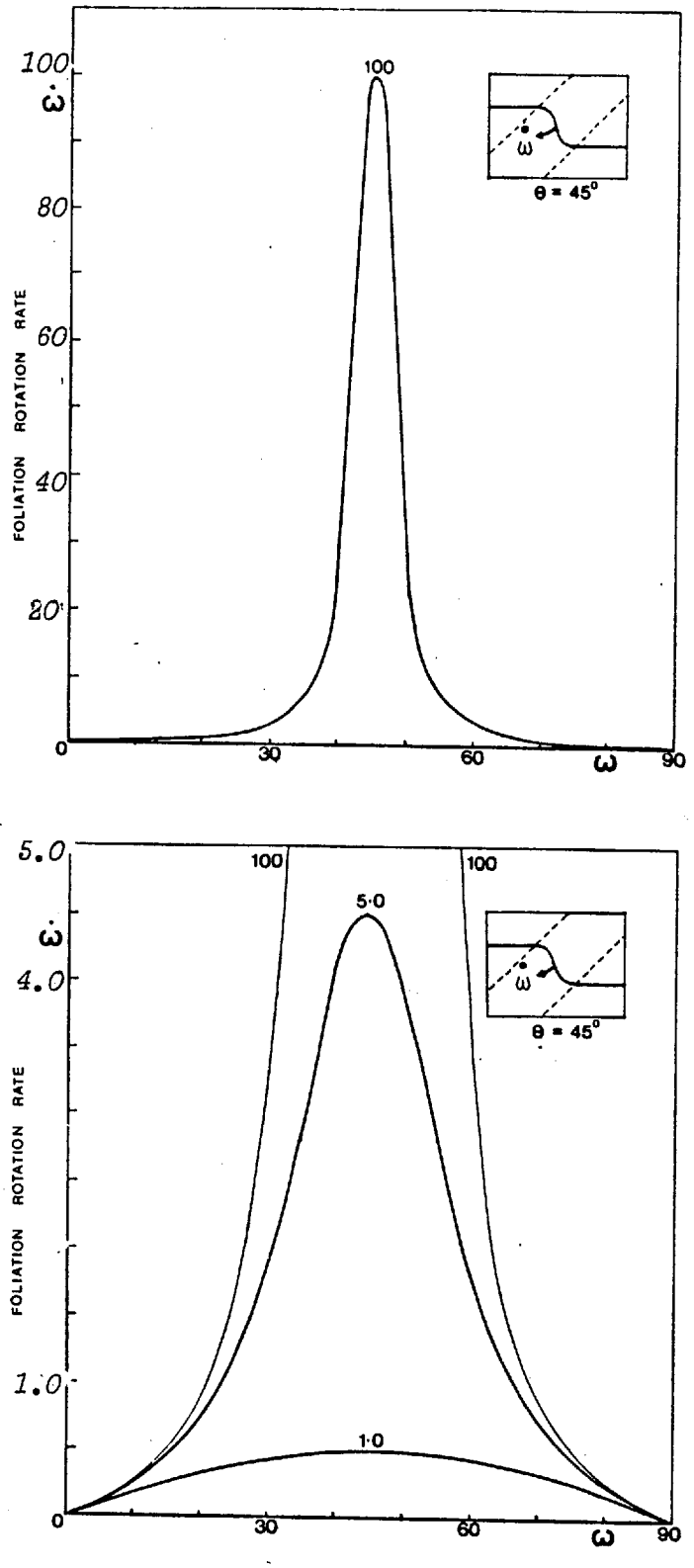


Figure 2.8 D $\dot{\omega}$ versus ω, $\Theta = 45^{\circ}$

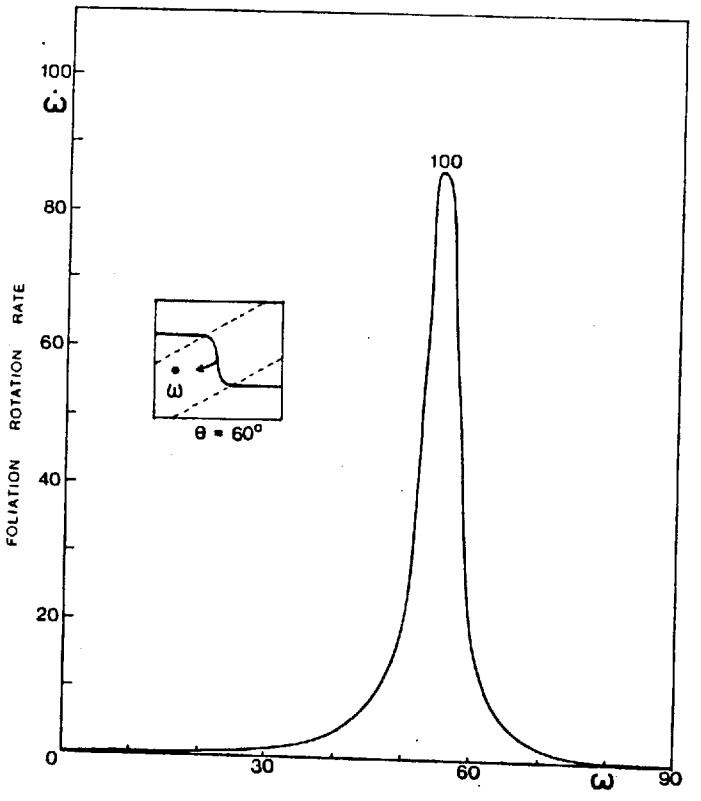


Figure 2.8 E $\dot{\omega}$ versus ω, $\theta = 60^{o}$

(N/Q = 100) illustrated in figs. 2.8. It will be shown later that this phenomenon leads to the prediction of "locking" of the foliation attitude during the later stages of foliation rotation and also indicates that the foliation within rotation domains inclined at angles less than 45° to the plane of the external foliation (i.e. $\theta > 45^{\circ}$) will have a high initial rotational stability.

The maximum influences of material anisotropy on the induced rate of incremental foliaton rotation is achieved at a foliation orientation given by $\omega = \theta$. This orientation corresponds to a foliation attitude normal to the boundaries of the rotation domain (see fig.2.3). This position marks the maximum rate of foliation rotation in materials with a significant degree of anisotropy. The rotation rate profiles corresponding to such materials (N/Q = 100) are significantly "peaked" and high rates of foliation are induced only over a restricted range of foliation attitudes about the band normal foliation position $\omega = \theta$. The development of a peak in the foliation rotation rate profiles is less marked, although still present, in the profiles corresponding to a material anisotropy ratio of 5.0. It should be noted that the foliation position corresponding to the maximum rotation rate drifts from the band normal foliation attitude $\omega = \theta$ towards the ubiquitous, isotropic position of $\omega = 45^{\circ}$ as the anisotropy ratio of the material decreases. (In the case of a rotation domain oriented at $\theta = 45^{\circ}$, the maximum foliation rotation rate occurs at $\omega = 45^{\circ}$), irrespective of anisotropy ratio - i.e. the foliation rotation rate profiles are symmetric about the $\omega = 45^{\circ}$ plane).

There is one exception to rule that the maximum rate of foliation rotation for N/Q = 100 occurs at the band normal foliation attitude $\omega = \theta$. This exception is the special case $\theta = 0^{\circ}$ (fig.2.8A). In this case, the condition $\omega = \theta$ obviously corresponds to no rotation. Inspection of fig. 2.8A shows that the maximum rate of foliation rotation occurs not at but close to the band normal position and in the limbs of symmetric similar fold ($\theta = 0$) the maximum rate of foliation rotation is achieved during the first increments of fold amplification.

(iii) In any structure the foliation rotation rate is zero for foliation attitudes $\omega = 0^{\circ}$ and $\omega = 90^{\circ}$. The condition $\omega = 0^{\circ}$ corresponds to orientation of the external foliation and clearly no rotation of the external foliation planes can occur under the assumed

external stress conditions. The externally applied, foliation parallel compression will induce rotation of foliation ($\dot{\omega} > 0$) only if an initial perturbation of the foliation is present ($\omega > 0$). The second condition ($\dot{\omega} = 0$ when $\omega = 90^{\circ}$) indicates that $\omega = 90^{\circ}$ represents the maximum possible internal foliation rotation under the conditions of the analysis.

Although a good deal of information can be obtained by detailed inspection of the incremental rotation rate profiles shown in figs. 2.8, the most interesting aspects of these graphical representations can be illustrated by considering their relevance to the problems of the finite deformation of monoclinic rotation domains. This problem is considered in the following sections.

2.3.2 Finite development of foliation rotation within an individual rotation domain element

This discussion in the previous section has been concerned with the variation in *incremental* foliation rotation rate as a function of internal foliation attitude, within a structure with boundaries oriented at a specific angle, θ, to the plane of the external foliation. Since this discussion applies only to one increment of deformation, it cannot be used to interpret the variation in incremental foliation rotation rate with time within any given foliation element or to quantify the finite rotation of foliation with such an element. In order to make this possible it is necessary to take account of the fact that no only will the attitude of the local foliation within a rotation domain change with finite deformation but also that the boundaries of rotation domain, themselves, will undergo a finite rotation with respect to the external foliation. Unfortunately, equation 2.39 cannot be integrated analytically to obtain an expression for finite rotation ω_f as a function of finite deformation or time. However the expression can be integrated by a numerical method which takes into account the influence of both the finite change in the orientation of the foliation within an element of the rotation domain and the finite rotation of the boundaries of the rotation domain on the incremental rate of internal foliation rotation.

The results of this analysis will be illustrated graphically by plotting the finite rotation, ω_f, of the foliation within a specific element of a rotation domain as a function of time. These graphs also represent the finite rotation of foliation within an angular rotation domain with a uniform internal foliation orientation). In calculating the finite rotation curves, it has been assumed that the initial angle of rotation of the internal foliation, ω_f, is 5°. The subsequent finite rotation of the internal foliation is illustrated in figs. 2.9 A to E for different values of the initial orientation, $\theta_o = 0^o$ (2.9A), 15° (2.9B), 30° (2.9C), 45° (2.9D) and 60° (2.9E)). The change in the angle of internal foliation rotation, is shown as a function of time. The elapsed time is given in dimentionless units which are derived by normalising the elapsed time to the stress level in the external foliation. (Elapsed time, t, is expressed as $t/(4N/\dot{\tau}^e_m)$). It should be noted that the units of elapsed time, expressed in this form, also correspond to the finite shortening within the external foliation (natural or logarethmic strain) measured along the direction of the plane of the external foliation.

In order to aid the description of the finite foliation rotation curves, the change in the angle of orientation of the rotation domain boundaries, with time, has been indicated on the vertical time axis. At each stage in the finite rotation of the internal foliation, the finite value of the domain orientation angle θ_f, can be determined from the intercept of a horizontal line drawn from the indicated value of θ_f on the finite foliation rotation curve.

This discussion is principally concerned with the development of foliation rotation within oblique rotation domains ($\theta_o > 0^o$) and the most significant aspects of this process can be described with reference to fig. 2.9C. The curves shown in this figure have been calculated for an initial orientation of the rotation domain boundaries of $\theta_o = 30^o$. In each of the graphs shown in fig. 2.9, three finite foliation rotation curves have been plotted which correspond to material anisotropy ratios of N/Q = 1 (isotropic), 5 and 100. The case N/Q = 1 is trivial since the rotation curves represent the passive rotation of a marker line on a body of isotropic material. The choice of initial domain orientation θ_o has no effect on the form of these passive rotation curves since the rotation domain will have no unique mechanical significant in such a material.

Figure 2.9 A

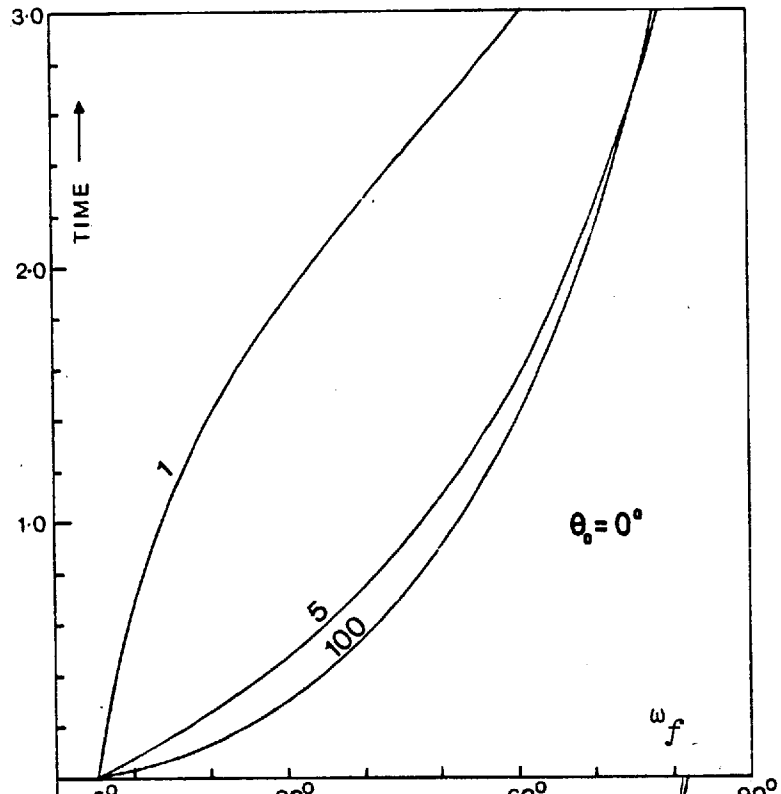
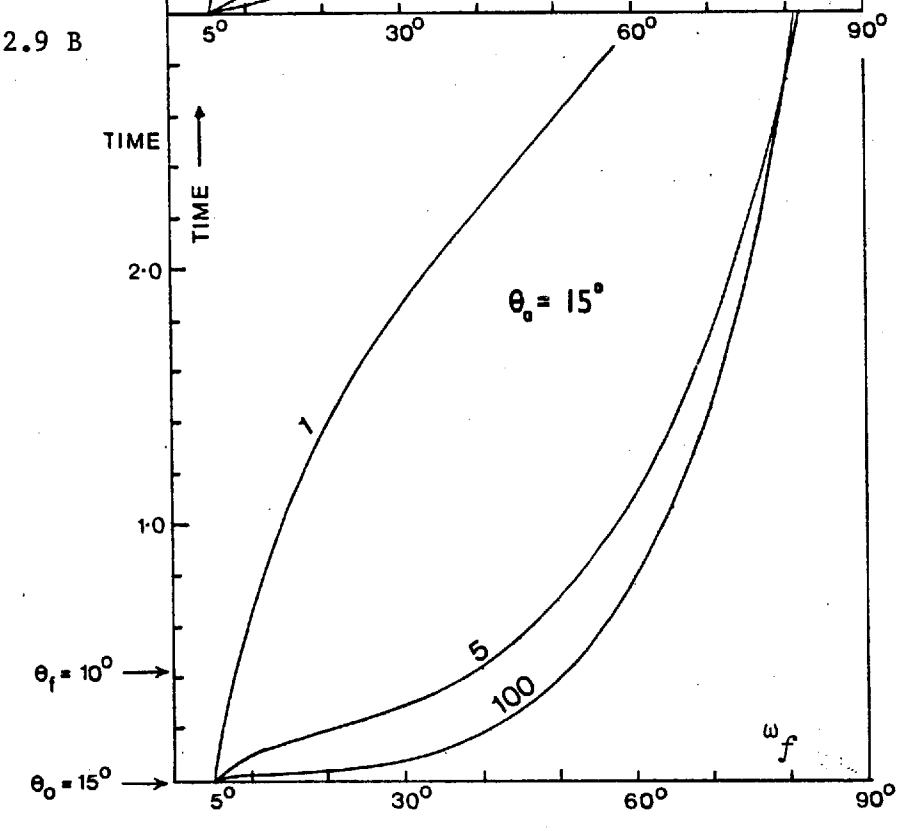


Figure 2.9 B



Figures 2.9 A to 2.9 E plot the finite change in the orientation of the plane of the internal foliation, ω_f, with time for a local element of internal foliation in which the initial foliation orientation ω_o is 5°. Each figure corresponds to a particular value for the initial domain orientation θ_o. Elapsed time is shown as normalised to the stress level in the external foliation. (ie. as $t_. (\tau^e_m/4N)$)

See text for further details.

Figure 2.9 C

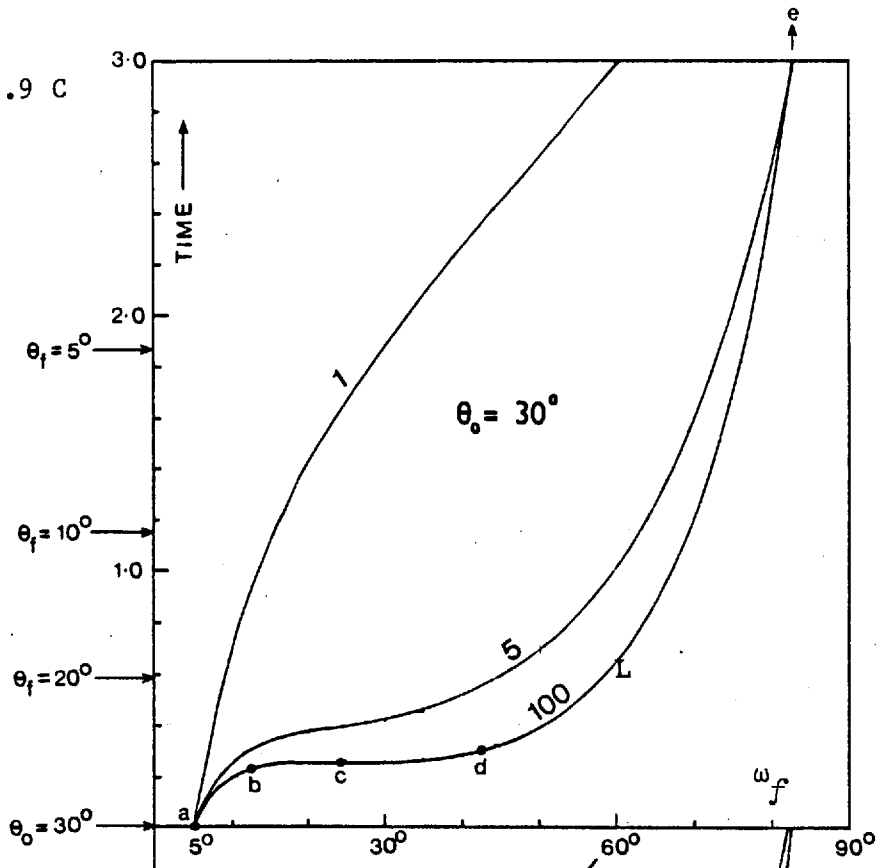


Figure 2.9 D

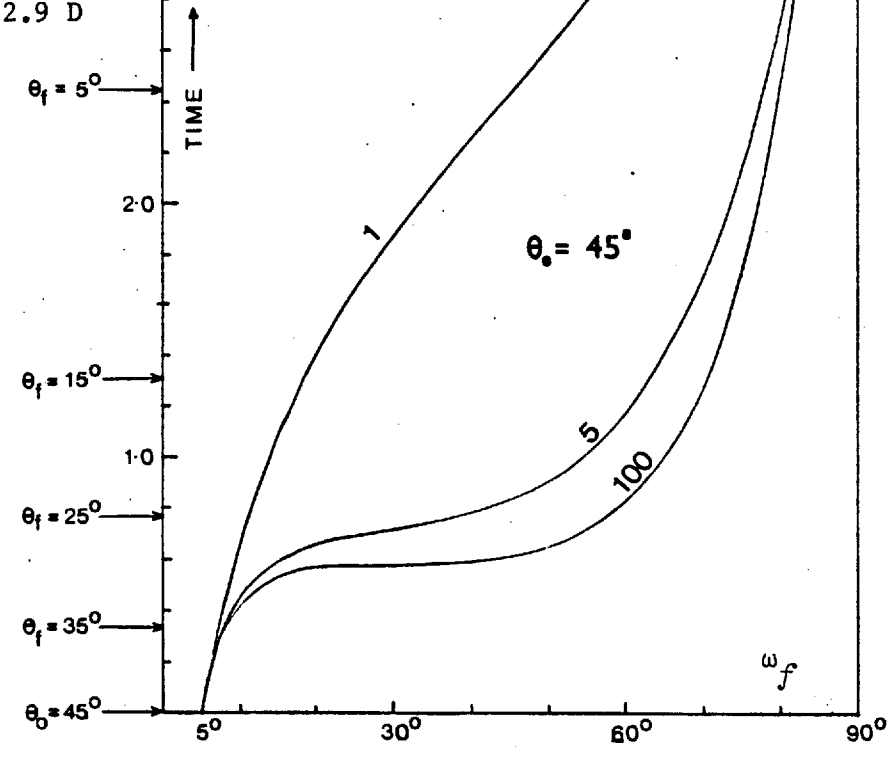
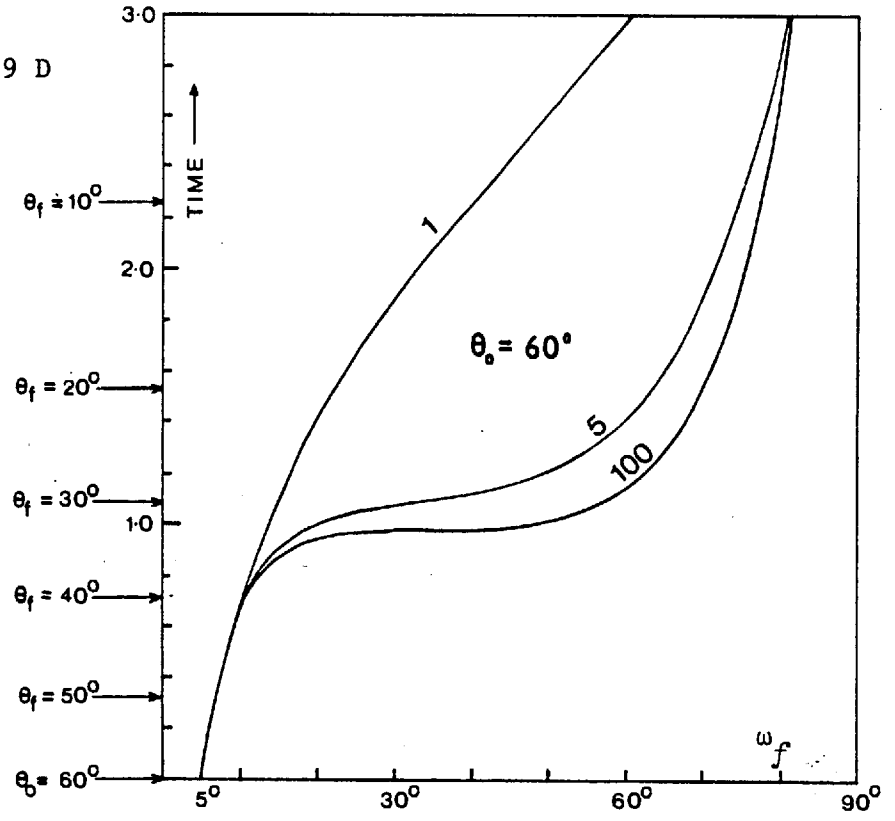


Figure 2.9 D


3·0
2·0
1·0
TIME
θf = 10°
θf = 20°
θf = 30°
θf = 40°
θf = 50°
θo = 60°
1
5
100
θo = 60°
ωf
5°
30°
60°
90°

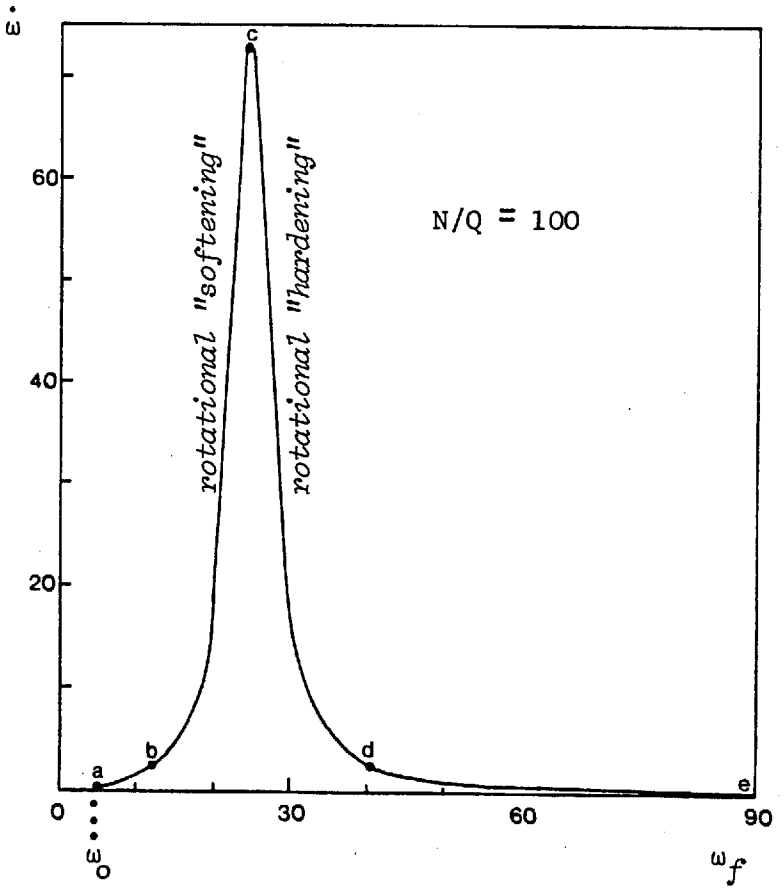


Figure 2.10 Change in the magnitude of $\dot{\omega}$ with change in the finite foliation orientation ω_f, corresponding to the finite foliation rotation curve for N/Q = 100 shown in fig. 2.9 C. ($\theta_o = 30^o$; $\omega_o = 5^o$)

The finite rotational response of the internal foliation in an anisotropic material can be broadly divided into three stages. These stages are most clearly defined in a material with a high degree of anisotropy and can best be discussed with reference to the curve corresponding to N/Q = 100 in fig. 2.9 C. The change in incremental foliation rotation rate, $\dot{\omega}$, with finite foliation rotation, ω_f , corresponding to this particular curve, has been illustrated graphically in fig. 2.10. As required, this graph is based on calculations which take into account the finite rotation of the rotation domain boundaries. The following stages can be recognised in fig. 2.9 C and can be related to the predicted change in incremental foliation rotation rate with finite foliation rotation, shown in fig. 2.10.

Stage 1 (defined by the curve segment a b in figs 2.9 C and 2.10)

During this initial phase of foliation rotation, there is a gradual increase in the incremental foliation rotation rate, $\dot{\omega}$. However, the magnitude of $\dot{\omega}$ over the range a b is relatively slow and of the same order as the rate of rotation of the rotation domain boundaries. This is expressed in fig. 2.9 C by the development of a significant rotation of the rotation domain boundaries during the initial stages of internal foliation rotations.

Stage 2 (defined by the curve segments bd in figs. 2.9 C and 2.10)

This subhorizontal section of the finite foliation rotation curve corresponds to the development of relatively rapid rates of incremental foliation rotation. This phase of significant rotational unstability occurs as the internal foliation approaches and passes through the domain normal foliation attitude $\omega_f = \theta_f$ and corresponds to the peaked section of the rotation rate curve plotted in fig. 2.10. During this phase of rotational instability, the rate of rotation of the internal foliation in highly anisotropic materials is significantly greater than that of the domain boundaries ($\dot{\omega} >> \dot{\theta}$). Thus the domain orientation, θ_f, remains relatively stable as the internal foliation undergoes a large finite rotation. The point C on the finite foliation rotation curve corresponds to the maximum incremental rate of internal foliation rotation and marks the inflexion point in the curve.

Stage 3 (defined by the curve sections de in figs. 219 C and 2.10)

During the later stages of finite foliation rotation, beyond the point d, the incremental rate of foliation rotation is very low in

comparison with the peak rate developed during the phase of maximum rotational instability. The magnitude of $\dot{\omega}$ is reduced to a level which is (as in Stage 1) of the same order as the rate of rotation of the domain boundaries, $\dot{\theta}$. Indeed, beyond the point L shown on the curve corresponding to N/Q = 100 in fig. 2.9 C, the magnitude of $\dot{\omega}$ is *less* than the rate of rotation which would be achieved at a corresponding value of foliation attitude, ω_f, if the foliation was mechanically passive (N/Q = 1). Thus, the effect of mechanical anisotropy is to stabilise the attitude of the internal foliation planes during the later stages of finite foliation rotation. This is a particularly important prediction of the rotation domain analysis. Casey (1976) and Cobbold (1976) have demonstrated that this effect also occurs in symmetric folds developed in anisotropic materials. The development of rotational stability or "locking" during the later stages of finite foliation rotation is a consequence of the effects of mechanical anisotropy alone.

It should be noted that, under the conditions of the analysis, a full finite rotation of $\omega_f = 90^\circ$ is theoretically possible in this model only after infinite finite strain in both the internal and external foliation for this limit, $\omega_f \rightarrow 90^\circ$ and $\omega_f \rightarrow 0^\circ$.

Each of the integrated foliation rotation curves calculated for oblique rotation domains developed in anisotropic materials show the stages of doliation rotation recognised in the discussion of the curve corresponding to N/Q = 100 and $\theta_o = 30^\circ$ in fig. 2.9 C. The curves differ in detail, however. The rate of incremental foliation rotation developed during the phase of maximum rotational instability, in a material with an anisotropy ratio of N/Q = 5 is slow in relation to the corresponding rate developed in the highly anisotropic material. In addition, the phase of maximum rotational instability is less well defined for N/Q = 5. The most significant difference between the curves shown in figs. 2.9 A to 2.9 D, however, concerns the amount of finite deformation required to rotate the internal foliation into a position of rotational instability (i.e. the duration of stage 1 in the finite foliation rotation curves). This point is considered in the following section in which the rotation domain analysis is used to construct a finite deformation model for the growth of specific types of low amplitude foliation perturbations in the form of kink like rotation domains.

2.3.3. FINITE DEFORMATION OF SPECIFIC LOW AMPLITUDE FOLIATION PERTURBATIONS

A computer program has been written, based on the rotation domain analysis, to model the finite deformation of a series of rotation domains oriented at various inclinations to the external foliation. The geometry of the initial foliation or layer disturbance that was used in this study is illustrated in fig. 2.11. The variation in initial foliation attitude within the domain of foliation disturbance is in the form of a half-sine curve constructed on a base axis parallel to the profile trace of the external foliation. The geometry of the initial foliation perturbation is constant along the length of the rotation domain, as required by the conditions of the rotation domain analysis. This geometry can be specified by two parameters:- a) $A_o' = A_o/\lambda$ - the ratio of the initial amplitude of the sinusoidal perturbion to the wave length, b) θ, - the inclination of the rotation domain boundaries to external foliation normal. Briefly, the operation of the programme involves the following stages:

i) The rotation domain is automatically divided into one hundred, equally spaced, band parallel elements

ii) The input value of the wavelenth ratio A_o' is used to compute the local angle of initial rotation, ω_o, within each element

iii) The incremental deformation within each element is calculated for small increments of time which correspond to increments of isotropic shortening within the external foliation of 0.001 units of natural strain (measured parallel to trace of the external foliation planes). Local incremental deformation and the corresponding local increments in foliation rotation are calculated using the analytical expressions for incremental strain rate, rigid body rotation and associated foliation rotation derived in the rotation domain analysis.

iv) Successive stages in finite deformations are modelled by numerically integrating the calculated incremental deformations. The local finite rotation, ω_f, and the finite orientation of the domain and element boundaries, θ_f, are constantly updated during this procedure.

The programme was designed to be run at an on-line computer graphics terminal* and was also designed to be fully interactive. Thus, the chosen values for the analysis variables could be input at the terminal in response to a series of programmed input commands. As a result the programme is very flexible and the effect changing the value of any of the input variables can rapidly be determined. The finite changes in geometry of a structure are displayed on the graphics terminal. It is possible to view the geometry of a structure at any stage in finite deformation. For convenience, however, the successive stages in deformation illustrated later in this section correspond to increments of 0.1 natural strain in the external foliation (i.e. successive frames of the computer display correspond to intervals of one hundred deformation increments).

Each display on the graphics terminal can be recovered and stored for permanent record either in the form of paper hardcopy or as microfilm. The diagrams included in the next section, illustrating successive stages in finite deformation, have been "xeroxed" directly from paper hardcopy obtained at the graphics terminal. It is emphasised that these figures do not show individual, discrete layers in a folded multilayer. The profile traces which define the geometry of the structures indicate only the trend of the foliation planes within the structure. The changes that occur in the distance between adjacent representative foliation planes do, however, reflect the finite strain developed in various parts of a structure.

Results of the computer analyses**

The most significant features of the finite deformation analysis can be illustrated by the representative computer runs shown in figs. 2.12 to 2.16. In each run, the amplitude ratio, A_o', of the initial sinusoidal perturbation is 0.05 and the finite deformation was calculated assuming a material anisotropy ratio of 5.0 . A different initial rotation domain orientation was used for each run ($\theta_o = 0^o$ (2.12), 15° (2.13), 30° (2.14), 45° 2.15), 60° (2.16)). In order to aid the description of the deformation shown in these figures, a graphical representation of the variation in local incremental foliation rotation rate, $\dot{\omega}$, across the rotation domain (normal to the rotation domain boundaries) is included at each stage in the development of the structures.

*Linked to the Imperial College Computer Center CDC 6600.

**Details of the programs used in the analysis are given in appendix 2.2

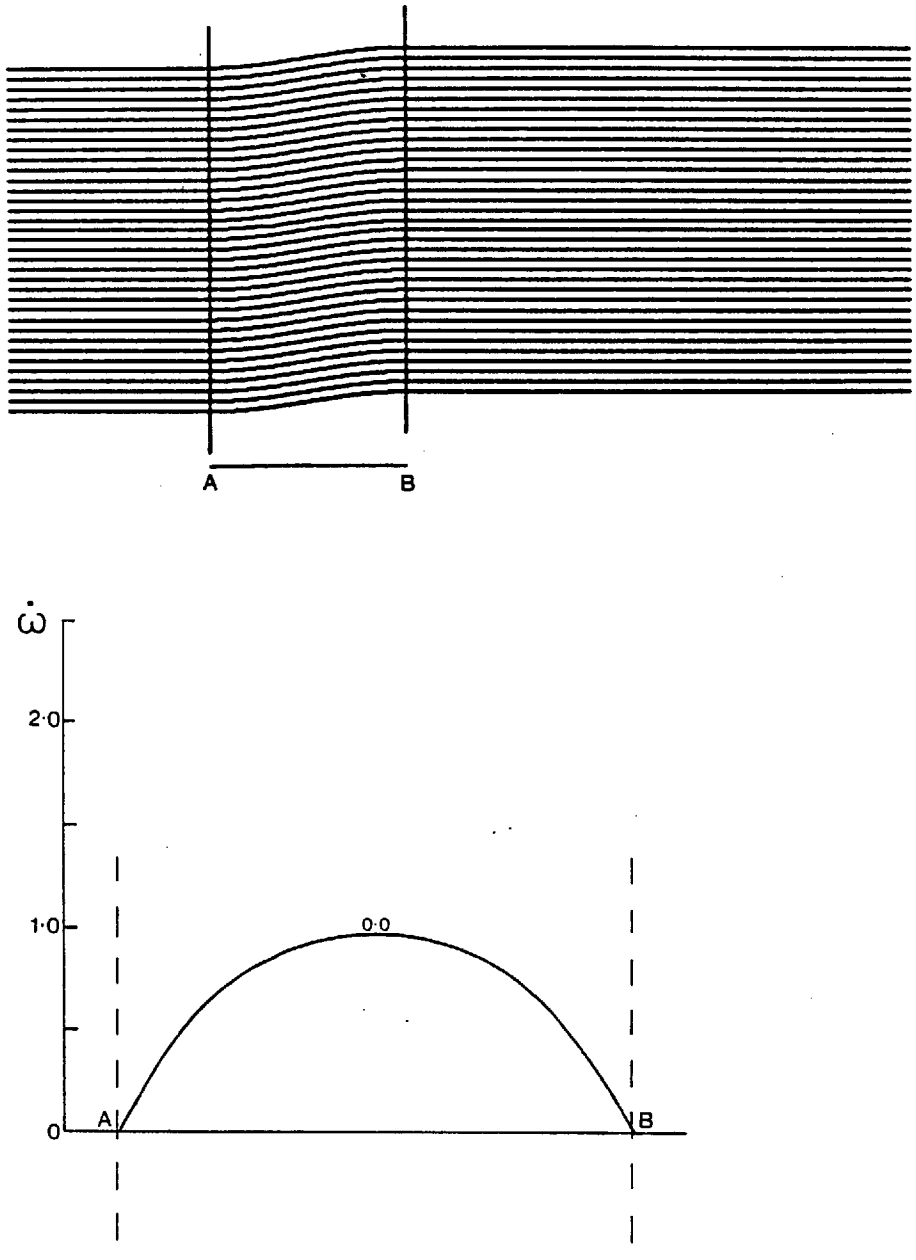


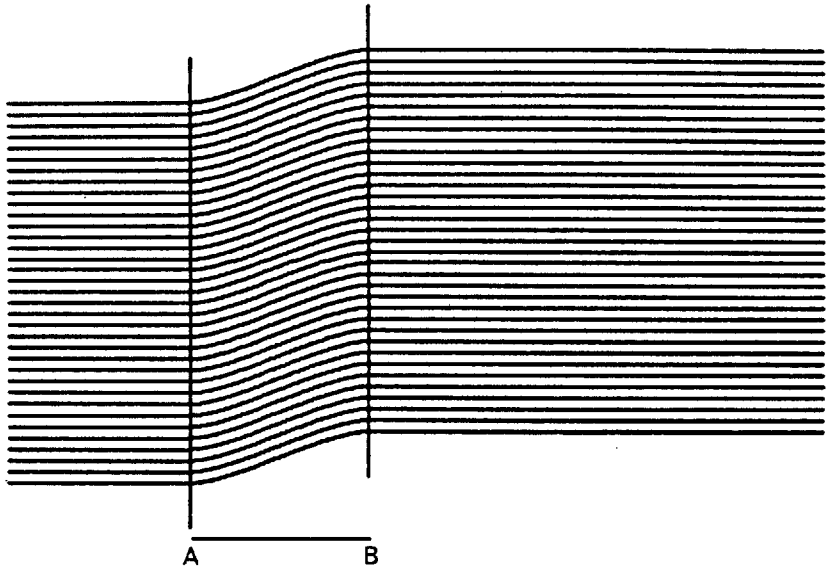
Figure 2.12 A

Initial rotation domain orientation, θ_o = 0°
Finite rotation domain orientation, θ_f = 0°

Deformation increment 0

Finite strain ε_{11} in the external foliation (natural strain) = 0.0

Anisotropy ratio, N/Q = 5.0



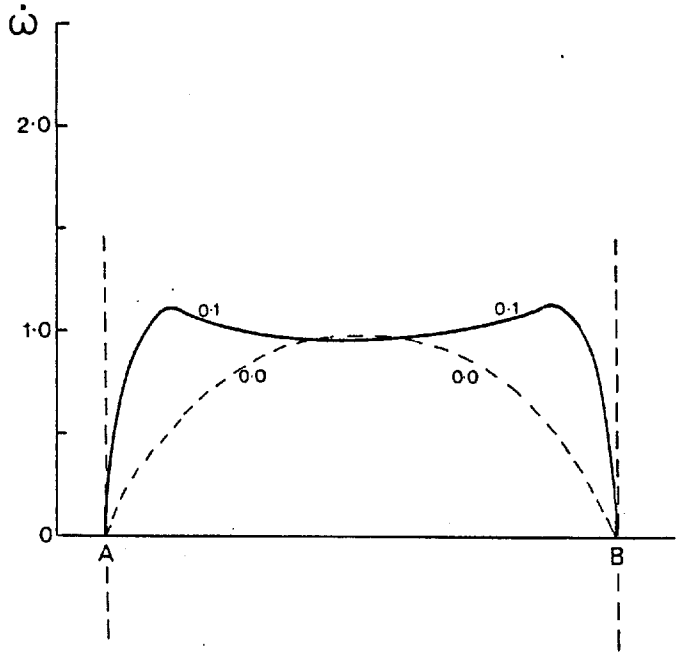
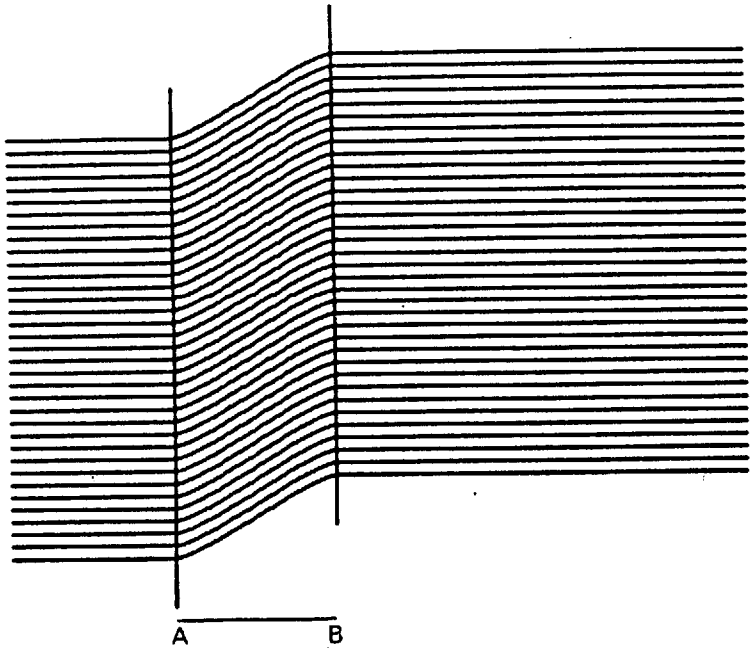


Figure 2.12 B

Initial rotation domain orientation, $\theta_o = 0^o$
Finite rotation domain orientation, $\theta_f = 0^o$

Deformation increment 100
Finite strain in the external foliation = 0.1



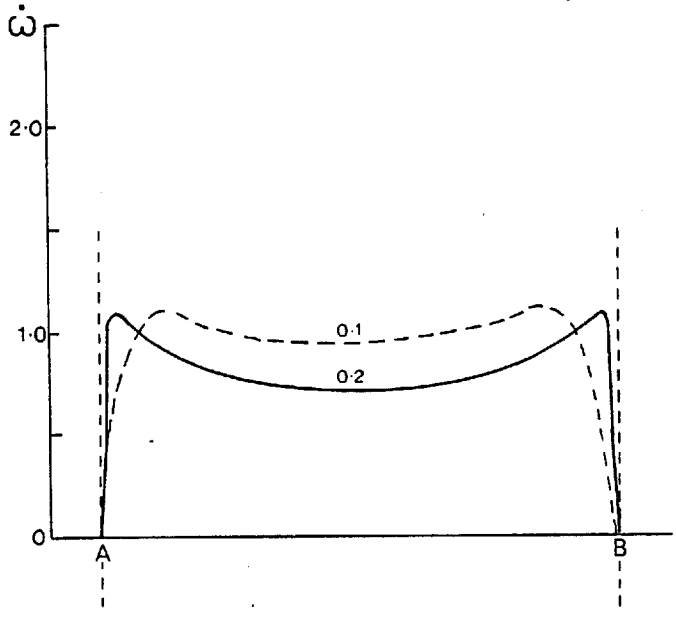


Figure 2.12 C

Initial rotation domain orientation, θ_o = 0°
Finite rotation domain orientation, θ_f = 0°

Defrmation increment 200
Finite strain in the external foliation = 0.2

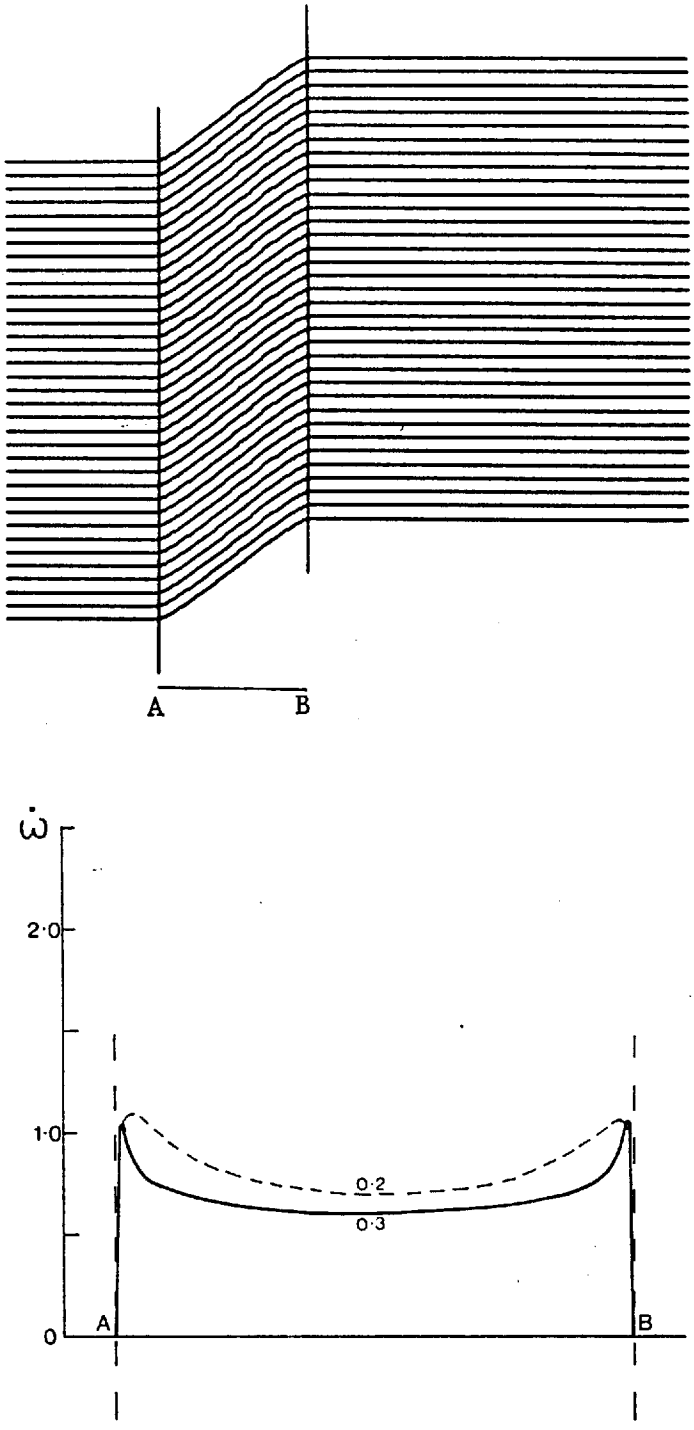


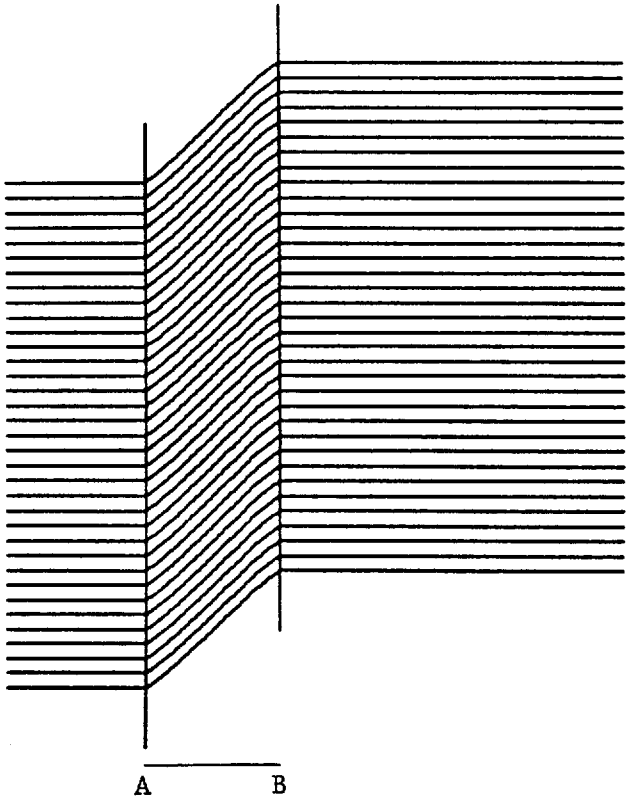
Figure 2.12 D

Initial rotation domain orientation, θ_o = 0°

Finte rotation domain orientation, θ_f = 0

Deformation increment 300

Finite strain in the external foliation = 0.3



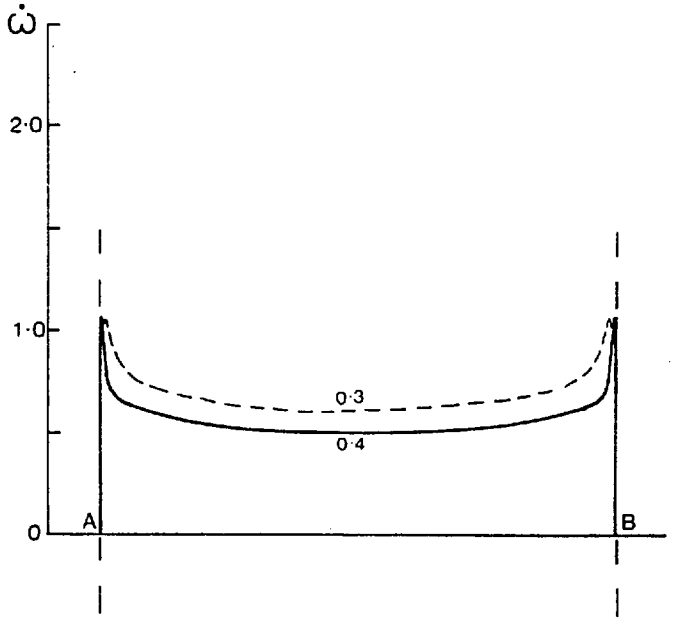
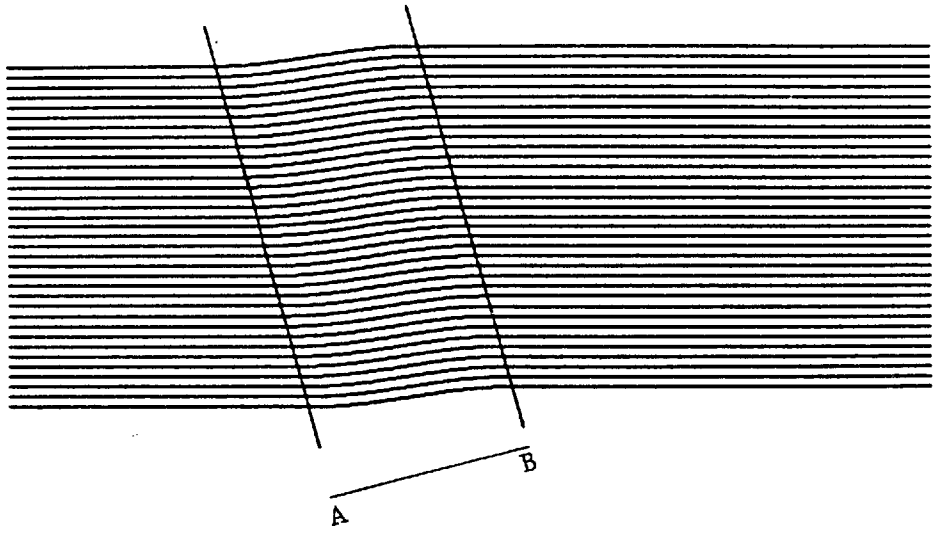


Figure 2.12 E

Initial rotation domain orientation, $\theta_o = 0^o$
Finite rotation domain orientation, $\theta_f = 0^o$

Deformation increment 400
Finite strain in the external foliation = 0.4



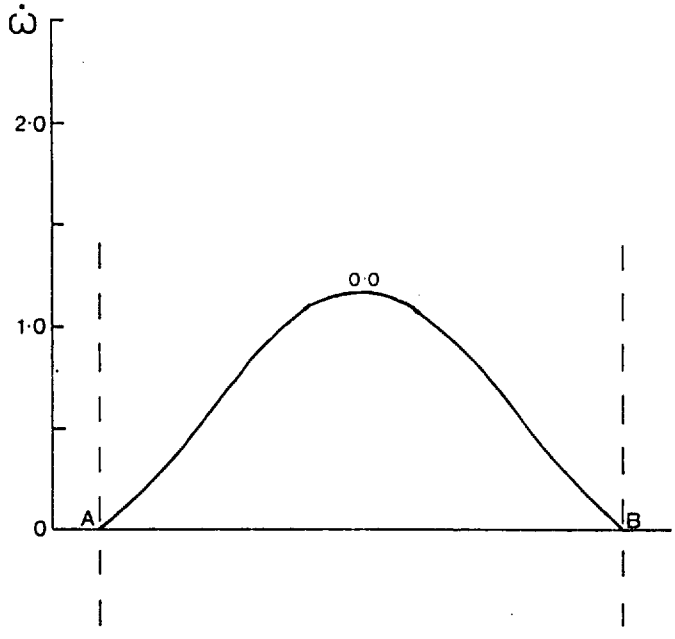
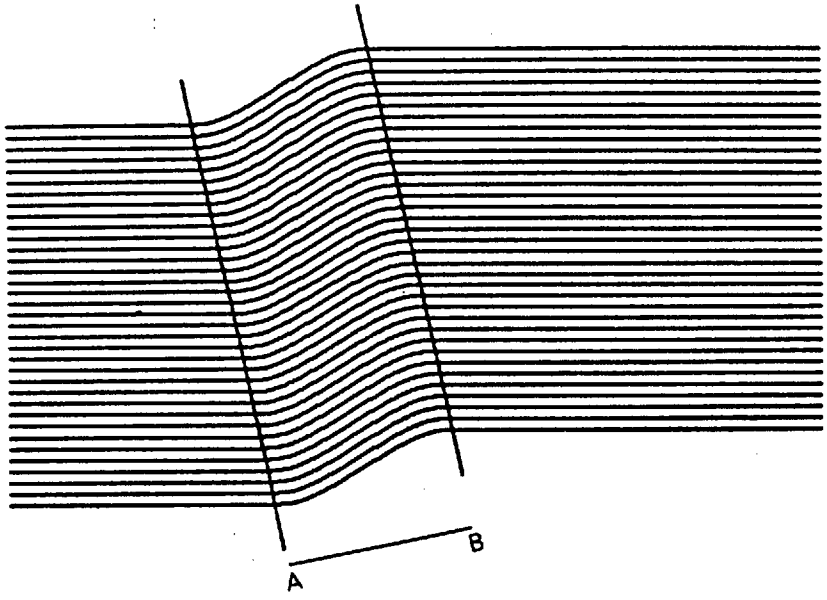


Figure 1.13 A

Initial rotation domain orientation, Θ_o = 15°
Finite rotation domain orientation, Θ_f = 15°

Deformation increment 0
Finite strain in the externalfoliation = 0.0

Anisotropy ratio, N/Q = 5.0



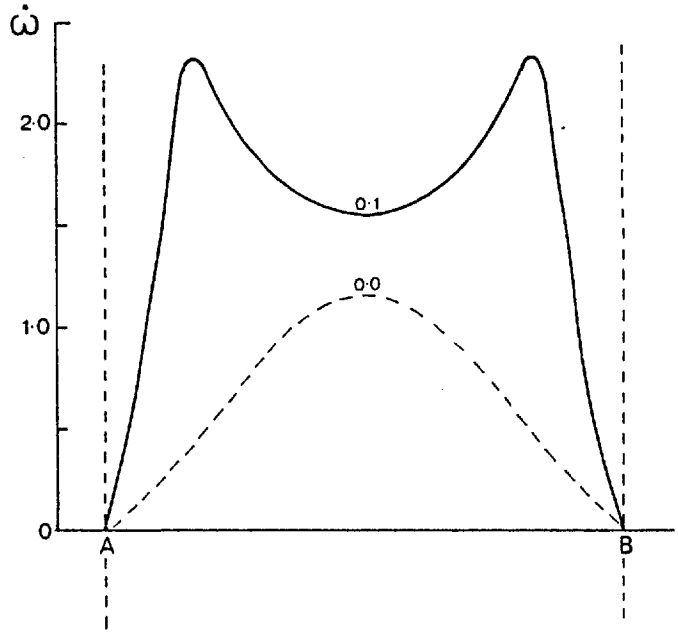
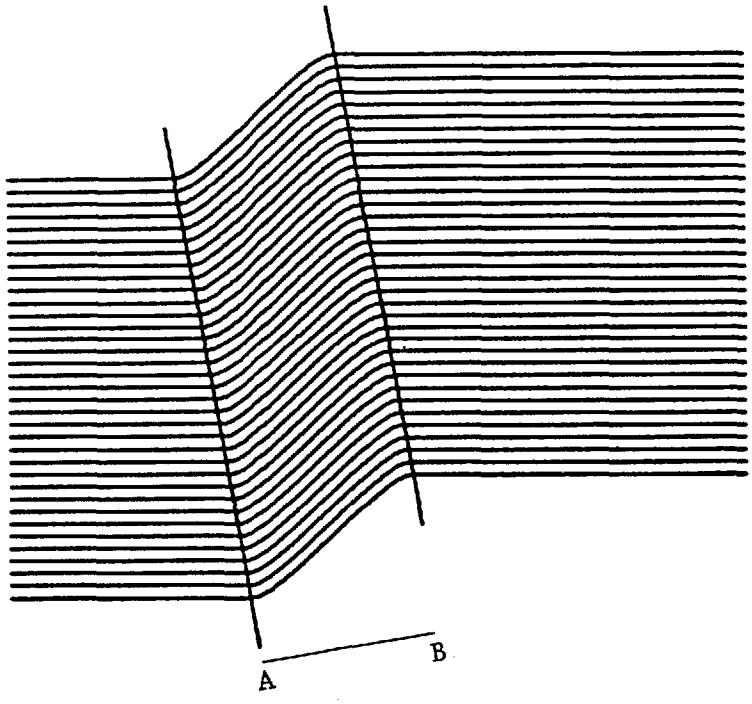


Figure 2.13 B

Initial rotation domain orientation, $\Theta_o = 15^o$
Finite rotation domain orientation, $\Theta_f = 12.5^o$

Deformation increment 100
Finite strain in the external foliation = 0.1



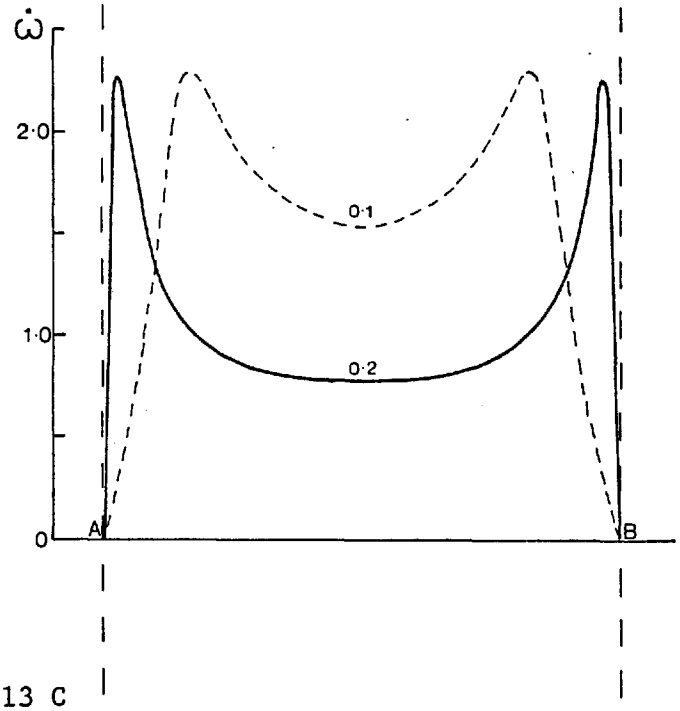
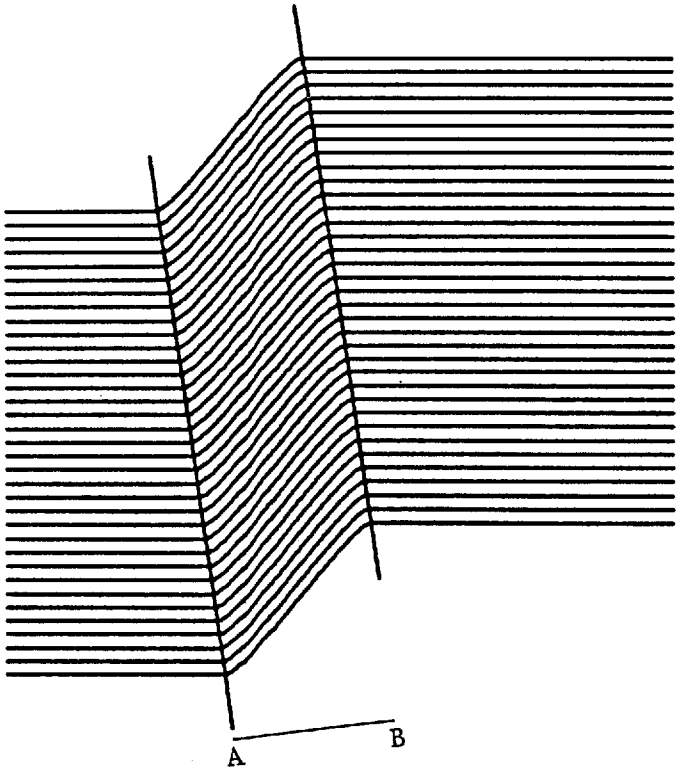


Figure 2.13 C

Initial rotation domain orientation, $\theta_o = 15^o$
Finite rotation domain orientation, $\theta_f = 10.3^o$

Deformation increment 200
Finite strain in the external foliation = 0.2



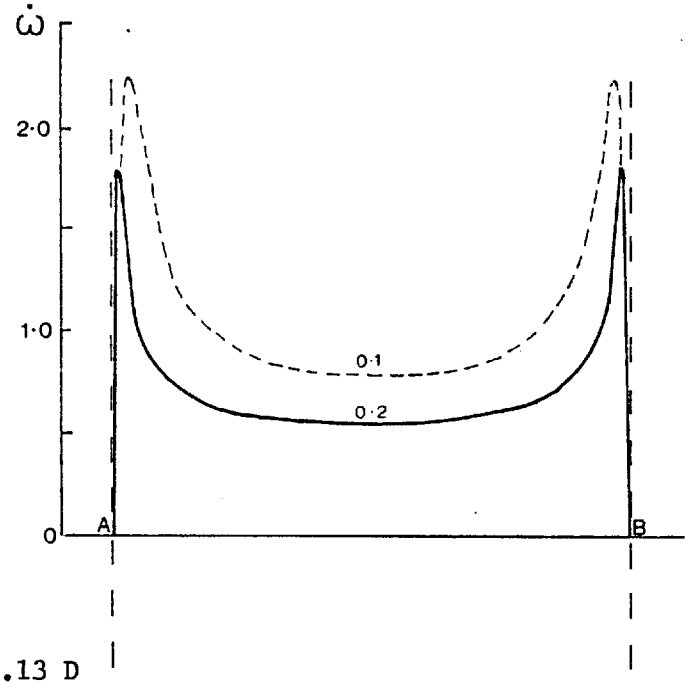


Figure 2.13 D

Initial rotation domain orientation, $\theta_o = 15^o$
Finite rotation domain orientation, $\theta_f = 8.5^o$

Deformation increment 300
Finite strain in the external foliation = 0.3

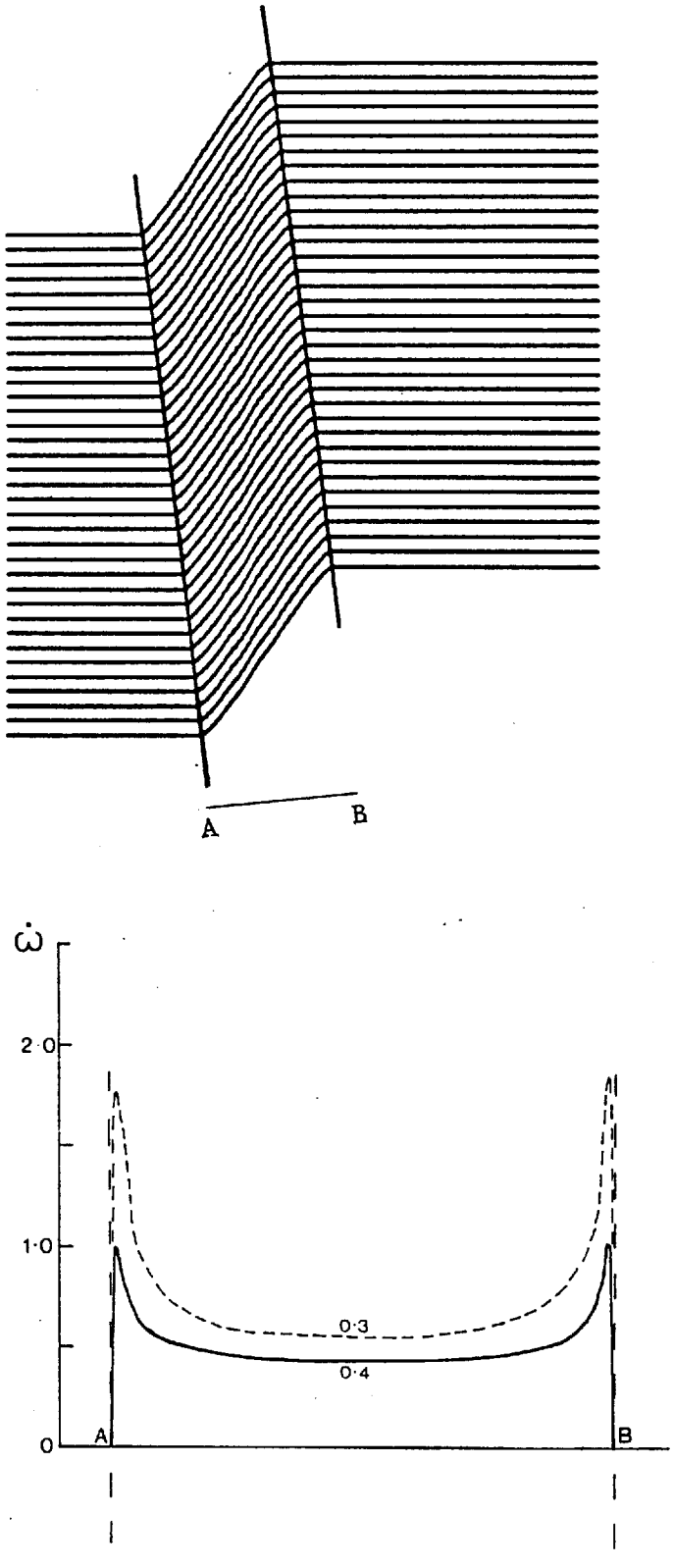


Figure 2.13 E

Initial rotation domain orientation, $\theta_o = 15^o$
Finite rotation domain orientation, $\theta_f = 6.9^o$

Deformation increment 400
Finite strain in the external foliation = 0.4

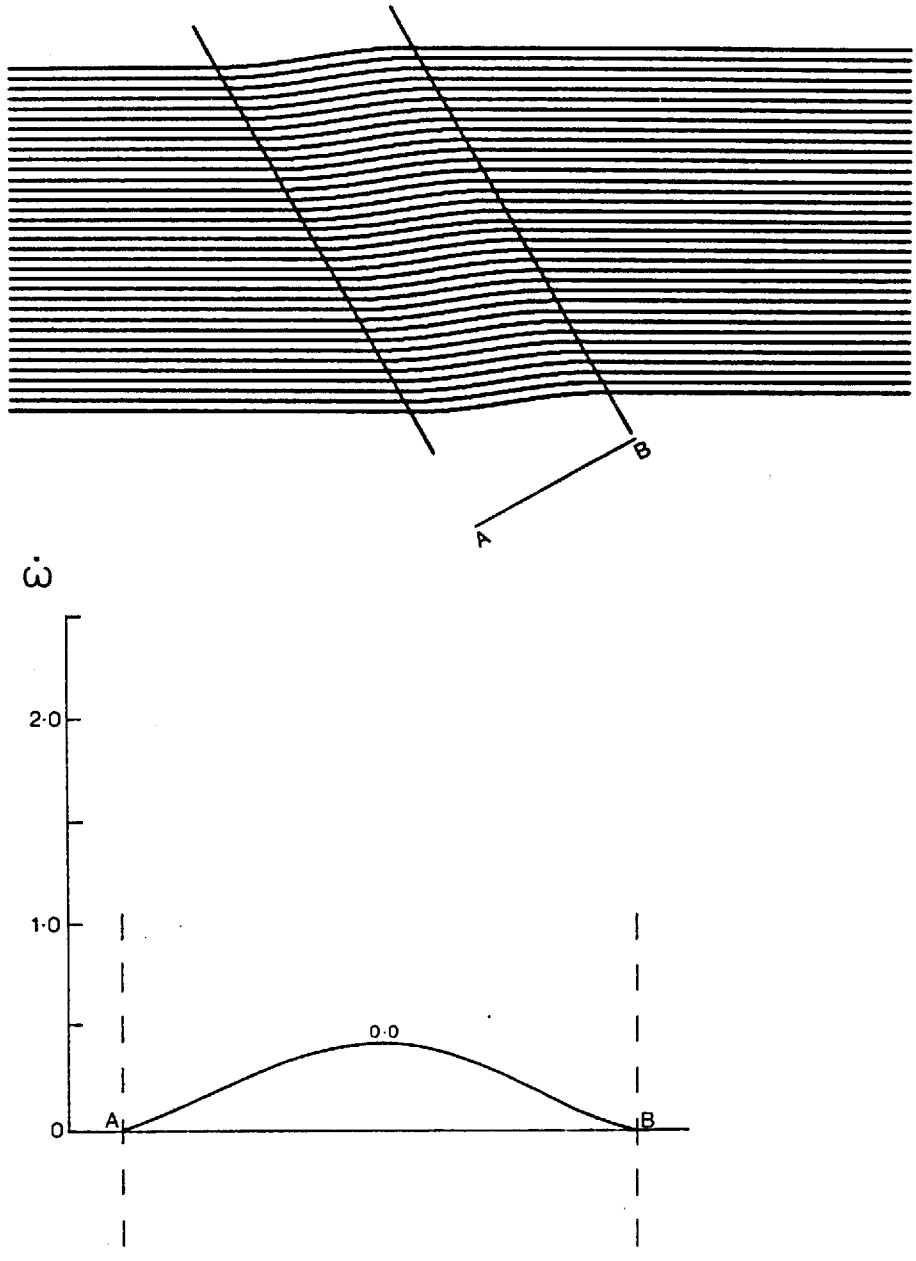


Figure 2.14 A

Initial rotation domain orientation, $\Theta_o = 30^o$
Finite rotation domain orientation, $\Theta_f = 30^o$

Deformation increment 0
Finite deformation in the external foliation = 0.0

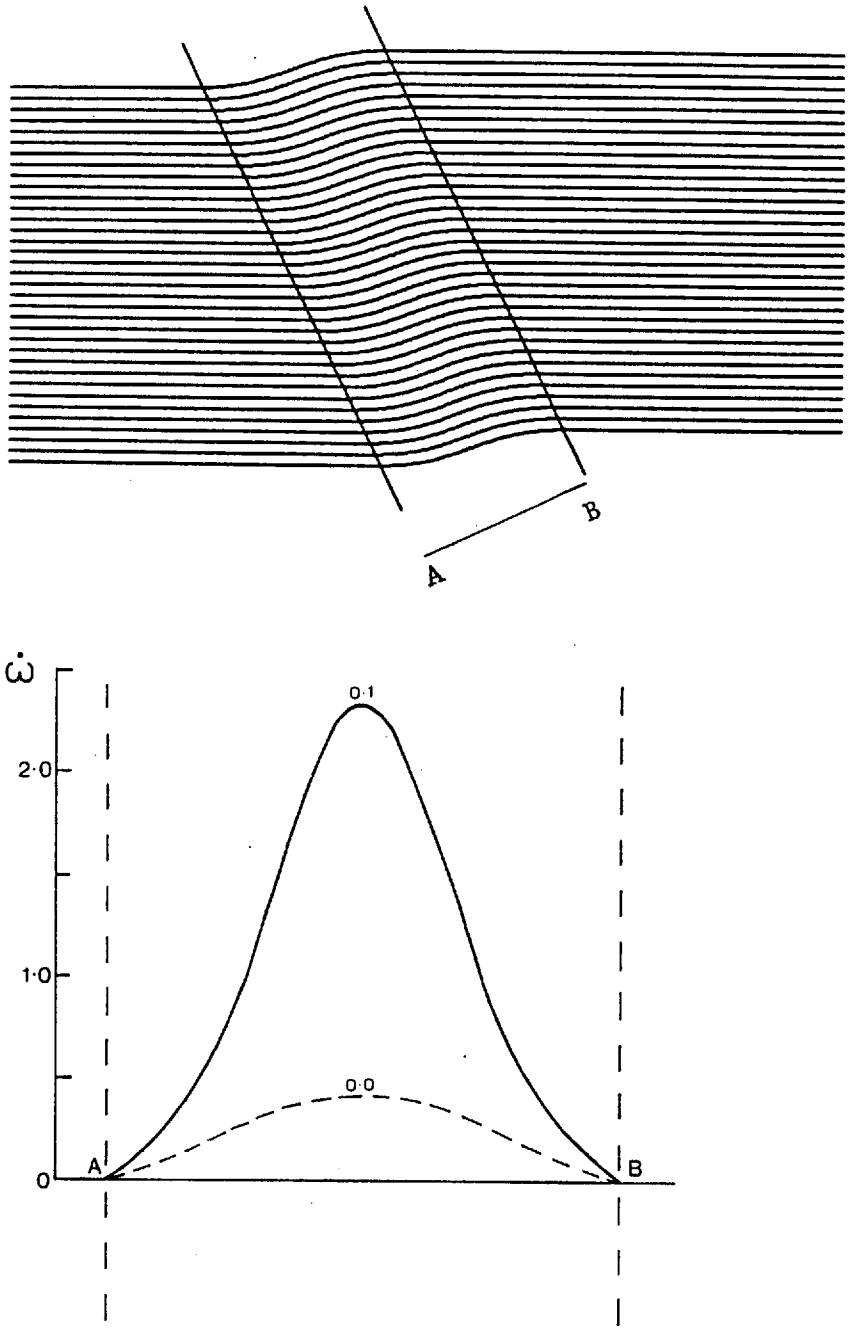


Figure 2.14 B

Initial rotation domain orientation, θ_o = 30

Finite rotation domain orientation, θ_f = 25.5°

Deformation increment 100

Finite strain in the external foliation = 0.1

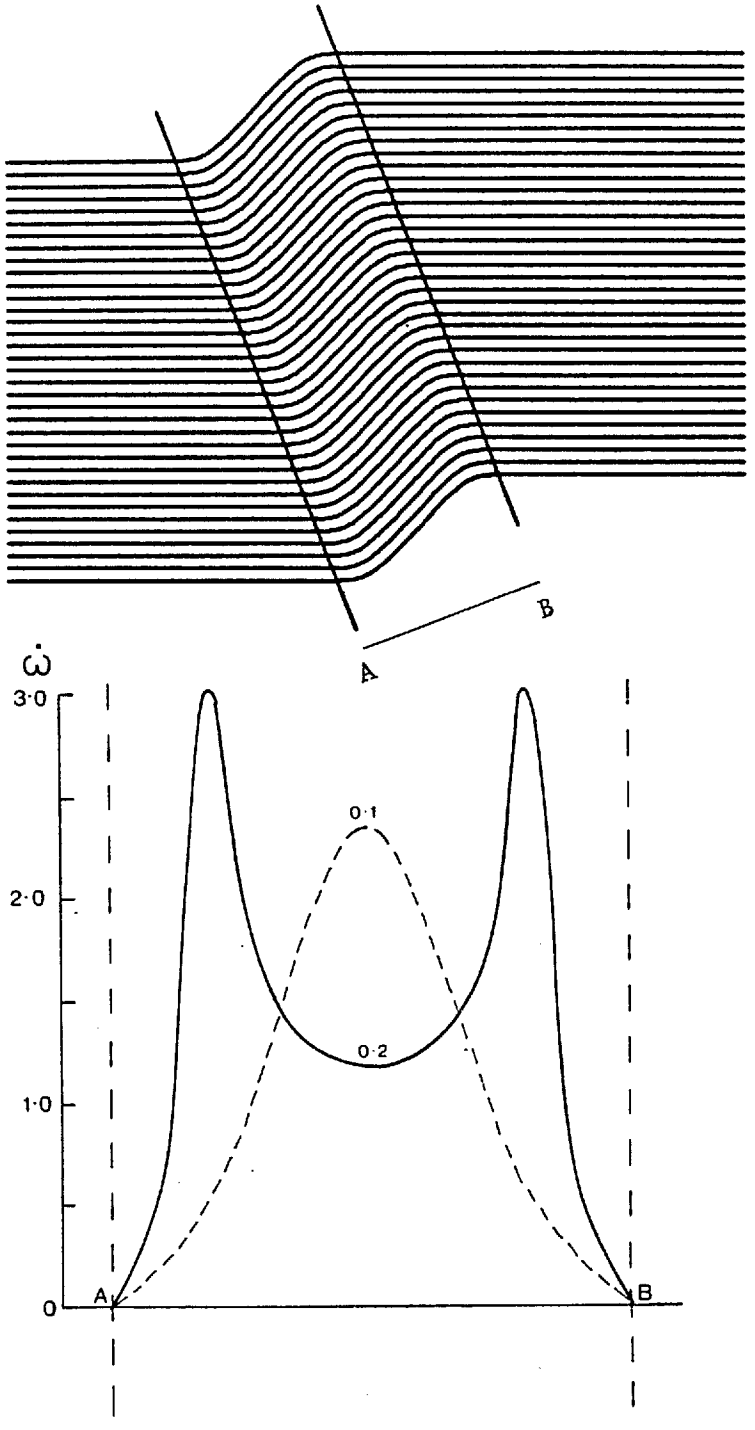


Figure 2.14 C

Initial rotation domain orientation, $\Theta_o = 30^o$
Finite rotation domain orientation, $\Theta_f = 21.3^o$

Deformation increment 200
Finite strain in the external foliation = 0.2

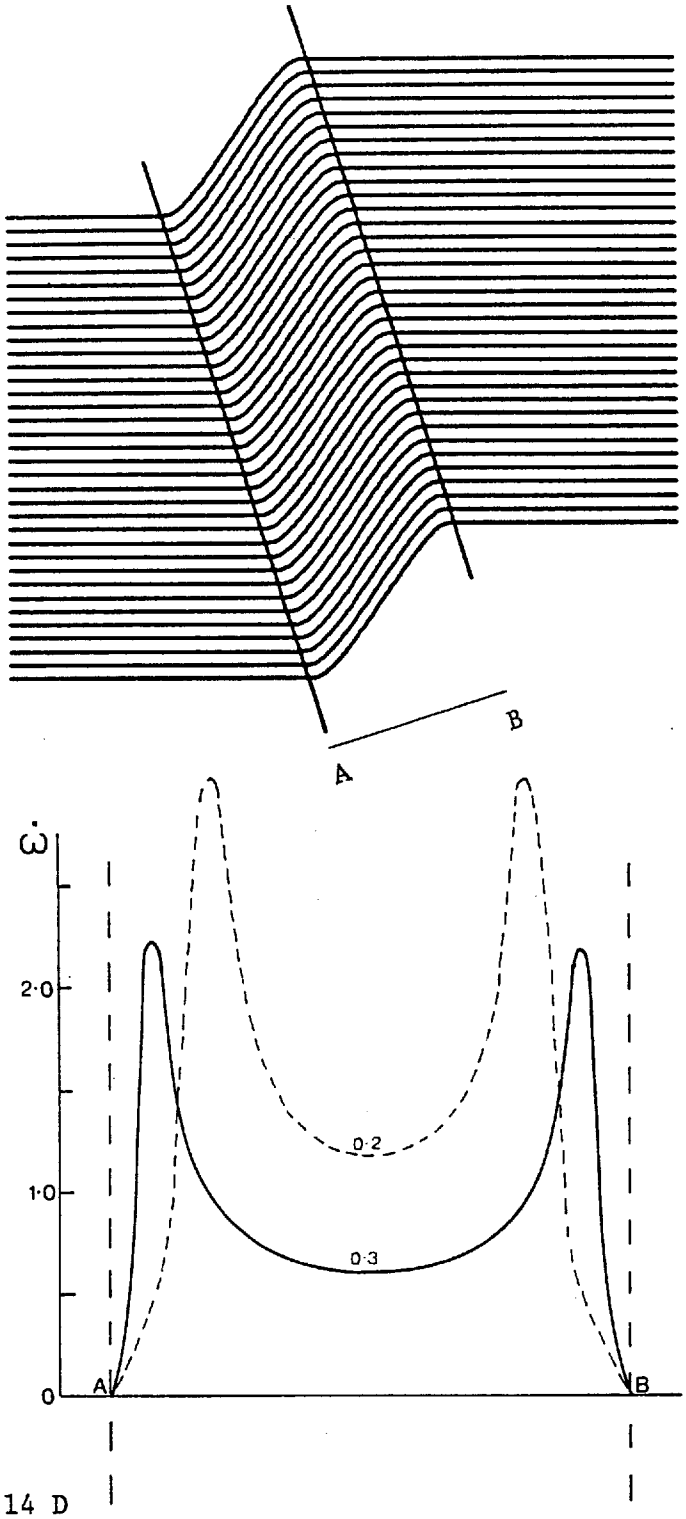
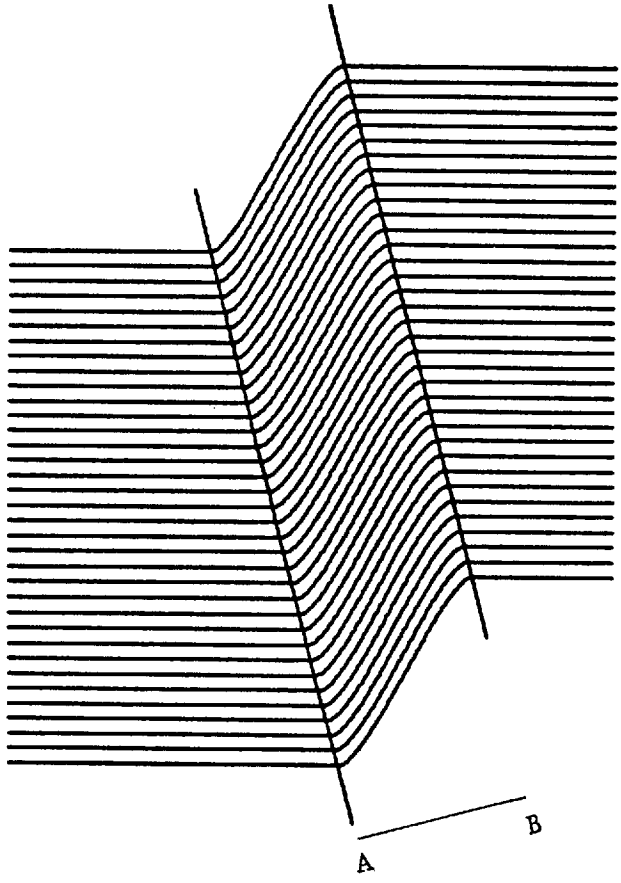


Figure 2.14 D

Initial rotation domain orientation, $\theta_o = 30^o$
Finite rotation domain orientation, $\theta_f = 17.7$

Deformation increment 300
Finite strain in the external foliation = 0.3



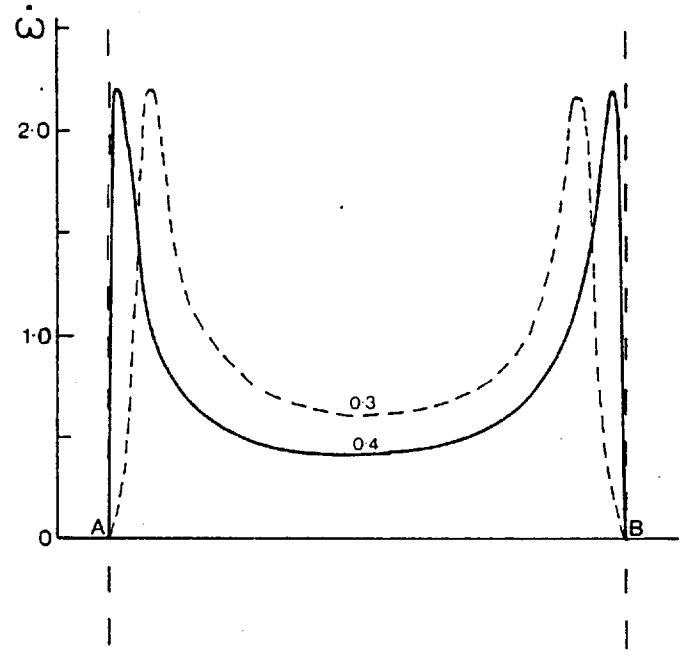


Figure 2.14 E

Initial rotation domain orientation, $\Theta_o = 30^o$
Finite rotation domain orientation, $\Theta_f = 14.7^o$

Deformation increment 400
Finite strain in the external foliation = 0.4

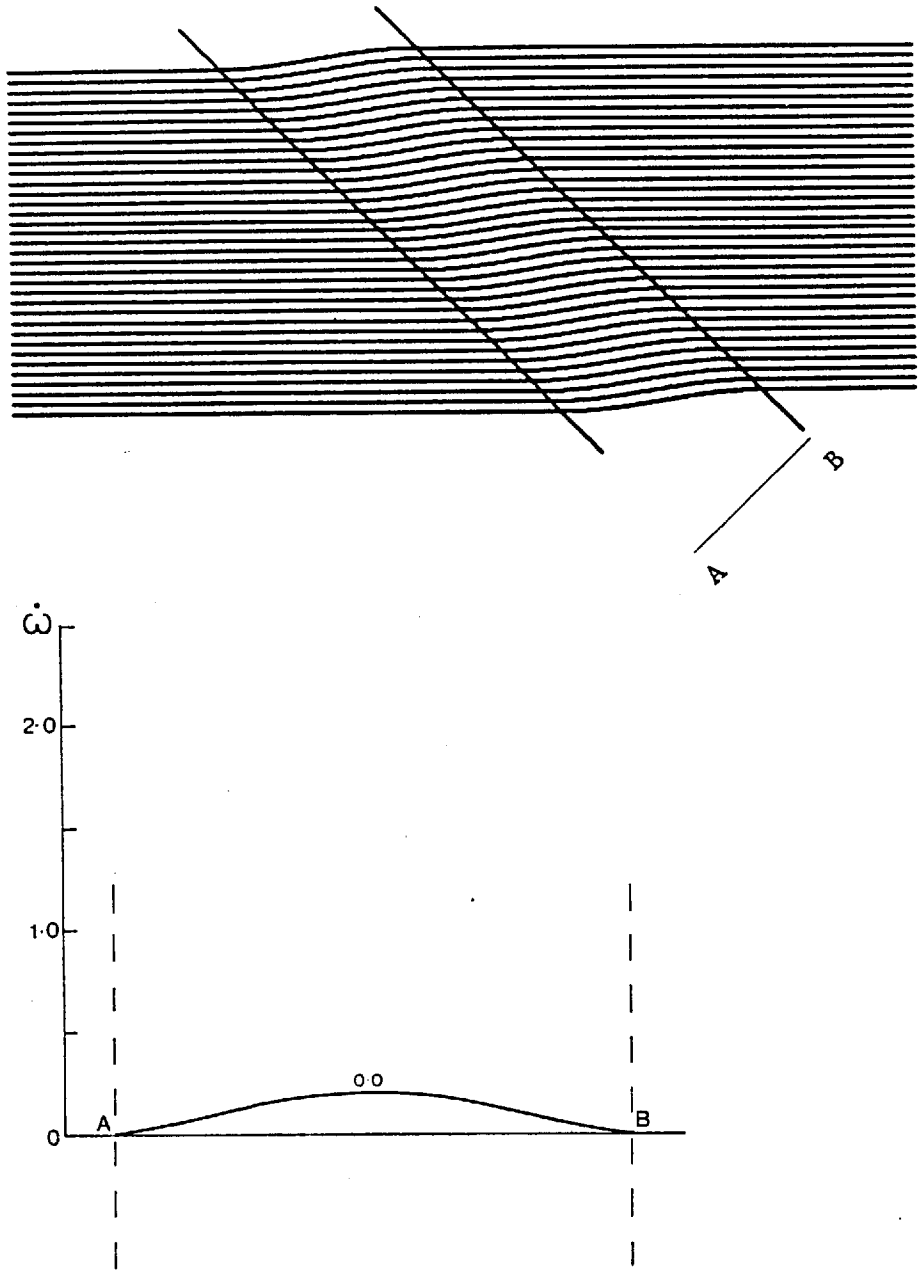


Figure 2.15 A

Initial rotation domain orientation, $\Theta_o = 45^o$

Finite rotation domain orientation, $\Theta_f = 45^o$

Deformation increment 0

Finite strain in the external foliation = 0 .0

Anisotropy ratio, N/Q = 5.0

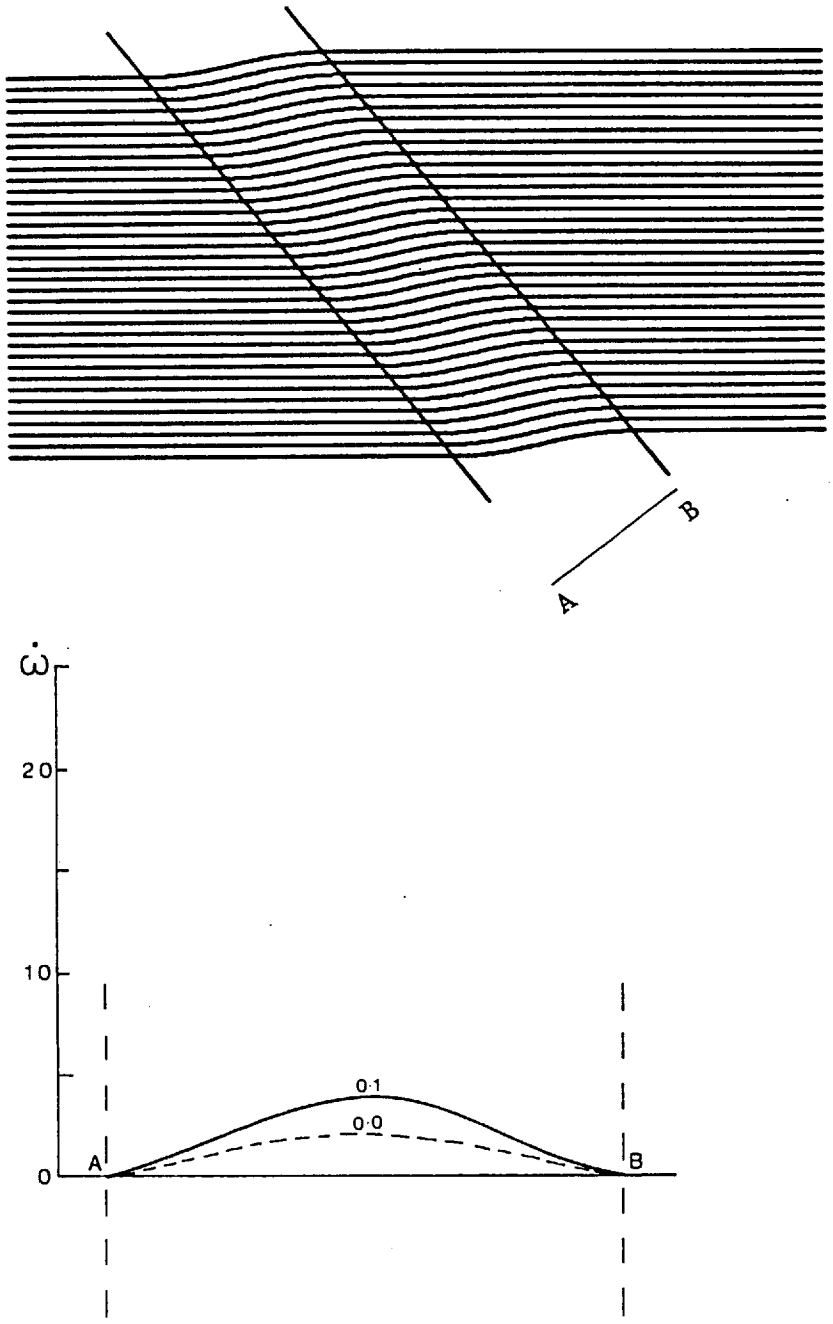
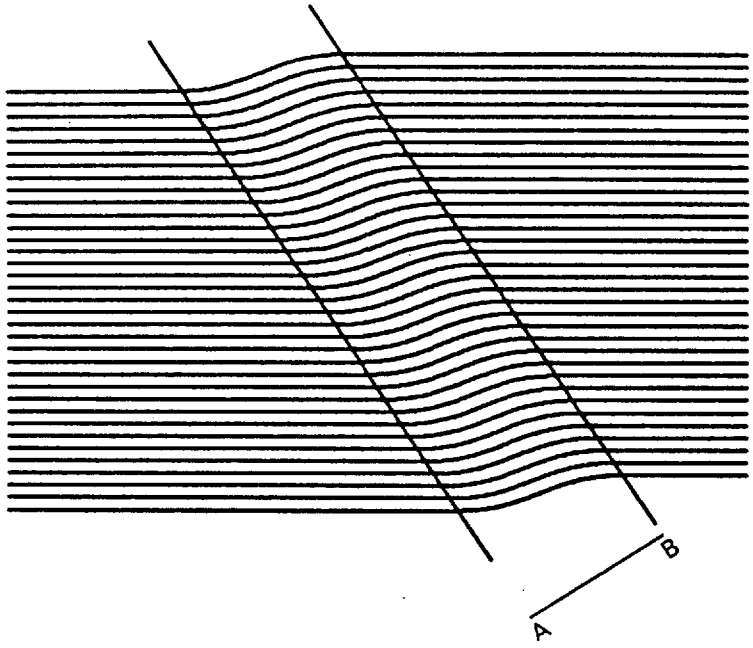


Figure 2.15 B

Initial rotation domain orientation, $\Theta_o = 45^o$
Finite rotation domain ntation, $\Theta_f = 39.6^o$

Deformation increment 100
Finite strain in the external foliation = 0.1



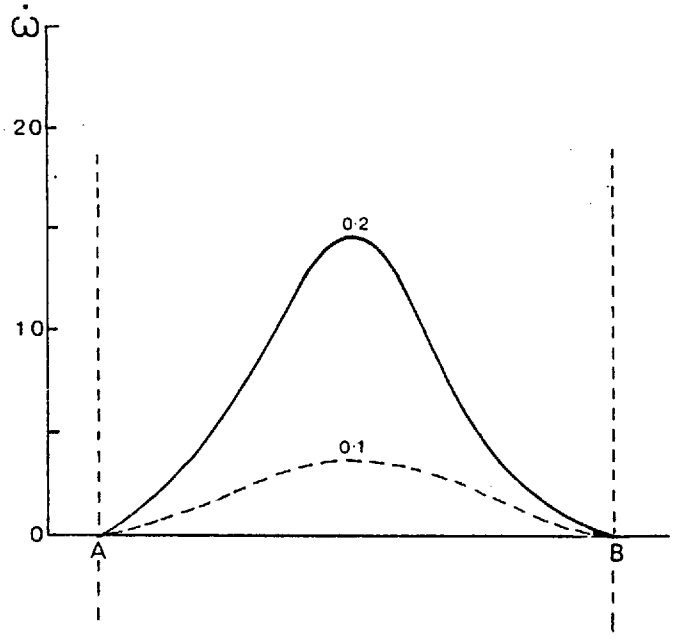


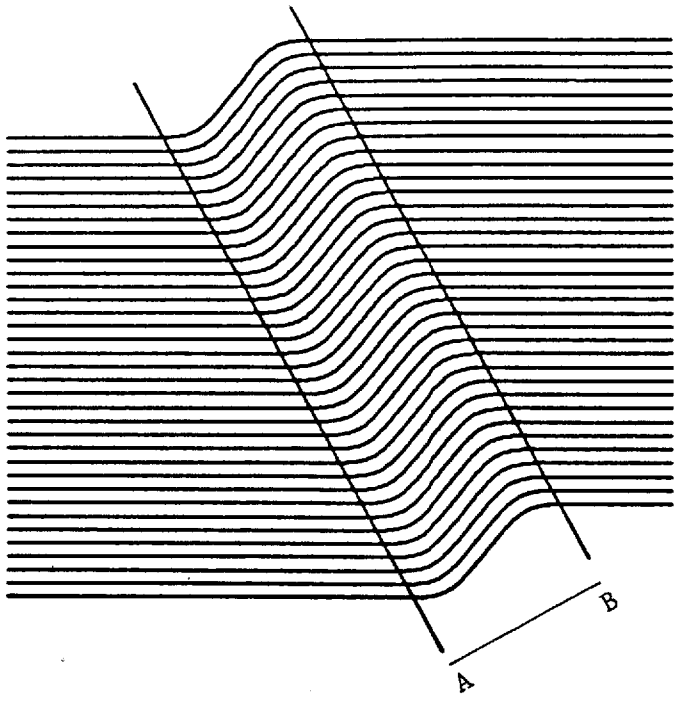
Figure 2.15 C

Initial rotation domain orientation, $\Theta_o = 45^o$

Finite rotation domain orientation, $\Theta_f = 34.1$

Deformation increment 200

Finite strain in the externalfoliation = 0.2



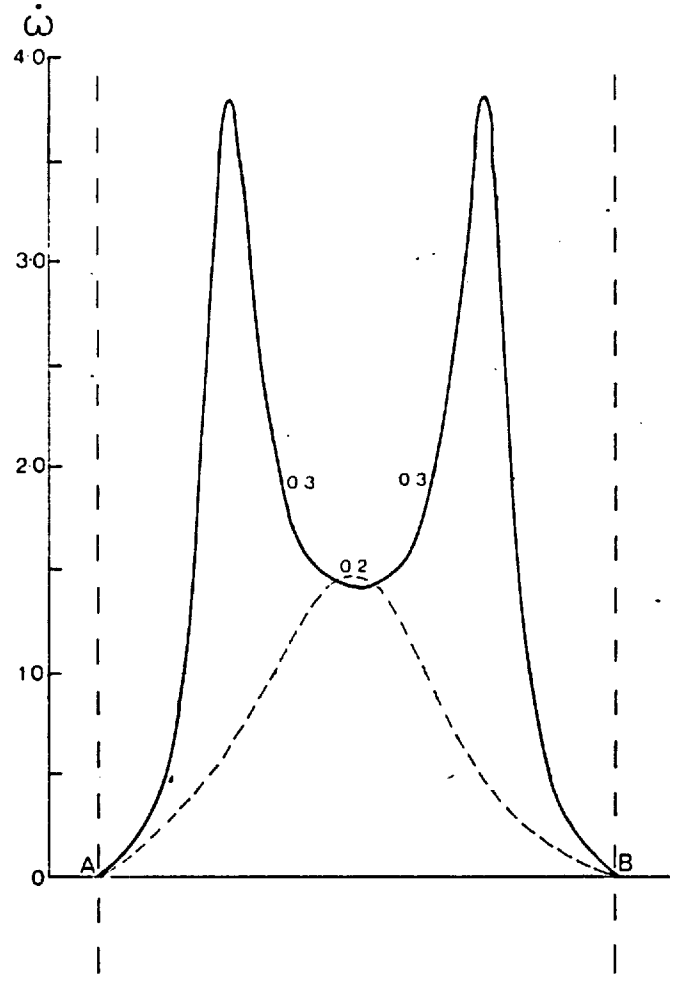
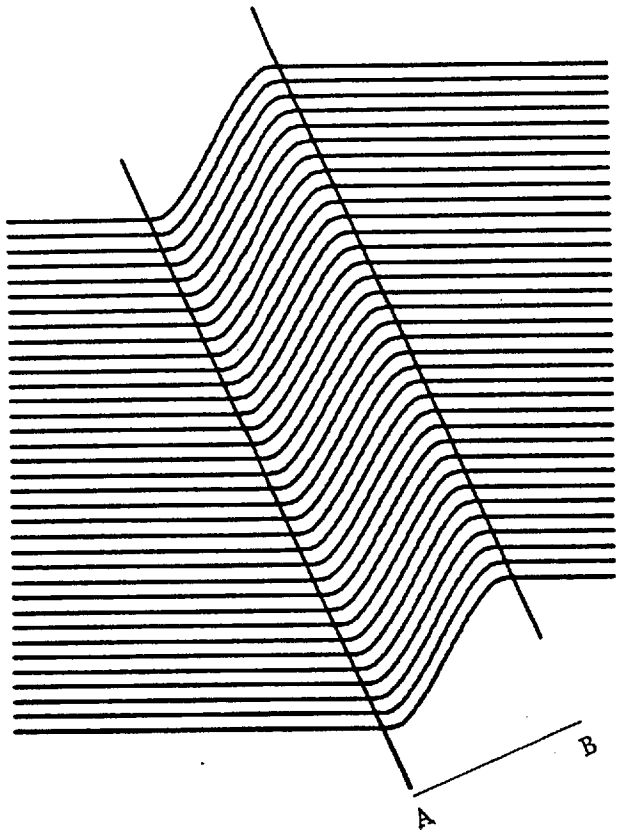


Figure 2.15

Initial rotation domain orientation, $\theta_o = 45^o$ Deformation increment 300

Finite rotation domain orientation, $\theta_f =$ ^{o}

Finite strain in the external foliation = 0.3



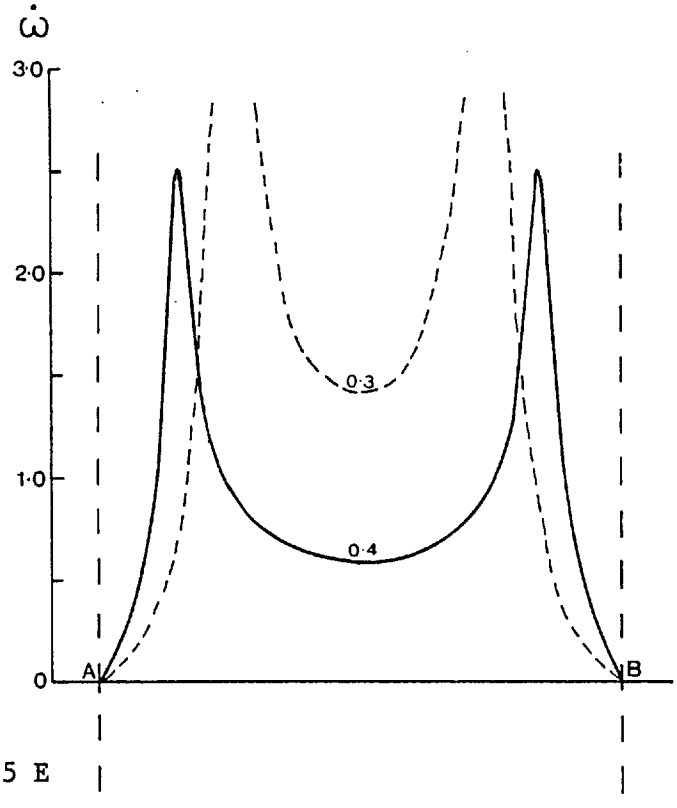


Figure 2.15 E

Initial rotation domain orientation, $\theta_o = 45^o$

Finite rotation domain orientation, $\theta_f = 24.4^o$

Deformation increment 400

Finite strain in the external foliation = 0.4

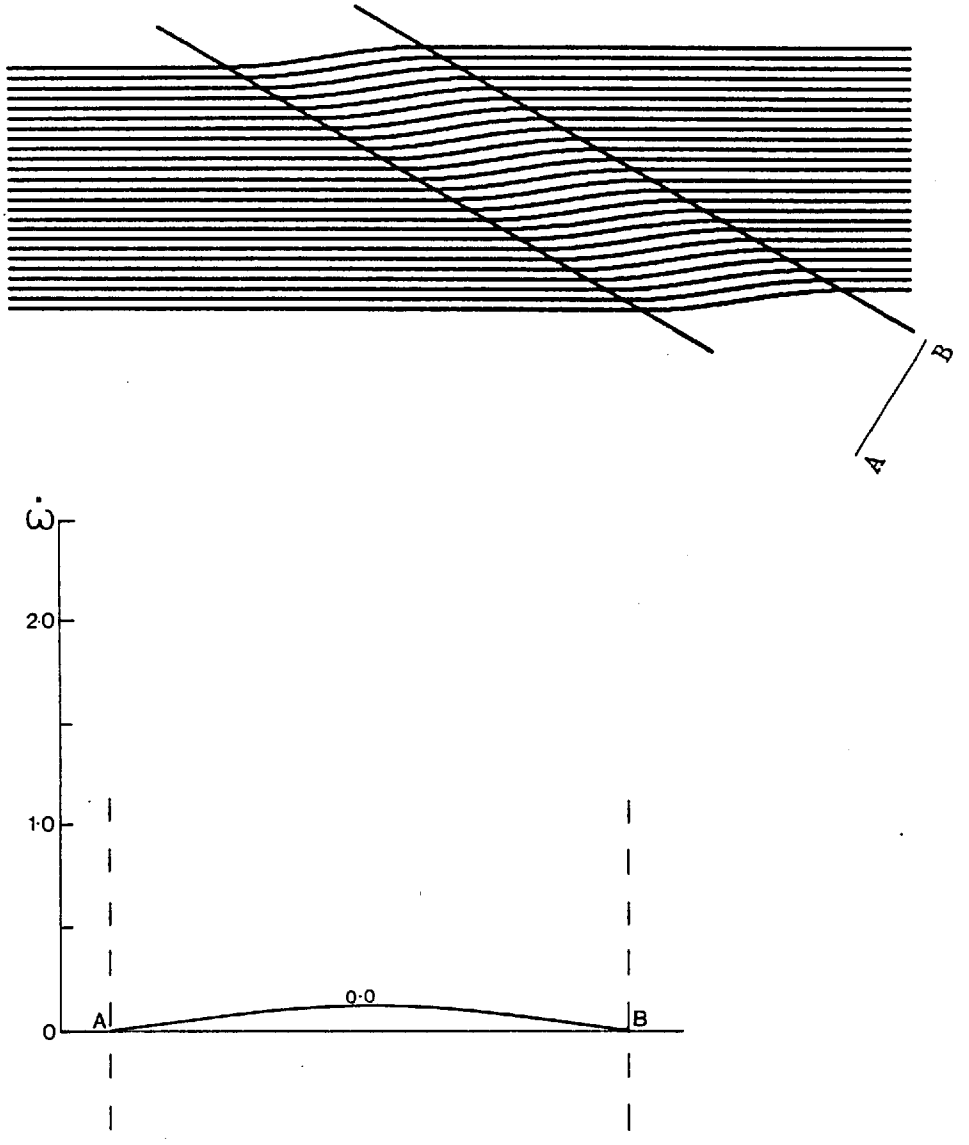


Figure 2.16 A

Initial rotation domain orientation, $\Theta_o = 60^o$
Finite rotation domain orientation, $\Theta_f = 60^o$

Deformation increment 0
Finite strain in the external foliation = 0.0

Anisotropy ratio, N/Q = 5.0

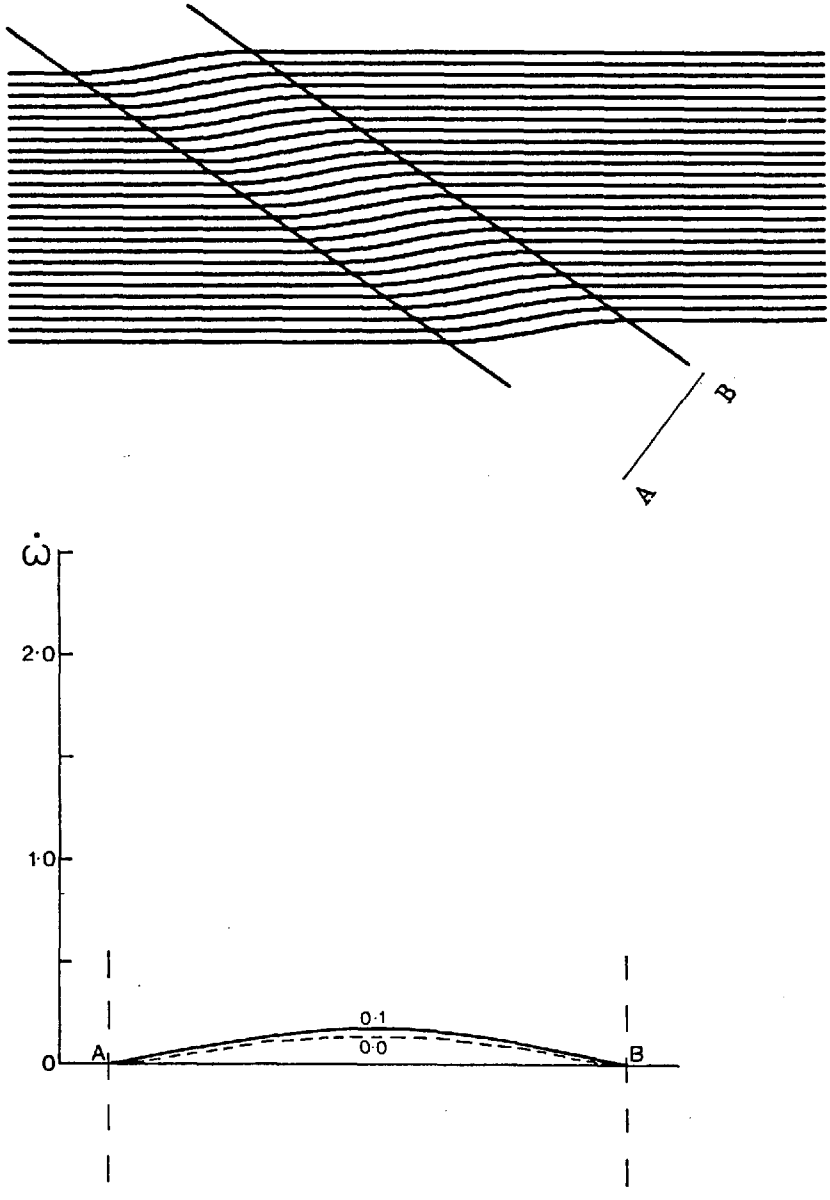


Figure 2.16 B

Initial rotation domain orientation, $\Theta_o = 60^o$
Finite rotation domain orientation, $\Theta_f = 55.1^o$

Deformation increment 100
Finite strain in the external foliation = 0.1

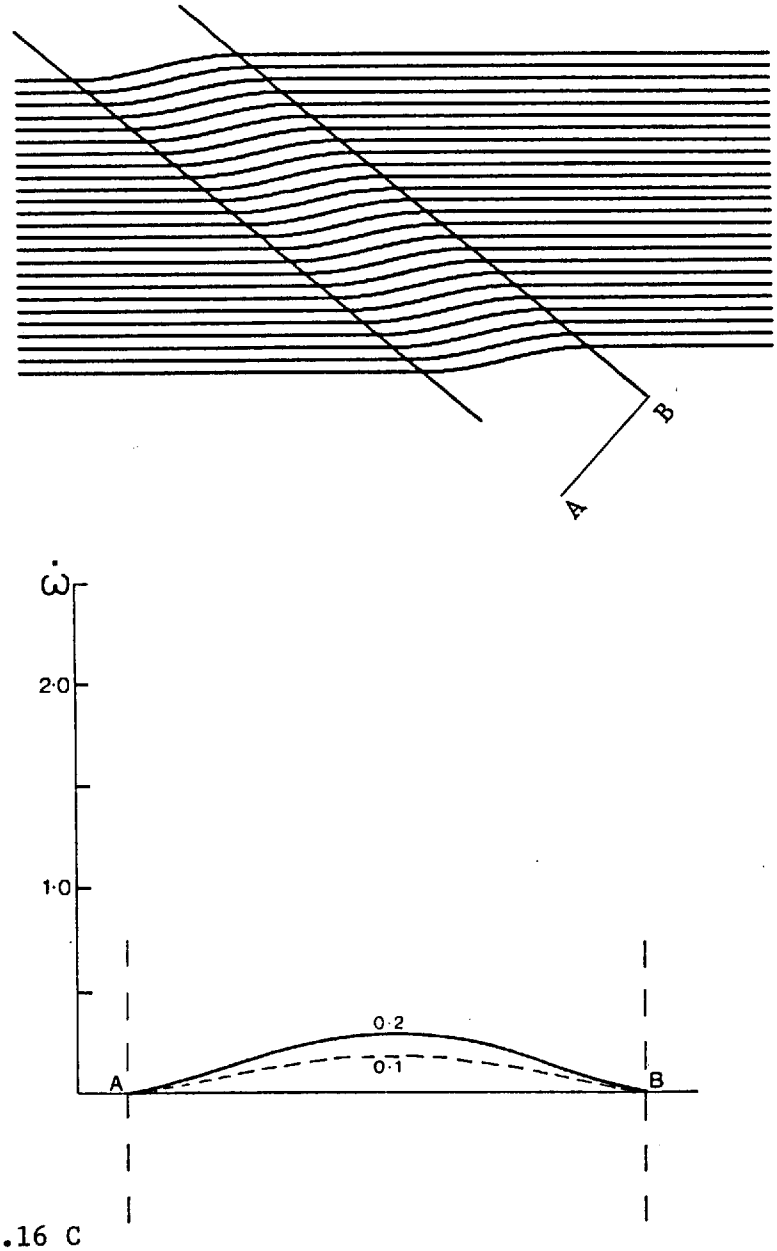


Figure 2.16 C

Initial rotation domain orientation, $\Theta_o = 60^o$
Finite rotation domain orientation, $\Theta_f = 49.5^o$

Deformation increment 200
Finite strain in the external foliation = 0.2

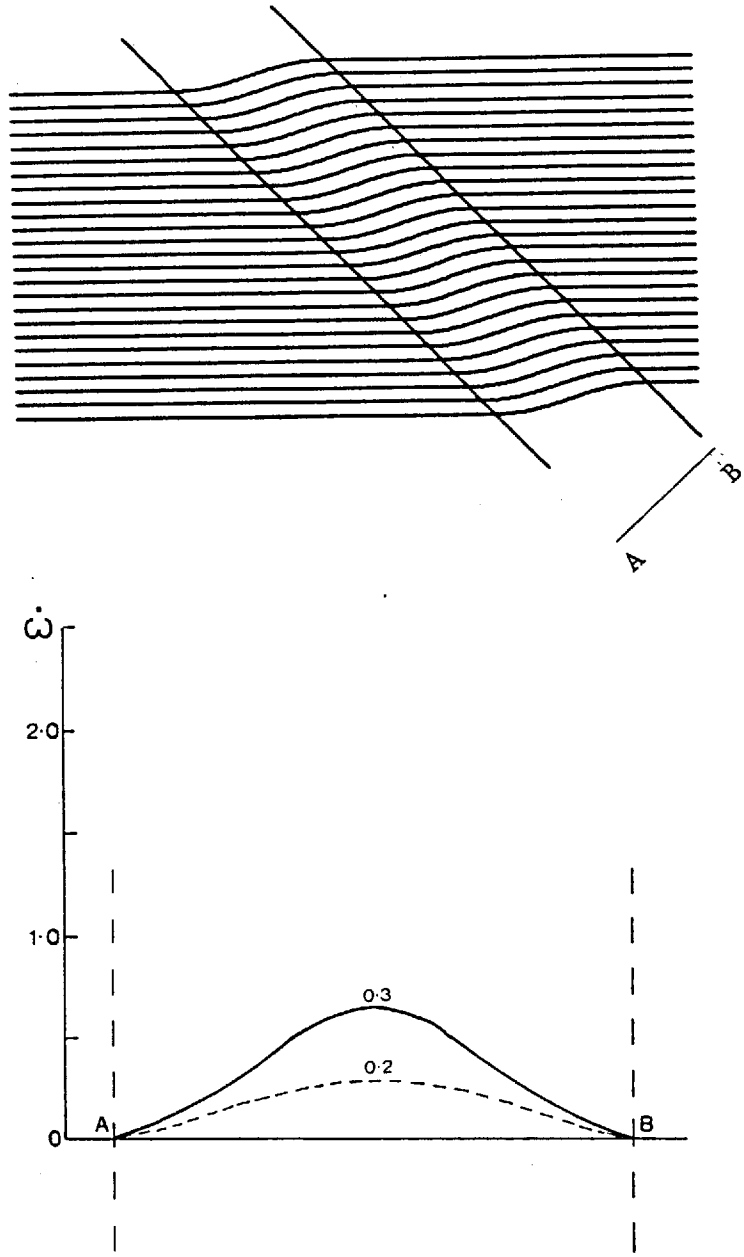


Figure 2.16 D

Initial rotation domain orientation, $\theta_o = 60^o$
Finite rotation domain orientation, $\theta_f = 43.8^o$

Deformation increment 300
Finite strain in the external foliation = 0.3

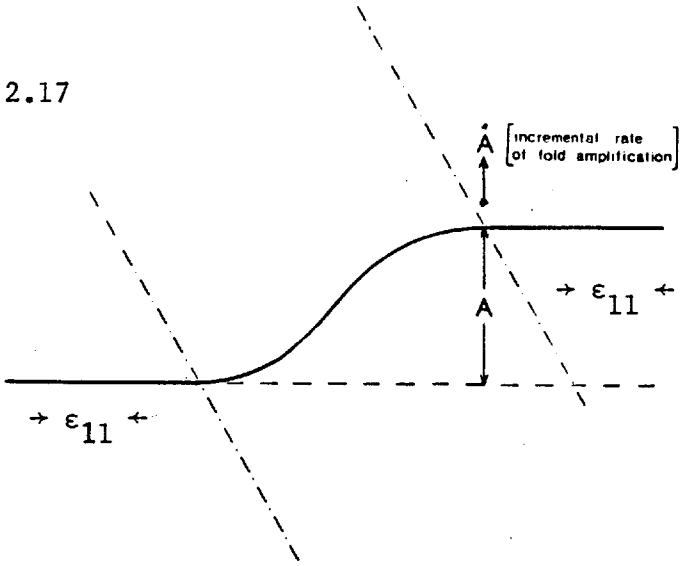
The main features of these computer models will be discussed with reference to the run shown in fig. 2.14. In this example, the initial orientation of the domain boundaries was set at $\theta_o = 30^o$.

During the initial stages of deformation (fig. 2.14 A, fig. 2.14 B) the maximum rate of incremental foliation rotation occurs within the central elements of the rotation domain.. The rate of foliation rotation increases as the foliation approaches the band normal foliation orientation and the central elements of the rotation domain are the first to be affected by the phase of rotational instability which characterise the band normal foliation attitude. The foliation within these elements then rotates relatively rapidly through the band normal position and then the attitude of these foliation planes begins to stabilise or "lock" (figs. 2.14 B, 2.14 C). This stabilisation results from the onset of rotational "hardening", as discussed earlier in section 2.3.2.

The development of initial rotational instability and subsequent rotational "hardening" gradually propagates from the central to the outer elements of the rotation domain. In effect, the finite foliation rotation within the outer elements "catches up" with that of the inner elements. This can be seen to result in a "straightening out" of the foliation within the rotation domain and the production of an increasingly angular fold geometry. Almost the whole of the rotation domain is stabilised at the stage in deformation represented in fig. 2.14 D.

It is possible to illustrate the role of foliation anisotropy ($N/Q = 5$) in producing active amplification of the structure shown in fig. 2.14 by a graphical method. This method involves producing a graph of finite amplitude of the structure as a function of finite strain and using the slope of this amplitude/strain curve to determine the amplification rate of the anisotropic structure, $\dot{A}_{aniso}$, at successive stages in deformation. Amplification is measured in a direction normal to the trace of the external foliation (fig. 2.17). It is then possible to take the geometry of the structure at any given stage of deformation, computed in the finite deformation analysis, and calculate what the incremental amplification rate would be if the material containing the structures were, *at that stage in deformation*, incrementally isotropic, rather than anisotropic. This rate is given by $\dot{A}_{iso}$. The influence of foliation anisotropy on the amplification

Figure 2.17



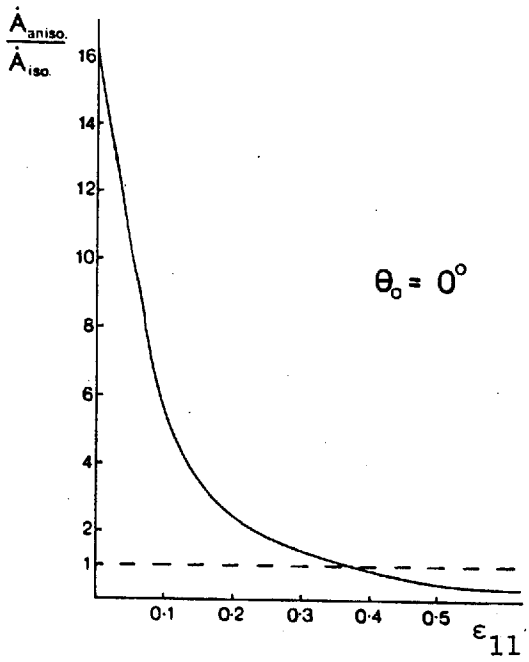


Figure 2.19 A Graphical representation of change in the rate of amplification of the structure shown in figs. 2.12(A-E) with finite deformation. Rate of amplification is expressed as the dimensionless ratio $\dot{A}_{aniso}/\dot{A}_{iso}$ (see text). ε_{11} corresponds to the finite shortening (natural strain) in the external foliation, along the trace of the external foliation. ($\theta_o = 0^o$; N/Q = 5.0)

Figure 2.18

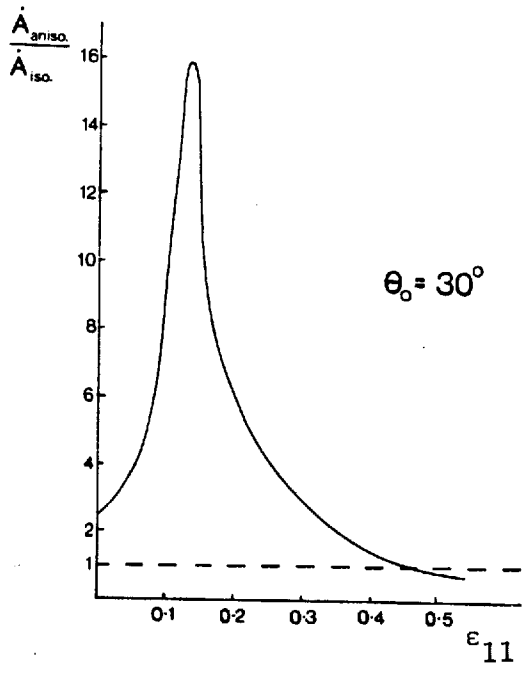
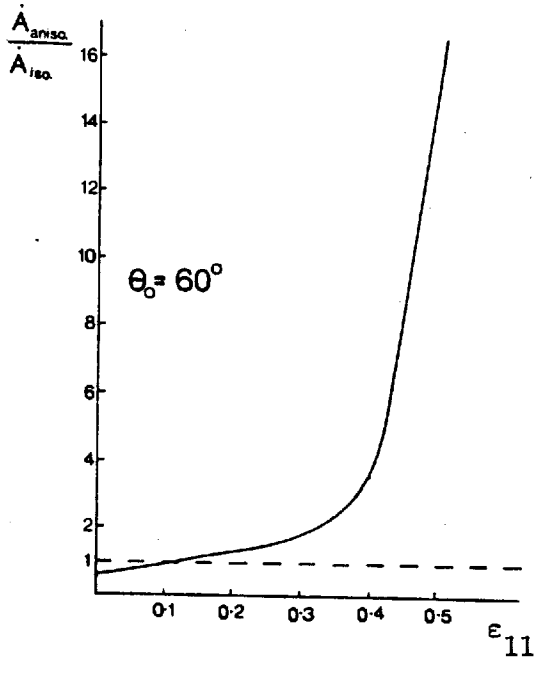


Figure 2.19 B



rate of the structure can then be expressed by the ratio of the anisotropic to isotropic incremental amplification rates (i.e. $\dot{A}_{aniso}/\dot{A}_{iso}$) at successive stages in deformation.

The results of such calculations for the model illustrated in fig. 2.14 are shown in fig. 2.18 where the ratio $\dot{A}_{aniso}/\dot{A}_{iso}$ is plotted as a function of finite strain in the external foliation parallel to the plane of the external foliation (ε_{11}). This graph clearly illustrate the initial increase and subsequent decrease in the rate of amplification associated with the onset and subsequent decay of rotational instability within the rotation domain. The purpose of this graph, however, is to demonstrate that, during the later stages of deformation, the incremental rate of amplification of the anisotropic structure is actually less than the rate which would be achieved at corresponding stages of deformation if the foliation was mechanically passive (i.e. $\dot{A}_{aniso}/\dot{A}_{iso} < 1$). This graph serves to illustrate the high degree of structural stability which is achieved after a large finite rotation of the internal foliation.

The general comments made with respect to the finite deformation illustrated in fig. 2.14 also apply to each of the computer runs shown in figs. 2.12 to 2.16. The development of rotational instability, subsequent stabilisation of the internal foliation attitude and the resulting development of an angular fold geometry can be seen in each of these finite deformation models. The initial orientation chosen for the rotation domain does, however, have a considerable effect on the degree of stability of the initial structure during the early stages of deformation. This is reflected in the amount of finite deformation which is required to rotate the internal foliation planes into a portion of maximum rotational instability.

This point can be clarified by first considering the stages of deformation shown for the upright rotation domain ($\theta = 0^{o}$) shown in fig. 2.12. In this model the boundaries of the rotation domain undergo no finite rotation (the direction of maximum extension in the external foliation is parallel to the trace of the boundaries throughout deformation). The finite deformation of this structure is characterised by the development of rotational instability and the subsequent development of structural angularity at a relatively early stage (fig. 2.12, A, B, C). (The maximum rate of foliation rotation occurs at a foliation rotation, ω, of approximately 15°).

The relatively high initial instability of the upright domain is illustrated graphically in fig. 2.19A. In this figure, the ratio of the anisotropic to the isotropic incremental amplification rate is plotted as a function of finite strain using the method described with reference to fig. 2.17. It can be seen from this graph that the mechanical anisotropy of the model illustrated in fig. 2.12 is most effective in producing an enhanced rate of amplification during the very first increments of deformation.

The initial rate of amplification of a foliation perturbation depends on the initial orientation chosen for the rotation domain boundaries. The greater the initial inclination of these boundaries to the external foliation and the applied external compression, the higher the degree of initial rotational stability of the internal foliation. This can be seen by comparing each of initial foliation rotation rate profiles shown in figs. 2.12 A to 2.16 A. The ratio of internal foliation rotation induced during the first increment of deformation of the most oblique structure ($\theta_o = 60^o$, fig. 2.16A) are actually less than would occur if the foliation were mechanically passive. Consequently, the initial rate of amplification of this structure is, itself, less than the amplification rate which would be achieved if the foliation were mechanically passive (fig. 2.19 B).

A second consequence of the high initial rotational stability of this structure is the fact that the boundaries of the rotation domain undergo a large finite rotation, associated with significant finite strain in the external foliation, before the internal foliation approaches the domain normal foliation attitude and enters the phase of maximum rotational instability. By the time this phase is reached in the model shown in fig. 2.16, the finite shortening, ε_{11}) in the external foliation is approximately 0.4 (fig. 2.16 E) and the orientation of the domain boundaries has changed from an initial value of $\theta_o = 60^o$ to a finite inclination of $\theta_f \simeq 40^o$.
The same effect isseen in each of the models in which the initial orientation of the rotation domain boundaries is oblique to the external foliation. The amount of domain boundary rotation which occurs before the phase of marked internal rotational instability is reached decreases with increase in the initial value chosen for θ_o.

The development of significant finite rotation of the domain boundaries, and associated strain in the external foliation, is not

restricted to materials with a low degree of anisotropy. The same effect has been demonstrated in the discussion of the finite foliation rotation curves corresponding to a material anisotropy ratio of N/Q = 100 (see section 2.3.2). This phenomenon may seem puzzling in the light of field evidence obtained from natural kink structures developed in highly anisotropic materials. Such structures tend to be characterised by little or no deformation within the external foliation surrounding the kink. In addition, most workers consider that the orientation of the kink boundaries remains stable during the rotation of the internal foliation. However, in examining this apparent contradiction between the predictions of the rotation domain analysis and evidence from natural structures a number of important points should be considered:

(i) The rotation domain analysis is based on the assumption of constant volume deformation. It will be demonstrated in Chapter 3 that the high initial stability of low inclination rotation domains ($\theta > 45^{o}$) is closely related to this deformation condition. It will also be shown that, if continuity of foliation across the domain boundaries is maintained, then deformation can only be restricted to the internal foliation if significant changes in the volume of this zone occur during foliation rotation. This process could involve, for example, the initial opening and subsequent closure of interlaminal voids within the rotation domain.

(ii) In order to make the problem considered in the analysis tractable, it has been assumed that a structure develops from an initial foliation perturbation which is of effectively infinite extent and is defined by plane parallel boundaries, i.e. the basic geometric features of the finite structure are present in, and inherited from, the initial foliation perturbation. Natural structures will propagate from more complex perturbations and the phase of development involved in the establishment of a well defined, tabular rotation domain from such perturbations is not considered in the author's analysis. However, if kinks were to propagate from localised perturbations, for example, then it is unlikely that this propagation would establish rotation domains along directions unfavourable to the subsequent rotation of the internal foliation. It can therefore be suggested, from the predictions of the author's analysis, that kink propagation will occur along directions inclined at a high angle to the external

foliation and that low inclination rotation domains such as those modelled in figs. 2.15 ($\theta_o = 45^o$) and 2.16 ($\theta_o = 60^o$) are unlikely to be established during the initial development of natural structures.

This suggestion is confirmed by field evidence obtained from natural conjugate kink structures which indicates that the majority of such structures form with symmetrically inclined axial surfaces which make an obluse angle with the external foliation and the applied, foliation parallel compression (Anderson, 1968; Weiss, 1968).

2.3.4. Variation in stress across a foliation rotation domain

Among the analytical expressions listed in table 2.I are a series of equations which can be used to specify the variation in the state of stress across a defined rotation domain during an increment of deformation. It is emphasised that these equations are valid only if the maximum and minimum principal stress trajectories are oriented, respectively, parallel with and normal to the plane of the external foliation in the external foliation zone. It is also important to note that the analytic expressions listed in table 2.I are derived from conditions of strain compatibility which are based on the condition of constant volume deformation. The operation of geologically feasible mechanisms of macroscopic volume change may act to modify the analytical predictions concerning the variation in stress across a station domain.

The derived equations for stress variation are particularly useful because they express local stress conditions within a rotation domain as a function of the angular parameters ω and θ. These angles can be measured in natural or experimental structures of the type investigated in the rotation domain analysis.

2.3.5. Variation in mean stress as a function of internal foliation orientation

ω It has been shown that the difference between the local mean stress within an element of the internal foliation $\bar{\sigma}^i$, and the mean stress within the external foliation, $\bar{\sigma}^e$, is given by equation 2.34.

The physical significance of this equation can be illustrated by examining the predicted variation in mean stress difference with internal foliation attitude, ω, across structures with boundaries oriented at various inclinations, θ, to the external foliation normal. A series of graphs illustrating this variation are shown in fig.s 2.20 to 2.24. These graphs refer to rotation domain oriented at $\theta = 0^{o}$ (2.20), 15° (2.21), 30° (2.22), 45° (2.23) and 60° (2.24). The variation in mean stress difference $\bar{\sigma}^{i} - \bar{\sigma}^{e}$ with ω is shown for two representative values of anisotropy ratio (N/Q = 5, 100).

The predicted mean stress difference, $\bar{\sigma}^{i} - \bar{\sigma}^{e}$ is expressed in units of maximum shear stress in the external foliation. If the principal stresses in the external foliation (i.e. σ_1^e, σ_2^e and σ_3^e) are defined, in real stress units, then it is a simple matter to convert the predicted local mean stress difference into real stress units. If, for example, the maximum (σ_1^e), intermeadiate (σ_2^e) and minimum (σ_3^e) principal stresses in the external foliation are defined as equal to 1,100 bars, 1,000 bars and 900 bars, respectively, then the mean stress ($\bar{\sigma}^{e}$) and the maximum shear stress (τ_m^e) in the external foliation are given by:

$$\bar{\sigma}^{e} = 1000 \text{ bars}$$
$$\tau_m^e = 100 \text{ bars}$$

Each unit of mean stress difference indicated on the vertical axes of figs. 2.20 to 2.24 then correspond to 100 bars
A mean stress difference of $\bar{\sigma}^{i} - \sigma^{e} = + 4.0$ corresponds to:

$$\bar{\sigma}^{i} - \bar{\sigma}^{e} = + 400 \text{ bars}$$
$$\bar{\sigma}^{i} = + 400 + 1000 = 1400 \text{ bars}$$

If $\bar{\sigma}^{i} - \bar{\sigma}^{e} = - 4.0$ units :

$$= 400 \text{ bars}$$
$$= - 400 + 1000 = 600 \text{ bars}$$

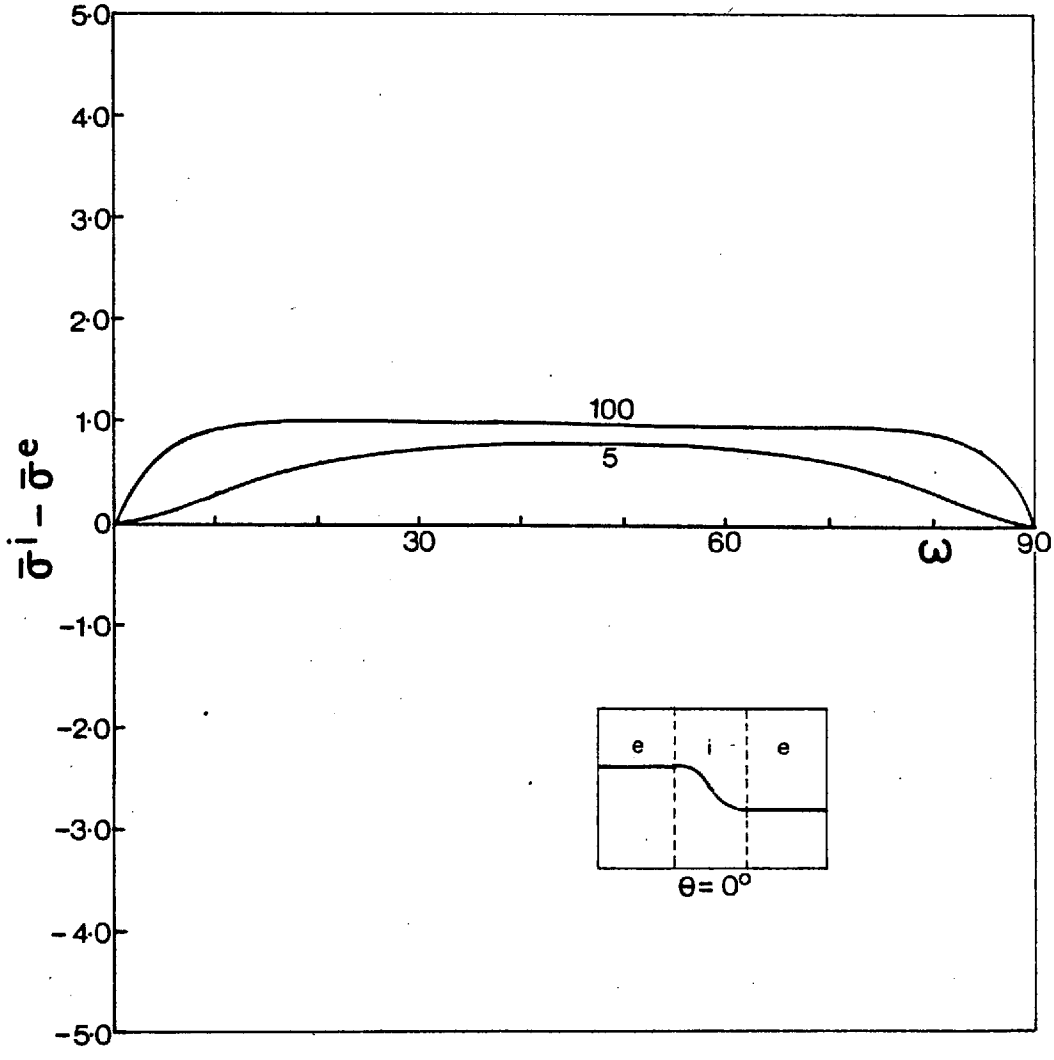


Figure 2.20 Relationship between the *local* mean stress difference $\bar{\sigma}^i - \bar{\sigma}^e$ and the *local* foliation inclination ω within a rotation domain oriented at $\theta = 0^o$. The variation in $\bar{\sigma}^i - \bar{\sigma}^e$ is shown for N/Q = 100.0 and 5.0. ($\bar{\sigma}^i - \bar{\sigma}^e = 0$ for N/Q = 1.0, for all ω, θ.) $\bar{\sigma}^i - \bar{\sigma}^e$ is shown in units which correspond to *units of mean stress in the external foliation (see text)*.

Note that the variation in mean stress with foliation attitude represented in fig. 2.20 is equivalent to the variation in mean stress with limb dip in a symmetric similar fold during an increment of deformation (see Casey,1976; Cobbold,1976)

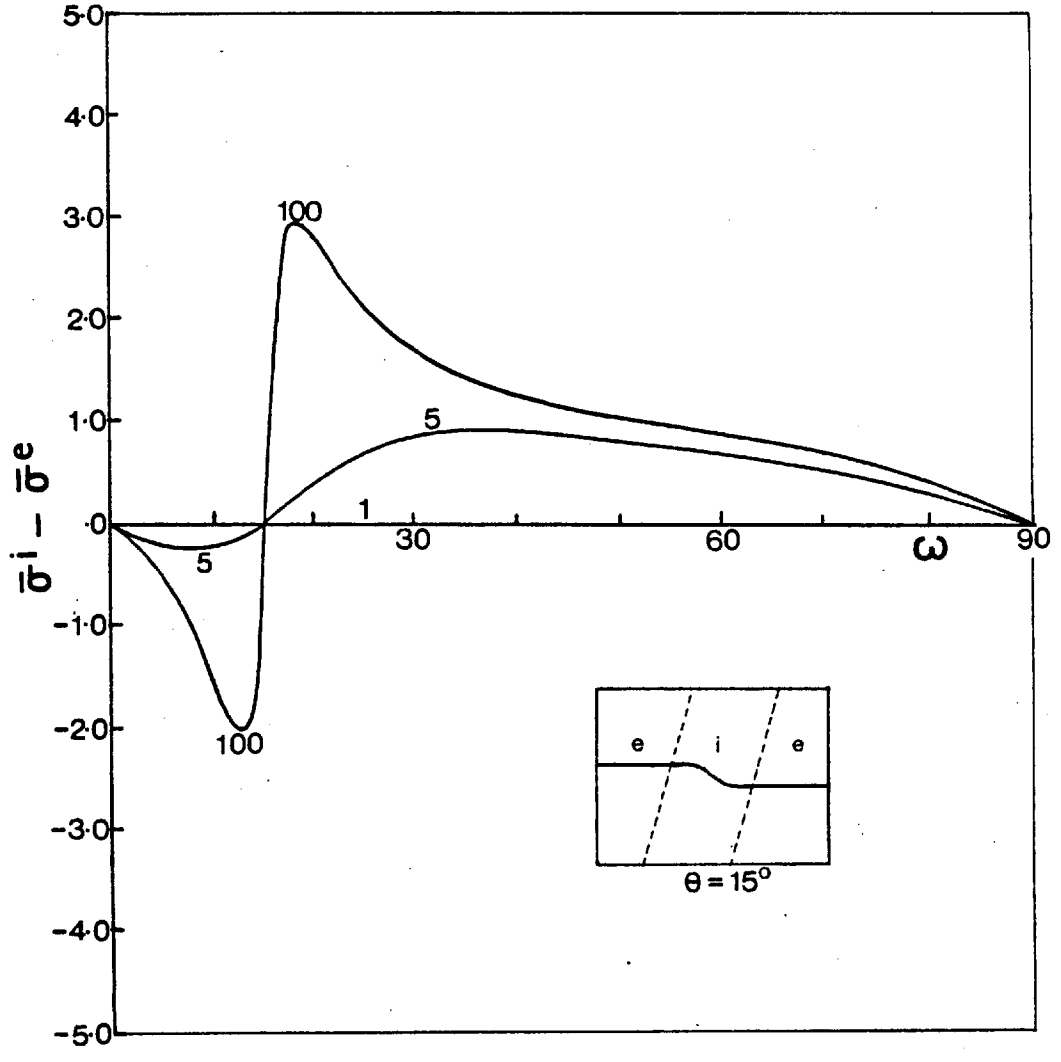


Figure 2.21 Relationship between *local* mean stress difference $\bar{\sigma}^i - \bar{\sigma}^e$ and the *local* foliation inclination ω within a rotation domain oriented at $\theta = 15^\circ$.

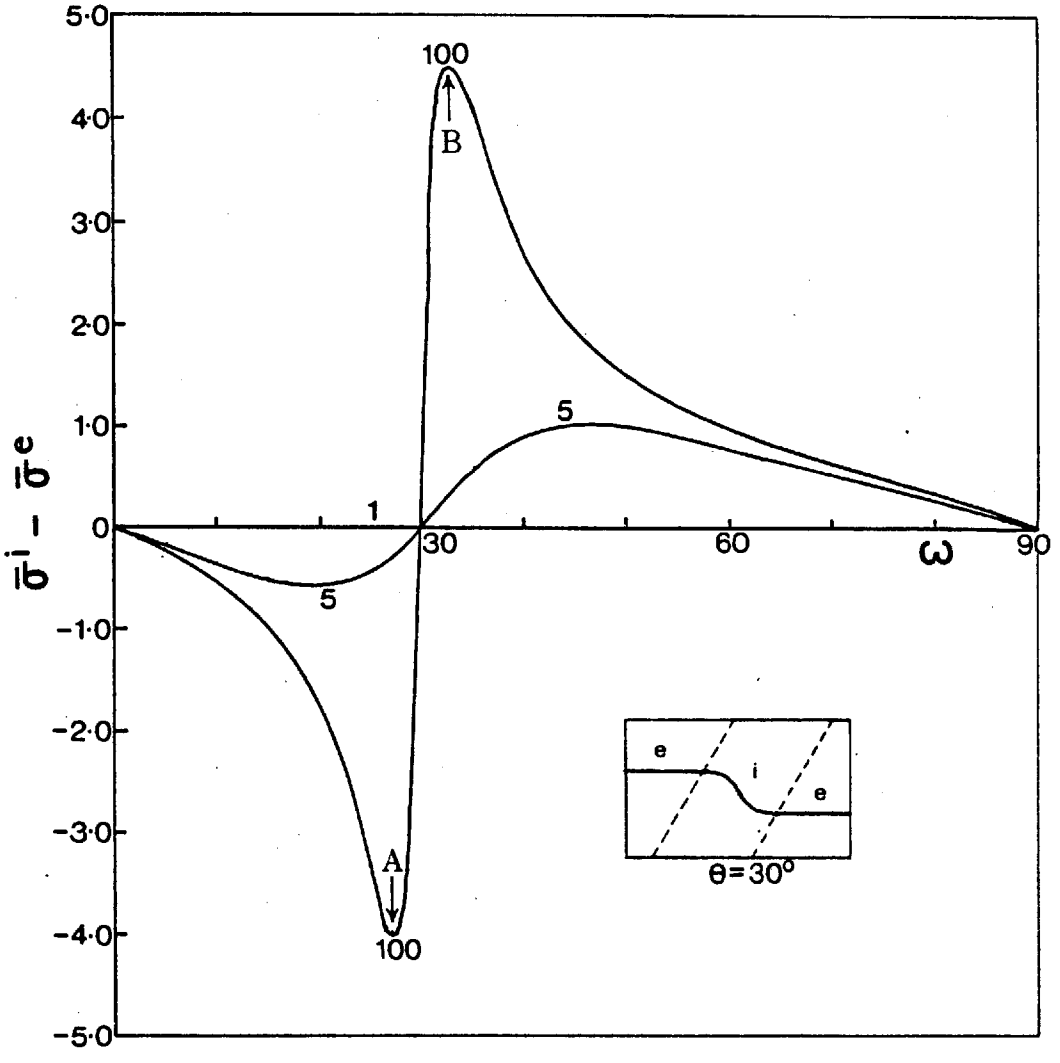


Figure 2.22 Relationship between the *local* mean stress difference $\bar{\sigma}^{i} - \bar{\sigma}^{e}$ and the *local* foliation inclination ω within a rotation domain oriented at $\theta = 30^{\circ}$.

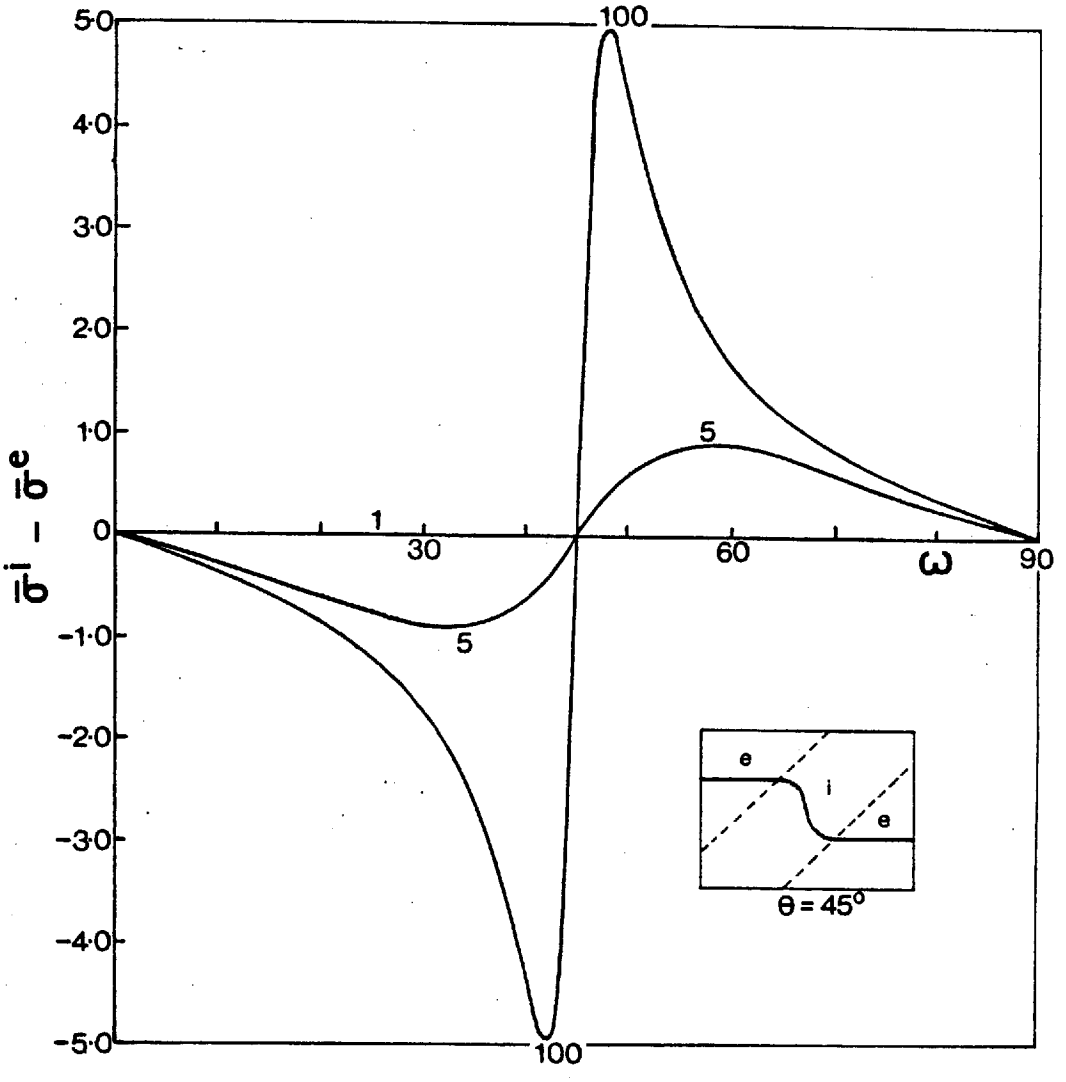


Figure 2.23 Relationship between the *local* mean stress difference $\bar{\sigma}^i - \bar{\sigma}^e$ and the *local* foliation inclination ω within a rotation domain oriented at $\theta = 45^o$.

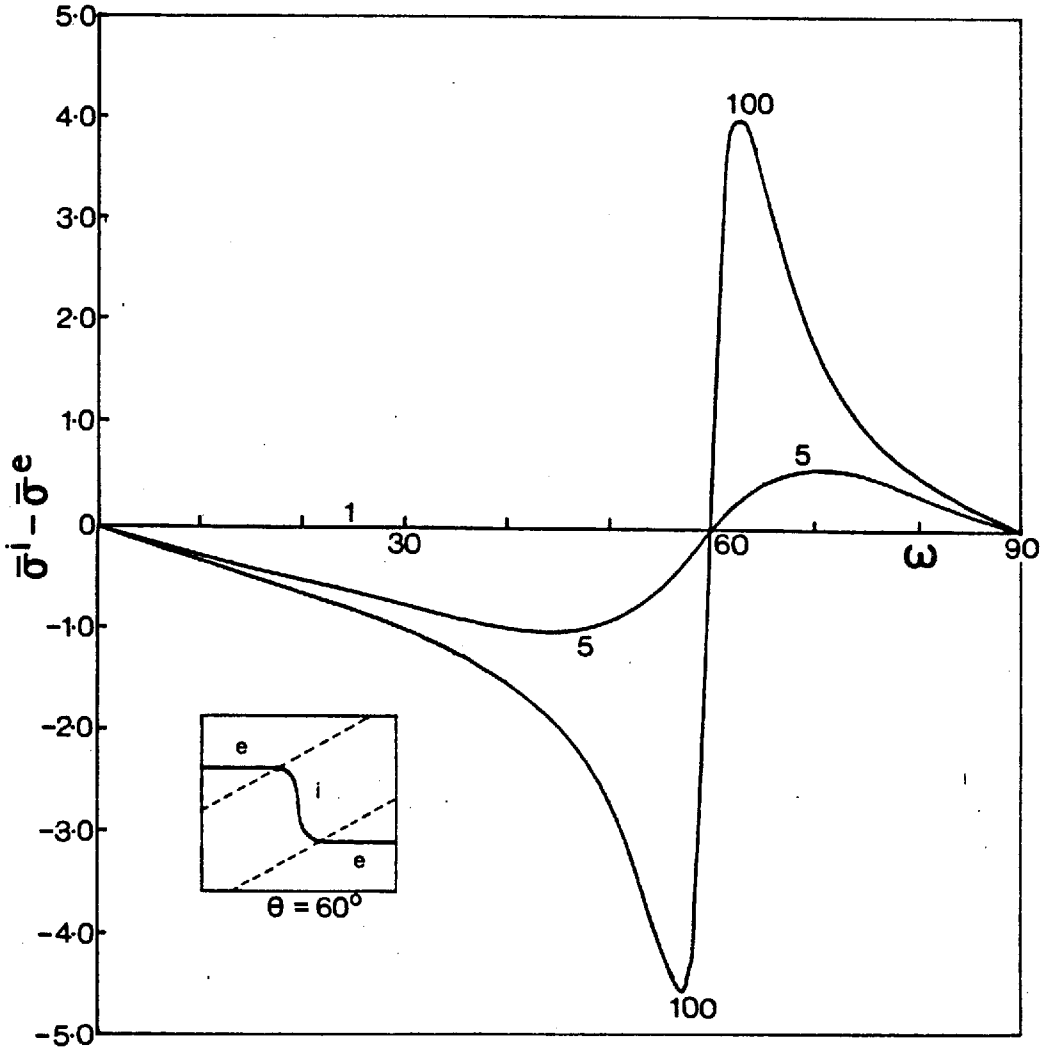


Figure 2.24 Relationship between the *local* mean stress difference $\bar{\sigma}^i - \bar{\sigma}^e$ and the *local* foliation inclination ω within a rotation domain oriented at $\theta = 60^\circ$.

The most significant features of the predicted mean stress profiles shown in figs. 2.20 to 2.24 can be summarised as follows :

(i) The magnitude of the local mean stress difference $\bar{\sigma}^i - \bar{\sigma}^e$ increases with increase in the material anisotropy ratio N/Q. Naturally, no modification of the externally applied stresses will occur in an "apparent" rotation domain developed in an isotropic body of material in which the foliation is mechanically passive. This is confirmed by inspection of equation 2.34 which indicates that, for N/Q = 1, $\bar{\sigma}^i - \bar{\sigma}^e = 0$ for all ω and θ.

(ii) Inspection of equation 2.34 also reveals a simple and important relationship between the sign of the mean stress difference $\bar{\sigma}^i - \bar{\sigma}^e$ and the relative magnitudes of the angular parameters ω and θ. This relationship folows from a consideration of the sign of the terms contained within the right hand side of equation 2.34 :

$$\bar{\sigma}^i - \bar{\sigma}^e = \tau_m^e \left[\frac{\left\{ \cos 2\theta - \cos 2(2\omega - \theta) \right\}}{(N/Q+1) - (N/Q-1)\cos 4(\theta - \omega)} \right]$$

(a) τ_m^e is positive by sign convention if $\sigma_1^e > \sigma_3^e$.

(b) $(N/Q - 1)$ is positive for $N/Q > 1$.

(c) The denominator $((N/Q+1) - (N/Q-1)\cos 4(\theta-\omega))$ is positive for all values of N/Q, ω and θ.

The sign of the mean stress difference depends, therefore, only on the sign of the bracketed trigonometrical numerator - $\left\{ \cos 2\theta - \cos 2(2\omega - \theta) \right\}$, all other terms being positive.

The following relationships exist between the sign of $\bar{\sigma}^i - \bar{\sigma}^e$ and the relative magnitudes of ω and θ. (Note the sign convention that compressive stress is positive) :

(a) For any value of ω in the range $0 < \omega < \theta$:

$$\cos 2\theta - \cos 2(2\omega - \theta) < 0$$

$$\bar{\sigma}^i - \bar{\sigma}^e < 0$$

Therefore, $\bar{\sigma}^i < \bar{\sigma}^e$ and the local mean stress within any element of internal foliation containing foliation oriented in this range of ω is less (relatively tensile) than the mean stress in the external foliation.

(b) For any value of ω in the range $\theta < \omega < 90^o$:

$$\cos 2\theta - \cos 2(2\omega - \theta) > 0$$

$$\bar{\sigma}^i - \bar{\sigma}^e > 0$$

Therefore, $\bar{\sigma}^i > \bar{\sigma}^e$ and the local mean stress within any element of the internal foliation containing foliation oriented over this range of is greater (relatively compressive) than the mean stress within the external foliation.

(c) When $\omega = \theta$ (also $\omega = 0^o$, $\omega = 90^o$):

$$\cos 2\theta - \cos 2(2\omega - \theta) = 0$$

$$\bar{\sigma}^i - \bar{\sigma}^e = 0$$

Therefore, $\bar{\sigma}^i - \bar{\sigma}^e = 0$ and the local mean stress within that element containing foliation oriented normal to the rotation domain boundaries is equal to the mean stress in the external foliation.

It can be seen from these relationships that a gradient in mean stress will exist across any rotation domain in which the attitude of the internal foliation varies. During an increment of deformation, an oblique rotation domain can be divided into outer zones of relatively tensile mean stress ($\bar{\sigma}^i < \bar{\sigma}^e$) and a central zone of relatively mean stress ($\bar{\sigma}^i < \bar{\sigma}^e$), separated by the line joining points of band normal foliation orientation (fig. 2.25).

A situation in which the boundaries of a rotation domain are oriented normal to external foliation ($\theta = 0$) represents a special case. It can be seen that for any value of ω within such a domain ω, must lie in the range $\theta(=0) < \omega < 90^o$. For this case the local mean stress within the rotation domain is always greater than the mean stress in the unrotated external foliation ($\bar{\sigma}^i - \bar{\sigma}^e > 0$). It has been indicated earlier in this chapter (fig. 2.7) that, for $\theta = 0$, the equations listed in table 2.1 represent incremental conditions within the opposing limbs of a symmetric similar fold. The "external foliation" is represented in such a fold by the unrotated foliation ($\omega = 0$) along the trace of the axial plane in profile section. The relationship $\bar{\sigma}^i > \bar{\sigma}^e$, for $\omega = 0$ implies that the mean stress within the hinge region of a symmetric similar fold (equivalent to $\bar{\sigma}^e$) is less than the mean stress within the limbs $\bar{\sigma}^i$) for any value of limb rotation, . Casey (1976) discussed the implications of such mean stress gradients in symmetric similar folds and suggested that these gradients may promote the development of soluble material migration by pressure solution in such structures. disolution in limb regions (relatively compressive mean stress) and deposition in hinge regions (relatively tensile mean stress)). Evidence provided by natural structures indicates that the mechanical effects of foliation anisotropy may account for the development of certain types of crenulation cleavage in symmetric micro-folds which exhibit chemical differentiation (see Cosgrove, 1972, 1976).

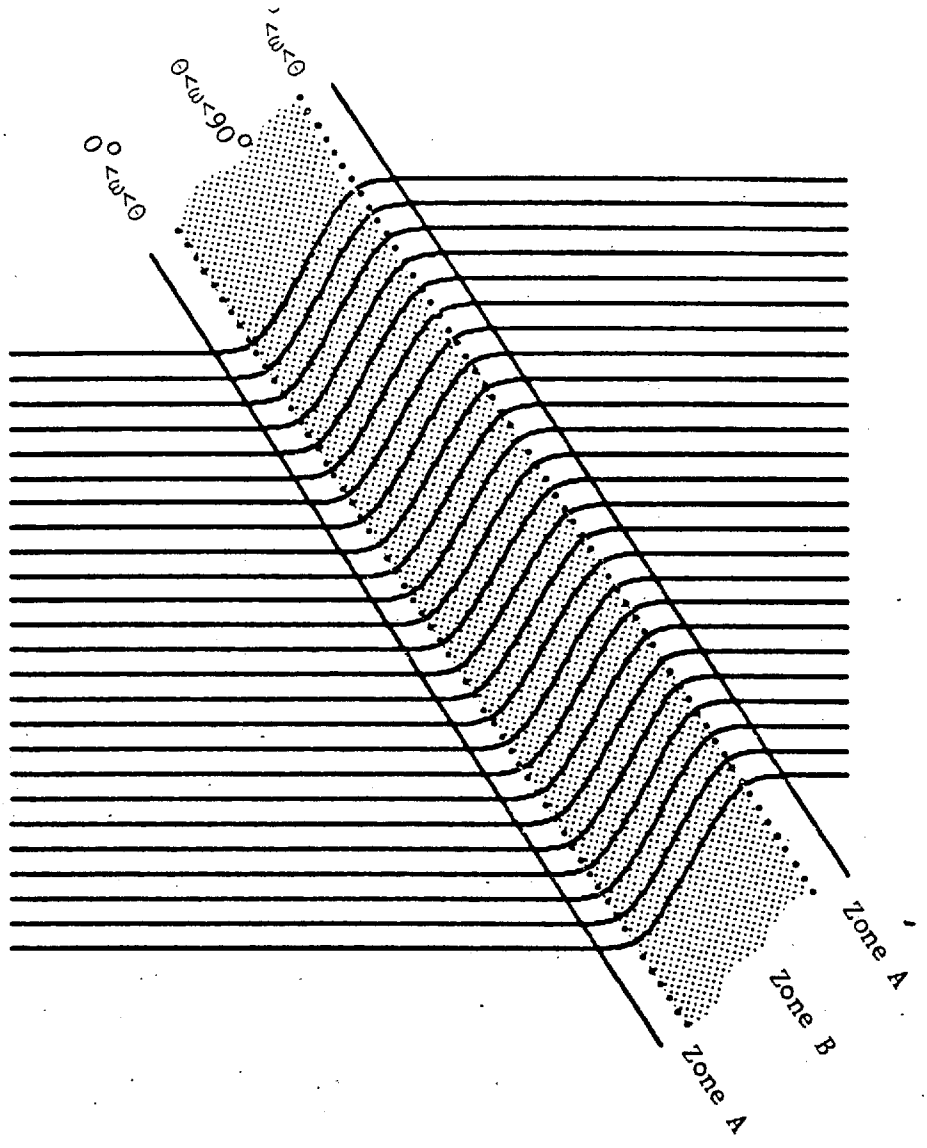


Figure 2.25

Zone A
$0 < \omega < \theta$

i. Zone of relatively tensile mean stress - $\bar{\sigma}^i < \bar{\sigma}^e$

ii. "Channelling" of maximum principal stress trajectories parallel with foliation.

Zone B
$\theta < \omega < 90^\circ$

i. Zone of relatively compressive mean stress - $\bar{\sigma}^i > \bar{\sigma}^e$

ii. "Channelling" of maximum principal stress trajectories normal to foliation.

Before considering the mean stress gradients which will be present in specific structures and the finite changes in mean stress which will accompany finite deformation, the predictions of the analysis with respect to the development of principal stress rotation within foliation rotation domains will be examined.

2.3.6 Variation in the orientation of principal stress trajectories as a function of foliation attitude.

Two equations, listed in table 2.1, can be used to quantify the local rotation of maximum principal stress trajectories with rotation domain as a function of the orientation of the domain boundaries, θ, the local attitude of the internal foliation, ω, and the material anisotropy ratio, N/Q.

The first of these equations (2.46) expresses the local rotation (ω_s) of σ_1^i with respect to the line of action of σ_1^e in the external foliation (foliation parallel). The angle ω_s is defined in fig. 2.7B.

$$\omega_s = \theta - \frac{1}{2}\arctan\left[\sin 2\theta \Big/ \left[\cos 2\theta - \frac{(N/Q-1)\left\{\cos 2\theta - \cos 2(2\omega-\theta)\right\}}{(N/Q+1) - (N/Q-1)\cos 4(\theta-\omega)}\right]\right]$$

Inspection of this equation shows that the magnitude of the local internal stress trajectory rotation, ω_s, is independent of the level of stress in the external foliation (τ_m^e). A number of other predictions can be obtained by direct inspection of this equation.

(i) No stress rotation will occur if the foliation is mechanically passive:

When N/Q = 1 : $\quad (N/Q-1) = 0$

Therefore : $\quad \omega_s = \theta - \frac{1}{2}\arctan(\sin 2\theta/\cos 2\theta)$

and : $\quad \omega_s = 0 \quad \ldots\ldots$ for all ω and θ.

(ii) No rotation of stress trajectories will occur within an upright rotation domain:

When $\theta = 0$: $\sin 2\theta = 0$

Therefore : $\omega_s = 0 - \frac{1}{2} \arctan(0)$

and : $\omega_s = 0$ ..... for all N/Q and ω.

This imples that σ_1 will act normal to axial surfaces of a symmetric similar fold throughout the structure. This result has been previously obtained by Casey (1976) and Cobbold (1976).

Rotation of stress trajectories must occur within an oblique rotation domain developed in a material with a mechanically significant foliation anisotropy ($\theta > 0$, $N/Q > 1$). The physical significance of the rotations can be illustrated most clearly by examining the predictions of the second of the stress rotation equation contained in table 2.1 (equation 2.47). The equation indicates the local angle of inclination, α_s, of the σ_1^i stress trajectories with respect to the local attitude of internal foliation planes. The angle α_s has been defined in fig. 2.7 B.

$$\alpha_s = \omega - \theta + \frac{1}{2} \arctan \left[\sin 2\theta \Big/ \left[\cos 2\theta - \frac{\left\{ (N/Q-1)\cos 2\theta - \cos 2(2\omega-\theta) \right\}}{(N/Q+1) - (N/Q-1)\cos 4(\theta-\omega)} \right] \right]$$

The variation in the angle α_s with internal foliation attitude is illustrated for a series of rotation domain orientations, ω, in figs.

2.26 to 2.29 ($\theta = 15^{o}$ (2.26); 30° (2.27); 45° (2.28); 60° (2.29)). The variation in the local magnitude of α_s with the corresponding local inclination, ω, of the foliation is shown in these figures for N/Q = 1.0, 5.0 and 100.0. These graphs illustrate the following predictions :

(i) As has been indicated, no stress trajectory rotation will occur within an "apparent" rotation domain developed in an isotropic material in which the foliation is mechanically passive. This is expressed in figs. 2.26 to 2.29 by the relationship :

For N/Q = 1 : $\alpha_s = 0$ ..... for all ω and θ.

(ii) If the foliation is mechanically active (N/Q > 1) then rotation of the internal principal stress trajectories will occur within an oblique rotation domain. The magnitude of this rotation is a function of the material anisotropy ratio. The most significant rotations are shown by the curves corresponding to an anisotropy ratio of N/Q = 100. Stress trajectory rotation will also occur, although the magnitude of the rotation will be lower, in oblique domains developed in materials with relatively low degrees of mechanical anisotropy.

(iii) In structures developed in highly anisotropic materials , the domain normal foliation attitude, $\omega = \theta$, marks a significant transition in the line of action of the principal stress trajectories. Inspection of figs. 2.26 to 2.29 shows that the σ_1^i trajectories will tend to lie parallel with the trend of the foliation within those zones of the internal foliation in which the angle defining the foliation attitude, ω, is less than the angle defining the orientation of the rotation domain boundaries, θ (ie. for $0 < \omega < \theta : \alpha \rightarrow 0$). This implies that σ_1^i trajectories will tend to rotate with the plane of foliation during the initial stages of foliation rotation within an oblique rotation domain. In contrast, σ_1^i will tend to act normal

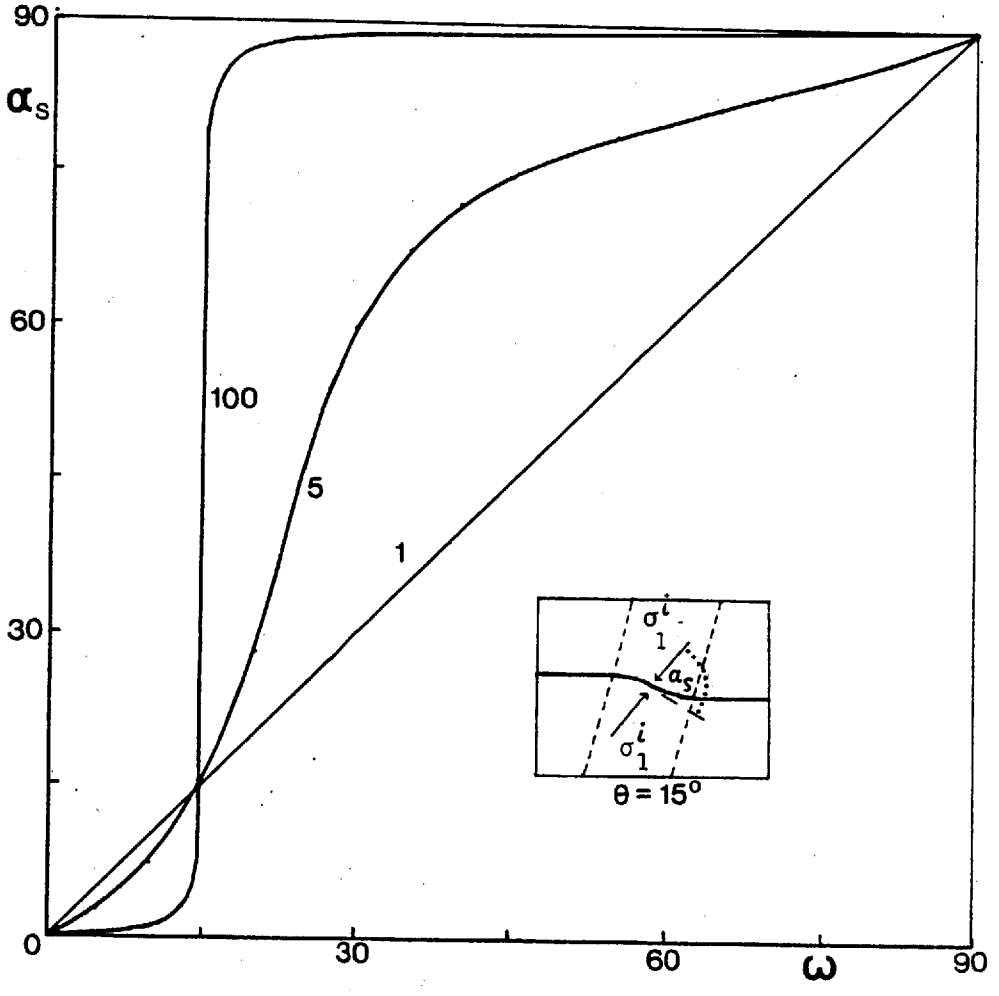


Figure 2.26 Relationship between the *local* magnitude of the stress inclination angle α_s and the *local* foliation inclination ω within a rotation domain oriented at $\theta = 15^o$. The angle α_s defines the *local* inclination of σ_1 stress trajectories with respect to the *local* attitude of the foliation plane and is measured anti-clockwise from the foliation plane (see fig. 2.7 B)

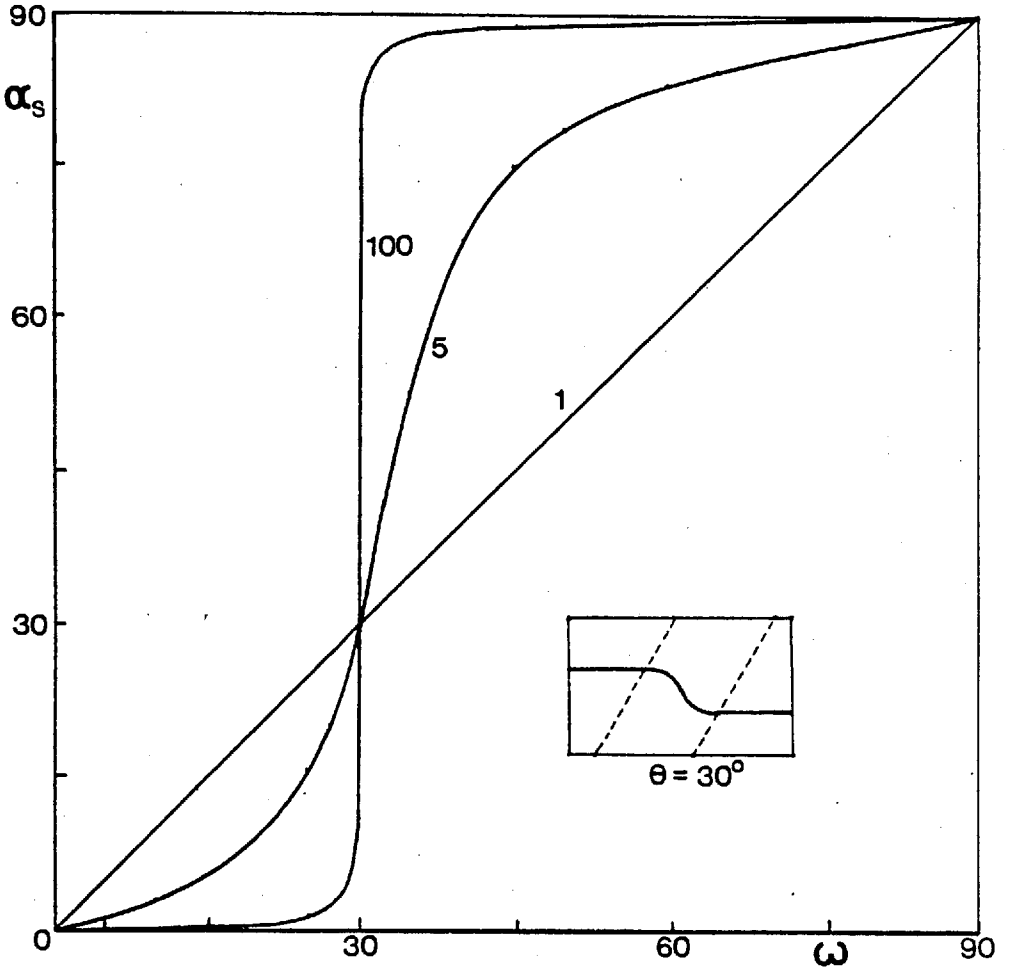


Figure 2.27 Relationship between the *local* magnitude of the stress inclination angle α_s and the *local* foliation inclination ω within a rotation domain oriented at $\theta = 30^\circ$.

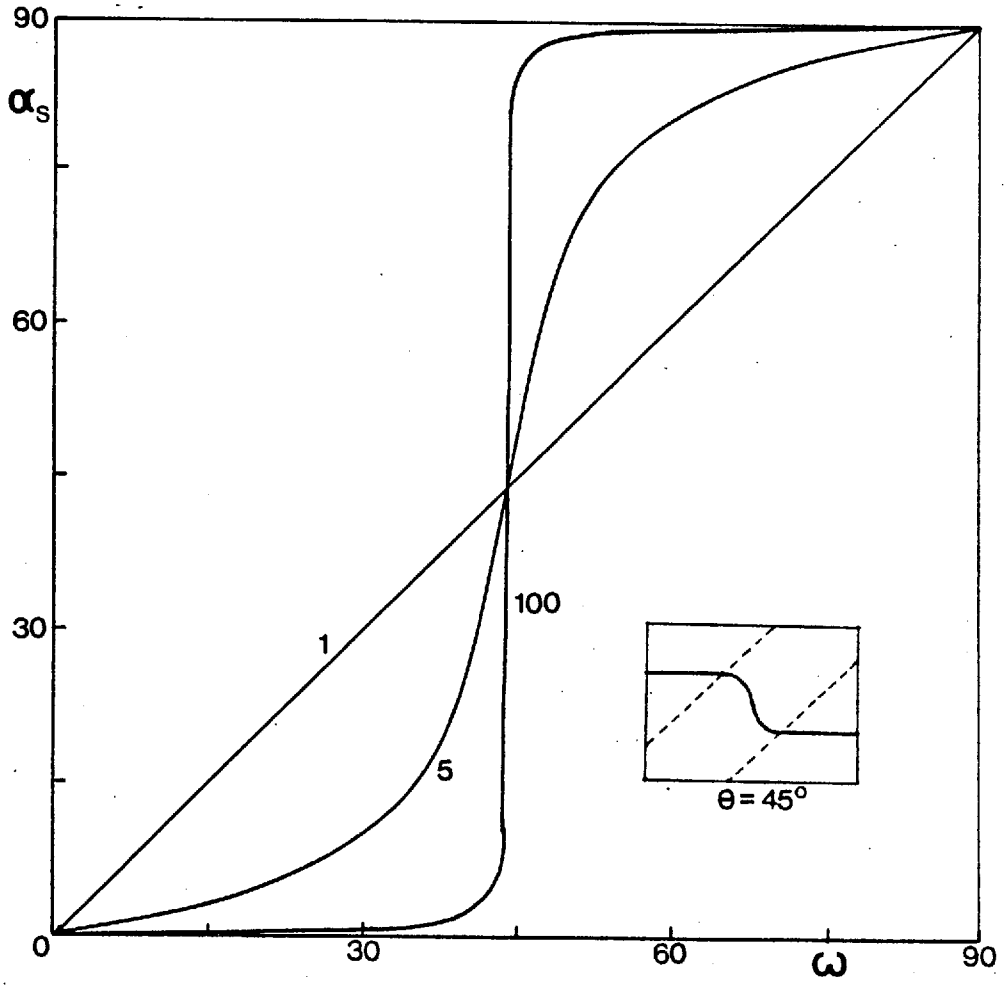


Figure 2.28 Relationship between the *local* magnitude of the stress inclination angle α_s and the *local* foliation inclination ω within a rotation domain oriented at $\theta = 45^{\circ}$.

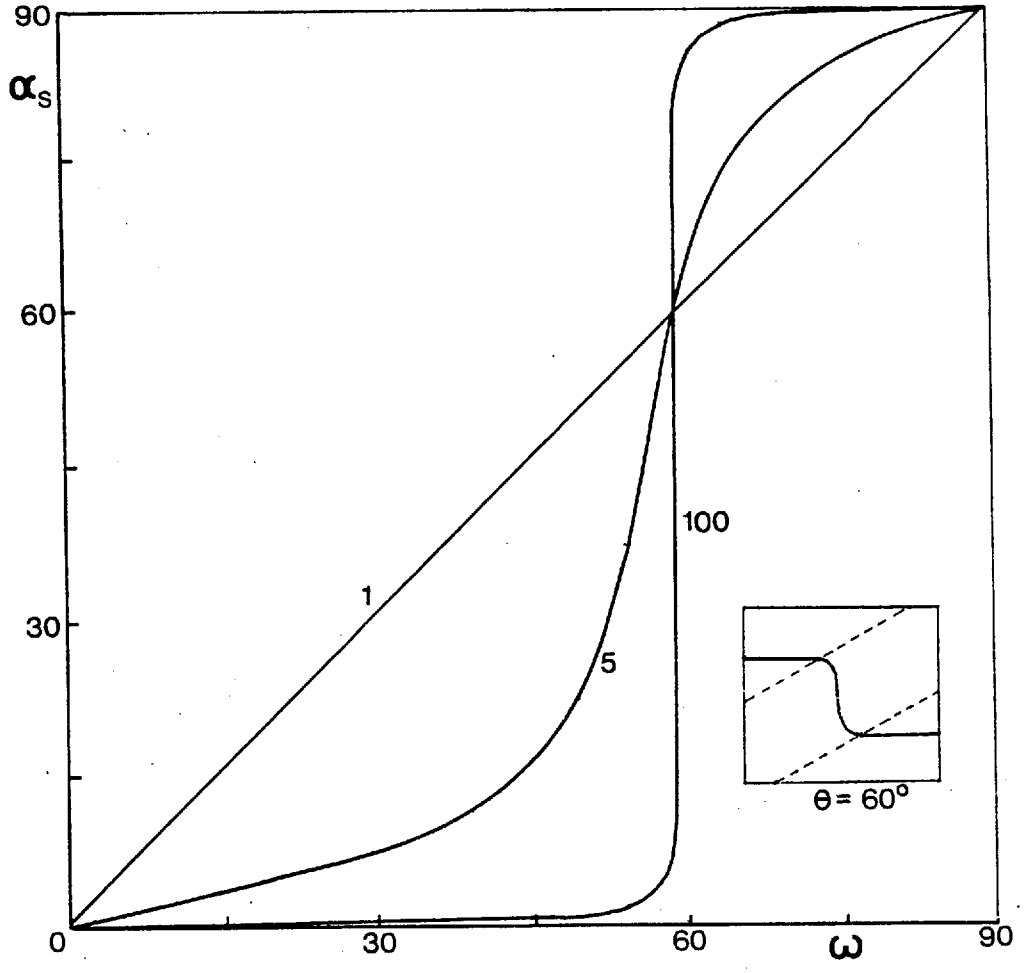


Figure 2.29 Relationship between the *local* magnitude of the stress inclination angle α_s and the *local* foliation inclination ω within a rotation domain oriented at $\theta = 60^{\circ}$.

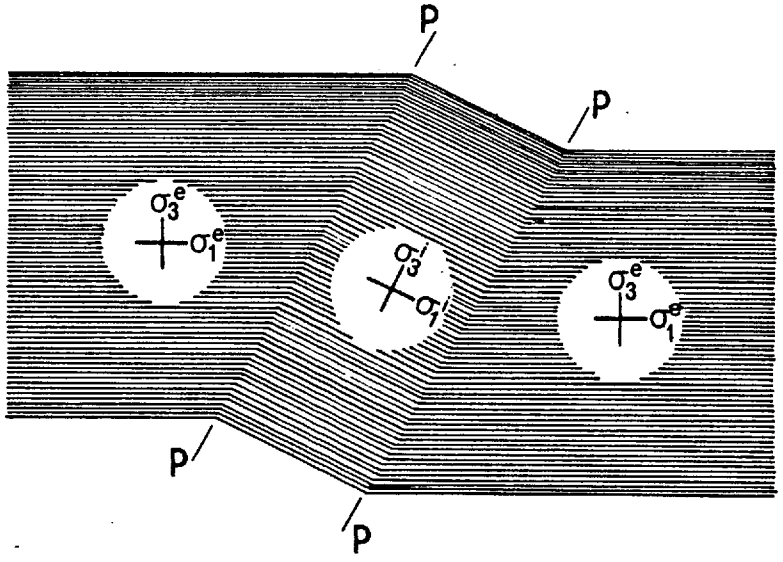
to the plane of foliation within elements containing foliation which has rotated past the domain normal foliation altitude (i.e. for $\theta < \omega < 90^{o}$).

It follows that, at a finite stage in deformation, an oblique rotation domain can be divided into a central zone in which σ_1^i lies at a high angle to the plane of foliation and outer zones in which σ_1^i lies approximately parallel with foliation. The zones of foliation parallel and foliation normal stress orientation correspond respectively, with the zones of relatively tensile and relatively compressive internal mean stress (fig. 2.25).

It is interesting to note that equation 2.47 predicts that σ_1^i must lie either parallel with foliation or normal to foliation within an oblique rotation domain developed in a material which is infinitely anisotropic i.e. if $N/Q = \infty$ then a) for $0 < \omega < \theta$, $\alpha_s = 0^{o}$; b) for $\theta < \omega < 90^{o}$ $\alpha_s = 0^{o}$. A discontinuity in stress magnitude and orientation will exist along the locus of points marking the domain normal foliation altitude $\omega = \theta$. This can be demonstrated by introducing a very high, effectively infinite, value for N/Q into the analytical expressions listed in table 2.I.

As has been indicated, it is possible to express the magnitude of the stress modifications which are predicted to occur within a rotation domain, under the conditions of the analysis, by defining the level of stress in the external foliation. Consider, for example, the two structural configurations shown in figs. 2.30 A and 2.31 A. These figures show a rotation domain with boundaries oriented at 30° to external foliation normal. For the purpose of this discussion it has been assumed that the internal foliation attitude is uniform within the rotation domain (ω constant) and the internal stress modification has been calculated for a material with a high degree of mechanical anisotropy (N/Q = 100). The foliation attitude illustrated in fig. 2.30 A corresponds to the maximum decrease in the relative magnitude of the internal mean stress $\bar{\sigma}^i$. The foliation attitude can be identified from the minimum in the graphical relationship between $(\bar{\sigma}^i - \bar{\sigma}^e)$ and ω shown in fig. 2.22 ($\omega = 27^{o}$, point A). In contrast, the foliation attitude illustrated in fig. 2.31 A corresponds to maximum increase in the relative

A.



B.

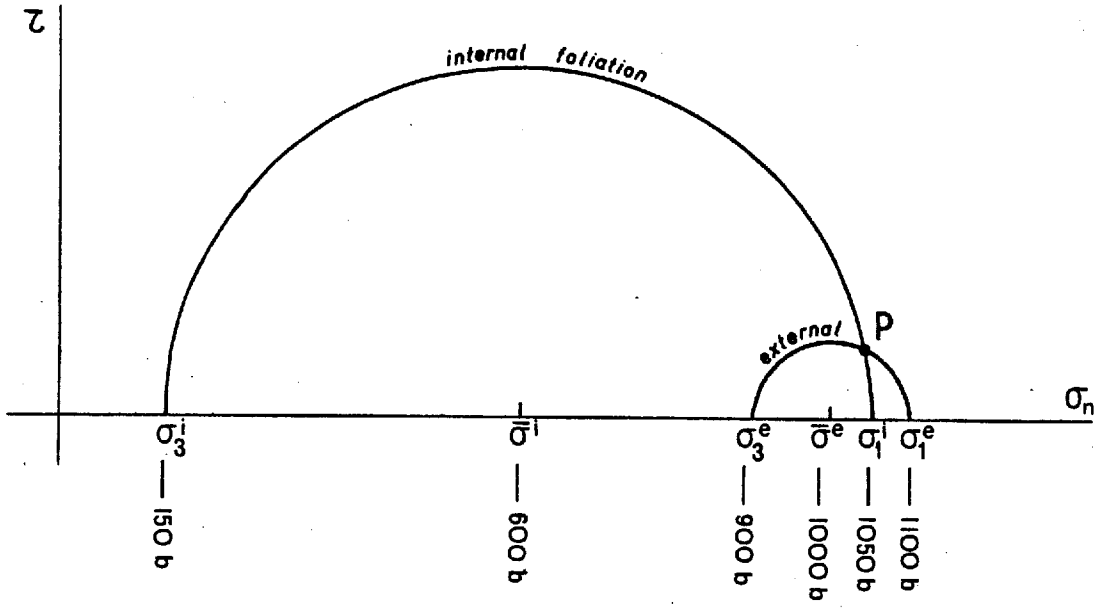


Figure 2.30 Mohr's circle representation of the states of stress in an angular rotation domain (N/Q = 100). Fig 2.30 B shows the contrast in stress within the external and internal foliation zones of the structure illustrated in fig. 2.30 A. The foliation inclination within the rotation domain corresponds to the maximum *reduction* in the relative magnitude of $\bar{\sigma}^i$. See text for further details.

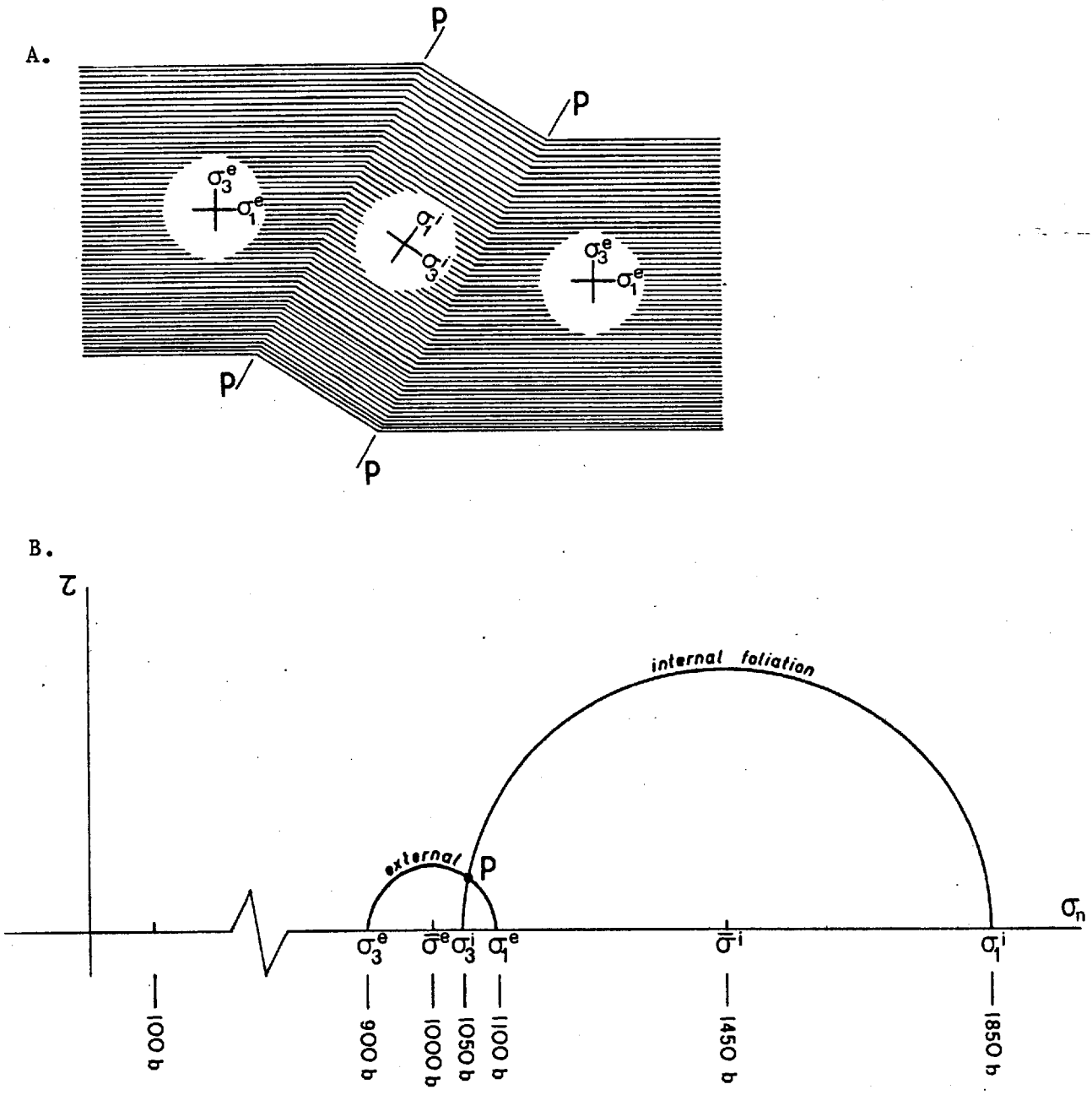


Figure 2.31 Mohr's circle representation of the states of stress in an angular rotation domain (N/Q = 100). Fig. 2.31 B shows the contrast in stress within the external and internal foliation zones of the structure illustrated in fig. 2.31 A. The foliation inclination within the rotation domain corresponds to the maximum *increase* in the relative magnitude of $\bar{\sigma}^{-i}$. See text for further details.

magnitude of $\bar{\sigma}^i$ and is identified by point B in fig. 2.22 ($\omega = 32^o$), The two figures represent the extremes of internal stress modification under conditions of constant volume deformation.

In each of the figures, Mohr's circle constructions are shown to represent the constrasting states of stress within the internal and external foliation (two dimensional stress representation for stresses acting in the x,y profile plane of the structure). The method of constructing of these figures (2.30 B, 2.31 B) has been discussed earlier in this chapter with reference to fig. 2.7. In order to illustrate the geological significance of the internal stress modification, the magnitude of principal stresses σ_1^i and σ_3^i has been calculated assuming the following stress levels in the external foliation:

σ_1^e = 1,100 bars
σ_3^e = 900 bars
$\bar{\sigma}^e$ = 1,000 bars
τ_m^e = 100 bars

The predicted rotation of internal principal stress trajectories for the two structures has been illustrated in figs. 2.30 A and 2.31 A by indicating the line of action of σ_1^i and σ_3^i.

It can be seen from fig. 2.30 that the significant reduction in the magnitude of the internal mean stress ($\sigma^i - \sigma^e = 400b = \tau_m^e$ σ^i = 600 bars) is associated primarily with a substantial decrease in the magnitude of σ_3^i. Since "channelling" of σ_1^i along the plane of the internal foliation occurs, this decrease in σ_3^i represents a substantial reduction in the stress acting normal to the foliation planes within the rotation domain (σ_3^e = 900 bars, σ_3^i = 150 bars).

It can be seen from fig. 2.31 that a very marked change in internal stress conditions accompanies a small rotation of the internal foliation planes through the domain normal foliation attitude. This change in the state of stress within the rotation domain is associated with a change in the orientation of σ_1^i to position approximately normal to the plane of the internal foliation. The internal mean stress for the configuration shown in fig. 2.31 A is 1,450 bars and

is significantly compressive with respect to the mean stress in the external foliation (1,000 bars).

The internal stress modifications shown in figs. 2.30 and 2.31 reflect the high degree of mechanical anisotropy assigned to the material containing the structure (N/Q = 100). Even more significant modifications in the magnitude of the internal principal stresses are predicted for materials with higher values of N/Q. It is possible to assign a value for N/Q which is sufficient to lead to the prediction of an actual tensile stress acting normal to internal foliation for the external stress levels and geometry indicated in fig. 2.30. As has been emphasised, however, the analytical predictions are derived from the condition of constant volume deformation. It is unlikely that the extreme modifications in internal stresses which are predicted for highly anisotropic materials could be sustained in a structure developed in a discretely layered system. The induction of tensile stresses, acting normal to internal foliation planes, during the initial stages of foliation rotation would tend to produce an opening of interlayer voids by the process of delamination. Field evidence supports this prediction. A number of authors have described natural kink structures in which evidence for the development of delamination is provided by the presence of quartz or calcite veins deposited along interlaminar partings (e.g. Dewey, 1965; Anderson, 1968; Ramsay, 1967, Verbeek, 1978). The effect of such processes on the development of a rotation domain is considered in detail in Chapter 3.

2.5.7. Change in the state of stress within specific structures during finite deformation

In this section the change in stress conditions during the finite deformation of particular initial foliation perturbations will be considered briefly. The discussion is concerned with the finite development of stress modification within the structures whose finite geometric development (figs. 2.12 to 2.16) has been described in section2.3.3. It will be recalled that the computer based finite deformation analysis illustrated in these figures was applied to low amplitude foliation perturbations in the form of a half sine curve. The anisotropy ratio assigned to the material containing these structures is given by N/Q = 5.

The stages in finite deformation illustrated in figs. 2.12 2.16 are reproduced in figs. 2.32 to 2.36. The finite changes in stress orientation and magnitude, predicted by the analysis, are illustrated graphically by a scan of local conditions along a direction (AB) normal to the rotation domain boundaries. The graphical scans show i) the variation in mean stress difference, $\sigma^i - \sigma^e$, expressed in units of maximum shear strain in the external foliation, ii) the variation in the angle of inclination, α_s, of the σ_1^i stress to the internal foliation planes. The most significant features of the changes which occur in internal stress variation during finite deformation can be illustrated with reference to the run shown in fig. 2.34. This initial value of the domain orientation θ, in this run, is 30^0 and the geometric development of this structure has been considered in section 2.3.3 with reference to figs. 2.14 (A-E).

(i) During the initial stages of deformation the internal mean stress is tensile relative to the mean stress in the external foliation ($\sigma^i - \sigma^e < 0$) throughout the rotation domain. The maximum principal stress trajectories within this domain tend to rotate with the foliation planes (α_s low) - fig. 2.34 A, B

(ii) As the foliation within the central zone of the rotation domain rotates through the domain normal foliation attitude the trajectories within this central zone undergo an opposed rotation and become oriented at a high angle to the plane of the internal foliation (α_s high - fig. 2.24 C). This effect is accompanied by a significant change in the stress conditions within the central zone. The mean stress increases to become relatively compressive with respect to the mean stress in the external foliation ($\sigma^i - \sigma^e > 0$). There is a significant gradient in both the magnitude and orientation of internal principal stresses across the boundaries between the zones of low and high internal mean stress. At each stage in deformation, this boundary corresponds with the locus joining points where the internal foliation is normal to the rotation domain boundaries.

(iii) During the later stages of deformation, the central zone of relatively compressive mean stress increases in width as the locus of points marking the domain normal foliation attitude migrates

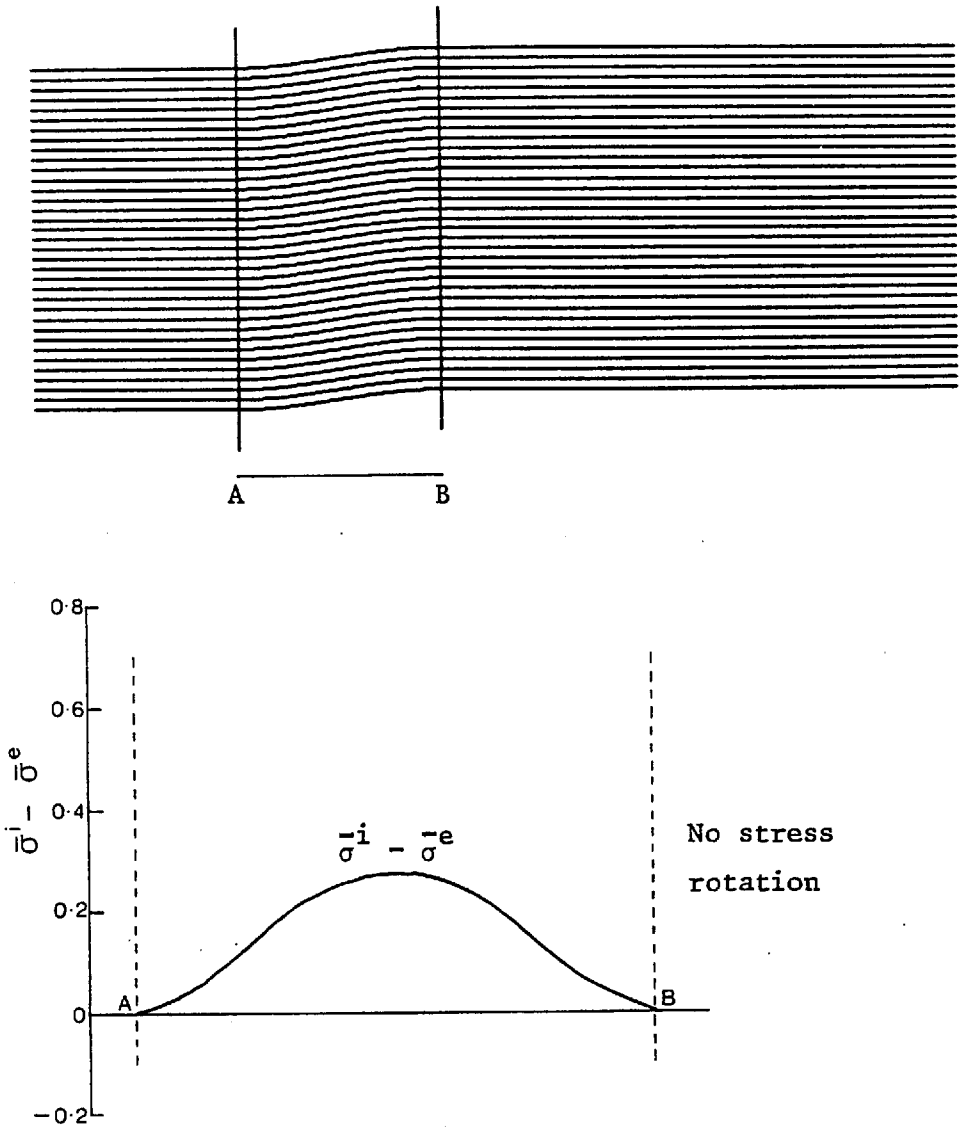
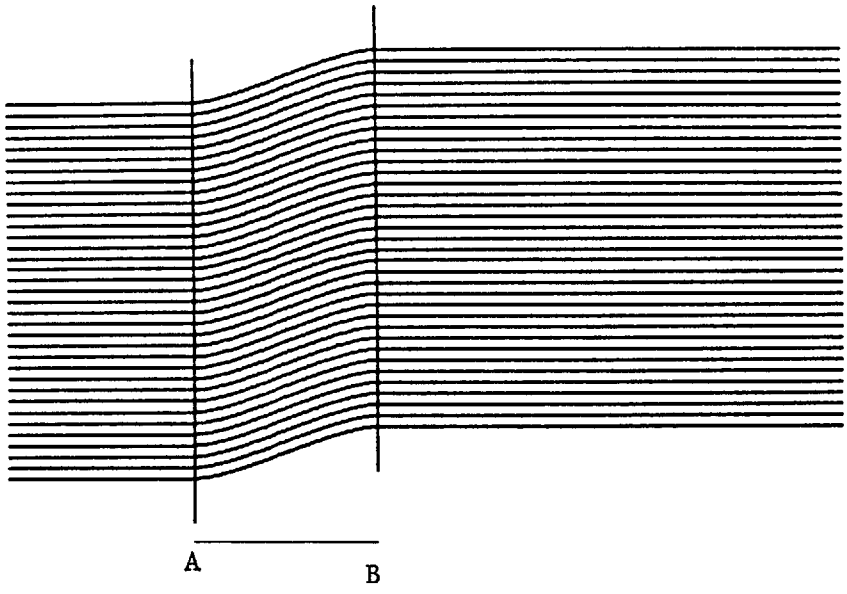


Figure 2.32 A

Initial rotation domain orientation, $\theta_o = 0^o$
Finite rotation domain orientation, $\theta_f = 0^o$

Deformation increment 0
Finite strain ε_{11} in the external foliation (natural strain) = 0.0

Anisotropy ratio, N/Q = 5.0



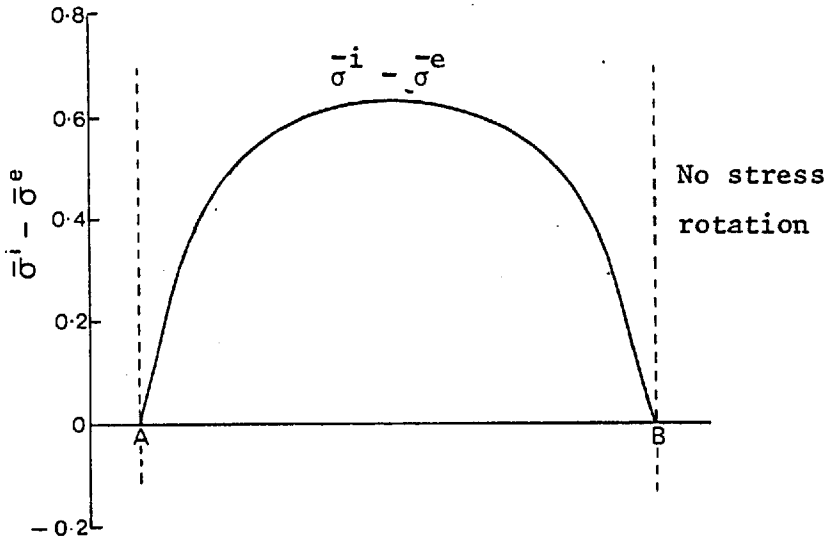


Figure 2.32 B

Initial rotation domain orientation, $\Theta_o = 0^o$
Finite rotation domain orientation, $\Theta_f = 0^o$

Deformation increment 100
Finite strain in the external foliation = 0.1

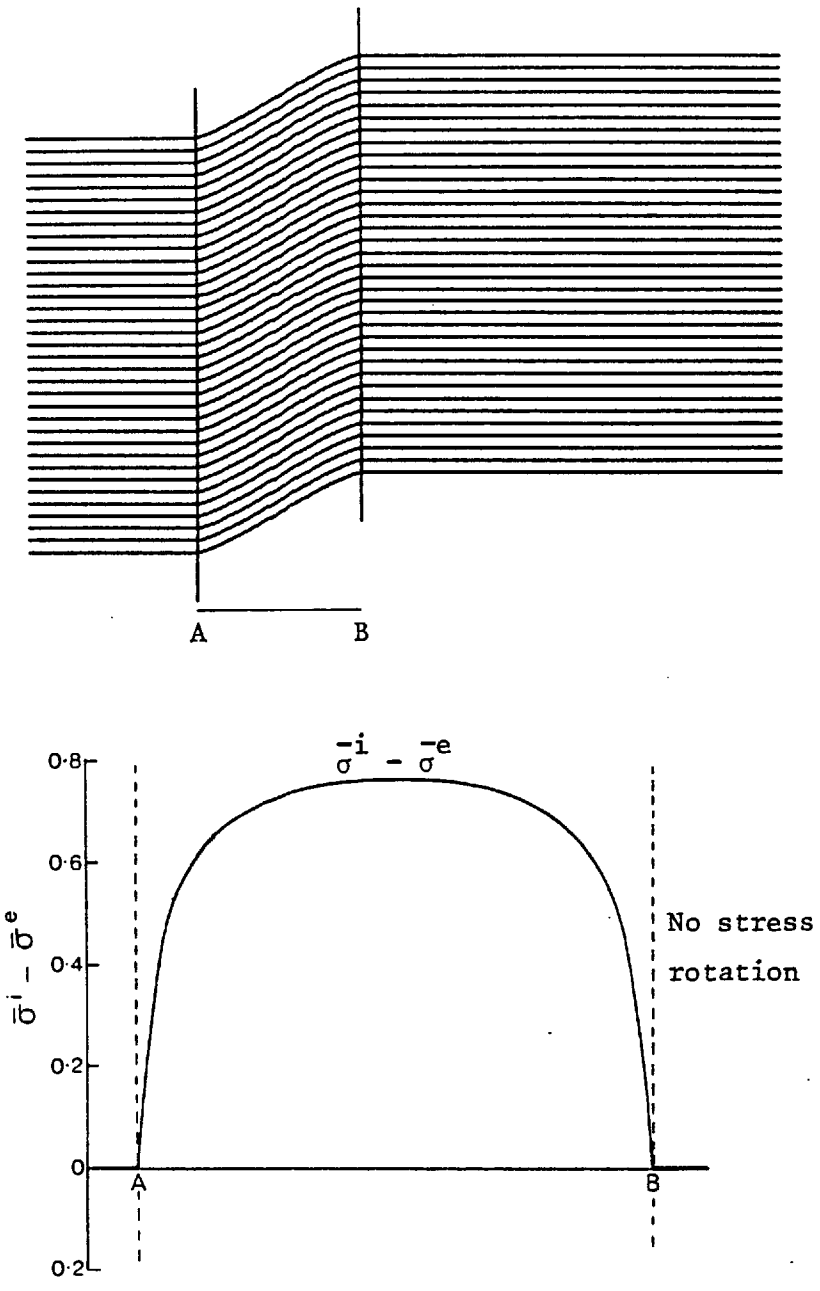


Figure 2.32 C

Initial rotation domain orientation, $\theta_o = 0^o$
Finite rotation domain orientation, $\theta_f = 0^o$

Deformation increment 200
Finite strain in the external foliation = 0.2

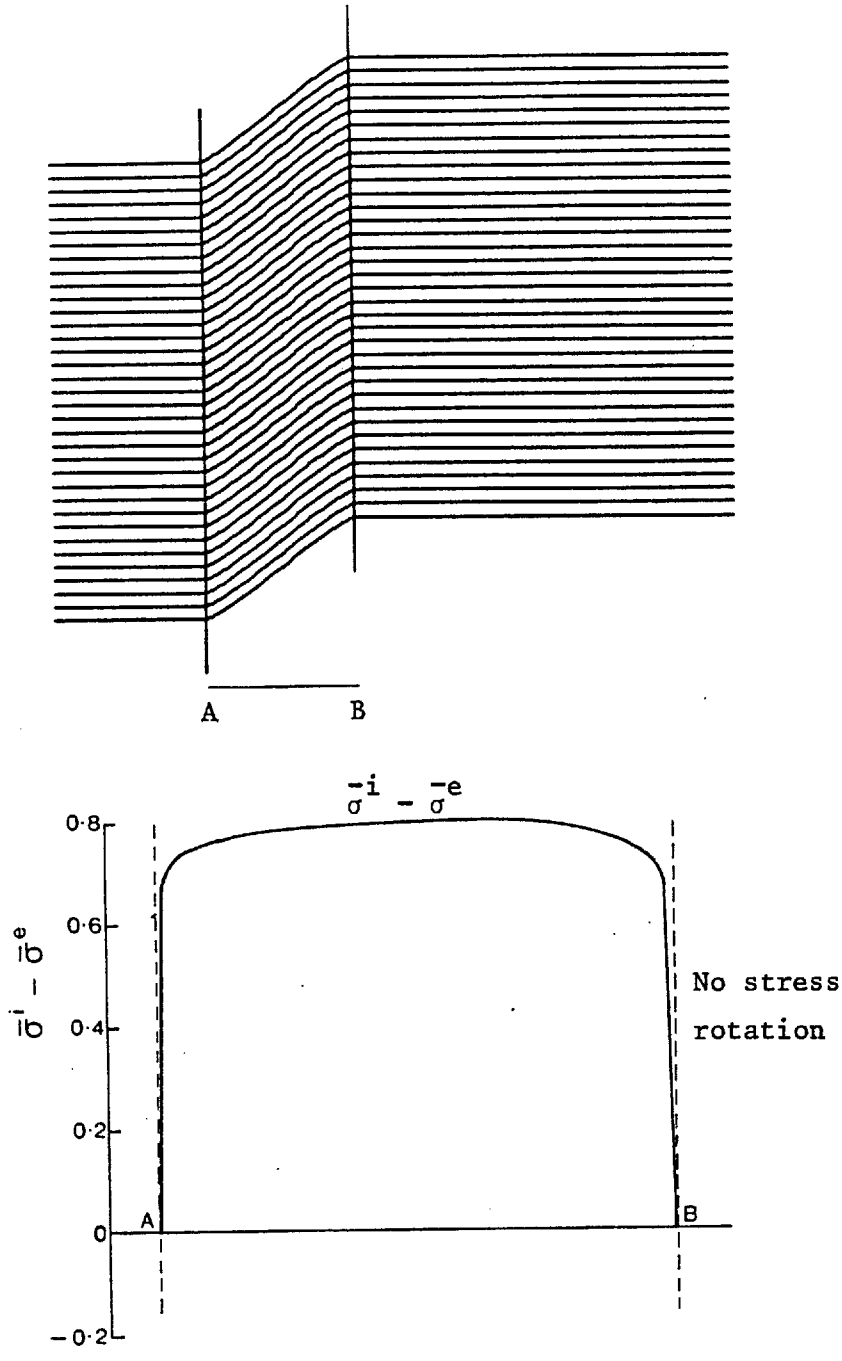


Figure 2.32 D

Initial rotation domain orientation, $\Theta_o = 0^o$
Finite rotation domain orientation, $\Theta_f = 0$

Deformation increment 300
Finite strain in the external foliation = 0.3

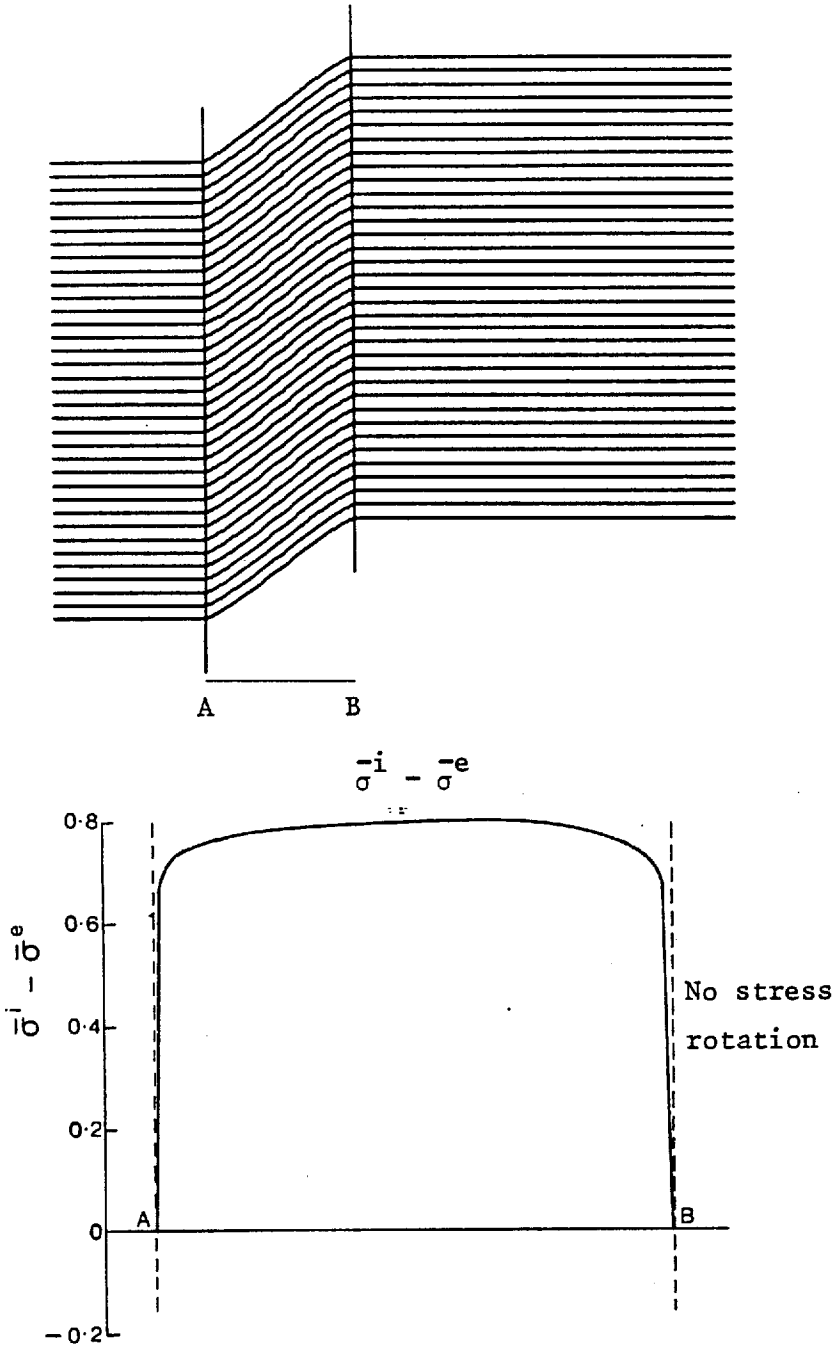


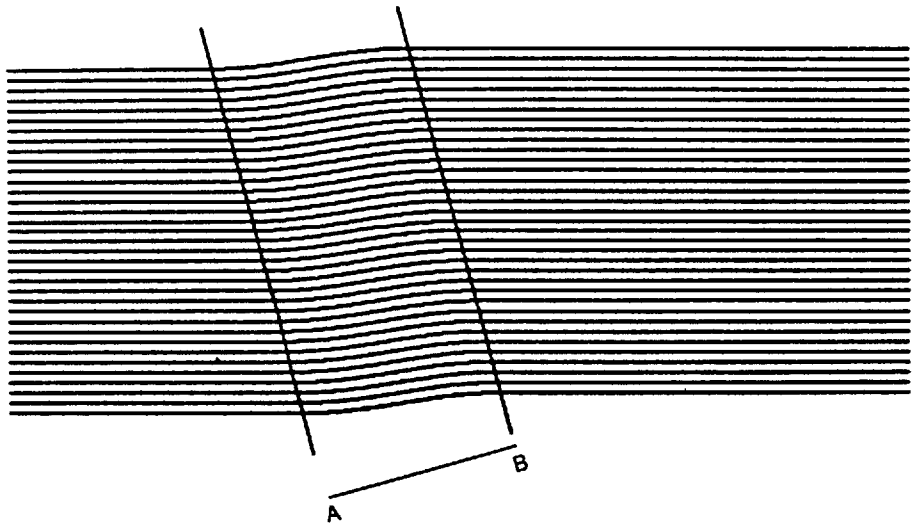
Figure 2.32 E

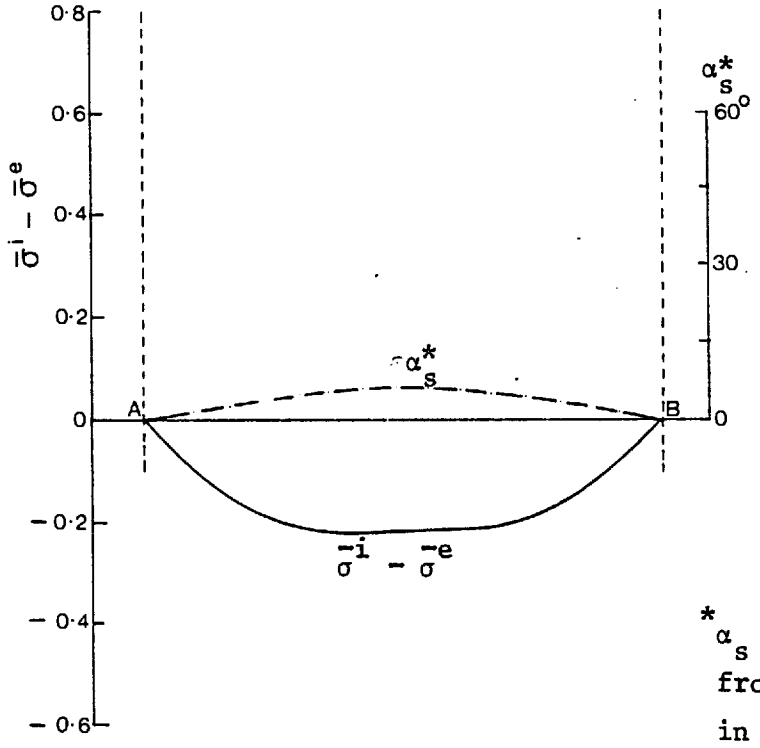
Initial rotation domain orientation, Θ_o = 0°

Finite rotation domain orientation, Θ_f = 0°

Deformation increment 400

Finite strain in the external foliation = 0.4





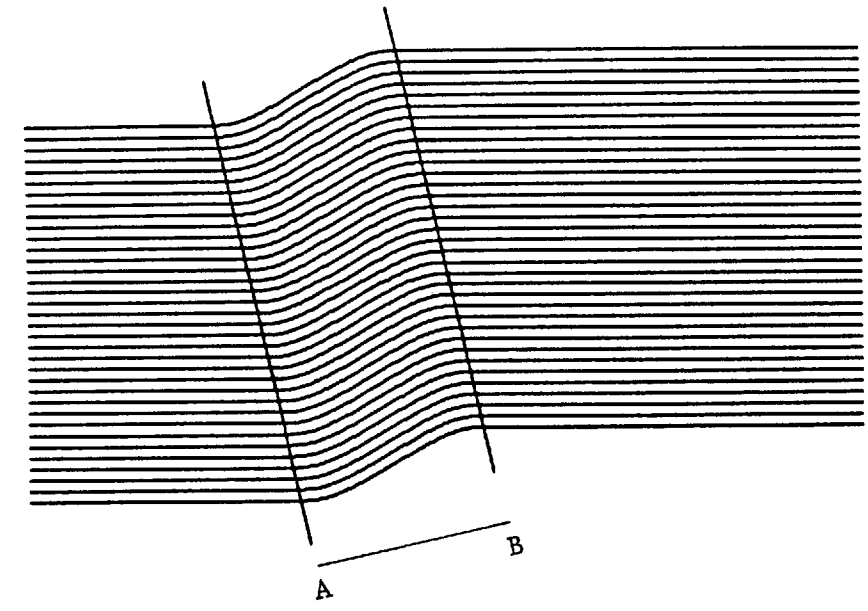
*α_s measured *clockwise* from foliation planes in figs. 2.33 to 2.36

Figure 2.33 A

Initial rotation domain orientation, θ_o = 15°
Finite rotation domain orientation, θ_f = 15°

Deformation increment 0
Finite strain in the external foliation = 0.0

Anisotropy ratio, N/Q =5.0



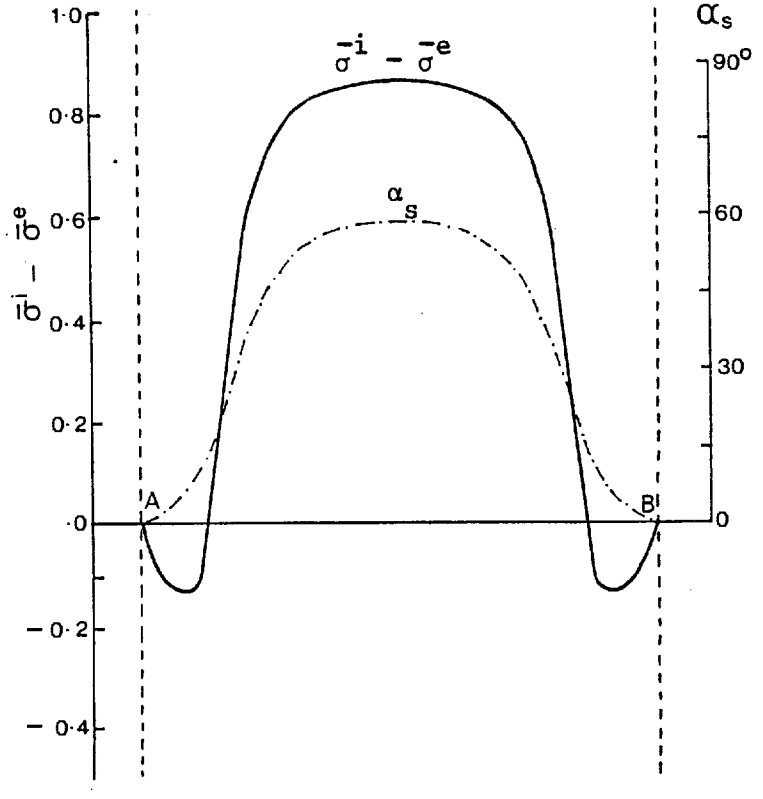
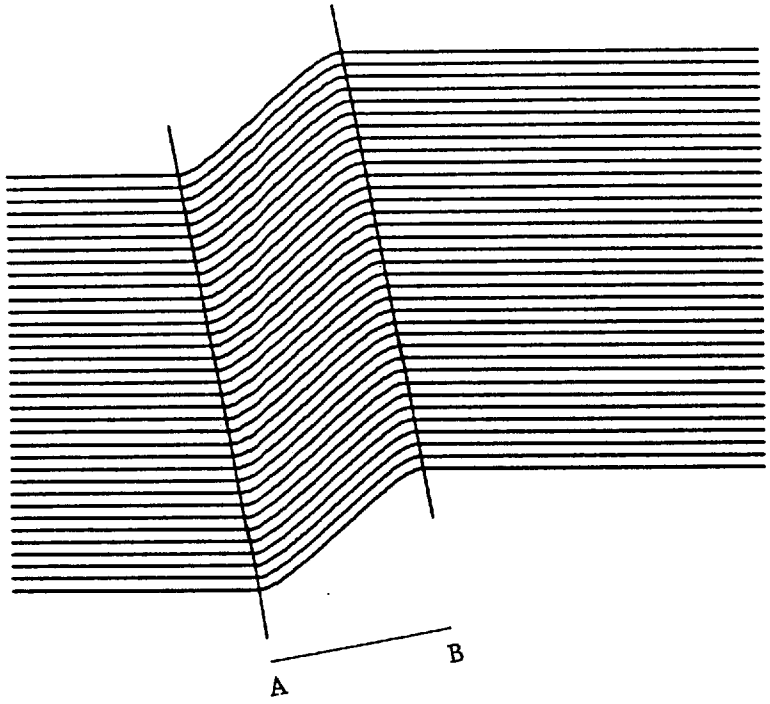


Figure 2.33 B

Initial rotation domain orientation, Θ_o = 15°
Finite rotation domain orientation, Θ_f = 12.5°

Deformation increment 100
Finite strain in the external foliation =0.1



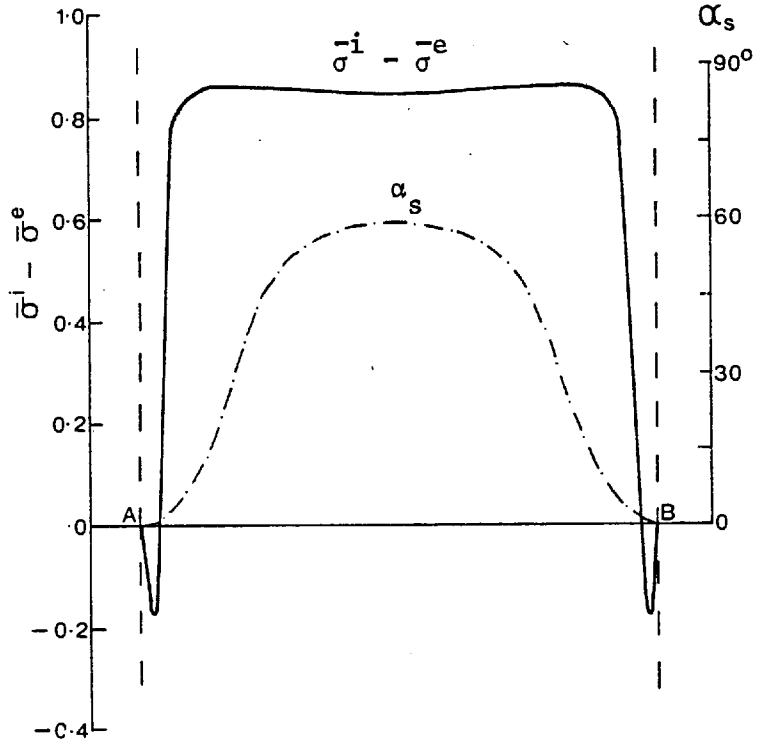
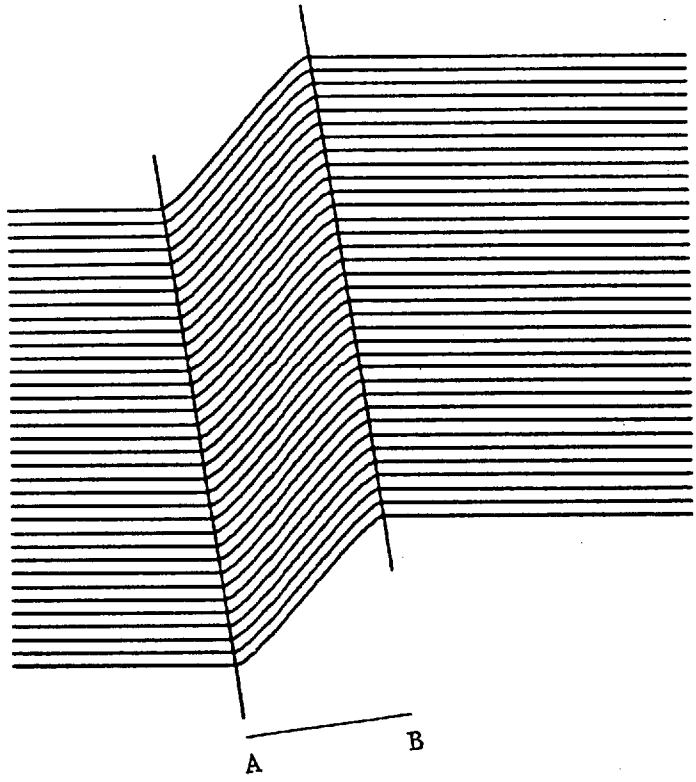


Figure 2.33 C

Initial rotation domain orientation, Θ_o = 15°
Finite rotation domain orientation, Θ_f = 10.3°

Deformation increment 200
Finite strain in the external foliation =0.2



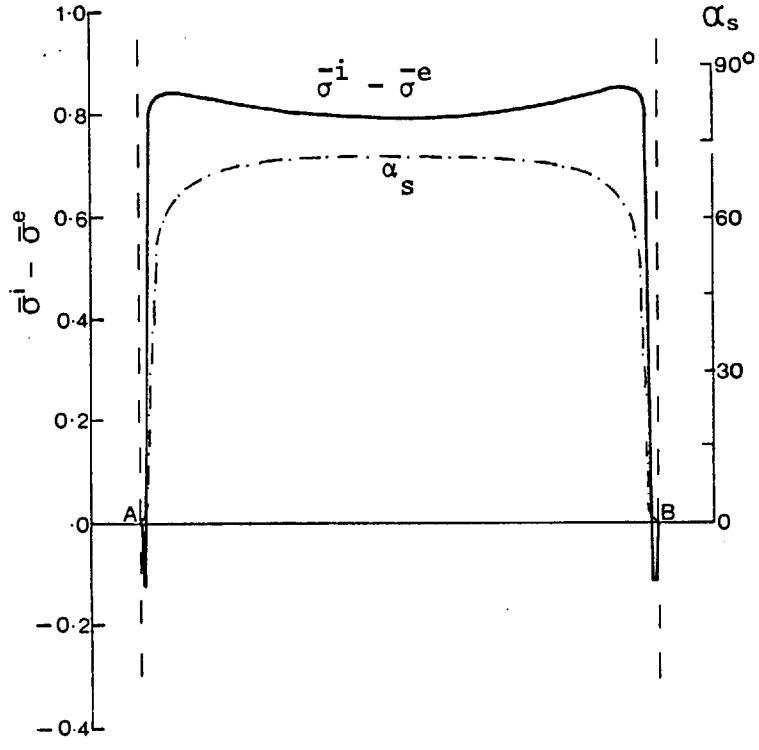
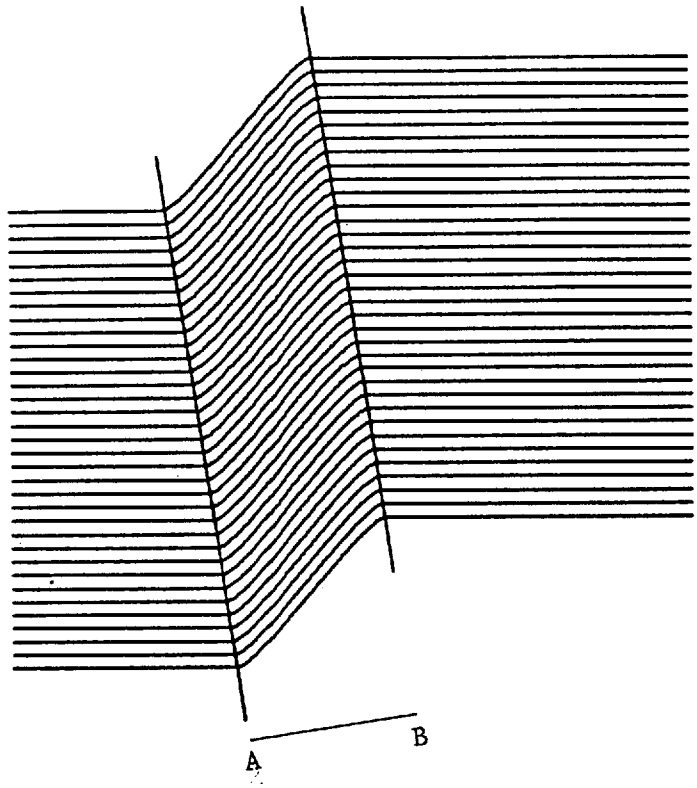


Figure 2.33 D

Initial rotation domain orientation, θ_o = 15°
Finite rotation domain orientation, θ_f = 8.5°

Deformation increment 300
Finite strain in the external foliation =0.3



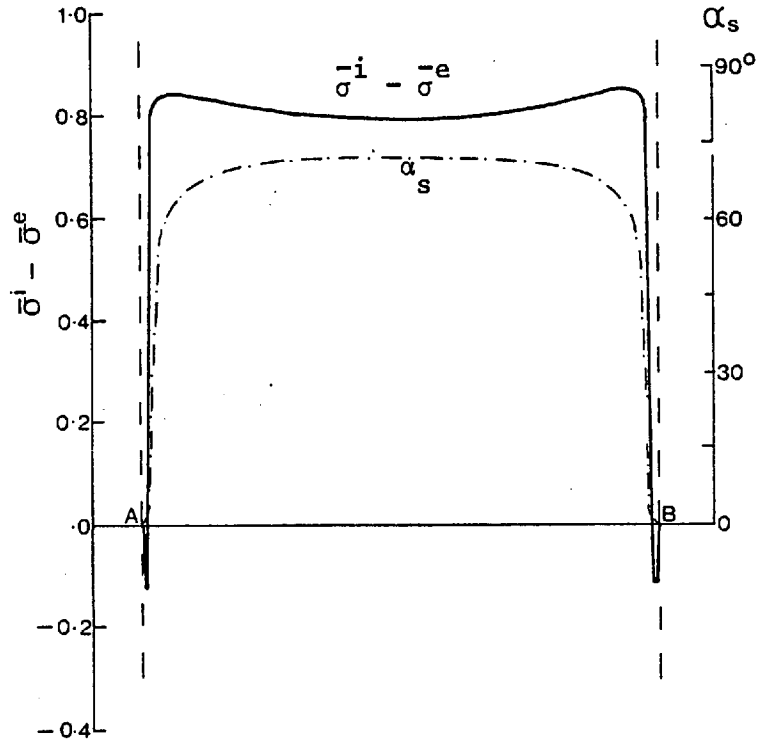


Figure 2.33 E

Initial rotation domain orientation, $\Theta_o = 15^o$
Finite rotation domain orientation, $\Theta_f = 6.9^o$

Deformation increment 400

Finite strain in the external foliation =0.4

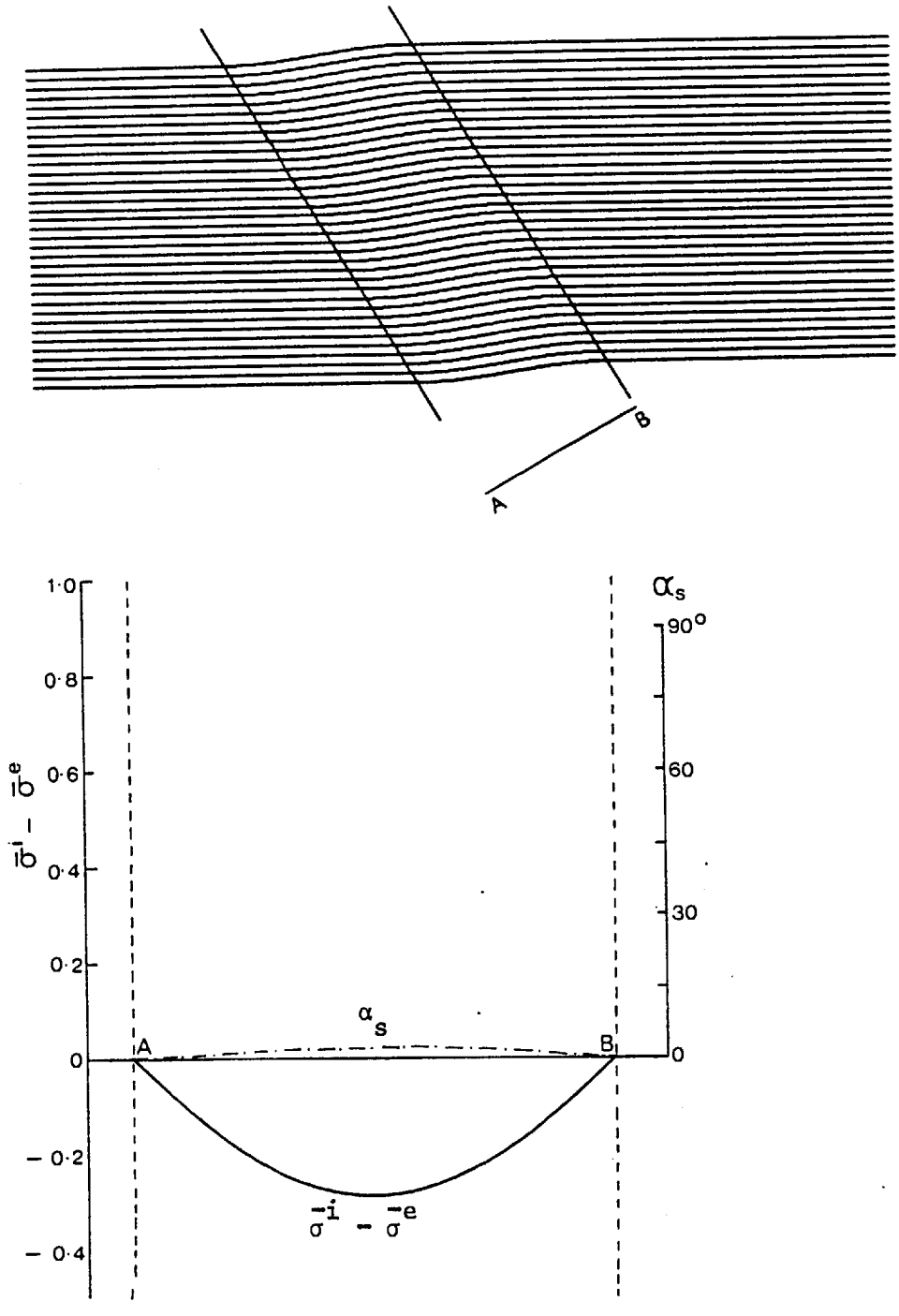
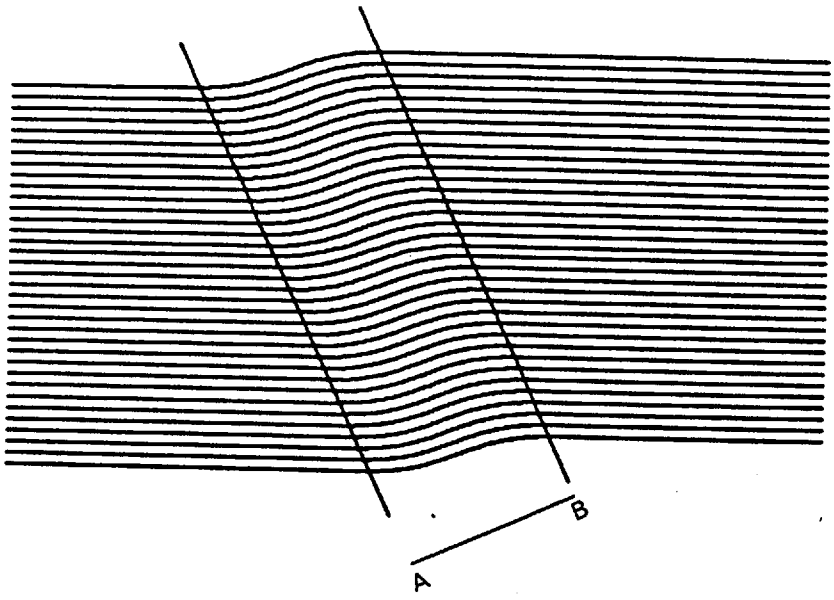


Figure 2.34 A

Initial rotation domain orientation, θ_o = 30°
Finite rotation domain orientation, θ_f = 30°

Deformation increment 0
Finite deformation in the external foliation =0.0



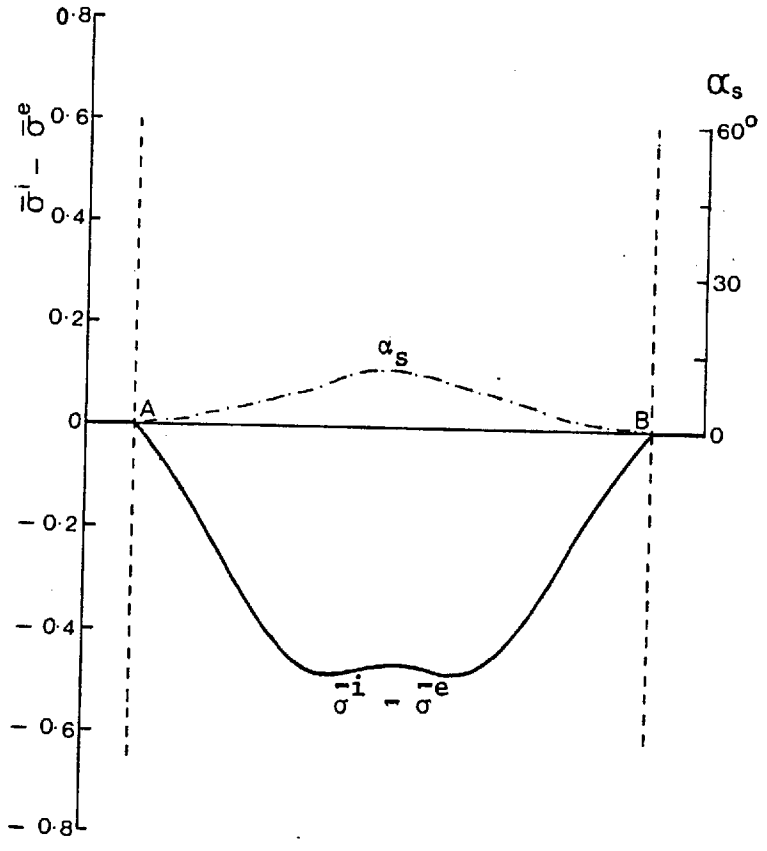
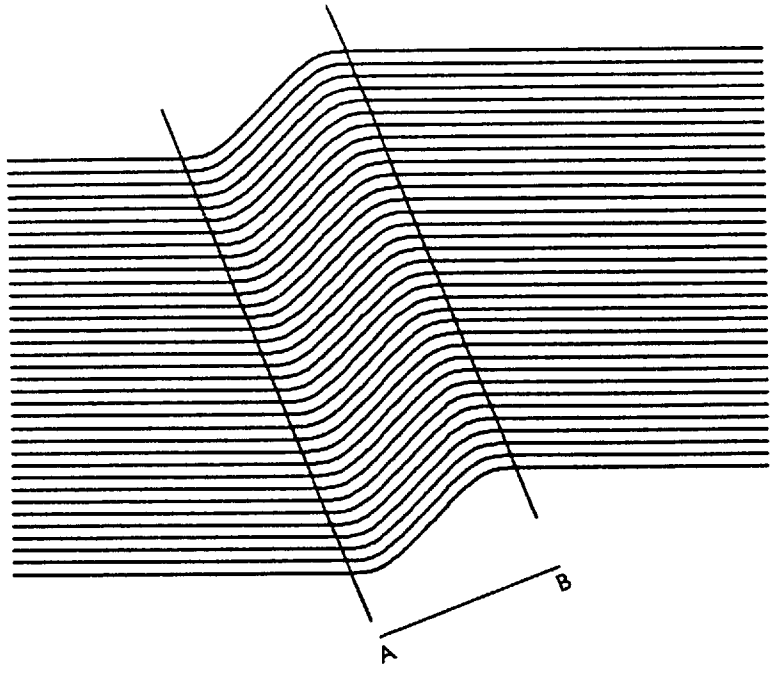


Figure 2.34 B

Initial rotation domain orientation, θ_o = 30°
Finite rotation domain orientation, θ_f = 25.5°

Deformation increment 100
Finite strain in the external foliation =0.1



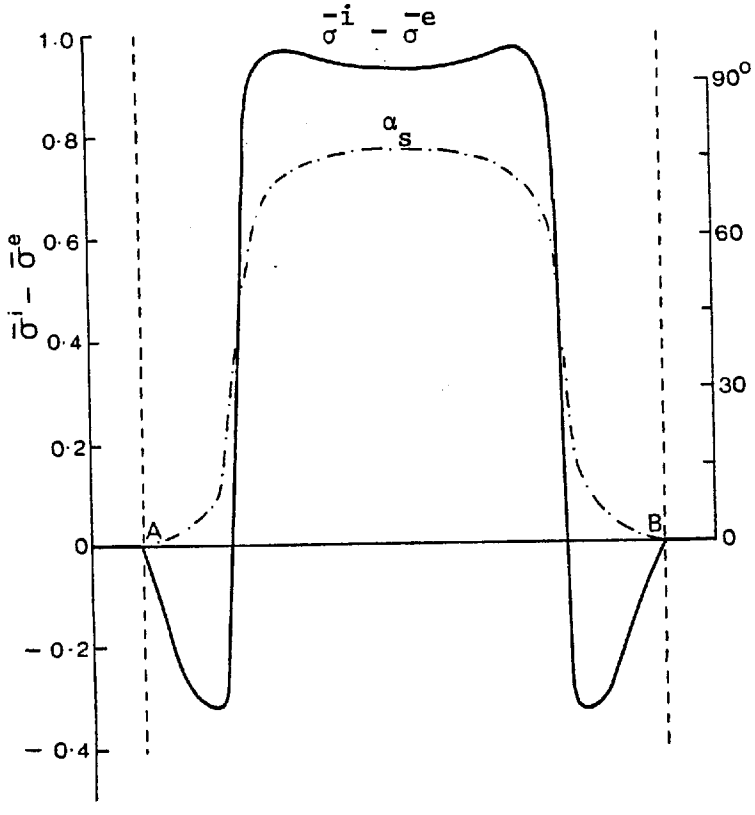


Figure 2.34 C

Initial rotation domain orientation, θ_o = 30°
Finite rotation domain orientation, θ_f = 21.3°

Deformation increment 200
Finites strain in the external foliation = 0.2

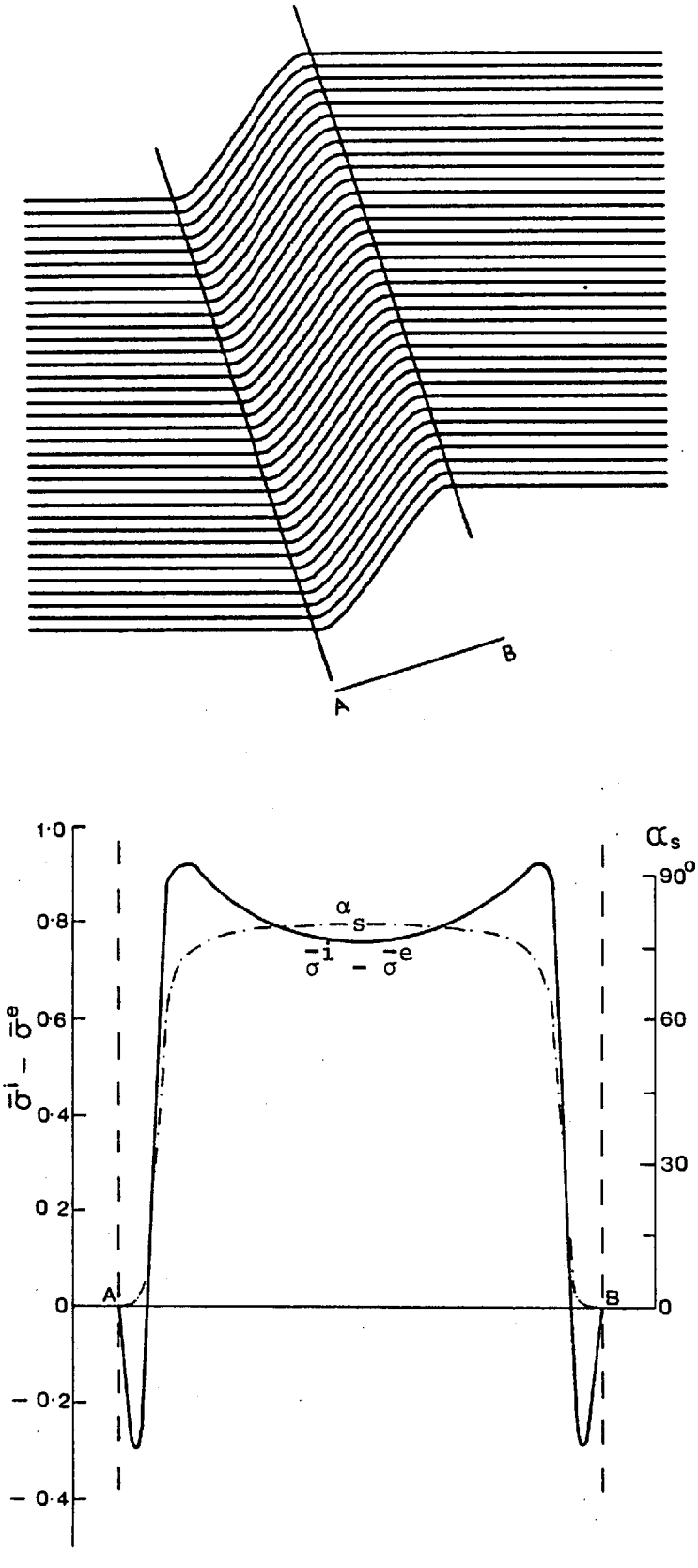
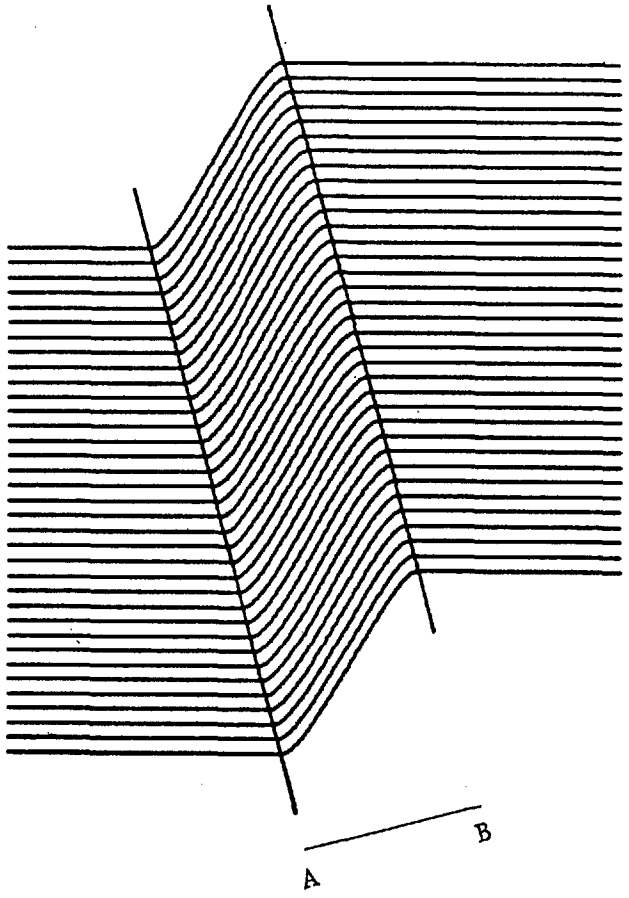


Figure 2.34 D

Initial rotation domain orientation, $_{o}$ = 30° Deformation increment 300

Finite rotation domain orientation, $_{f}$ = 17.7°

Finite strain in the external foliation = 0.3



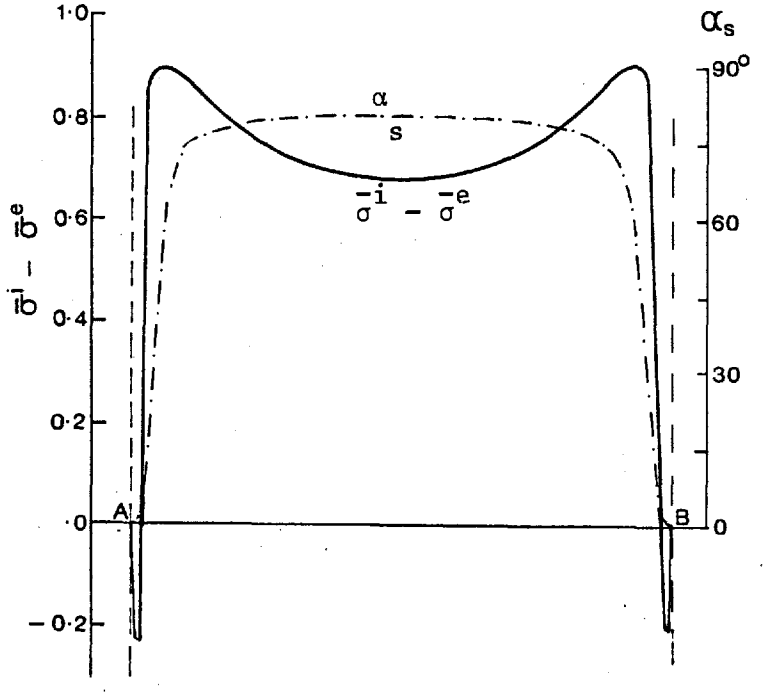


Figure 2.34 E

Initial rotation domain orientation, $\theta_o = 30^\circ$
Finite rotation domain orientation, $\theta_f = 14.7^\circ$

Deformation increment = 400
Finite strain in the external foliation = 0.4

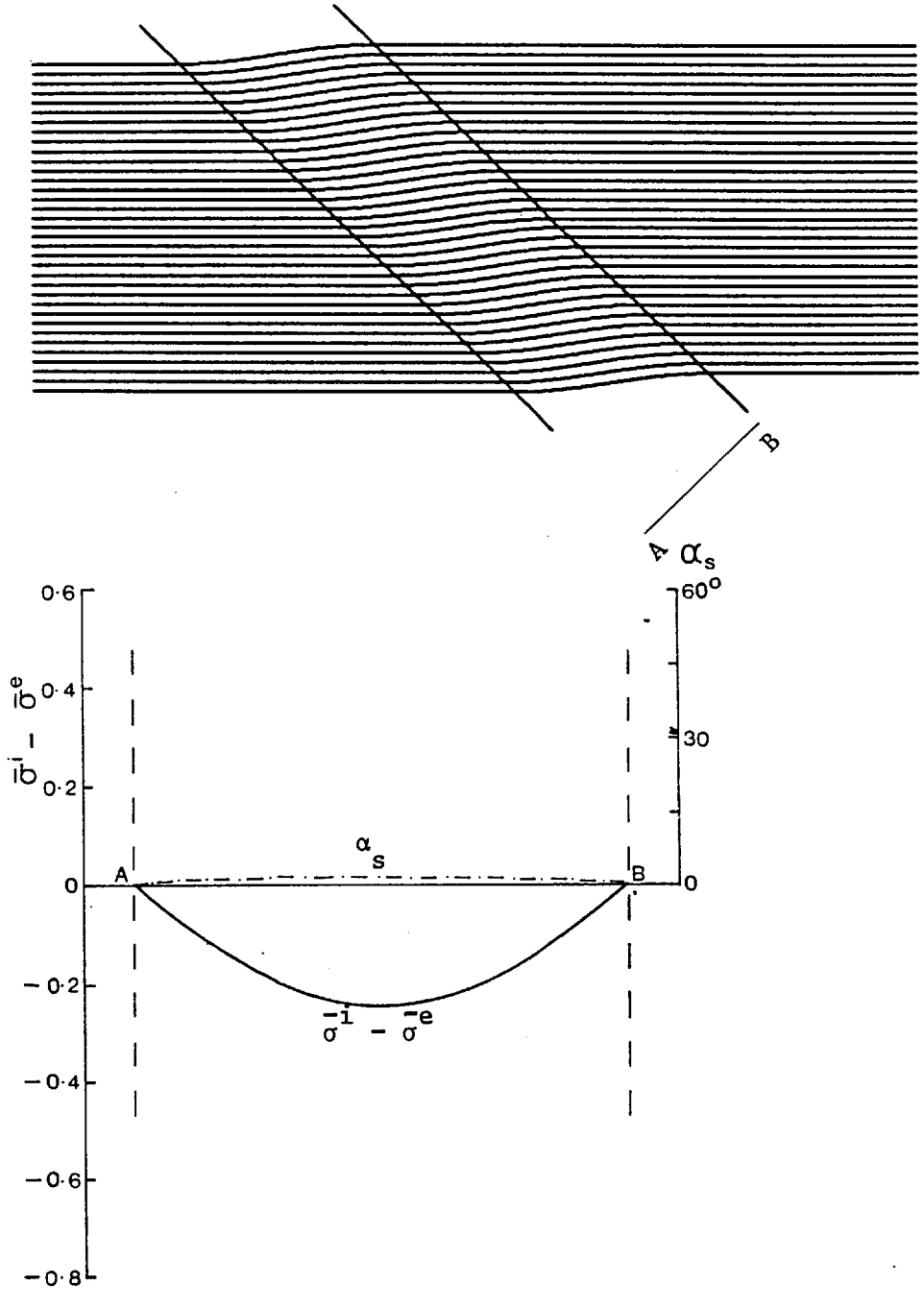


Figure 2.35 A

Initial rotation domain orientation, Θ_o = 45°
Finite rotation domain orientation, Θ_f = 45°

Deformation increment 0
Finite strain in the external foliation = 0.0

Anisotropy ratio, N/Q = 5.0

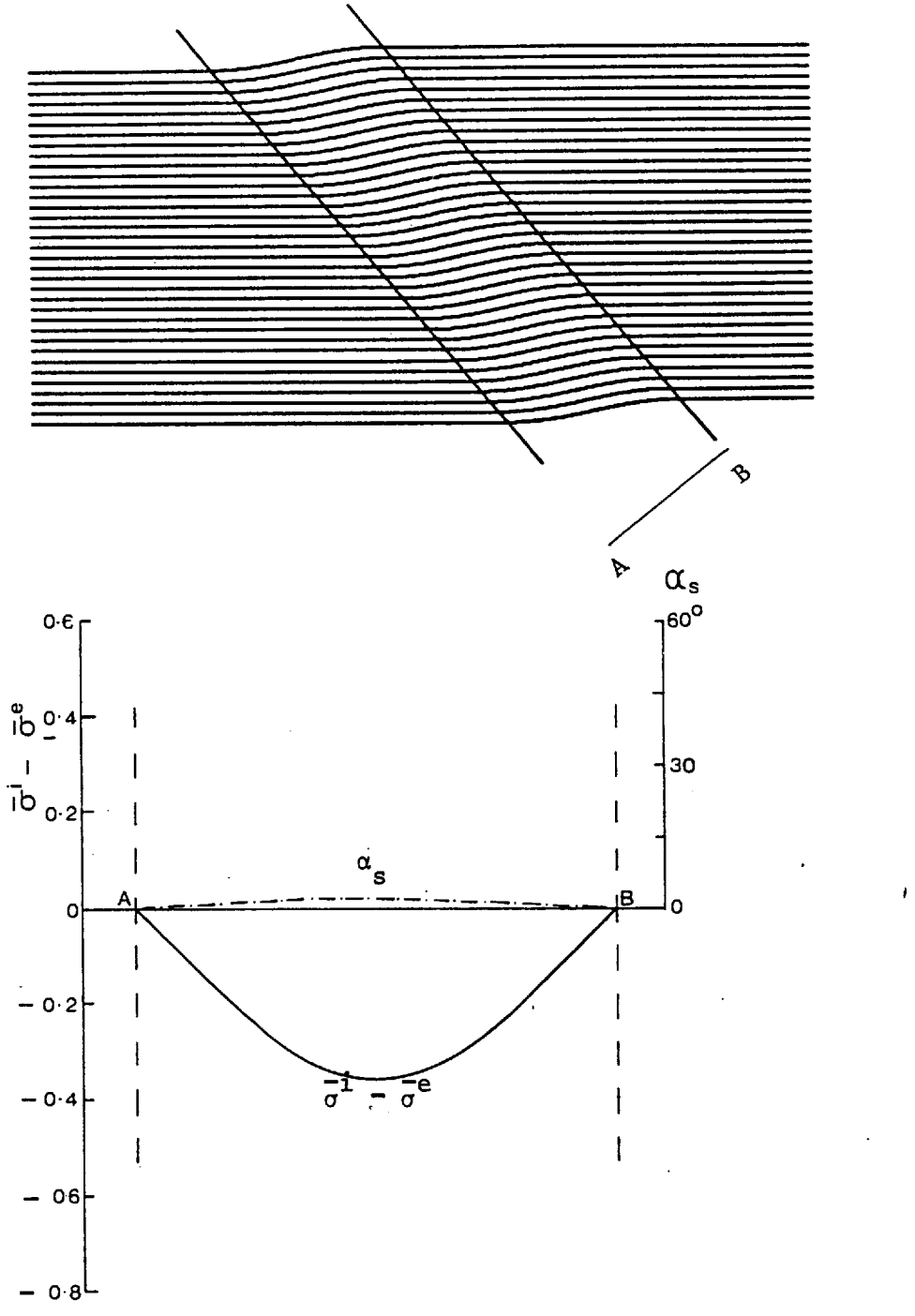


Figure 2.35 B

Initial rotation domain orientation, $\Theta_o = 45^o$
Finite rotationdomain orientation, $\Theta_f = 39.6^o$

Deformation increment 100
Finite strain in the external foliation = 0.1

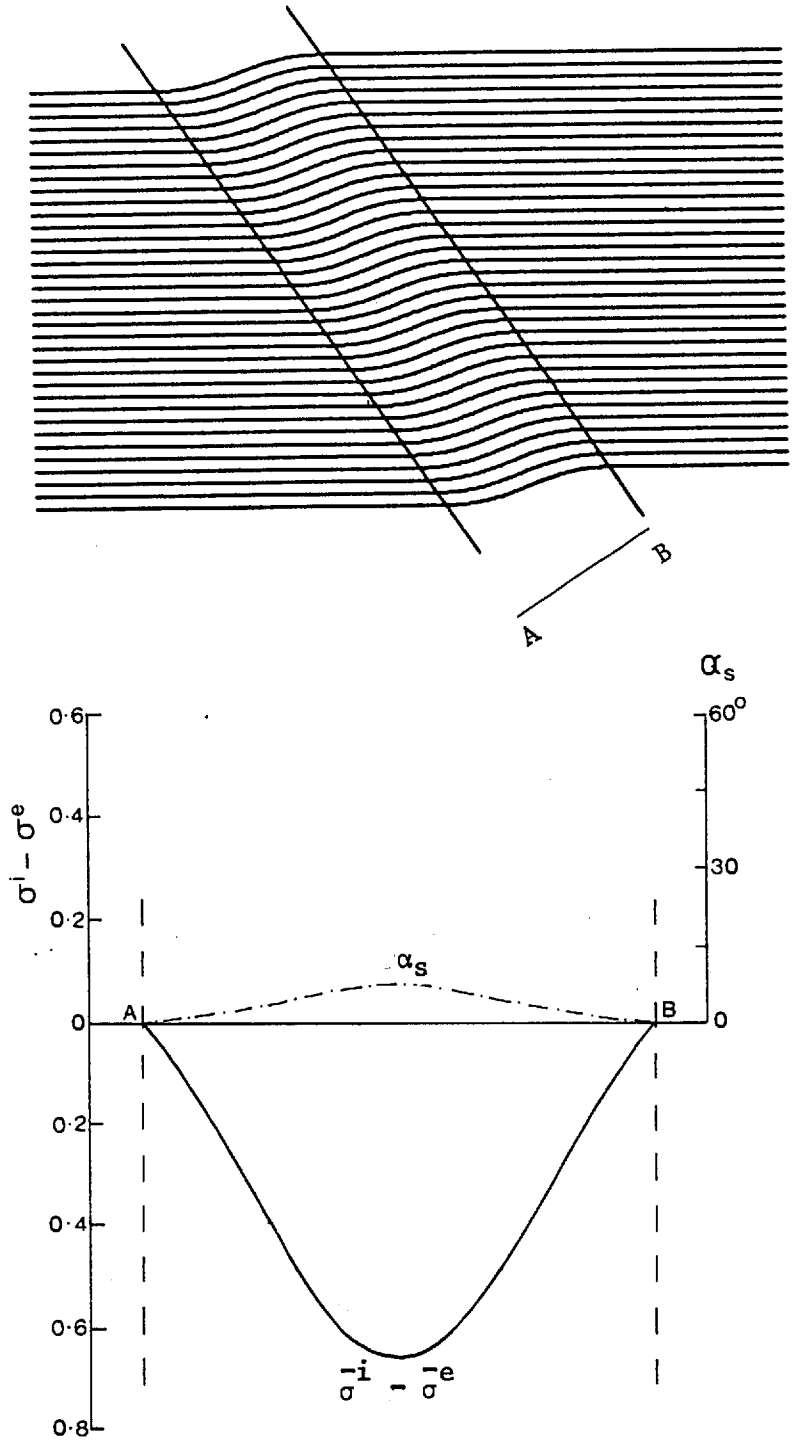


Figure 2.35 C

Initial rotation domain orientation, Θ_o = 45°
Finite rotation domain orientation, Θ_f = 34.1

Deformation increment 200
Finite strain in the external foliation = 0.2

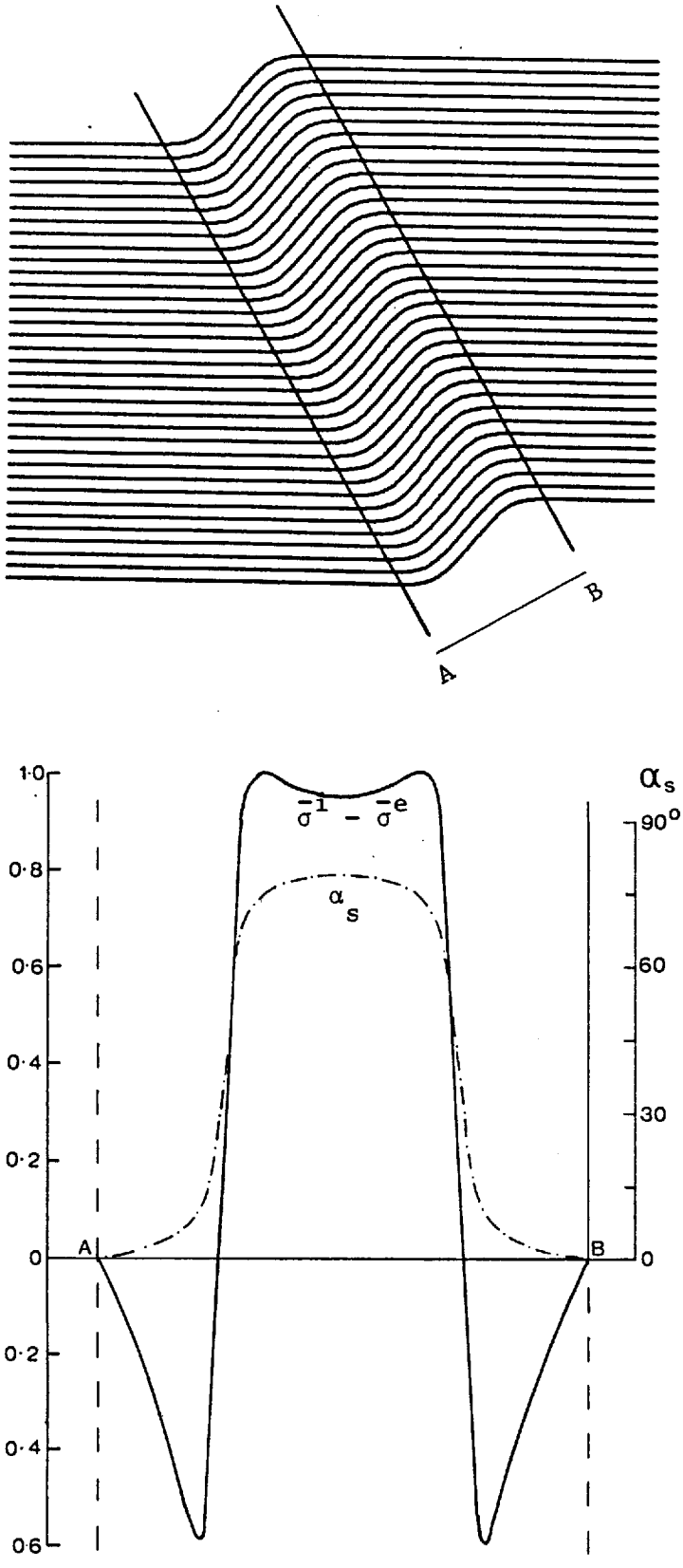


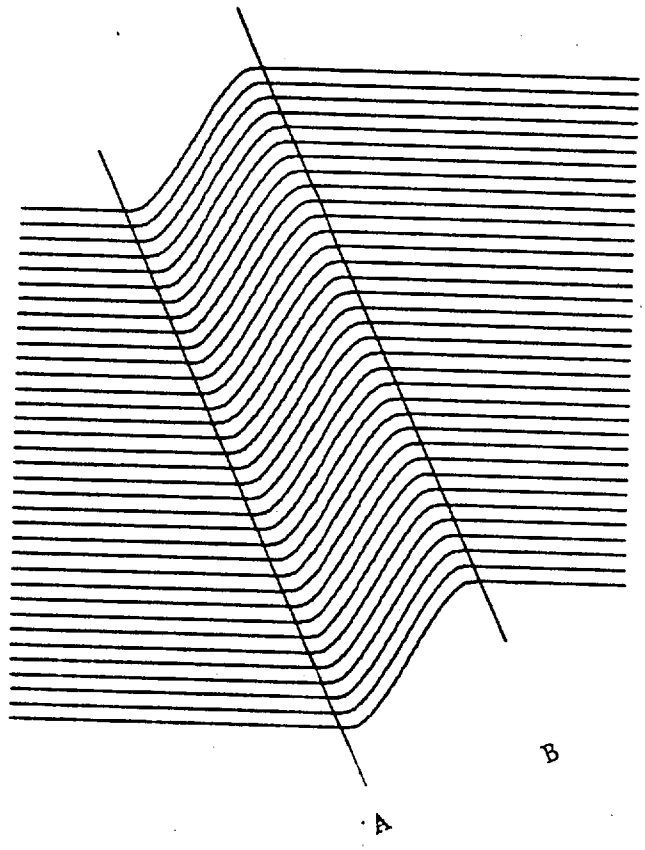
Figure 2.35 D

Initial rotation domain orientation, $\theta_o = 45^o$

Finite rotation domain orientation, $\theta_f =$

Deformation increment 300

Finite strain in the external foliation = 0.3



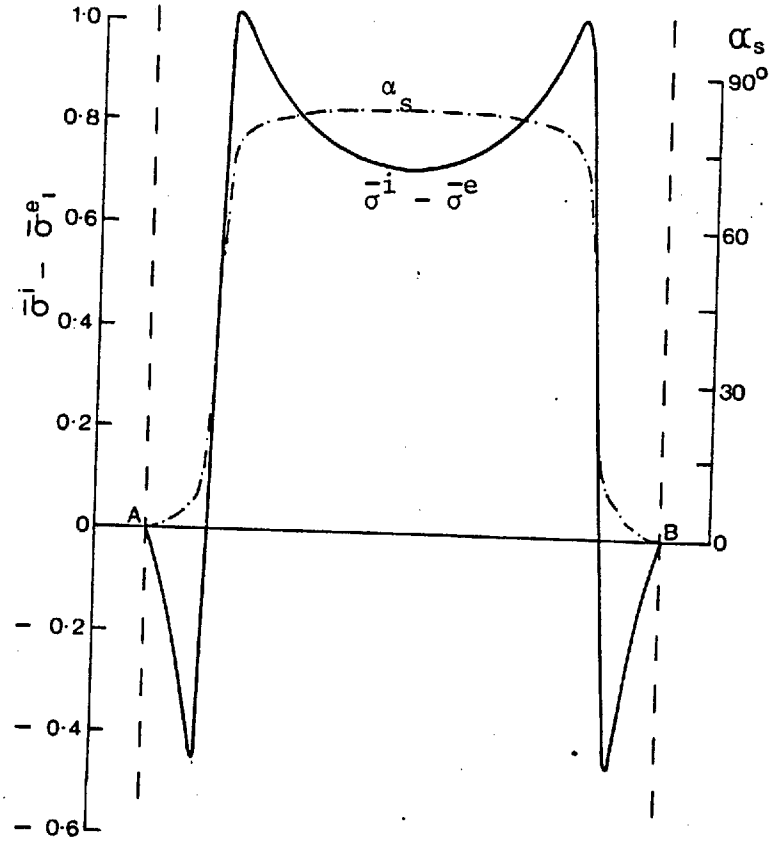


Figure 2.35 E

Initial rotation domain orientation, $\theta_o = 45^o$

Finite rotation domain orientation, $\theta_f = 24.4^o$

Deformation increment 400

Finite strain in the external foliation = 0.4

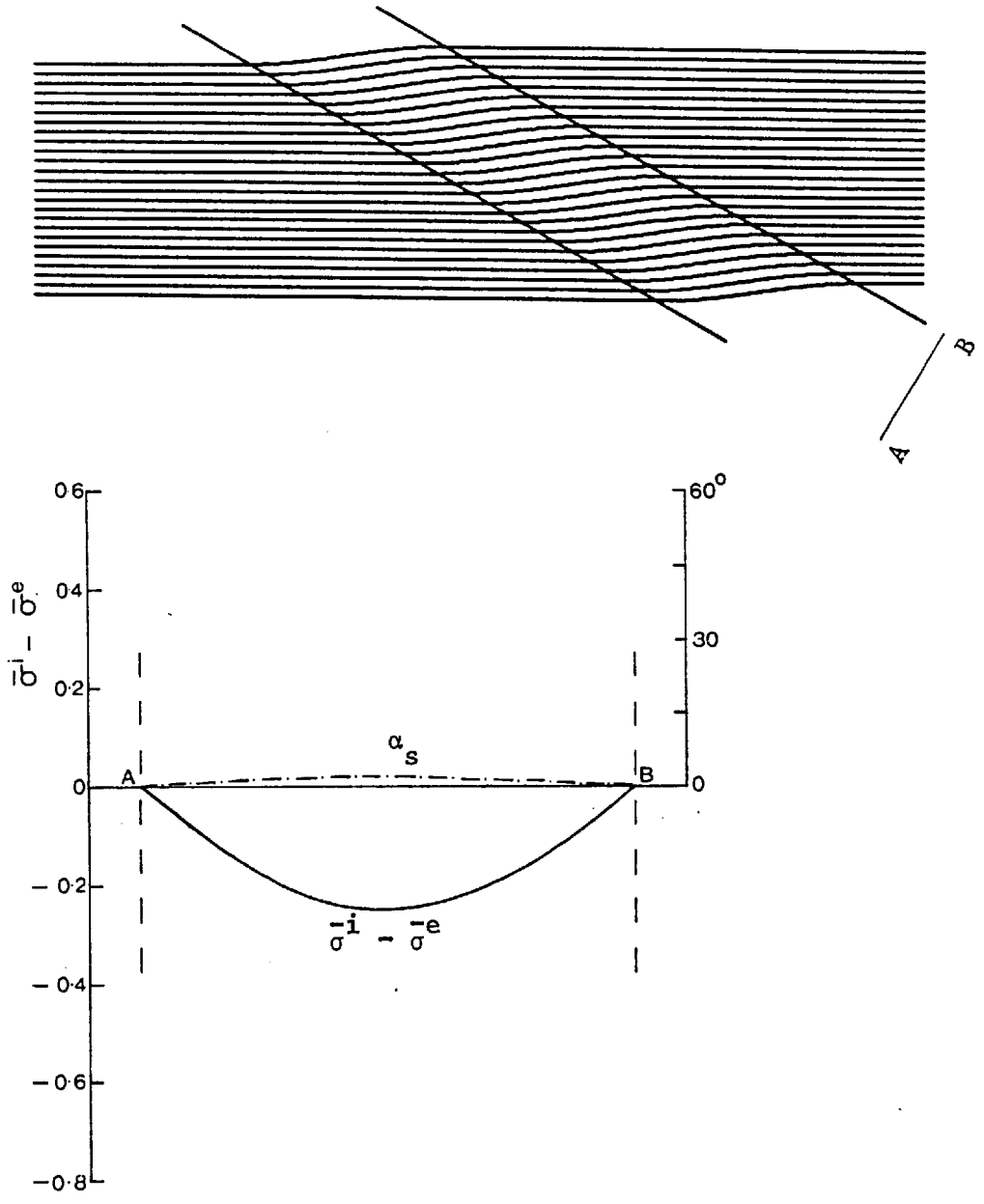


Figure 2.36 A

Initial rotation domain orientation, $\theta_o = 60^o$
Finite rotation domain orientation, $\theta_f = 60^o$

Deformation increment 0
Finite strain in the external foliation =0.0

Anisotropy ratio, N/Q = 5.0

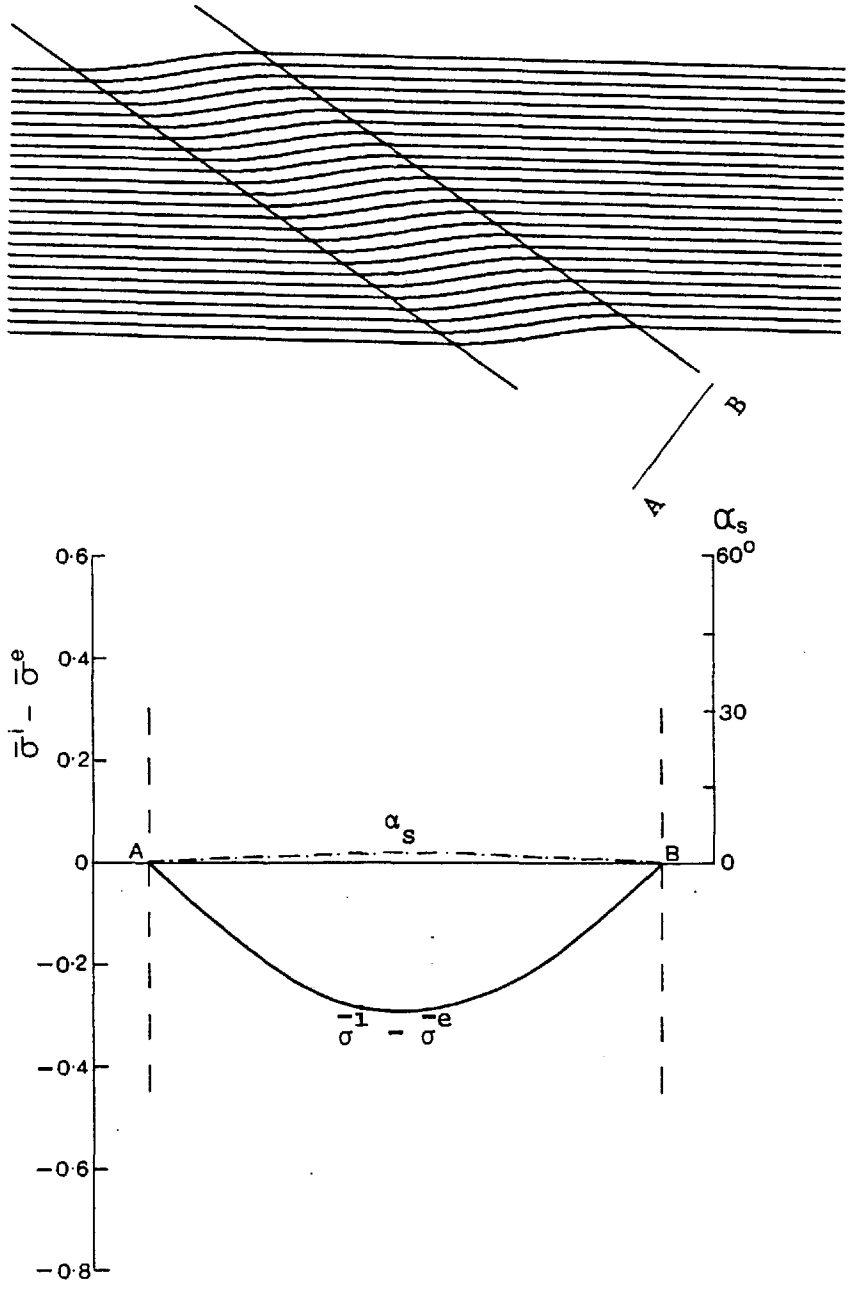


Figure 2.36 B

Initial rotation domain orientation, θ_o = 60°
Finite rotation domain orientation, θ_f = 55.1°

Deformation increment 100
Finite strain in the external foliation =0.1

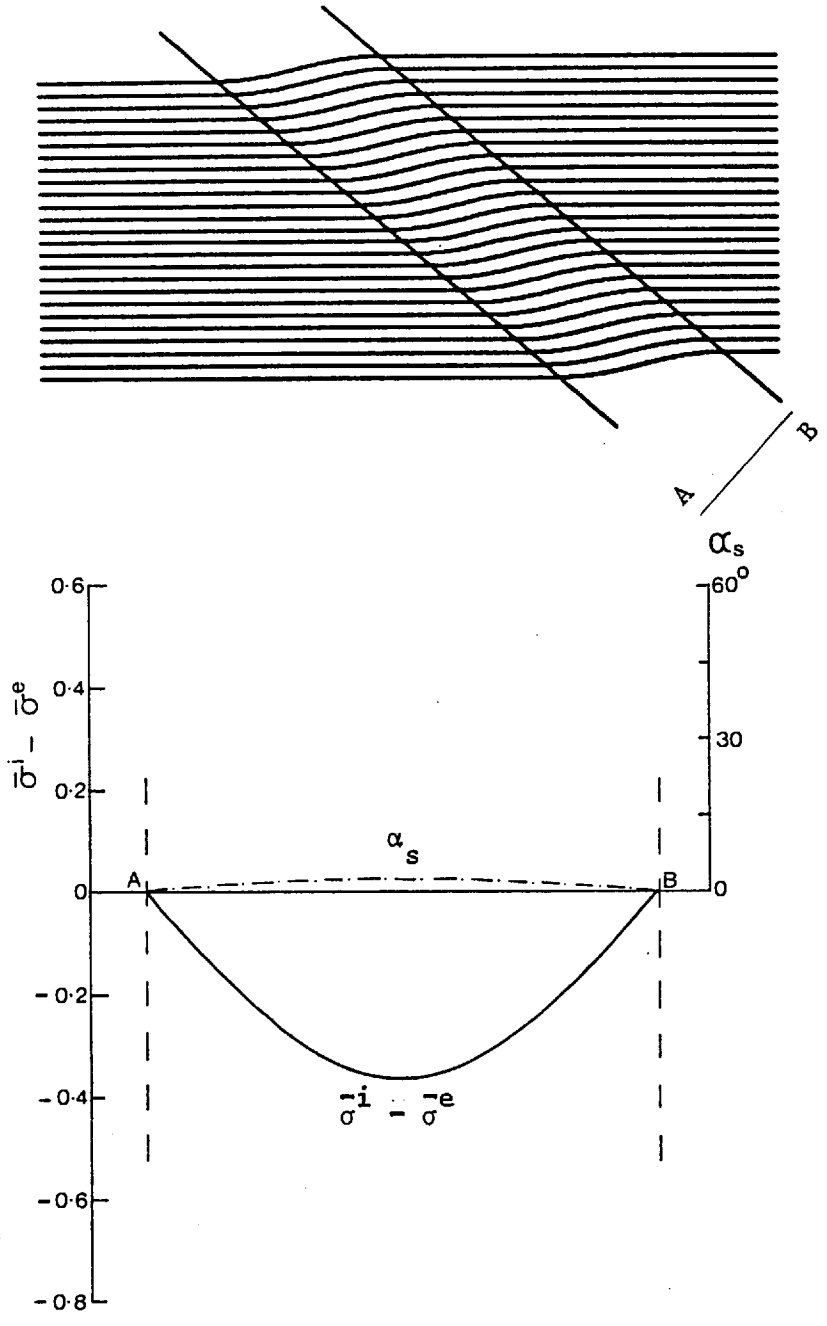


Figure 2.36 C

Initial rotation domain orientation, Θ_o =60°
Finite rotation domain orientation, Θ_f = 49.5°

Deformation increment 200
Finite strain in the external foliation =0.2

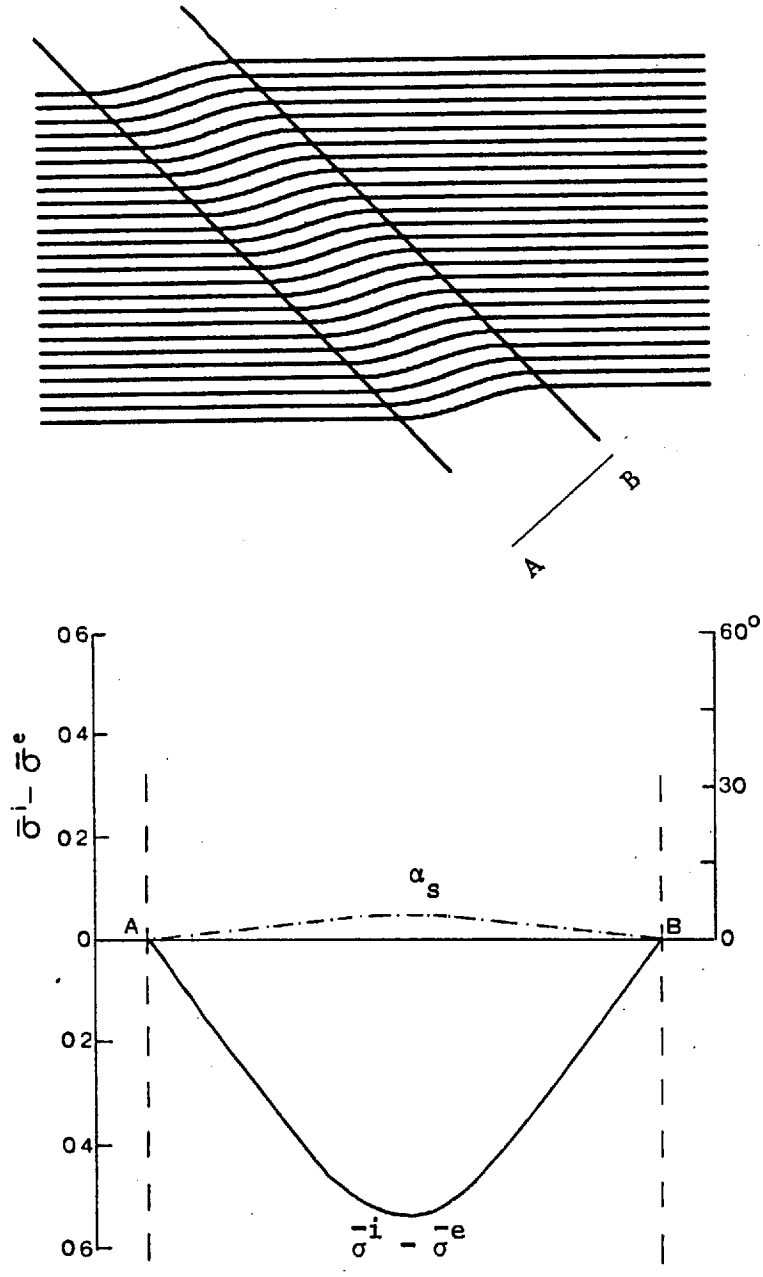
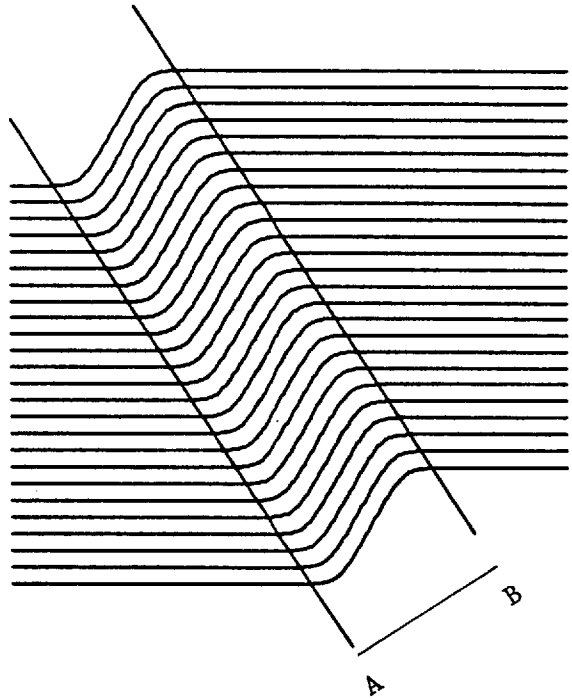


Figure 2.36 D

Initial rotation domain orientation, θ_o = 60°
Finite rotation domain orientation, θ_f = 43.8°

Deformation increment 300
Finite strain in the external foliation = 0.3



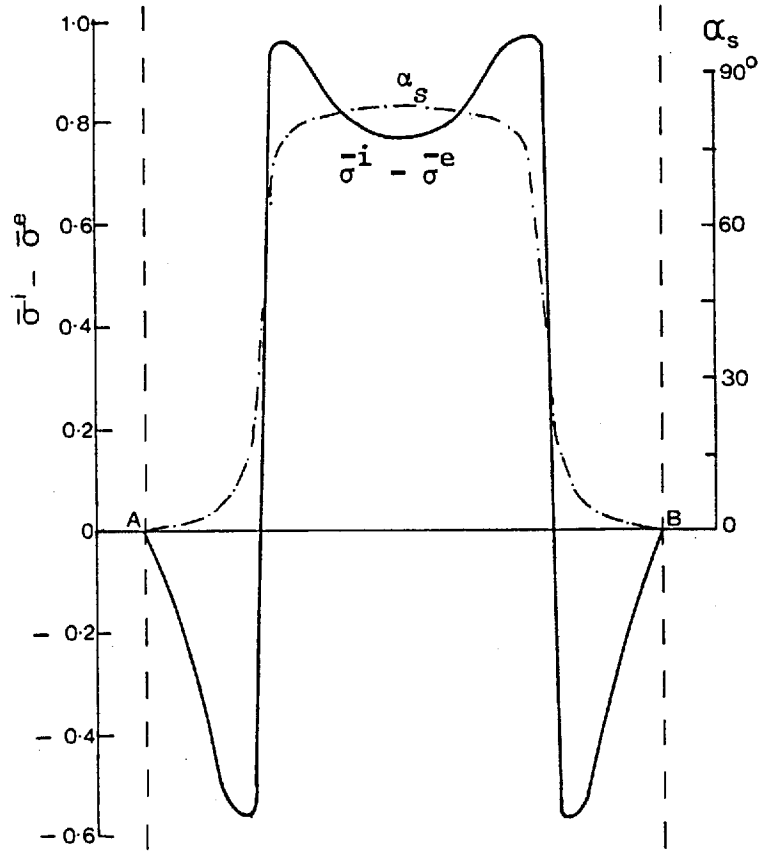


Figure 2.36 F

Initial rotation domain orientation, $\Theta_o = 60^o$
Finite rotation domain orientation, $\Theta_f = 32.8^o$

Deformation increment 500

Finite strain in the external foliation = 0.5

towards the boundaries of the rotation domain - fig. 2.33 D, E. The state of stress within this expanding central zone also becomes more uniform as the attitude of the internal foliation begins to stabilise and as the structure becomes increasingly angular. Eventually, the zone of relatively tensile mean stress becomes confined to narrow strips along the angular hinge zones and the boundaries of the rotation domain become sites of a significant gradient in stress orientation and magnitude. During these later stages of deformation, the maximum principle compressive stress is oriented at a high angle to the plane of internal foliation throughout almost the whole rotation domain. There is a marked change, at the domain boundaries, in the line of action of σ_1 trajectories from a position sub-normal to foliation within the rotation domain to a position parallel to foliation in the external foliation.

The stages in development of internal stress conditions noted in the preceeding paragraphs can be recognised in each of the computer finite deformation sinulations shown in figs. 2.33 to 2.36 ($\omega_o > 0$) It should be noted that, if a structure were to contain fluids which could migrate through the structure under a mean stress gradient, then an oblique rotation domain would tend to act as a "fluid pump". During the initial phase of low internal mean stress conditions, fluids would tend to be drawn into the rotation domain. Subsequently, fluids would be expelled from the domain under a reversed mean stress gradient.

CHAPTER 3

3.1 INTRODUCTION

The rotation domain analysis of Chapter 2 gives rise to a number of important predictions about the physical phenomena which may contribute to the finite development of certain types of symmetric and asymmetric folds in uniformly bedded or foliated geological systems. If the analysis is to be applied to natural deformations, however, it is essential to appreciate the implications of the various simplifying assumptions that are built into the analysis and to consider the geological validity of these assumptions. The main assumptions concern:

(i) The use of a homogeneous anisotropic continuum as a model for the behaviour of a foliated or layered geological system.

(ii) The symmetry of the externally applied stresses with respect to a structure.

(iii) The nature of the initial and finite geometry of a structure.

3.2 THE USE OF A HOMOGENEOUS ANISOTROPIC CONTINUUM AS A MODEL FOR A LAYERED OR FOLIATED GEOLOGICAL SYSTEM

The assumption of equivalence between the behaviour or stress response of a viscous anisotropic continuum and that of a discretely layered or foliated viscous material is fundamental to the analysis. The analogy is obviously valid only if the incremental response to stress of an element of the homogeneous continuum is an accurate reflection of the equivalent macroscopic response of a defined element of foliated or layered material.

3.2.1 STATISTICAL HOMOGENEITY

The homogeneous anisotropic continuum analogy, and therefore the analysis, can only be applied to geological materials which have the property of statistical homogeneity. The concept of statistical homogeneity in a geological context has been discussed by Turner and Weiss

(1963, pp. 16 to 17) and by Cobbold et al., (1971). Multilayered materials are, by definition, heterogeneous at the level of individual layer components. However, such materials can be considered statistically homogeneous if their physical characteristics are uniform throughout a large, representative body of the material, containing a substantial number of layer units. In the context of the rotation domain analysis, this means that the whole body of the layered material containing the defined structure must be macroscopically uniform, each defined element of the rotation domain must contain a large number of effective layer units and the thickness of individual units must be small in comparison to width of the structure. Examples of natural, anisotropic geological materials or systems which can be considered as statistically homogeneous include:

(i) Thick monotonous sequences of well bedded sedimentary rocks - sandstone/greywacke/shale alternations/turbidites; uniform limestone/shale alternations; chert/shale alternations, etc. Laubscher (1976), for example, has suggested that the Mesozoic sedimentary sequence of the Jura region "may to a first approximation, be compared to a homogeneous orthotropic medium".

(ii) Uniform geological materials with a planar mineral fabric such as slates, phyllites, schists, etc.

3.2.2 EFFECT OF BENDING RESISTANCE WITHIN LOCALLY DEFINED FOLIATION ELEMENTS

It was emphasized, in the derivation of the rotation domain analysis, that the response equations for a continuum element do not include terms which would reflect the individual and combined bending resistance of "stiff" or competent layer components within an equivalent layered or foliated material element, i.e. the homogeneous anisotropic continuum has no internal resistance which is specifically related to bending deformation. It was shown in chapter 1 that Biot (1965a) amended his incremental internal buckling analysis, based initially on the anisotropic continuum analogy, to quantify the effect of this resistance term on the behaviour of a simple two component multilayer. In a later paper Biot (1966) presented a more elegant and rigorous analysis of the influence of internal bending resistance on the incremental response of an element of a homogeneous anisotropic continuum by using the

complex concept of couple stresses. It would, however, be extremely difficult to incorporate this approach into a finite deformation analysis of the type discussed in this thesis.

The influence of competent component bending resistance on the incremental and finite deformation of structures will decrease with a decrease in the thickness of individual competent laminae with respect to the total size of a structure. For this reason, the predictions of the rotation domain analysis and the finite fold growth simulations illustrated in figs. 2.12 to 2.16 can be applied, with most confidence, to finely laminated geological systems with fold wavelength to laminar thickness ratios of 100 : 1 or more. The most obvious effect of an increase in the relative thickness of individual laminae on finite fold development would be an increase in the width of fold hinge regions relative to the span or wavelength of a structure. This has been demonstrated by Bayly (1974) for a simple model of the finite development of chevron folds in a two component, viscous multilayer, based on energy considerations.

Increase in the relative contribution of competent component bending resistance to the finite development of structures in uniform layered or foliated systems favours the development of more rounded fold profiles. As has been shown in the rotation domain analysis, mechanical anisotropy and the finite effects of rotational instability favour the development of distinctly angular fold profiles. The relative influence of each effect on the finite geometry of a fold will be reflected in the degree of angularity of the structure.

3.2.3 EFFECT OF CHANGE IN THE VOLUME OF LOCALLY DEFINED FOLIATION ELEMENTS

Probably the most critical assumption of the analysis is that representative elements of a particular structure deform at constant macroscopic volume. This assumption is essential if the constant volume continuum equations 1.16 and 1.17 are to be used. There are in fact a number of geologically important processes which could operate in natural layered or foliated materials to invalidate this condition. If the results of the rotation domain analysis are to be used as a basis for understanding the finite development of natural structures then the influence of these processes must be taken into account.

Once the possibility of change in the macroscopic volume of defined foliation elements is introduced into the analysis, the problem of quantifying the finite development of structures becomes far more complex. In order to approach this problem it is necessary to answer a number of questions.

(i) What is meant by macroscopic volume change of foliation elements in the context of the analysis?

(ii) What kind of processes might produce such volume changes in natural foliated or layered systems?

(iii) Is there any way to quantify the effect of volume change on the incremental response equations derived in chapter 2?

(iv) How would the possibility of volume change affect the quantitative predictions of the rotation domain analysis and the finite response of a particular structures to externally applied stress?

The first two questions will be considered with reference to the hypothetical structure illustrated in fig. 3.1. This figure is intended to illustrate how macroscopic volume change of defined, domain parallel foliation elements (width d in the undeformed state) could be expressed in the hinge and limb regions of a kink-like asymmetric fold. at a finite stage in the development of internal foliation rotation. For the purpose of this discussion it has been assumed that deformation and foliation rotation are confined within the boundaries of the rotation domain. It will be shown later in this section that this is only possible if change in the volume of the rotation domain occurs. A series of detailed views (I, II, III, IV) showing local deformation in the region of the initially defined foliation elements are included in fig. 3.1 to illustrate how change in the volume of these elements could be expressed in two idealised types of multilayered materials.

Two component multilayer (I, II)

The first type of idealised multilayer to be considered is made up of regular alternations of competent (unshaded) and incompetent (shaded) laminae. If there is a significant contrast between the strength or competence of the two components then the most efficient mechanism of element volume change which could operate in such a system is the

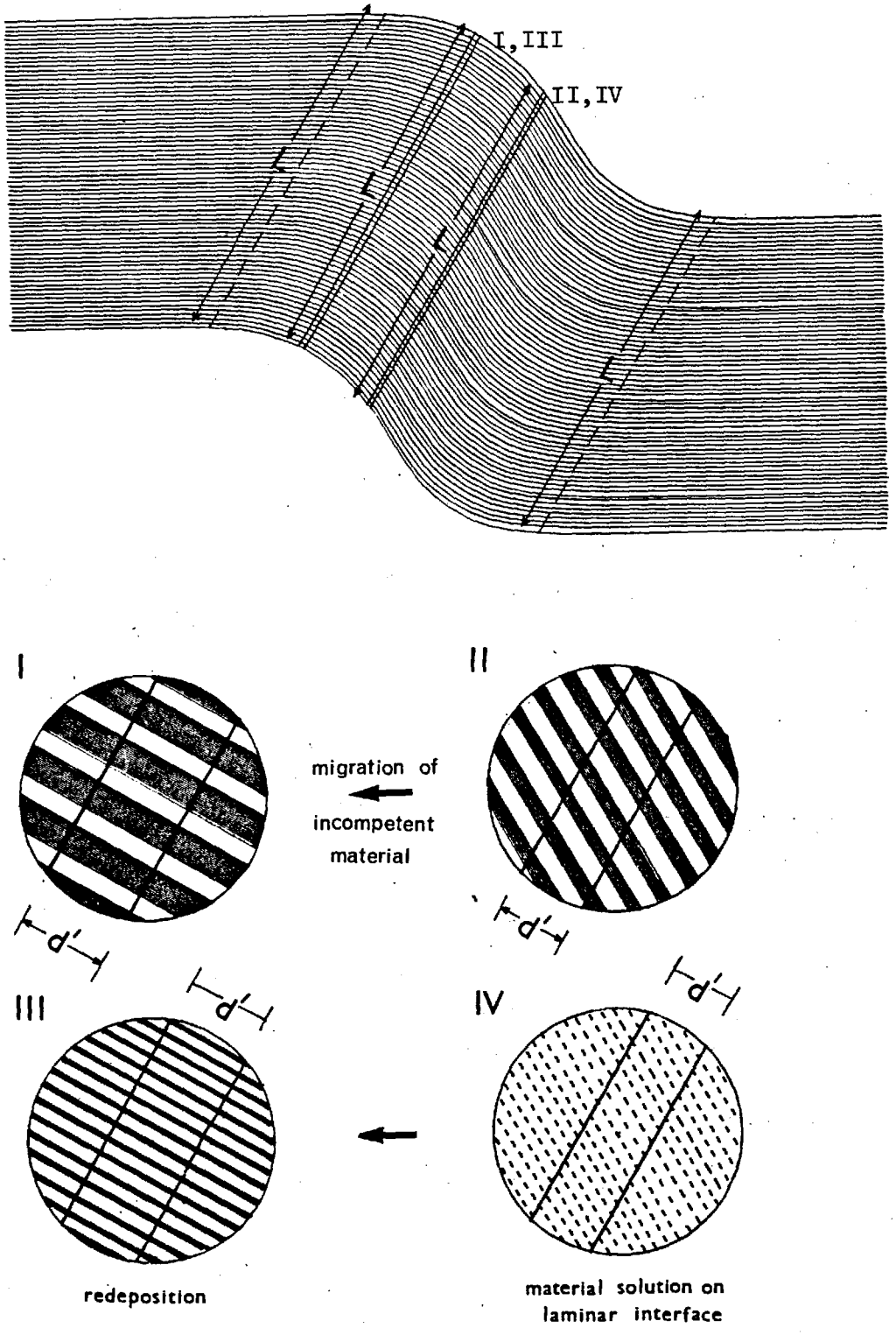


Figure 3.1 See text for details

transfer of incompetent material from element to element within a structure. Transfer of weak material out of a particular element will produce a macroscopic volume decrease expressed as a decrease in the profile area of that element; transfer of weak material into an element will produce a volume increase. In the detailed sketches I and II shown in fig.3.1 such processes are shown to produce a local increase in element volume within the hinge regions (I) and a decrease in volume of foliation elements within the central zone of the rotation domain (II). It should be noted that incompetent material migration is equally effective in producing volume increase or volume decrease provided, of course, that sufficient incompetent material is available for transfer. Continued volume reduction by this process cannot proceed once the competent laminae are brought into contact.

"Card deck" multilayer

The second type of idealised multilayer is made up of a uniform sequence of identical laminae in direct contact. Such a material would have the laminar characteristics of a 'card deck' with layer anisotropy reflected in localised slip between adjacent laminae. In this type of system incompetent material migration is not available as a mechanism of local element volume change. However, macroscopic increase in the volume of defined foliation elements will occur if partings or voids develop between individual laminae. This mechanism, which will be called delamination, is shown in fig. 3.1 to operate in the hinge region of the structure (III). A complimentary volume decrease mechanism in a card deck multilayer (IV) must involve the indirect removal of material. This could be achieved, in a natural layered system, by diffusion or the removal of soluble material in solution (pressure solution). It should be noted that, since the mechanism which controls the rate of volume gain is different from that which controls the rate of volume loss, it is unlikely that the two mechanisms would occur at equivalent, compensating rates within a particular structure.

Although the phenomena illustrated in fig. 3.1 may play important roles in the development of natural structures, it would be extremely difficult to extend the continuum approach, used in the rotation domain analysis, to incorporate these effects in any realistic, quantitative model. This would require the development of very complex,

anisotropic compressibility matrices to model, macroscopically, specific volumetric strain mechanisms such as incompetent material migration, delamination, etc. It is possible, however, to use the constant volume continuum equations derived in chapter 2 to understand how the anisotropic properties of layered or foliated materials tend to promote the development of zones of macroscopic dilation or volume loss in symmetric and asymmetric similar folds and to determine the relationship between such zones in specific structures. It can also be shown that the type of effects identified in fig.3.1 may significantly increase the rate of amplification of structures. In order to do this it is necessary to examine the modifications which local volumetric strain will introduce into the macroscopic strain compatibility conditions which were derived for constant volume deformation in chapter 3.

Modification of strain compatibility conditions introduced by element volumetric strain

It will be recalled from chapter 2 that a number of basic geometrical assumptions were used which make it possible to investigate the incremental and finite response of a rotation domain to external stress in terms of the response of a series of narrow, domain parallel foliation elements. These assumptions are:

(i) The boundaries of the rotation domain remain plane and parallel throughout deformation although, in the case of an oblique rotation domain, they may rotate with respect to the plane of the external foliation.

(ii) There is no change in the profile geometry of successive foliation surfaces along the direction of the domain boundaries, parallel to the y coordinate direction.

Incremental deformation is referred to coordinate axes x and y which lie, respectively, normal to and parallel with, the rotation domain boundaries. By basing the analysis on this coordinate system it is possible to resolve the local incremental deformation of a structure into three incremental strain components which express the total incremental strain individual foliation elements (including representative, band parallel foliation elements within external foliation). These components are:

(i) a pure shear deformation, measured by the local increments in direct strain e_{xx} and e_{yy}

(ii) a simple shear deformation measured by the local increment in shear strain e_{xy}

(iii) a rotation of the element with respect to the external folition measured by the angular increment, $\Delta\theta$.

An attempt has been made in fig. 3.2 to illustrate the physical significance of these macroscopic strain components by identifying the separate effect of each component on the total deformation of representative elements of internal (i) and external (e) foliation in an oblique rotation domain with a non-uniform internal foliation orientation. The rotation domain analysis of chapter 2 is based on a series of conditions which place specific restrictions on the variation of these macroscopic strain components across a structure. These conditions can be expressed in terms of gradients in incremental strain (e_{ij}) or strain rate ($\dot{e}_{ij}$) along the x and y coordinate directions.

(i) No variation in any strain component can occur along the y coordinate direction

$$\frac{\partial e_{ij}}{\partial y} = 0$$

$$\frac{\partial \dot{e}_{ij}}{\partial y} = 0 \qquad \ldots\ldots 3.1$$

(ii) The incremental direct strain component e_{yy} must be uniform across the structure (constant from element to element) :

$$\frac{\partial e_{yy}}{\partial x} = 0$$

$$\frac{\partial \dot{e}_{yy}}{\partial x} = 0 \qquad \ldots\ldots 3.2$$

(iii) There is no constraint on the variation of the shear component of element deformation across the structure

$$\frac{\partial e_{xy}}{\partial x} \neq 0$$

$$\frac{\partial \dot{e}_{xy}}{\partial x} \neq 0 \qquad \ldots\ldots 3.3$$

Conditions (i), (ii) and (iii) apply even if changes in the volume of foliation elements occur during deformation. The most significant difference between the response of a structure under the contrasting conditions of constant volume deformation and change in element volume during deformation concerns the variation in the band normal direct strain component e_{xx}. If, as is assumed in chapter 2, deformation of foliation elements occurs at *constant* macroscopic volume, then:

$$e_{xx} + e_{yy} = 0$$

$$\dot{e}_{xx} + \dot{e}_{yy} = 0$$

Differentiating with respect to x :

$$\frac{\partial e_{xx}}{\partial x} + \frac{\partial e_{yy}}{\partial x} = 0 \quad ; \quad \frac{\partial \dot{e}_{xx}}{\partial x} + \frac{\partial \dot{e}_{yy}}{\partial x} = 0$$

And :

$$\frac{\partial e_{yy}}{\partial x}, \frac{\partial \dot{e}_{yy}}{\partial x} = 0 \rightarrow \frac{\partial e_{xx}}{\partial x}, \frac{\partial \dot{e}_{xx}}{\partial x} = 0$$

$\ldots\ldots$ 3.4

This condition is fundamental to the derivation of the constant volume rotation domain analysis and the equations listed in table 2.1 of chapter 2

If, however, the volume of defined foliation elements does change during an increment of deformation then:

$$e_{xx} + e_{yy} \neq 0$$

$$\dot{e}_{xx} + \dot{e}_{yy}$$

$$\frac{\partial e_{xx}}{\partial x} + \frac{\partial e_{yy}}{\partial x}$$

$$\frac{\partial \dot{e}_{xx}}{\partial x} + \frac{\partial \dot{e}_{yy}}{\partial x} \neq 0$$

In this case the basic geometric condition $\partial e_{yy}/\partial x = 0$ no longer implies the additional condition $\partial e_{xx}/\partial x = 0$ and a gradient in domain normal direct strain can develop across a structure.

i.e.

$$\frac{\partial e_{xx}}{\partial x} \neq 0$$

$$\frac{\partial \dot{e}_{xx}}{\partial x} \neq 0 \qquad \ldots\ldots 3.5$$

The macroscopic strain compatibility conditions 3.2 and 3.5 can be recognised in the idealised models illustrated in fig. 3.1 (I,II,III,IV) which incorporate geologically realistic mechanisms of element volume change. In constructing these models it has been assumed that deformation is restricted to the internal foliation between the boundaries of the rotation domain. If this is so, all components of strain and strain rate in the external foliation must be zero. In particular:

$$e^{e}_{yy} = 0$$

and

$$\dot{e}^{e}_{yy} = 0$$

The basic geometric conditions $\partial e_{yy}/\partial x = 0$ and $\partial \dot{e}_{yy}/\partial x = 0$ then imply

that :

$$e_{yy} = 0$$

$$\dot{e}_{yy} = 0$$

..... throughout the structure. These macroscopic strain compatibility conditions can be recognised in fig . 3.1 by the condition that the distance, L, between any two points measured along the y coordinate direction remains constant throughout deformation. In contrast, however, the conditions $\partial e_{xx}/\partial x = 0$ and $\partial \dot{e}_{xx}/\partial x \neq 0$ place no constraint on the local development of band normal direct strain e_{xx} and this is expressed in the models by local contraction or expansion in the width of individual foliation elements. ($d \rightarrow d'$). During an increment of deformation the macroscopic change in volume of an individual foliation element is given by:

$$\Delta V = e_{xx} + e_{yy}$$

For the particular condition of no deformation or dilation within the extremal foliation:

$$\Delta V = e_{xx} + e_{yy}$$

A finite increase in the volume of an initially defined foliation element is associated with an expansion in the width of that element ($d' > d$); a finite decrease in volume is associated with a finite decrease in width ($d' < d$).

It can be seen from this discussion that the complex mechanisms of local volumetric strain illustrated in fig. 3.1 can be expressed in terms of macroscopic strain by a relatively simple modification of the conditions of element to element strain compatibility derived for the constant volume rotation domain analysis.

(i) Constant volume deformation - the induced rate of band normal direct strain, $\dot{e}_{xx}$, within individual foliation elements must be constant across a structure and equal to the equivalent rate of resolved direct strain in the external foliation ($\partial\dot{e}_{xx}/\partial x = 0$)

(ii) Dilatational deformation - the induced rate of band normal direct strain, $\dot{e}_{xx}$, within individual foliation elements may vary across a structure and the rate developed within internal foliation elements need not be equal to the equivalent rate of resolved direct strain in the extremal foliation ($\partial\dot{e}_{xx}/\partial x \neq 0$). The degree to which internal and external direct strain rates $\dot{e}_{xx}$ are 'de-coupled' will depend on the efficiency of volume change as a mechanism of local deformation.

For reasons outlined in the introduction to this section, it is not possible to construct a quantitative rotation band model which incorporates in any realistic way the mechanisms of local volumetric strain shown in figs. 3.1 . The problem of volumetric strain can be approached, however, by considering the implications of a breakdown in conditions of band normal direct strain compatibility on the formulation of the rotation domain analysis. This can be achieved by investigating the incremental response of three contrasting rotation domain models (figs. 3.2A, B, C) to a compression parallel to the external foliation. In order to illustrate the differences in the conditions of direct strain compatibility which characterise the three models, the properties of the models are demonstrated in terms of an upright rotation domain ($\theta = 0^{o}$) with a uniform internal foliation orientation. The contrasting response of internal and external foliation is shown by the deformation of rectangular elements. The marker lines which define these elements are parallel to the analysis coordinates x and y in the undeformed state (fig. 3.2A (i), (ii) and (iii)). In order to clarify the discussion of the models the separate contribution of direct strains e_{xx} and e_{yy} (figs. 3.2 A(ii), B(ii), C(ii)) and shear strain e_{xy} (fig.3.2 A(iii), B(iii), C(iii)) to the total deformation of the initially defined rectangular elements is illustrated. The final configuration of the structures and the associated element deformation is shown in fig. 3.2A(iv), B(iv) and C(iv). The compatibility of internal and external strain components will be discussed in terms of incremental strains e_{ij} and strain rates $\dot{e}_{ij}$ although, for clarity, the deformations illustrated in fig.3.2

show large finite strain. It should be noted that an upright rotation domain has been used to demonstrate the properties of the models because this case is relatively simple to illustrate in diagrammatic form. The compatibility conditions which will be listed for each of the models also apply to corresponding models of an oblique rotation domain ($\theta > 0^{o}$). (In this case, strain and strain rates are referred to axes x and y which are oblique to the external foliation). A series of diagrams for an oblique domain, corresponding to those included in fig. 3.2 for an upright domain, would be more complex since they would include a rotation of element boundaries with respect to the external foliation. This would lead to unnecessary confusion in the description of the conditions of incremental strain compatibility.

Model A (fig. 3.2 A)

This model is constrained to deform under the strict compatibility conditions required by the rotation domain analysis of chapter 2. Material continuity is maintained across element boundaries during deformation and both internal and external foliation deform at constant volume. The conditions of strain compatibility across the structure can be expressed in terms of equality of internal and external strain and strain rate components.

Direct strain (fig. 3.2 A (ii))

$$e^{i}_{xx} = e^{e}_{xx}$$

$$\dot{e}^{i}_{xx} = \dot{e}^{e}_{xx}$$

$$e^{i}_{yy} = e^{e}_{yy}$$

$$\dot{e}^{i}_{yy} = \dot{e}^{e}_{yy}$$

Shear strain (fig. 3.2A (iii))

$$e^{i}_{xy} \neq e^{e}_{xy}$$

$$\dot{e}^{i}_{xy} \neq \dot{e}^{e}_{xy}$$

Figure 3.2 A

MODEL A

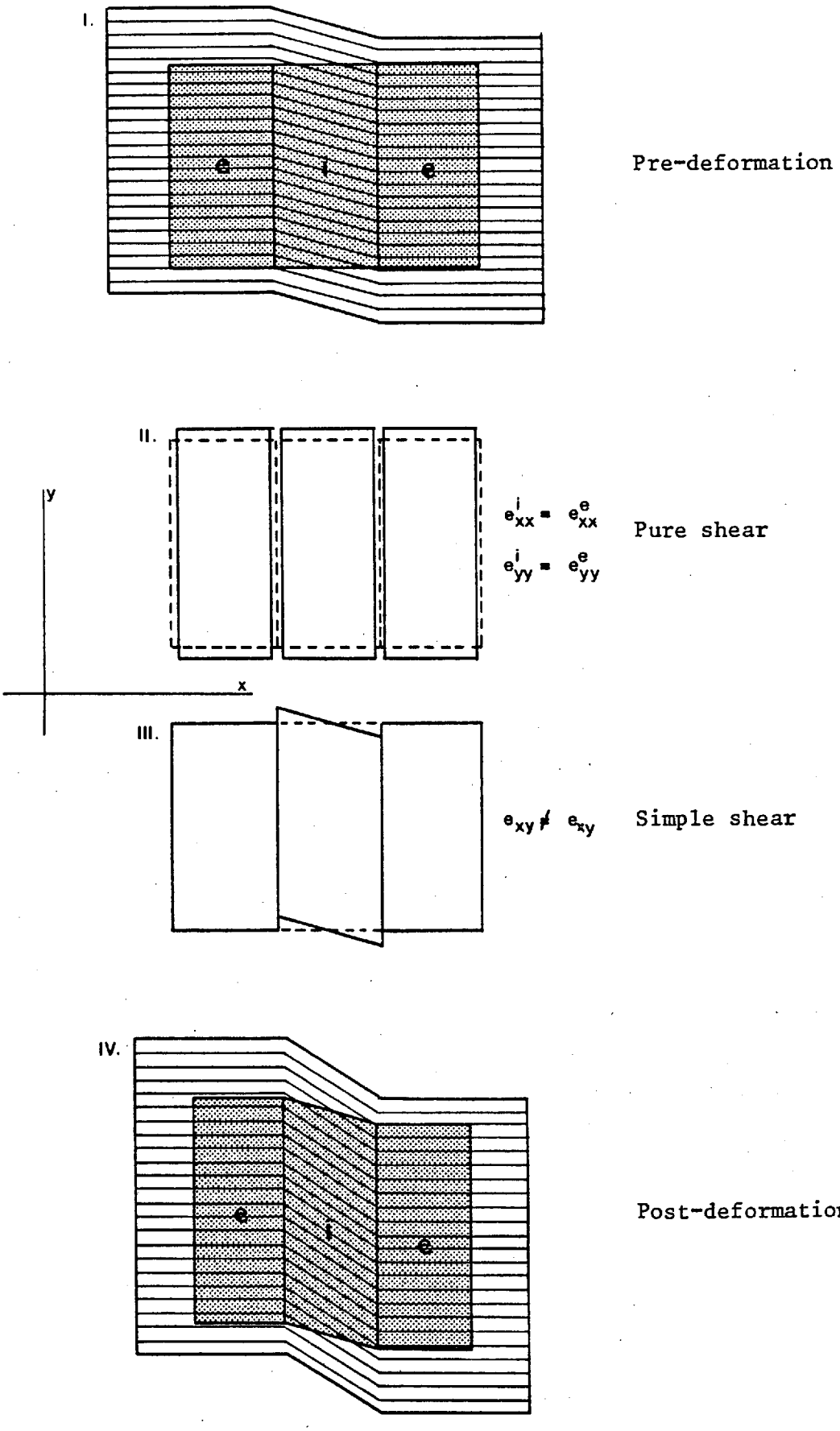
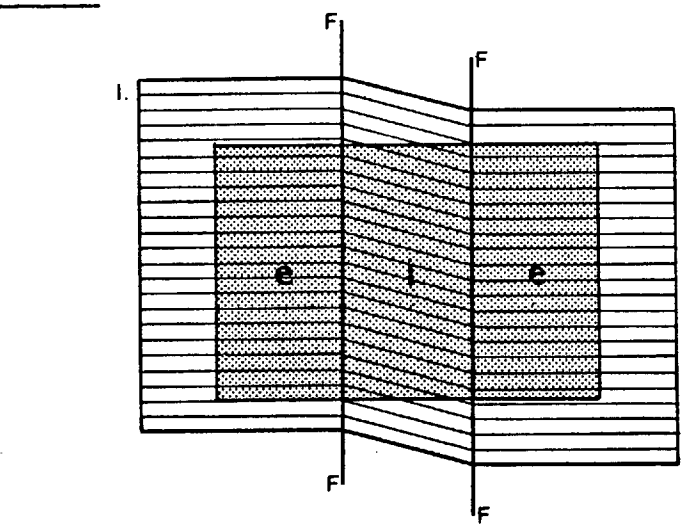


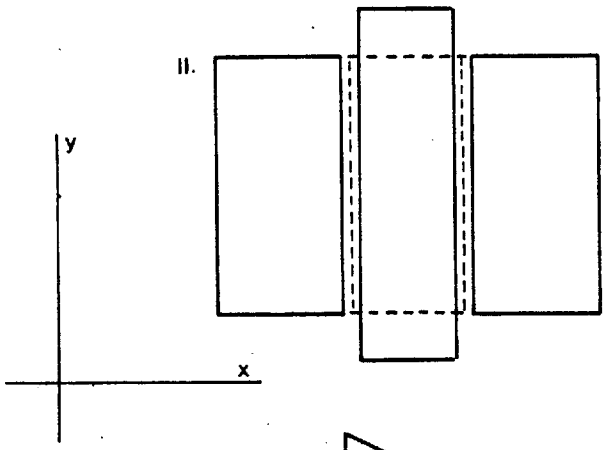
Figure 3.2 B

MODEL B



P

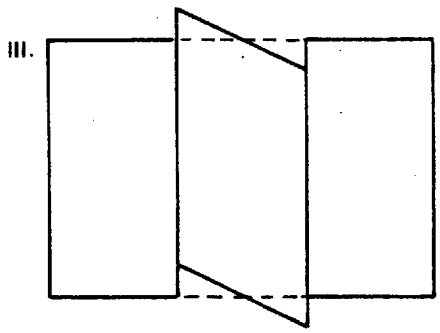
Pre-deformation



$e^i_{xx} \neq e^e_{xx}$

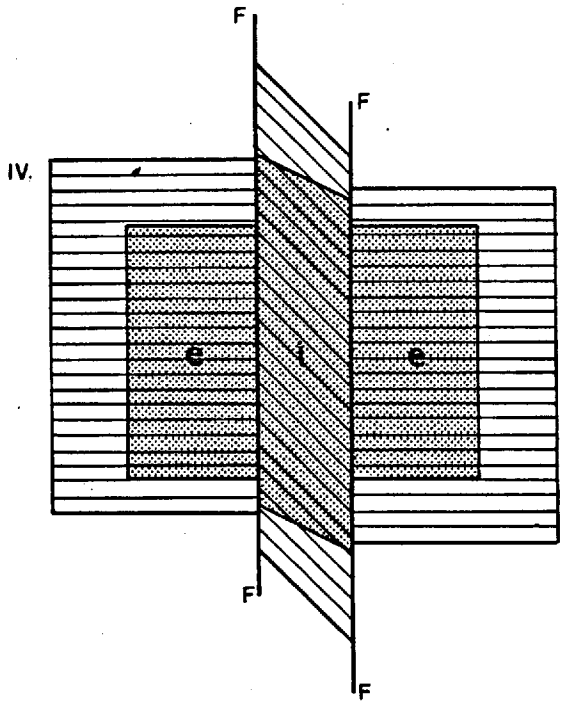
$e^i_{yy} \neq e^e_{yy}$

Pure shear



$e^i_{xy} \neq e^e_{xy}$

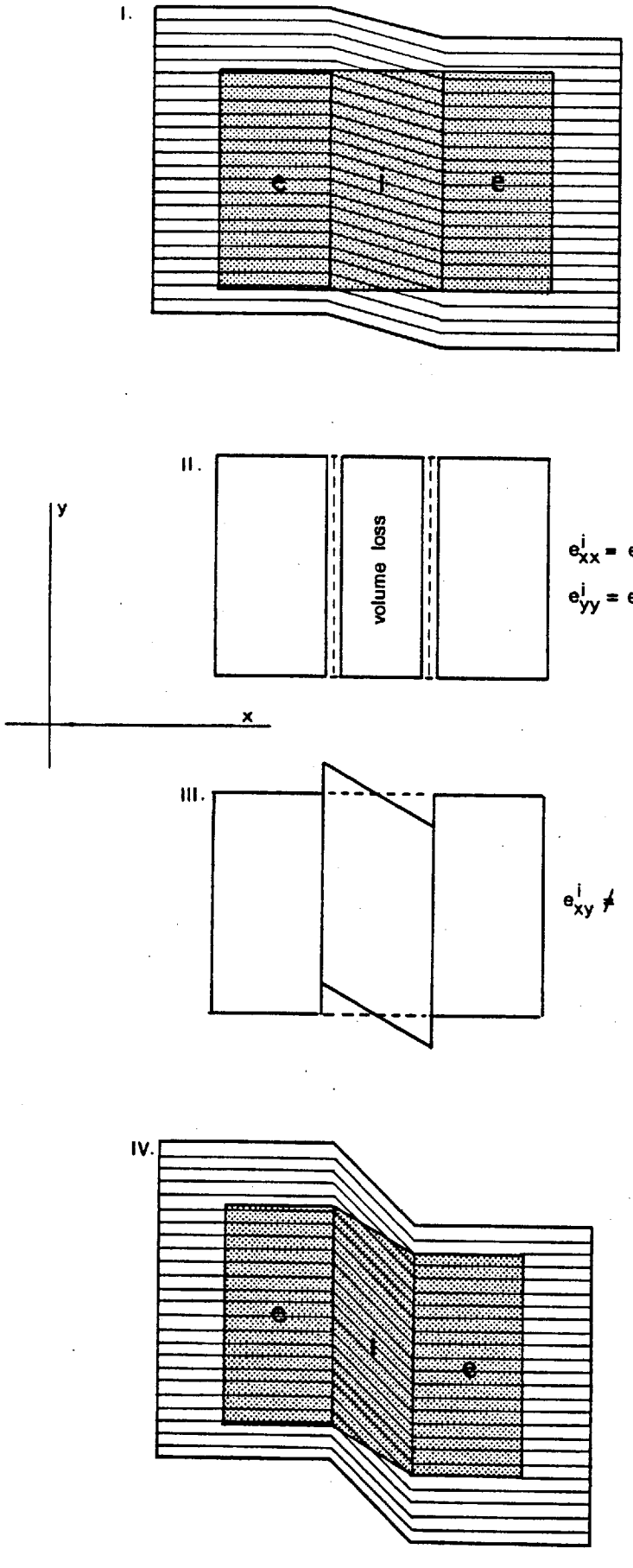
Simple shear



Post-deformation

Figure 3.2 C

MODEL C



For deformation at constant volume :

$$\left.\begin{matrix} e^{i}_{xx} + e^{i}_{yy} \\ \dot{e}^{i}_{xx} + \dot{e}^{i}_{yy} \end{matrix}\right\} = 0 \qquad \left.\begin{matrix} e^{e}_{xx} + e^{e}_{yy} \\ \dot{e}^{e}_{xx} + \dot{e}^{e}_{yy} \end{matrix}\right\} = 0$$

Model B (fig. 3.2B)

This model is characterised by discrete fractures at the boundaries of the rotation domain. These fractures represent a strain discontinuity and there is no requirement for compatibility of direct strains across the element boundaries.

In terms of equality of internal and external strain and strain rate components:

Direct strain (fig. 3.2B (ii))

$$e^{i}_{xx} \neq e^{e}_{xx}$$
$$\dot{e}^{i}_{xx} \neq \dot{e}^{e}_{xx}$$
$$e^{i}_{yy} \neq e^{e}_{yy}$$
$$\dot{e}^{i}_{yy} \neq \dot{e}^{e}_{yy}$$

Shear strain (fig. 3.2B (iii))

$$e^{i}_{xy} \neq e^{e}_{xy}$$
$$\dot{e}^{i}_{xy} \neq \dot{e}^{e}_{xy}$$

As in model A, it is assumed that both internal and external zones deform at constant volume.

$$\left.\begin{matrix} e^{i}_{xx} + e^{i}_{yy} \\ \dot{e}^{i}_{xx} + \dot{e}^{i}_{yy} \end{matrix}\right\} = 0 \qquad \left.\begin{matrix} e^{e}_{xx} + e^{e}_{yy} \\ \dot{e}^{e}_{xx} + \dot{e}^{e}_{yy} \end{matrix}\right\} = 0$$

In constructing fig. 3.2B is has been assumed, for diagramatic simplicity, that deformation is confined within the fracture bounded rotation domain, (i.e. all components of incremental strain e_{ij} and finite strain ε_{ij} are zero in the external foliation).

The hypothetical model shown in fig. 3.2 B has been proposed as a model for the development of certain types of small scale fracture bounded kink bands by Dewey (1965). Dewey called such structures 'joint drags'. He analysed the properties of the model on purely geometric grounds by assuming that the isolated foliation within the kink zone rotates as a stack of rigid plates. It will be shown later in this section that the simple geometric model proposed by Dewey can be quantified in terms of mechanical behaviour by using methods developed in the rotation domain analysis. The model will be based on equations derived for the response of a foliation rotation domain, bounded by strain discontinuities in the form of fractures, to layer parallel external compression. The behaviour predicted for this mechanical model matches exactly Dewey's assumption that the internal foliation rotates as a series of rigid plates if a very high (effectively infinite) degree of foliation anisotropy, N/Q, is introduced into the derived response equations.

It should be noted that model B is proposed only as an intermediate step in the discussion of the effects of change in the volume of foliation elements on the deformation of structures. Structures which develop as fracture bounded kink zones ('joint drags') are relatively rare in nature. In addition, model B is geologically realistic only for a rotation domain with a uniform internal foliation orientation. An equivalent model of a rotation domain with a non-uniform internal foliation orientation would need to incorporate a large nuber of domain parallel fractures bounding locally homogeneous foliation elements .

Model C - fig. 3.2C

As in model A, material continuity is maintained across the boundaries of the rotation domain. However in this case change in the macroscopic volume of internal and external foliation elements occur during deformation. This model represents a simplification of the macroscopic strain compatibility conditions which apply to the types of behaviour shown in fig. 3.1 . The following strain and strain rate compatibility

conditions apply to model C.

Direct strain (fig. 3.2C (ii))

$$e^{i}_{xx} \neq e^{e}_{xx}$$

$$\dot{e}^{i}_{xx} \neq \dot{e}^{e}_{xx}$$

$$e^{i}_{yy} = e^{e}_{yy}$$

$$\dot{e}^{i}_{yy} = \dot{e}^{e}_{yy}$$

Shear strain (fig. 3.2C (iii))

$$e^{i}_{xy} \neq e^{e}_{xy}$$

$$\dot{e}^{i}_{xy} \neq \dot{e}^{e}_{xy}$$

In constructing fig 3.2C it has been assumed, for geometric simplicity, that deformation and volumetric strain is confined within the boundaries of the uniform rotation domain. It will be shown later in this section that more complex variations in local volumetric strain can occur across non-uniform rotation domains and that volumetric strain may not be restricted to the internal foliation.

If macroscopic volume changes occur:

$$\left.\begin{matrix} e^{i}_{xx} + e^{i}_{yy} \\ \dot{e}^{i}_{xx} + \dot{e}^{i}_{yy} \end{matrix}\right\} = 0 \qquad \left.\begin{matrix} e^{e}_{xx} + e^{e}_{yy} \\ \dot{e}^{e}_{xx} + \dot{e}^{e}_{yy} \end{matrix}\right\} = 0$$

By comparing the sets of strain and strain rate compatibility conditions listed for the three models illustrated in figs. 3.2A, B and C it can be seen that the constraints on deformation of model C are intermediate between the extreme cases of model A (total compatibility of internal and external direct strain rate components across element boundaries - $\dot{e}^{i}_{xx} = \dot{e}^{e}_{xx}$, $\dot{e}^{i}_{yy} = \dot{e}^{e}_{yy}$) and model B (total discontinuity in direct strain rate components across element boundaries -

$\dot{e}^{i}_{xx} \neq \dot{e}^{e}_{xx}$, $\dot{e}^{i}_{yy} \neq \dot{e}^{e}_{yy}$). It will be shown that the effect of local volumetric strain on the response of a rotation domain to externally applied stress can be understood by contrasting the behaviour of models A and B, both of which can be analysed in terms of constant volume continuum equations.

Contrast in the behaviour of models A and B - effect of a total breakdown in direct strain compatibility.

Two equations were derived in chapter 2 which can be used to obtain the magnitude of the direct ($\dot{e}_{xx}$, $\dot{e}_{yy}$) and shear ($\dot{e}_{xy}$) components of incremental deformation of individual foliation elements making up a tabular rotation domain.

$$\dot{e}_{xx} = \frac{1}{4N}\left(-\left((N/Q+1) - (N/Q-1)\cos 4(\theta-\omega)\right)\sigma'_{xx} + (N/Q-1)\sin 4(\theta-\omega)\,\sigma_{xy}\right) \quad .. \ 2.19$$

$$\dot{e}_{xy} = \frac{1}{4N}\left(-\left((N/Q-1)\sin 4(\theta-\omega)\right)\sigma'_{xx} + \left((N/Q+1) - (N/Q-1)\cos 4(\theta-\omega)\right)\sigma_{xy}\right) \quad .. \ 2.19a$$

These equations can be applied to both models A and B because they contain no assumptions about conditions of element to element direct strain compatibility.

In any defined rotation domain the magnitude of the domain parallel shear stress, σ_{xy}, can be obtained from the stress equilibrium condition :

$$\frac{\partial \sigma_{xy}}{\partial x} = 0$$

This condition, which applies to both models A and B, indicates that the magnitude of σ^{i}_{xy} acting on any band parallel foliation element is given by the resolved shear stress, σ^{e}_{xy}, acting the boundaries of the rotation domain in the external foliation.

$$\sigma^{i}_{xy} = \sigma^{e}_{xy} = \tau^{e}_{m} \sin 2\theta$$

and :

$$\dot{e}_{xx} = \frac{1}{4N} \left\{ - (N/Q-1) \sin 4(\theta-\omega)\, \sigma'_{xx} + \left[(N/Q+1) + (N/Q-1)\cos 4(\theta-\omega)\right] \tau^{e}_{m} \sin 2\theta \right\} \quad \ldots\ldots 2.22$$

$$\dot{e}_{xy} = \frac{1}{4N} \left\{ - \left[(N/Q+1) - (N/Q-1)\cos 4(\theta-\omega)\right] \sigma'_{xx} + (N/Q-1) \sin 4(\theta-\omega)\, \tau^{e}_{m} \sin 2\theta \right\} \quad \ldots\ldots 2.23$$

It will be recalled from chapter 2 that these two equations are not sufficient to determine the total incremental response of specific foliation elements because they contain an unknown, i.e. the magnitude of the deviatoric stress component, σ'_{xx}, within the internal foliation. This component cannot be determined from conditions of stress equilibrium alone. In order to calculate the magnitude of σ'_{xx} it is necessary to examine the implications of the conditions of element to element strain compatibility required for models A and B. Consider first the implications of equations 2.23 and 2.22 for the deformation of the *external foliation*. In this zone the state of stress is completely defined by the magnitude of the principal stress components σ^{e}_{1} and $\sigma_{3}{}^{e}$.

$$\sigma'^{e}_{xx} = \tau^{e}_{m} \cos 2\theta$$

Thus the total strain rate tensor in the external foliation can be determined. The band normal direct strain rate, $\dot{e}^{e}_{xx}$, is given by:

Thus :

$$\dot{e}_{xx} = \frac{\tau_m^e}{4N} \left\{ - \left[(N/Q+1) - (N/Q-1)\cos 4(\theta-\omega) \right] \cos 2\theta + (N/Q-1) \sin 4(\theta-\omega) \sin 2\theta \right\}$$

Within the external foliation ($\omega = 0$) :

$$\dot{e}^e_{xx} = \frac{\tau_m^e}{4N} \left\{ - \left[(N/Q+1) - (N/Q-1)\cos 4\theta \right] \cos 2\theta + (N/Q-1) \sin 4\theta \sin 2\theta \right\}$$

$$\dot{e}^e_{xx} = \frac{\tau_m^e}{4N} \left\{ - (N/Q+1) \cos 2\theta + (N/Q-1) \cos 2\theta \right\}$$

$$\dot{e}^e_{xx} = \frac{\tau_m^e}{4N} \left\{ - 2 \cos 2\theta \right\} \qquad \ldots\ldots 2.32$$

This equation indicates that, as was demonstrated in chapter 2, the external foliation reacts to the applied foliation symmetric principal stresses as if it were an isotropic material with an isotropic stiffness coefficient given by the principal stiffness coefficient N of the anisotropic material. The magnitude of $\dot{e}^e_{xx}$ given by equation is equivalent to the rate of direct strain, resolved at θ to the applied maximum compression, which would develop in such an isotropic material (assuming linear viscous behaviour). It is important to note that the rate is independent of the material anisotropy ratio N/Q and would be the same in an isotropic material (N/Q = 1) as in very highly anisotropic materials ($N/Q \to \infty$) given the same level of applied stress in the external foliation ($\tau^e_m/4N$). This placed a very significant constraint on the response of the internal foliation under the direct strain compatibility conditions obtaining in model A. In this model modification of the internal stress tensor is required to restrict the rate of incremental pure shear deformation within the rotation domain to the slow, effectively isotropic rate induced in the external foliation. This stress modification, which has been discussed in detail in chapter 2, acts to inhibit the development of

anomously high or low rates of band normal direct strain, $\dot{e}^{i}_{xx}$, within the internal foliation. The development of a heterogeneous stress field across particular structures can be compared with the essentially similar phenomenon of the local modification of a homogeneous stress field which would result from the presence of an inclusion of relatively "weak" or "stiff" isotropic material in a contrasting, uniform isotropic continuum. In both cases, local stress modification is the result of the combined requirements of stress equilibrium and strain compatibility across material elements with contrasting material properties. In a foliation rotation domain the contrast in the local "stiffness" of foliation elements is a finite effect which is related to local rotation of the foliation planes with respect to the externally applied stress.

The need to maintain total direct strain compatibility across the boundaries between adjacent foliation elements was used in the constant volume rotation domain analysis to calculate the local magnitude of σ'^{i}_{xx} and to complete the response equations 2.22 and 2.23. This is achieved by combining equations 2.22 and 2.32 and using the condition $\dot{e}^{i}_{xx} = \dot{e}^{e}_{xx}$ to solve for the unknown σ'^{i}_{xx}. The resultant equations for the pure shear and simple shear components of incremental deformation are:

$$\dot{e}^{i}_{xx} = \frac{\tau^{e}_{m}}{4N}\left[-2\cos 2\theta\right] \qquad \ldots\ldots\ldots \quad 2.32$$

$$\dot{e}^{i}_{xy} = \frac{\tau^{e}_{m}}{4N}\left[\frac{4(N/Q) - 2(N/Q-1)\sin 4(\theta-\omega)\cos 2\theta}{(N/Q+1) - (N/Q-1)\cos 4(\theta-\omega)}\right] \qquad \ldots\ldots\ldots \quad 2.35$$

These expressions are also used to express the incremental rate of foliation rotation, $\dot{\omega}$, by combining equations 2.32 and 2.35 with: 2.39 :-

$$\dot{\omega} = \sin 2(\theta-\omega) \ldots \dot{e}_{xx} + 2\cos^{2}(\theta-\omega) \cdot \dot{e}_{xy} + \dot{\theta} \qquad \ldots\ldots\ldots \quad 2.39$$

where :
$$\dot{\theta} = -\frac{\tau^{e}_{m}}{4N}\left[2\sin 2\theta\right]$$

The full expression for $\dot{\omega}$ is given by equation 2.43 :

$$\dot{\omega} = \frac{\tau_m^e}{4N}\left\{ - 2\cos 2\theta . \sin 2(\theta-\omega) + 2\cos^2(\theta-\omega)\left[\frac{4(N/Q) - 2(N/Q-1)\sin 4(\theta-\omega)\cos 2\theta}{(N/Q+1) - (N/Q-1)\cos 4(\theta-\omega)}\right] - 2\sin 2\theta \right\} \quad \ldots\ldots 2.43$$

A similar series of expressions can be derived for the incremental response to externally applied stress of model B as follows:

(i) The total response of the external foliation of model B is identical to that of model A (effectively isotropic).

$$\dot{e}^e_{xx} = \frac{\tau_m^e}{4N}\left[- 2\cos 2\theta \right]$$

$$\dot{e}^e_{xy} = \frac{\tau_m^e}{4N}\left[2\sin 2\theta \right]$$

(ii) In contrast to model A there is no requirement for internal modification of the externally applied stress tensor. The existence of discontinuities in direct strain at the rotation domain boundaries implies a breakdown in the compatibility condition $\dot{e}^i_{xx} = \dot{e}^e_{xx}$. It is therefore possible to quantify the direct strain and shear strain response of the rotated internal foliation in model B by assuming a state of *homogeneous stress* throughout a structure. This assumption, which is fully justified by the conditions of the analysis, allows the problem of the unknown internal deviatoric stress component, σ'_{xx}, to be resolved by equating the internal and external stress components σ'^i_{xx} and σ'^e_{xx} .

i.e. $$\sigma'^i_{xx} = \sigma'^e_{xx} = \tau_m^e \sin 2\theta$$

(iii) Introducing this identity into equations 2.22 and 2.23 :

$$\dot{e}_{xx} = \frac{\tau_m^e}{4N}\left\{-\left[(N/Q+1) - (N/Q-1)\cos 4(\theta-\omega)\right]\cos 2\theta + \left[(N/Q-1)\sin 4(\theta-\omega)\right]\sin 2\theta\right\}$$

$$\dot{e}_{xy} = \frac{\tau_m^e}{4N}\left\{-\left[(N/Q-1)\sin 4(\theta-\omega)\right]\cos 2\theta + \left[(N/Q+1) + (N/Q-1)\cos 4(\theta-\omega)\right]\sin 2\theta\right\}$$

Simplifying these equations :

$$\dot{e}_{xx} = \frac{\tau_m^e}{4N}\left\{(N/Q-1)\cos 2(2\omega-\theta) - (N/Q+1)\cos 2\theta\right\} \quad \ldots\ldots 3.6$$

$$\dot{e}_{xy} = \frac{\tau_m^e}{4N}\left\{(N/Q+1)\sin 2\theta - (N/Q-1)\sin 2(2\omega-\theta)\right\} \quad \ldots\ldots 3.7$$

An expression can be obtained for the incremental rate of foliation rotation, $\dot{\omega}$, under conditions of homogeneous stress and boundary strain discontinuity by combining equations 3.6 , 3.7 and 2.39 :

$$\dot{\omega} = \frac{\tau_m^e}{4N}\left\{\begin{array}{l}\sin 2(\theta-\omega)\left((N/Q-1).\cos 2(2\omega-\theta) - (N/Q+1).\cos 2\theta\right) \\ \quad + 2\cos^2(\theta-\omega)\left((N/Q+1)\sin 2\theta - (N/Q-1)\sin 2(2\omega-\theta)\right) \\ \quad - 2\sin 2\theta\end{array}\right\} \quad \ldots\ldots 3.8$$

Contrast in incremental response to externally applied stress of models A and B.

The most significant differences between models A and B can be illustrated by comparing the rates of incremental band normal direct strain, $\dot{e}_{xx}$, and incremental foliation rotation, $\dot{\omega}$, predicted for the two models. This will be done by analysing the incremental response of a simple rotation domain with a uniform internal foliation orientation. The boundaries of the domain are assumed to be oriented at 30°

to the external foliation normal, ($\theta = 30^{o}$).

Variation in the magnitude of $\dot{e}_{xx}$ with internal foliation attitude ω.

The variation in the magnitude of the domain normal incremental strain rate component $\dot{e}_{xx}$ is illustrated in figs. 3.4 and 3.5 for the contrasting strain compatibility conditions of models B and A respectively. The relationships between $\dot{e}_{xx}$ and ω plotted in these figures have been calculated for the incremental deformation of an oblique rotation domain, $\theta = 30^{o}$, and the relationships are shown for three values of N/Q (N/Q=100, 5.0, 1.0). Following the convention adopted in chapter 2, the strain rate $\dot{e}_{xx}$ is shown as normalised to the stress level in the external foliation. Consider first the relationships shown in fig. 3.3 for model B.

Model B (fig. 3.3).

The variation in $\dot{e}_{xx}$ with foliation attitude ω is given by equation 3.6 .

(i) The point corresponding to $\omega = 0$ indicates the magnitude of resolved direct strain, $\dot{e}^{e}_{xx}$, in the unrotated external foliation. For $\omega = 0$ equation 3.6 reduces to:

$$\dot{e}^{e}_{xx} = \frac{\tau^{e}_{m}}{4N}\left[-2\cos 2\theta\right]$$

A negative value for $\dot{e}^{e}_{xx}$ indicates an incremental contraction along the direction normal to the rotation domain boundaries in the effectively isotropic, external foliation. (Note that $\dot{e}^{e}_{xx}$ is negative for any domain orientation in the range $0^{o} \leqslant \theta < 45^{o}$ and positive (i.e. extensional) over the range $45^{o} < \theta \leqslant 90^{o}$).

(ii) The contrast in direct strain response of the internal and external foliation to a state of homogeneous stress can be understood by comparing the magnitude of $\dot{e}^{e}_{xx}$ ($\omega = 0$) with the magnitude of $\dot{e}^{i}_{xx}$ for $\omega > 0$. (As would be expected the contrast in response of the effectively isotropic external foliation and the rotated internal foliation will increase with increase in the anisotropy ratio of the material.) The

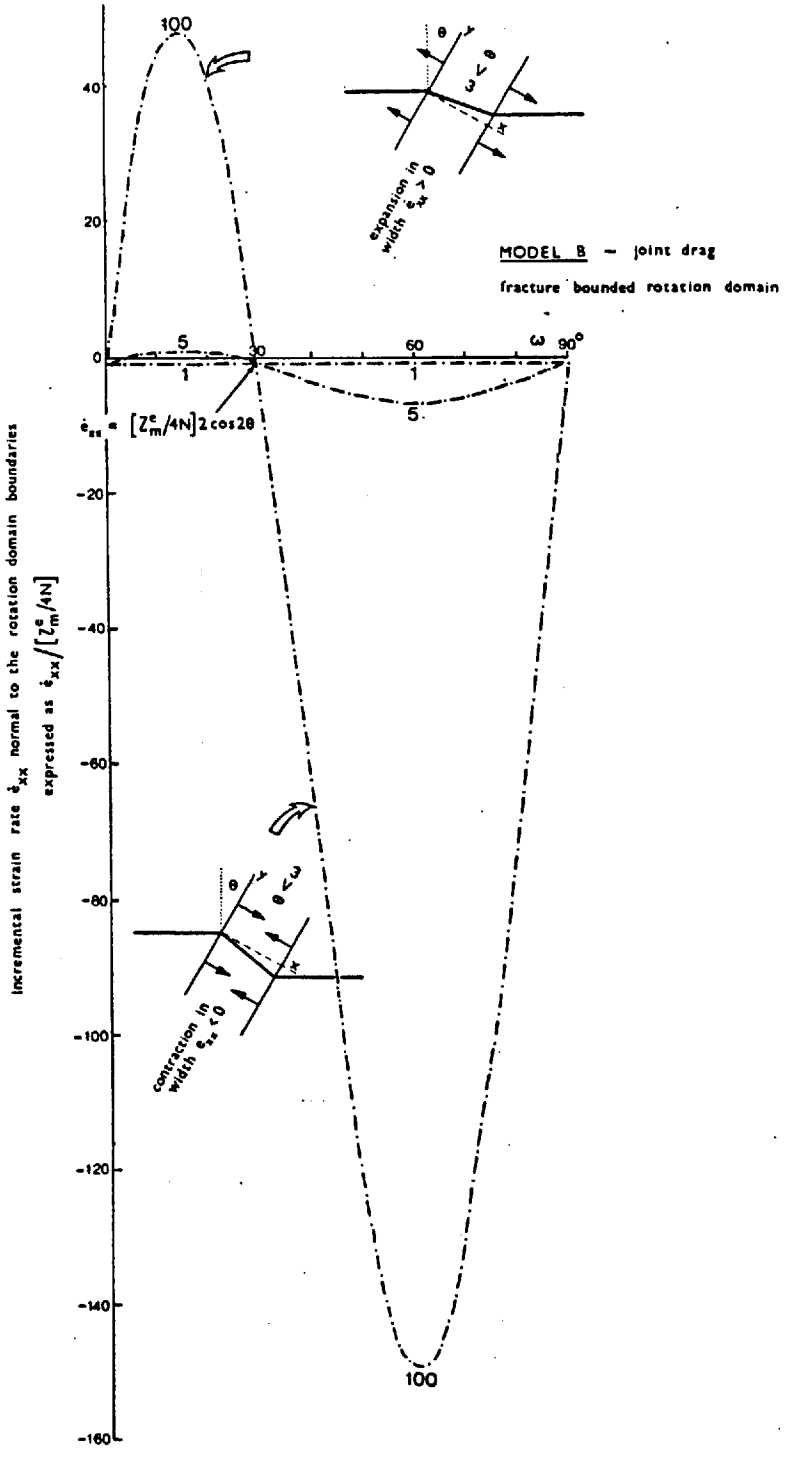


Figure 3.3 Variation in the incremental strain rate component $\dot{e}_{xx}$ as a function of foliation attitude ω calculated for the the deformation conditions of model B (fracture bounded rotation domain).

mechanical significance of foliation anisotropy and its influence on the unconstrained, non-coaxial deformation of the rotation domain can be most clearly seen in the curve corresponding to a high degree of anisotropy (N/Q = 100). Two important features are demonstrated by the form of this curve.

(a) Throughout almost the whole range of foliation attitude $0 < \omega < 90^{o}$ the magnitude of the induced band normal direct strain rate within the rotation domain is significantly greater than the equivalent strain rate component in the external foliation. The exceptions are for foliation attitudes close to the band normal orientation $\omega = \theta$ and for $\omega = 90^{o}$. Note that:

When $\omega = \theta$:

$$\dot{e}^{i}_{xx} = \frac{\tau^{e}_{m}}{4N}\left[(N/Q-1)\cos 2(2\theta-\theta) - (N/Q+1)\cos 2\theta\right]$$

$$\dot{e}^{i}_{xx} = \frac{\tau^{e}_{m}}{4N}\left[(N/Q-1)\cos 2\theta - (N/Q+1)\cos 2\theta\right]$$

$$\dot{e}^{i}_{xx} = \frac{\tau^{e}_{m}}{4N}\left[-2\cos 2\theta\right] \qquad \ldots\ldots \text{3.6a}$$

When $\omega = 90^{o}$:

$$\dot{e}^{i}_{xx} = \frac{\tau^{e}_{m}}{4N}\left[(N/Q-1)\cos 2(\pi-\theta) - (N/Q+1)\cos 2\theta\right]$$

$$\dot{e}^{i}_{xx} = \frac{\tau^{e}_{m}}{4N}\left[(N/Q-1)\cos 2\theta - (N/Q+1)\cos 2\theta\right]$$

$$\dot{e}^{i}_{xx} = \frac{\tau^{e}_{m}}{4N}\left[-2\cos 2\theta\right] \qquad \ldots\ldots \text{3.6b}$$

It can be seen from equation 3.6a that the internal and external strain rates, $\dot{e}_{xx}$, are identical if the internal foliation is normal to the rotation domain boundaries. This prediction holds for *any* domain orientation θ and *any*

value of material anisotropy ration N/Q.

(b) Throughout almost the whole range of foliation attitude $0 < \omega < \theta$ the induced direct strain rate in the unconstrained internal foliation is positive. This indicates that under a state of homogeneous stress the width of the rotation domain will increase during incremental deformation. In contrast, if the internal foliation has rotated past the band normal position (i.e. $0 < \omega < 90^{o}$) a state of homogeneous stress will induce incremental contraction in the width of the domain ($\dot{e}_{xx}$ negative). It should be noted that $\dot{e}_{xx}$ is positive over the whole range $0 < \omega < \theta$ and negative over the whole range $\theta < \omega < 90$ only for an infinite degree of anisotropy ($N/Q = \infty$).

These relationships can be compared directly with the properties of the 'joint drag' model of kink band development proposed by Dewey (1965). This model (fig. 3.5) is concerned with the special case of a fracture bounded kink zone with a uniform internal foliation orientation. The foliation within the kink zone is assumed to rotate as a stack of rigid plates which are freely pivoted at the kink zone boundary. Dewey's analysis of this model is purely geometric. It is clear from fig. 3.5 that the cut off length (ab) can only remain constant if the width of the kink zone changes during deformation. It is a trivial matter to show that the width of the zone will increase for rigid rotation of the foliation up to the band normal position ($0 < \omega < \theta$ - fig. 3.5 A - B). Further incremental rotation of the kinked foliation ($\theta < \omega < 90$ - fig. 3.5 B - C) produces an incremental decrease in the width of the zone. These relationships between incremental expansion or contraction of the rotation domain and internal foliation attitude are identical to those predicted by continuum model B for a highly anisotropic material. It is also possible to demonstrate that a finite deformation analysis, based on the incremental equations derived for model B, models exactly the total external and internal finite strains which are implicit in Dewey's description of the properties of the 'joint drag' (for $N/Q \rightarrow \infty$).

(iii) The contrast in resolved direct strain rate $\dot{e}_{xx}$ of the internal and external foliation becomes less marked with decrease in foliation anisotropy N/Q. In the limit $N/Q \rightarrow 1$ the foliation is mechanically passive and the magnitude of $\dot{e}_{xx}$ in the internal foliation is independent of

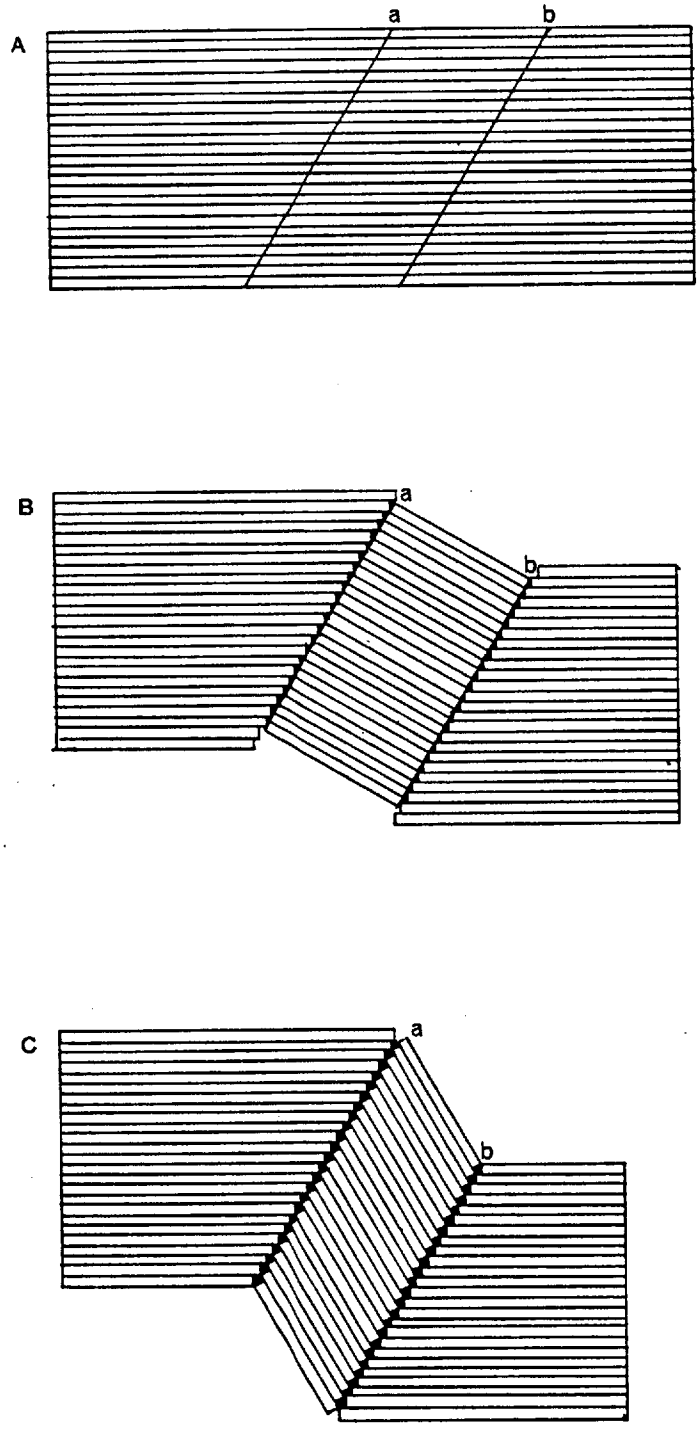


Figure 3.5 'Joint drag' model of kink development proposed by Dewey (1965). See text for details.

foliation attitude, ω, and equal to the isotropic rate induced in the external foliation. The deformation of the whole structure is homogeneous and isotropic/coaxial).

When N/Q = 1 :

$$\dot{e}^{i}_{xx} = \frac{\tau^{e}_{m}}{4N}\left[(N/Q-1)\cos 2(2\omega-\theta) - (N/Q+1)\cos 2\theta\right]$$

$$\dot{e}^{i}_{xx} = \frac{\tau^{e}_{m}}{4N}\left[-2\cos 2\theta\right] \quad \text{(for all } \omega\text{)}$$

Model A (fig. 3.4)

This model incorporates internal stress modification in order to maintain the strain rate compatibility condition $\dot{e}^{i}_{xx} = \dot{e}^{e}_{xx}$. The magnitude of the effective band normal direct strain rate is, as a result, independent of the internal foliation attitude and the material anisotropy. The relationship between internal foliation attitude, ω, anisotropy ratio, N/Q, and the required internal stress modification can be understood from the previous discussion of direct strain response under homogeneous stress.

It has been shown that if, as in model B, no internal modification of the externally applied stress tensor occurs then a contrast in internal and external band normal direct strain rates must develop. This contrast can be expressed by the difference $\dot{e}^{i}_{xx} - \dot{e}^{e}_{xx}$. Combining equations 2.32 and 3.6 :

$$\dot{e}^{i}_{xx} - \dot{e}^{e}_{xx} = \frac{\tau^{e}_{m}}{4N}\left[(N/Q-1)\ (\cos 2(2\omega-\theta) - (N/Q+1)\cos 2\theta - 2\cos 2\theta\right]$$

$$\dot{e}^{i}_{xx} - \dot{e}^{e}_{xx} = \frac{\tau^{e}_{m}}{4N}\left[(N/Q-1)\ (\cos 2(2\omega-\theta) - \cos 2\theta)\right]$$

..... 3.9

In model A the internal stress modification which acts to inhibit the development of a variation in $\dot{e}_{xx}$ across a structure can be expressed by the difference between the extremal deviatoric stress component σ'^{i}_{xx}. The difference, $\sigma'^{i}_{xx} - \sigma'^{e}_{xx}$ between these resolved stresses is

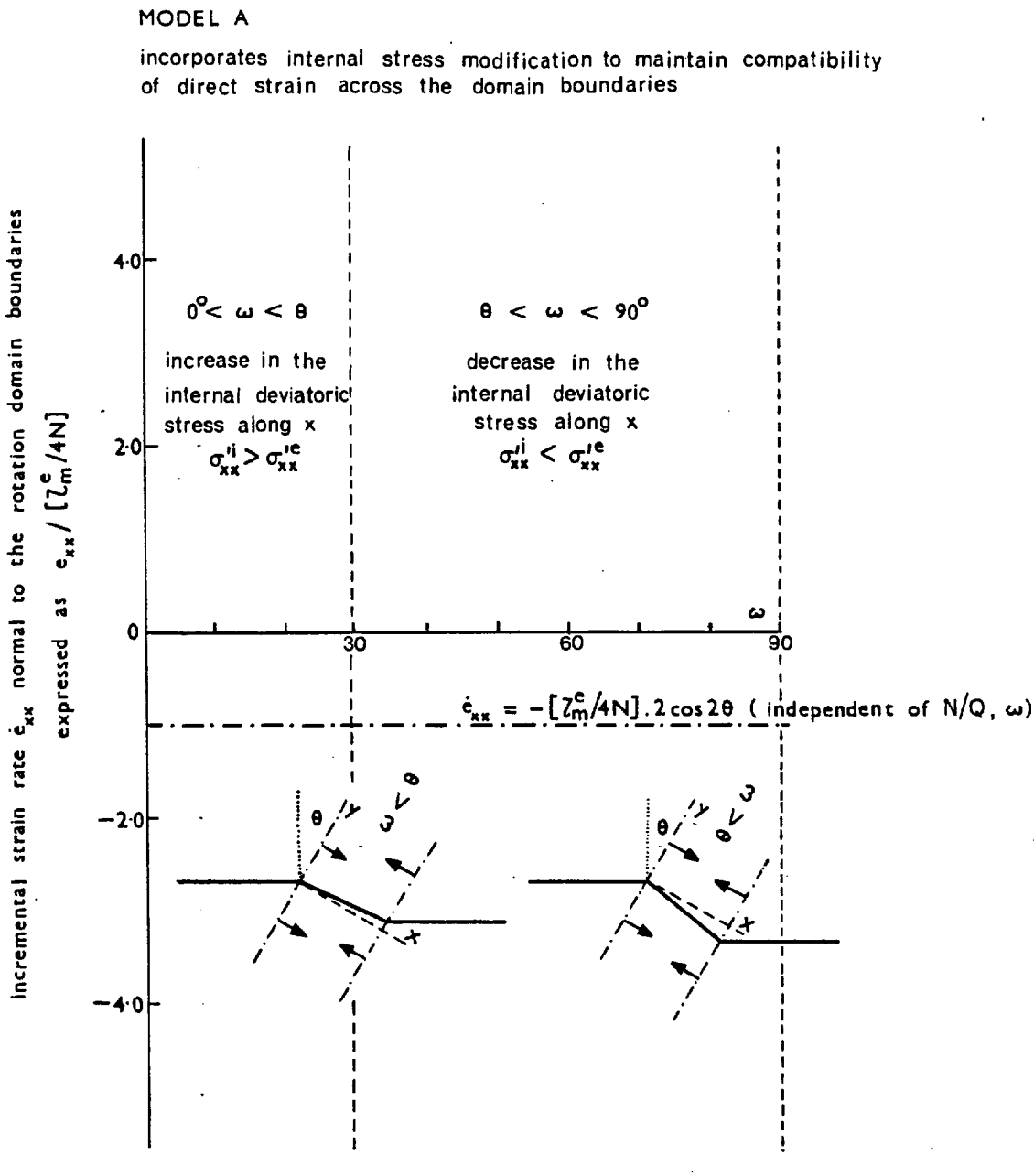


Figure 3.4 Variation in the strain rate component $\dot{e}_{xx}$ as a function of foliation attitude ω calculated for the deformation conditions of model A (rotation domain analysis of chapter 2).

given by:

$$\sigma'^{i}_{xx} - \sigma'^{i}_{xx} = \tau^{e}_{m}\left[\frac{(N/Q-1)\ (\sin 4(\theta-\omega)\sin 2\theta) + 2\cos 2\theta}{(N/Q+1) - (N/Q-1)\cos 4(\theta-\omega)} - \cos 2\theta\right]$$

Simplifying :

$$\sigma'^{i}_{xx} - \sigma'^{e}_{xx} = \tau^{e}_{m}\left[\frac{(N/Q-1)\ (\cos 2(2\omega-\theta) - \cos 2\theta)}{(N/Q+1) - (N/Q-1)\cos 4(\theta-\omega)}\right] \quad \ldots\ldots 3.10$$

There is a direct correlation between the contrast in internal and external direct strain rate, $\dot{e}_{xx}$, predicted for model B (equation 3.9), and the contrast in internal and external deviatoric stress, σ^{1}_{xx}, predicted for model A (equation 3.10). Inspection of equations 3.9 and 3.10 shows that the sign of the terms $(\dot{e}^{i}_{xx} - \dot{e}^{e}_{xx})$ and $(\sigma^{1i}_{xx} - \sigma^{1e}_{xx})$ depends only on the sign of the bracketed expression (cos $2(2\omega-\theta)$ - cos 2θ). All other terms on the right hand side of equations and are positive. It is a simple matter to show that:

(a) <u>When $0 < \omega < \theta$</u> :

$$\cos 2(2\omega-\theta) - \cos 2\theta > 0$$

$$\rightarrow \quad \dot{e}^{i}_{xx} > \dot{e}^{e}_{xx} \qquad \text{Model B}$$

$$\rightarrow \quad \sigma'^{i}_{xx} > \sigma'^{e}_{xx} \qquad \text{Model A}$$

Under the sign convention used in the analysis (extensional strain positive) the response predicted for model B indicates that $\dot{e}^{i}_{xx}$ will be relatively extensional. This may be expressed as a relatively slow rate of contraction across the internal foliation ($\dot{e}^{e}_{xx} < \dot{e}^{i}_{xx} < 0$) or as an induced incremental extension across the internal foliation ($\dot{e}^{e}_{xx} < 0 < \dot{e}^{i}_{xx}$), (depending on the internal foliation attitude and the material anisotropy ratio (fig. 3.3)). In contrast the condition $\dot{e}^{i}_{xx} = \dot{e}^{e}_{xx}$ is maintained in model A by an increase in the magnitude of σ_{xx} in the internal foliation ($\sigma'^{i}_{xx} > \sigma'^{e}_{xx}$). This internal stress modification acts to inhibit the development of anomalous incremental extension across the rotation domain. As was shown in

chapter 2, the increase in internal σ'_{xx} is associated with a relative decrease in the mean stress within the rotation domain and the channeling of maximum principal stress trajectories along the direction of the internal foliation.

(b) When $\theta < \omega < 90^{o}$:

$$\cos 2(2\omega-\theta) - \cos 2\theta < 0$$

$$\dot{e}^{i}_{xx} < \dot{e}^{e}_{xx} \qquad \text{Model B}$$

$$\sigma'^{i}_{xx} < \sigma'^{e}_{xx} \qquad \text{Model A}$$

The response predicted for model B indicates that $\dot{e}^{i}_{xx}$ will be relatively contractional over the range $\theta < \omega < 90^{o}$. The condition $\dot{e}^{i}_{xx} = \dot{e}^{e}_{xx}$ is maintained in model A by a relative decrease in the magnitude of the internal deviatoric stress component σ'^{i}_{xx} ($\sigma'^{i}_{xx} < \sigma'^{e}_{xx}$), an associated relative increase in the magnitude of the internal mean stress ($\overline{\sigma}^{i} > \overline{\sigma}^{e}$), and a rotation of the maximum principal compressive stress trajectories to a position normal to the internal foliation.

(c) When $\omega = \theta$:

$$\cos 2(2\omega-\theta) - \cos 2 = 0$$

$$\dot{e}^{i}_{xx} = \dot{e}^{e}_{xx} \qquad \text{Model B}$$

$$\sigma'^{i}_{xx} = \sigma'^{e}_{xx} \qquad \text{Model A}$$

Under homogeneous stress, internal and external strain rates $\dot{e}_{xx}$ are equal if the internal foliation is oriented normal to the boundaries of the rotation domain (This condition applies to any rotation domain orientation θ, or material anisotropy ratio). Consequently, this foliation attitude represents a special case in which there is no requirement for internal stress modification under the direct strain

compatibility conditions of model A. This fact underlies the unique significance of the band normal foliation orientation in the constant volume rotation domain analysis.

Incremental rate of foliation rotation, $\dot{\omega}$

It can be shown that the direct strain compatibility conditions of model A place a significant constraint on the rate of rotation of the internal foliation which can develop in this model. This constraint, which effectively inhibits the degree of rotational instability of model A, is not present in model B and will also be relaxed if macroscopic volume change of defined foliation elements is available as a mechanism of deformation. (Model C). This can be understood by comparing the magnitude of $\dot{\omega}$ predicted under the contrasting compatibility conditions of models A and B.

Model A

$$\dot{\omega} = \frac{\tau_m^e}{4N} \left\{ \begin{array}{l} \text{Pure Shear} \\ -2\cos 2\theta \cdot \sin 2(\theta-\omega) \\ \\ \text{Simple shear} \\ +2\cos^2(\theta-\omega)\left[\dfrac{4(N/Q) - 2(N/Q-1)\sin 4(\theta-\omega)\cos 2\theta}{(N/Q+1) - (N/Q-1)\cos 4(\theta-\omega)}\right] \\ \\ \text{Rotation of the foliation element walls} \\ -2\sin 2\theta \end{array} \right\} \quad \ldots\ldots\ldots 2.43$$

$$\dot{\omega} = \frac{\tau_m^e}{4N} \left\{ \begin{array}{l} \text{Pure Shear} \\ \sin 2(\theta-\omega)\left[(N/Q-1).\cos 2(2\omega-\theta) - (N/Q+1).\cos 2\theta\right] \\ \\ \text{Simple Shear} \\ +2\cos^2(\theta-\omega)\left[(N/Q+1)\sin 2\theta - (N/Q-1)\sin 2(2\omega-\theta)\right] \\ \\ \text{Rotation of the foliation element walls} \\ -2\sin 2\theta \end{array} \right\} \quad \ldots\ldots\ldots 3.8$$

Each of the equations contains three terms which quantify the separate contribution of ....

(a) Incremental direct strain ($\dot{e}_{xx}$, $\dot{e}_{yy}$) - pure shear

MODEL B

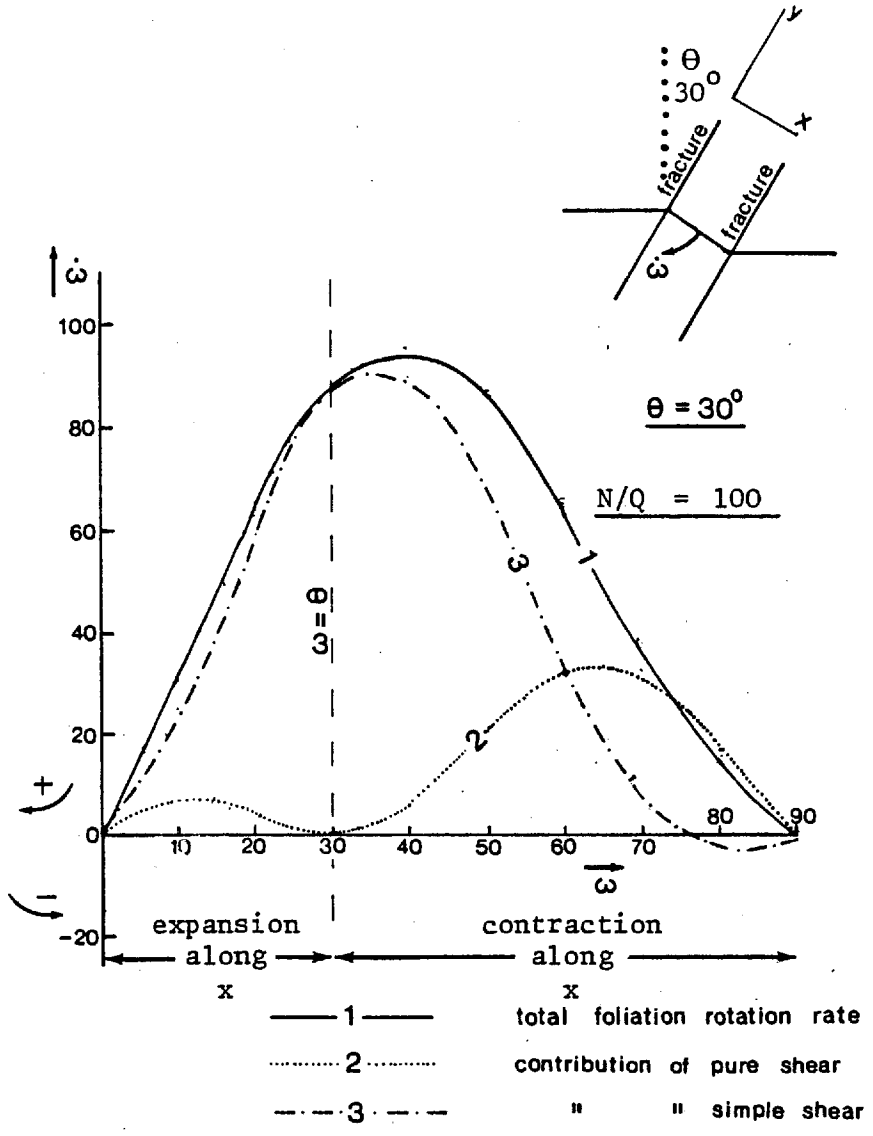


Figure 3.6 Relationship between the incremental rate of foliation rotation $\dot{\omega}$ and foliation attitude ω calculated for the strain compatibility conditions of Model B (constant volume deformation, total strain discontinuity across the domain boundaries in the form of discrete fractures, homogeneous stress throughout the structure). The total foliation rotation rate is shown (curve 1) is shown together the separated contributions of pure shear (curve 2) and simple shear (curve 3) to the total rate. In contrast to Model A (fig. 3.7), both shear parallel to the domain boundaries ($\dot{e}_{xy}$) and direct strain normal to the domain boundaries ($\dot{e}_{xx}$) contribute to the development of foliation rotation.

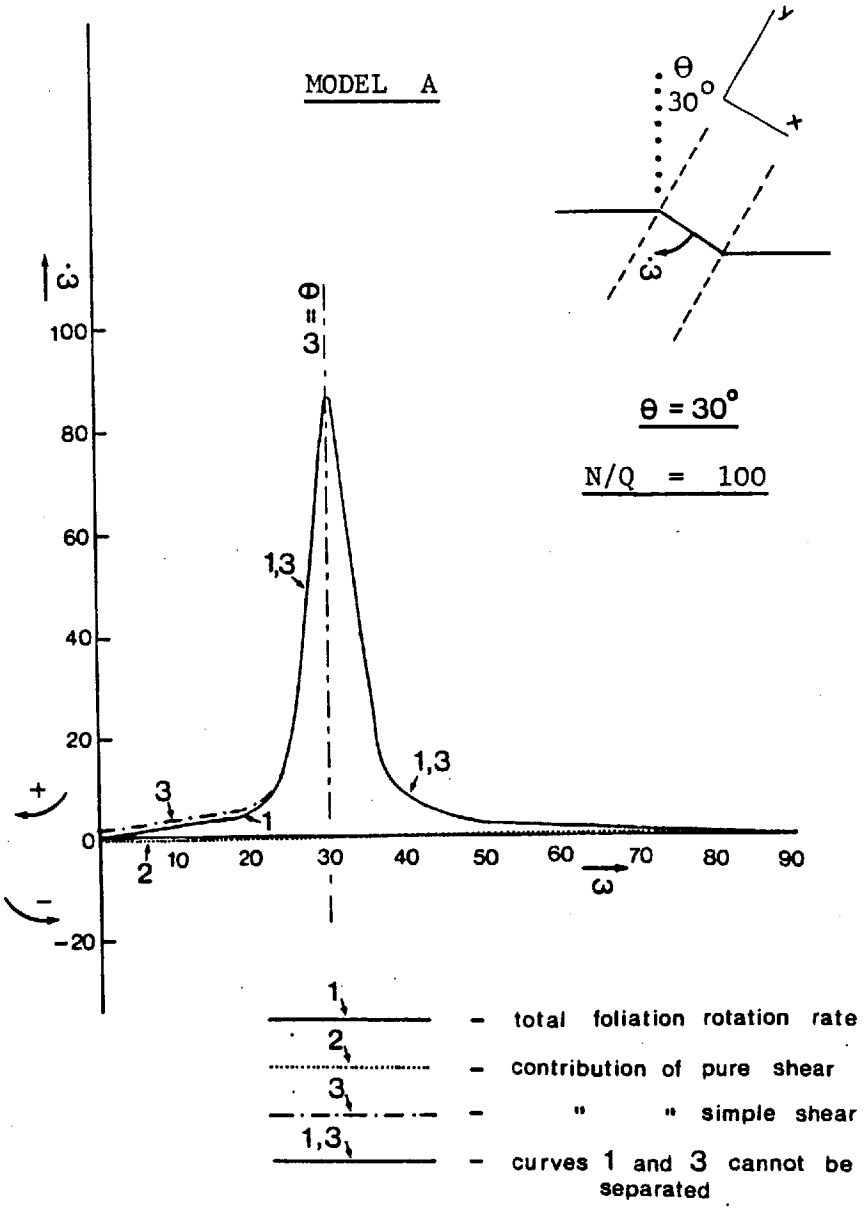


Figure 3.7 Relationship between the incremental rate of foliation rotation $\dot{\omega}$ and foliation attitude ω calculated for the strain compatibility conditions of Model A. (constant volume deformation, strain continuity across the rotation domain boundaries) The total foliation rotation rate is shown (curve 1) together with the separated contributions of pure shear (curve 2) and simple shear (curve 3) to the total rate Deformation of the rotation domain is dominated by domain parallel simple shear in this model. (this curve has been previously discussed as fig. 2.8 C in chapter 2.)

(b) Incremental shear strain ($\dot{e}_{xy}$) ..... simple shear

(c) Incremental rotation of the element boundaries w.r.t the external ($\dot{\theta}$).

... to the total incremental foliation rotation rate. These equations have been applied to a representative oblique rotation domain ($\theta = 30^{o}$) developed in a material with an anisotropy ratio of 100. The variation in induced foliation rotation rate with internal foliation attitude, ω, has been plotted in figs. 3.7 (model A) and 3.6 (model B). In order to clarify the discussion of these figures the total foliation rotation rate curve (continuous line) is shown together with the separated contributions of incremental pure shear and incremental simple shear (referred to the x,y coordinate frame) to the total foliation rotation rate $\dot{\omega}$.

Model B (fig. 3.7)

The foliation rotation rate is relatively high throughout the whole range of internal foliation attitude $0 < \omega < 90^{o}$. Inspection of fig. 3.6 shows that both direct strain and shear strain contribute significantly to the total foliation rotation rate at different values of foliation attitude ω. The uninhibited contribution of the pure shear component of deformation is associated with an expansion in the width of the rotation domain for foliation oriented in the range $0 < \omega < \theta$ and a contraction in the width of the rotation domain for foliation oriented in the range $\theta < \omega < 90^{o}$.

Model A (fig 3.7)

In this model the contribution of the direct strain component of deformation to the rotational response of the internal foliation is almost totally suppressed. Fig. 3.7 clearly shows how the direct strain compatibility conditions of model A restrict the development of rotational instability to a narrow range of foliation attitudes strad - ling the band normal foliation orientation $\omega = \theta$. The peak rate of foliation rotation which occurs at the band normal orientation in highly anisotropic materials is due entirely to a significant contribution from band parallel shear.

Figs. 3.6 and 3.7 illustrate the incremental rotational response of an element of internal foliation as a function of foliation attitude. The contrast in finite response of a rotation domain under the strain compatibility conditions of models A and B is illustrated by the finite deformation models shown in figs. 3.8 and 3.9. These figures indicate the finite development of strain and foliation rotation across

the internal and external foliation of a rotation domain, initially oriented at $\theta_0 = 30^\circ$. The structure has a uniform internal foliation orientation and the initial attitude of the internal foliation, ω_0, is 5°. The finite development of the structure under the compatibility conditions of model B (fig. 3.8.) and model A (fig. 3.9.), has been calculated by integrating the relevant incremental strain rate and rotation rate equations, assuming a material anisotropy ratio of 100. The elapsed time in each model is expressed by the finite shortening of the external foliation, resolved parallel to the internal foliation (natural strain units). This quantity can be used to compare, directly, the rates of development of the two models. The contrasting finite response shown in figs. 3.8 and 3.9 reflect the differences in incremental response discussed in the preceeding paragraphs. The most important differences between the geometrical development of the two models are:

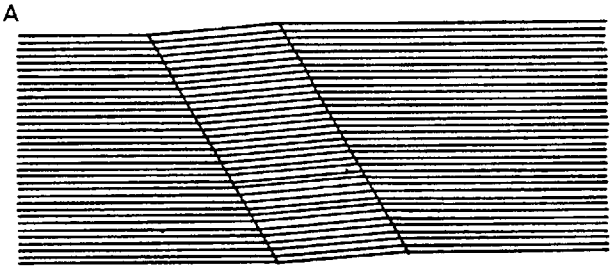
(i) The time required to produce large finite rotations of the internal foliation is significantly less in model B than in model A. In the former case, finite deformation is confined, almost entirely, to the unconstrained rotation domain. The extremal foliation undergoes a relatively small finite deformation and, in consequence, the orientation of the rotation domain boundaries remains relatively stable. In contrast, significant finite deformation of both internal and external foliation occurs in model A (see discussion, section 2.3.3). The deformation of the external foliation is reflected in the finite rotation of the boundaries of the rotation domain. The orientation of the domain is stable only as the internal foliation enters and passes through the phase of marked rotational instability associated with the band normal foliation orientation (fig. 3.7, B - C). During this phase, deformation in the form of band parallel shear is confined within the boundaries of the rotation domain.

(ii) Fig. 3.8 clearly illustrates the finite changes in the width of the rotation domain (initial expansion, subsequent contraction) which result from the unconstrained response of the highly anisotropic internal foliation to unmodified, homogeneous stress. The high relative magnitude of the foliation parallel direct stiffness coefficient, N, effectively prohibits any significant incremental and finite extension or contraction along the direction of the

MODEL B

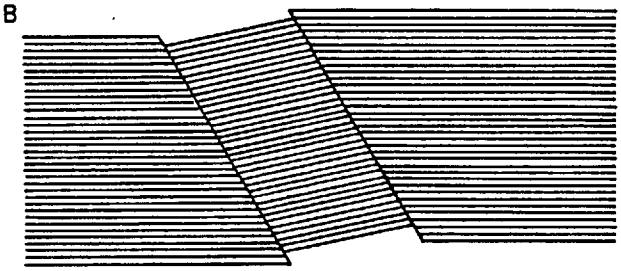
Finite strain ϵ_{11} in the external foliation

A



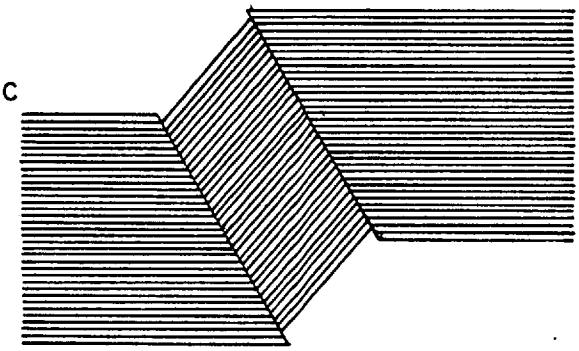
0.0

B



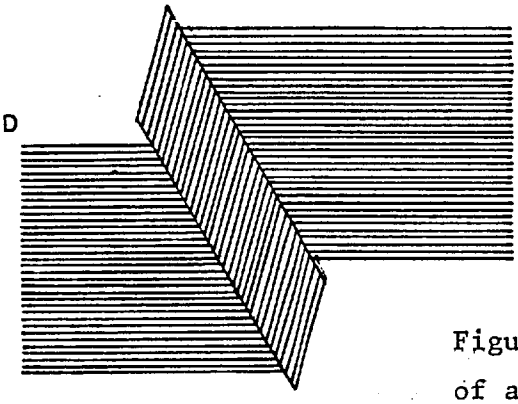
0.005

C



0.014

D



0.022

Figure 3.8 Finite development of an angular rotation domain under the deformation conditions of model B. (initial foliation inclination $\omega_o = 5^o$, initial domain orientation $\theta_o = 30^o$, N/Q = 100.0)

foliation and finite deformation of the rotation domain is produced, almost entirely, by progressive shear parallel to the foliation. The response illustrated in fig. 3.8 simulates the rotation of a stack of rigid plates as described in Dewey's geometrical 'joint drag' model of kinking. In Dewey's model, the change in the width of the domain (ac - fig. 3.5 can be expressed in terms of the length of the internal foliation (ab - constant), the domain orientation, θ, and the internal foliation orientation, ω, as :

$$(ac) = (ab) \cos (\theta - \omega)$$

This relationship is an exact description of the mechanical response predicted by the equations derived for model B as the anisotropy ratio approaches infinity. Note that the width of the rotation domain corresponding to no foliation rotation ($\omega = 0$) is equal to the finite width at $\omega = 2\theta$ and that the maximum extension across the domain occurs at $\omega = \theta$. Model B and the 'joint drag' model both assume constant volume deformation of internal and external foliation. (Laminae remain in contact in the 'joint drag' model). This is expressed in fig. 3.8 and 3.9 by the initial contraction and subsequent expansion of the distance between specific material points measured parallel to the length of the rotation domain.

(iii) An important difference between the finite response of the two models concerns the development of 'locking' of the foliation during the later stages of foliation rotation. This phenomenon is closely associated with the constant volume direct strain compatibility conditions which govern the response of model A. It is expressed in the stabilisation of internal foliation attitude seen in fig. 3.9 (D) , and in the dramatic decrease in incremental foliation rotation rate for $\omega > \theta$ illustrated graphically in fig. 3.5. Both effects are intimately related to the internal stress modifications which act to reduce the induced internal band normal direct strain rate to the effectively isotropic rate in the external foliation. Locking of the foliation attitude will not occur if discontinuities (or gradients) in band normal direct strain rate can develop across a structure throughout finite deformation. Thus there is no tendency for stabilisation of the

MODEL A

Finite strain ε_{11} in external foliation.

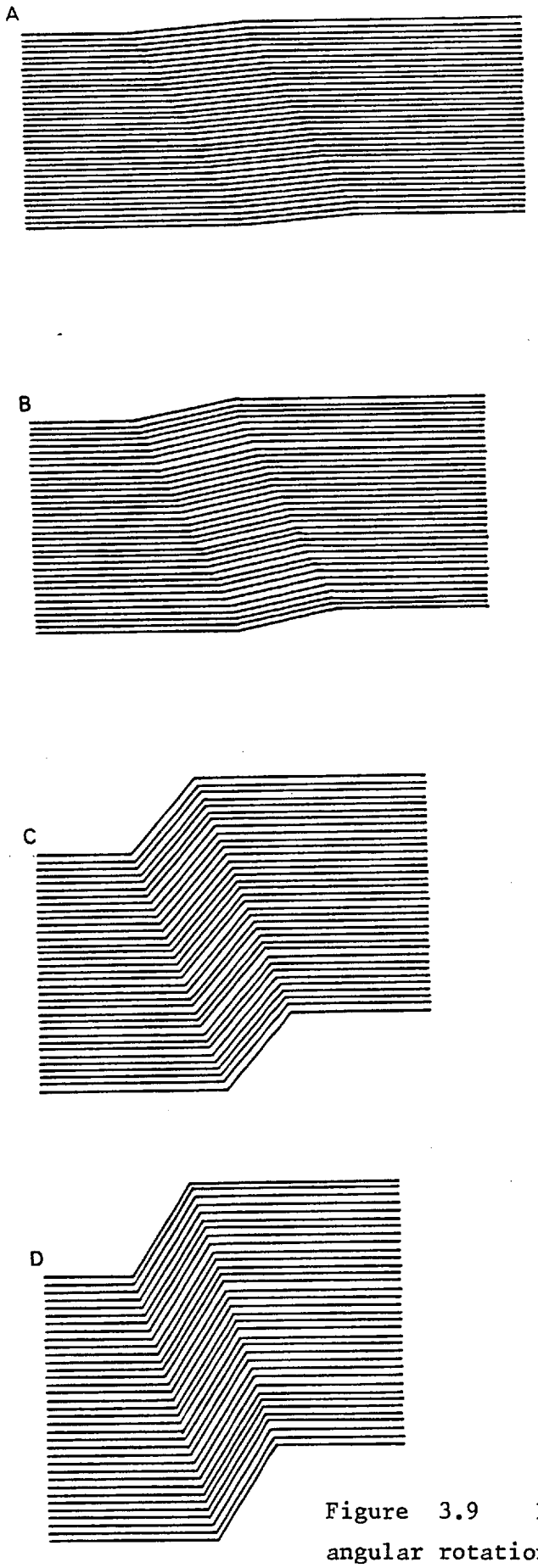


Figure 3.9 Finite development of an angular rotation domain under the deformation conditions of model A. (initial foliation inclination $\omega_o = 5^o$, initial domain orientation $\theta_o = 30^o$, N/Q = 100.0)

foliation to develop beyond the band normal foliation attitude, $\dot{\omega} = \theta$, in the finite deformation model shown in fig. 3.8. The absence of locking or "rotational hardening" in model B is also apparent from a comparison of the shape of the incremental foliation rotation rate profile predicted for this model (fig. 3.6) with that predicted for model A (fig. 3.7).

Relevance of models A and B to the problem of the effect of volumetric strain on the predictions of the rotation domain analysis

The significant differences between the behaviour quantified for models A and B can be directly related to the total breakdown in the conditions of direct strain compatibility in the latter model. Now, as has been demonstrated earlier in this section, the conditions of direct strain compatibility which underly the derivation of the constant volume rotation domain analysis of chapter 2 (model A) will also be relaxed if volumetric strain is available as a mechanism of deformation (model C). It has been shown that, in this case, although the rate of domain parallel direct strain, $\dot{e}_{yy}$, must be uniform across a structure ($\partial\dot{e}_{yy}/\partial x = 0$ as in model A), the associated strain compatibility condition, $\partial\dot{e}_{xx}/\partial x$, no longer applies ($\partial\dot{e}_{xx}/\partial x \neq 0$ as in model B). Thus, if local volumetric strain of defined foliation elements can occur, then the local incremental strain rate, $\dot{e}_{xx}$, induced within the structure is no longer conditioned by the slow, effectively isotropic rate induced within the external foliation. The development of volumetric strain will tend to increase the rate of foliation rotation by allowing local incremental expansion or contraction in the width of foliation elements to contribute to the development of foliation rotation. The main constraint on the extent to which volumetric strain will contribute to the rate of amplification of a structure developed in a particular material is the energy required to produce volumetric strain at a given stage in deformation. Although it has not been possible to construct a quantitative model which incorporates volumetric strain, the influence of the mechanical effects of material anisotropy on the development of volumetric strain within a structure developed in a discretely layered material can be illustrated by considering the contrasting types of behaviour predicted for the deformation conditions of models A and B. In particular, it can be demonstrated that:

i) The variation in volumetric strain, induced across a particular structure during an increment of deformation, will tend to reflect the gradients in mean stress which have been predicted for the deformation conditions of model A.

ii) The local expression of volumetric strain will tend to reflect the development of gradients in induced, domain normal strain rate, $\dot{e}_{xx}$, which are predicted for the deformation conditions of model B. In contrast to model B, which is constrained to deform at constant volume, these gradients in domain normal direct strain rate are not accompanied by the development of sympathetic gradients in domain parallel direct strain rate.

These points can be clarified by examining the behaviour of the simple model shown in fig. 3.10. The structure shown in this figure represents an angular rotation domain (uniform internal foliation orientation) developed in a layered material with the laminar characteristics of a "card deck". The model has been proposed as a geometric model of kink development by Donath (1968) and Clifford (1968). It is assumed that the laminae within the kink or rotation domain rotate as rigid plates which are effectively "hinged" at the domain boundaries. The kinked laminae retain both constant length (ab) and constant orthogonal thickness during rotation. Deformation is assumed to be confined to the rotation domain and the orientation of the domain boundaries remains fixed. The *a priori* assumption that the length of the kinked limbs remains invariant is equivalent to the assumption that the laminated material is infinitely anisotropic ($N/Q = \omega$).

It is a simple matter to demonstrate that, under the conditions noted above, the kinked laminae must separate during initial rotation up to the domain normal position $\omega = \theta$ (fig. 3.10 A, B) and that dilation within the rotation domain is maximum when $\omega = \theta$. With continued rotation, past the domain normal position, the laminae will close and return to a position of contact when the angle of rotation $\omega = 2\theta$ (fig. 3.10 C).

The initial expansion and subsequent contraction in the volume of the rotation domain illustrated in fig. 3.10 can be related

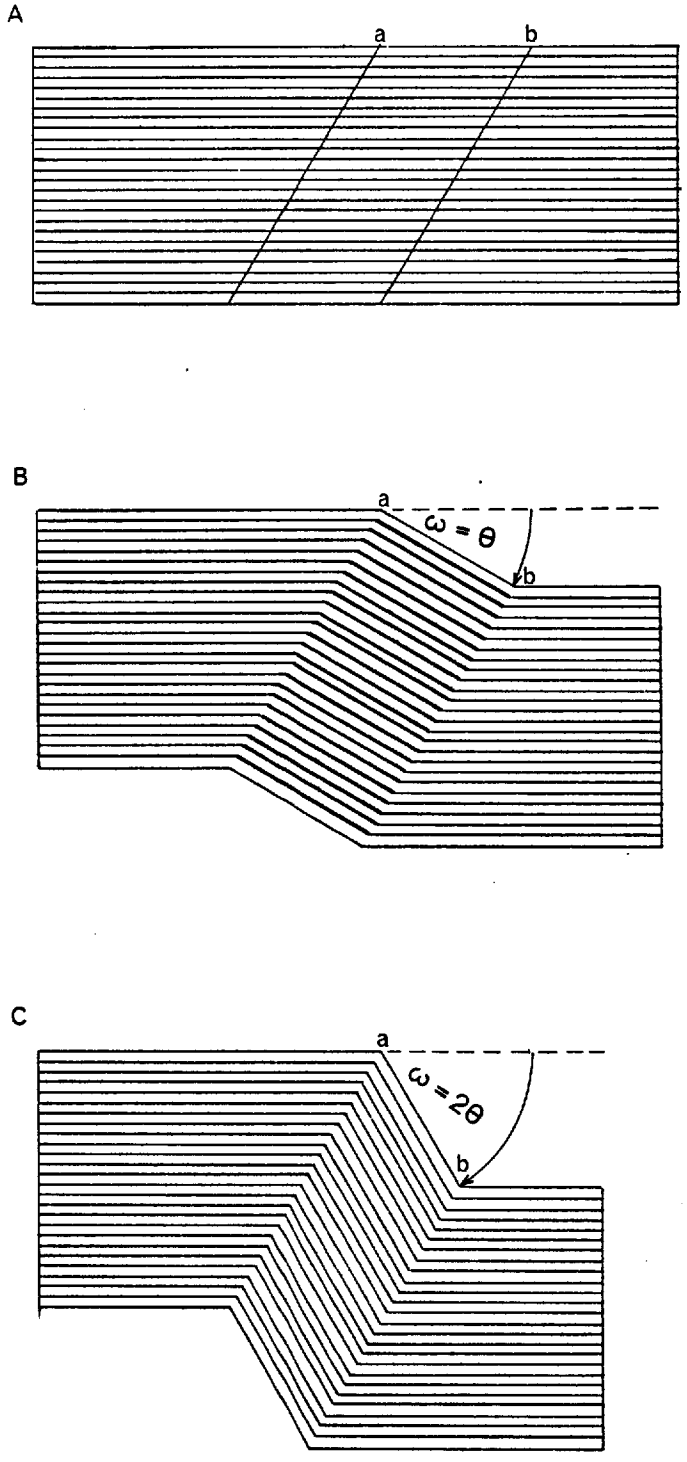


Figure 3.11 'Rotation-dilation' model of kink development in card deck multilayer. See text for details.

to the contrast in internal and external mean stress which must develop under the constant volume compatibility conditions of model A. It will be recalled from the discussion of internal stress modification in section 2.3.5 that a decrease in the relative magnitude of the internal mean stress is predicted for foliation rotation up to domain normal position $\omega = \theta$. For foliation rotation past the domain normal position, an increase in the magnitude of the internal mean stress relative to the mean stress in the external foliation is predicted. If volumetric strain can occur then it would be anticipated that volume increase would be expected in zones of relatively low (relatively tensile) mean stress and that volume decrease would be expected in zones of relatively high (compressive) mean stress. If this argument is applied to the model illustrated in fig. 3.10, in which volumetric strain of the unrotated external foliation is prohibited, then an increase in the volume of the rotation domain would be anticipated over the range $0^0 < \omega < \theta$ and a subsequent volume decrease would be anticipated over the range $\theta < \omega < 90^0$. This is exactly the behaviour which is shown by the model illustrated in fig. 3.10.

The relevance of model B to the development of volumetric strain in the angular rotation domain shown in fig. 3.10 can be seen in the macroscopic expression of volumetric strain within the rotation domain. It has been demonstrated in a discussion of the properties of model B that an angular rotation domain which is unconstrained by conditions of boundary strain compatibility will tend to undergo an increase in width for foliation rotation over the range $0^0 < \omega < \theta$ and that the width of the domain will subsequently decrease for further foliation through the range $\theta < \omega < 90^0$. In model B the expansion and subsequent contraction in the width of the domain is accompanied by a complimentary contraction and subsequent expansion in the length of the domain, measured parallel to the domain boundaries.

An examination of the behaviour of the model illustrated in fig. 3.10 shows that a similar initial increase ($0^0 < \omega < 90^0$) and subsequent decrease ($\theta < \omega < 90^0$) in the width of the angular rotation domain occurs during finite rotation of the internal laminae. In contrast to model B, however, there is no compensating contraction and subsequent expansion in the orthogonal direction, along the length of the domain. The distance between any two points within the rotation

domain, measured along the domain parallel y coordinate, is constant throughout the rotation of the laminae reflecting the macroscopic strain compatibilty conditions $\partial \dot{e}_{yy}/\partial x = 0$ and $\dot{e}_{xx}^{\,i} = \dot{e}_{xx}^{\,e}$ (= 0 for no deformation of the external foliation).

As in model B, local expansion and subsequent contraction in the width of the rotation domain contributes to an enhanced rate of foliation rotation and the rotation domain boundaries may remain effectively fixed in position (no deformation in the external foliation). for a large finite rotation of the internal laminae. Once the laminae have returned to a position of contact (fig. 3.10 C), however, continued volumetric strain within the rotation domain requires a finite decrease in the volume of the rotation domain. A decrease in the volume of the rotation domain in a 'card deck' multilayer can only be achieved by a process which involves the indirect removal of material from this zone in solution or by diffusion. Such processes are likely to occur at rates which are insignificant in comparison with the rate of volumetric expansion and contraction achieved during the initial phase of delamination. Therefore, once the type of structure illustrated in fig. 3.10 has reached the configuration shown in fig. 3.10 C, the subsequent contribution of macroscopic volumetric strain to the development of rapid laminar rotation will be negligible. It is therefore possible to apply the constant volume equations derived in chapter 2 to deformation of the structure beyond the stage reached in fig. 3.10 C ($\omega = 2\theta$). Inspection of any the incremental rotation rate profiles illustrated in figs. 2.8 A - E indicates that a foliation orientation given by $\omega = 2\theta$ is highly stable for any rotation domain orientation $\theta > 45^0$. Therefore, the structure shown in fig. 3.10 will become effectively locked in the configuration shown in fig. 3.10 C, as has been suggested on geometric grounds by Donath (1968) and others.

CHAPTER 4

4.1 INTRODUCTION

In this chapter, a series of model experiments, which were designed to simulate the development of large scale fold structures in simple sedimentary rock multilayers are described and illustrated. The design of these experiments was based on a simple conceptual model in which a horizontally layered multilayer is laterally compressed above a décollement horizon. The configuration of the models and the apparatus used in the experiments is illustrated in fig. 4.1. The models were various types of multilayers built up from thin sheets of paraffin wax, alternating with seams of lubricant The upper surface of the models were free (unconfined) and the models were separated from the rigid base of the apparatus by a zone of lubricant which acted as a décollement horizon. The apparatus is a simple. rectangular *perspex* tank with vertical sides and a vertical piston is fitted to the open end of the tank. Deformation and folding within the models was induced by the piston, which was driven horizontally, at a constant rate, by a geared electric motor.

The design of these simple experiments is similar to the design of early model experiments, simulating large scale tectonic folding, carried out by Cadell (1889), Willis (1891) and others. Although these early experiments produced a number of interesting results (Willis, for example, demonstrated the significance of initial, low amplitude flexures, at the base of a multilayer sequence, in localising the subsequent development of folding) little attempt was made to control or measure the properties of the model materials and the experiments were designed without any quantitative appreciation of the requirements of scale model theory. (See: Hubbert, 1937). The model materials used to represent indurate sedimentary beds in these experiments were generally to "strong" and, as a result, the role of gravitational body stresses in the development of natural large scale fold structures was not simulated with any accuracy. Willis found it necessary to load his models with a subatantial thickness of lead shot to counteract, artificially, the effects of using model materials

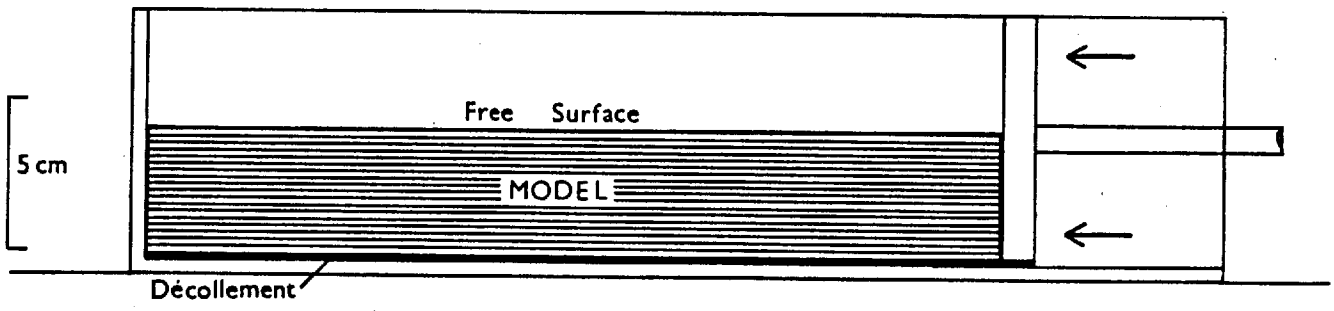


Figure 4.1 Profile sketch of the deformation tank used in the fold simulation experiments. Depth of the model into the plane of the figure, approximately 3 cm.

with a flow strength which is far too high to meet the requirements of scale model theory.

The relevance of scale model theory to experiments which attempt to simulate tectonic processes has been discussed in detail by Hubbert (1937). Hubbert demonstrated that in any experiment designed to simulate a large scale tectonic process it is necessary to reproduce with reasonable accuracy the influence of gravitational body stresses and the relationship between gravitational stresses and other stresses present in a tectonic system. He showed that this places a significant restriction on the magnitude of flow stresses which can be induced within a laboratory model of a large scale process and that the restriction limits the choice of model materials to materials which are rheologically weak. The main features of Hubbert's discussion of scale model theory are outlined in section 4.2.

The experiments described in this chapter were not designed to simulate the development of fold structures in a specific region. However, the design of the experiments is such that the results of the experiments can be compared with natural fold structures developed in a supra-crustal sedimentary sequence, laterally stressed above a décollement horizon. The most obvious comparison is with fold structures developed in the Jura region of S. W. France. In this region the main controls on deformation style within a relatively thin Mesozoic sedimentary blanket were the presence of a décollement horizon at the base of the sedimentary sequence (Triassic evapourites), an underlying basement which was effectively rigid during folding of the overlying sediments and a source of lateral compression within the sedimentary cover. (Buxtorf, 1916; Laubscher, 1973, 1976b). These features are reproduced in simplified form in the author's experiments. However, no attempt was made to reproduce detailed features of the Jura fold belt such as specific variations in thickness within the sedimentary sequence or the presence of fault steps within the basement which may have influenced the development of individual Jura fold structures (see: Laubscher, 1976b).

The first fold simulation experiments carried out by the author were an extension of a previous series of experiments carried out by P. Blay at Imperial College. Blay (1974) developed a technique of constructing model multilayers using gelatine as a model material. He studied the development of structures by simulating (A) Gravity

gliding produced by localised uplift applied to base of a model and (B) simple lateral compression of a horizontally laminated model. This author used Blay's experimental technique and gelatine as a model material to study, in more detail, the development of folds under lateral compression. The results of some of these experiments are illustrated in Blay, Cosgrove and Summers (1977).

Layered models of gelatine were prepared from weak solutions of gelatine powder in water. Each layer component was formed in the apparatus by pouring a solution of known concentration and allowing the solution to gel. The strength and related properties of the resulting gel were controlled by varying the concentration of the solution. In this way, multilayers with particular variations in layer thickness and strength characteristics could be constructed. The model preparation method developed by Blay resolved the problem of handling individual layer components during the preparation of a weak multilayer. However, the method is laborious, requiring up to a week to prepare a single model. Also, models were frequently partially destroyed and made useless at some stage in preparation due to difficulties encountered in pouring successive layers.

In addition to these practical difficulties, there are a number of factors which limit the usefulness of gelatine as model material and should be carefully considered in the interpretation of the results of experiments. On the basis of a series of rheological tests, Blay suggested that gelatine is a visco-elastic material with rheological properties that simulate, with reasonable accuracy, the time dependent creep behaviour observed in a range of indurate sedimentary rock types. In the author's opinion, the rheological tests were somewhat poorly designed and Blay's interpretation of the results of the tests is suspect. Gelatine, at low concentration, is capable of storing large, recoverable elastic strains, even at the slow applied strain rate of approximate 10^{-5} per sec. induced in a typical experiment. In consequence, the development of fold structures incorporated the accumulation and release of elastic strains which were too large to simulate, realistically, the contribution of elastic strain recovery to the development of natural folds. This places an obvious limitation on the geological interpretation of the gelatine experiments. Similar problems also arise in the interpretation of small scale fold simulation experiments using elastic

materials (eg. Honea and Johnson, 1976; Ramberg and Johnson, 1976).

Because of these problems of interpretation, the results of the author's experiments using gelatine as a model material will not be described in this thesis.

An investigation was made of alternative model materials for use in experiments simulating large scale folding. On the basis of a series of rheological tests it was decided that refined paraffin wax was the most suitable material for this purpose. The results of these tests are discussed in section 4.3 and in section 4.4 the theory of scale modelling is applied to these test results to estimate the prototype rock properties which are simulated in the wax multilayer experiments. The results of these fold simulation experiments are considered in section 4.5.

4.2. RELATIONSHIP BETWEEN THE DEFORMATION OF A MODEL AND A PROTOTYPE SYSTEM - THE PRINCIPLES OF SCALE MODELLING.

The classic paper on the principles of scale modelling, as applied to laboratory models designed to simulate tectonic processes, is that of Hubbert (1937). Using a series of simple, idealised examples, Hubbert presented a quantitative discussion of the principles which govern the similarity between a laboratory model deformation and the deformation of an equivalent tectonic prototype. He listed a series of scaling equations (based on the reductions in length scale and time scale which are incorporated in the design of a particular experiment) which can be used to examine the suitability of particular model materials for use in simulation of particular types of tectonic deformation. Hubbert was principally concerned with laboratory models which are designed to simulate large scale tectonic processes in which gravitational potential plays an important role in development of structures. Such experiments would include, for example, models which attempt to simulate the development of diapirism in which gravitational potential is the principal parameter which drives the deformation process. Gravity also plays an important role in modifying the

development of large scale décollement folds of the type investigated in the experiments described in this chapter. In this case, gravity acts as constraint on the amplification of individual fold structures.

The design of any laboratory model of a large scale tectonic process inevitably involves a significant reduction in the scale of the process. This reduction can be defined by the model ratio of length (L_r) which is the ratio of the distance between equivalent points measured in the model (L_m) and in the prototype (L_p).

$$L_r = \frac{L_m}{L_p}$$

In the simulation of a large scale process the magnitude of L_r will usually be in the range 10^{-4} (1 cm. in the model equivalent to 100m. in the prototype) to 10^{-5} (1 cm. in the model equivalent to 1 km. in the prototype). Hubbert demonstrated that, in reducing the scale of the process of interest by this magnitude, it is also necessary to reduce the "strength" of individual components of the model. This reduction follows directly from a consideration of the role of gravitational potential in the model and prototype deformation. The discussion of the scaling of rheological properties given by Hubbert will be outlined briefly in the following paragraphs and will be used to estimate the type of prototype system which was simulated in the author's décollement fold experiments.

The principle which governs the similarity between a model and a prototype is that the relationship between significant physical quantities measured at different locations within a model will be the same as the relationship between the equivalent physical quantities measured at equivalent locations within the prototype. In a model of a dynamic process, the list of significant physical quantities which affect the process include a series of inter-related parameters including length, area, strain, strain rate, stress, flow "strength", etc. Similarity between the behaviour of a model and a prototype at a particular stage in deformation involves:

(i) geometric similarity - a model and prototype are geometrically similar if all angles within the model are equal to the corresponding angles in the prototype. This implies that the ratio between any two eqivalent lengths measured in model and in prototype is a constant

(ii) kinematic similarity - a model and a prototype are kinematically similar if they are geometrically similar at all equivalent stages in the deformation of each.

(iii) dynamic similarity - a model and prototype are dynamically similar if the ratio between any two equivalent components of stress in model and prototype is equal to the ratio between all other equivalent components of stress in model and prototype.

Hubbert's discussion of the necessary relationship between the rheological properties of a model and a large scale tectonic prototype is based on the conditions of dynamic similarity and can be described by an examination of the relationship between components of stress in model and prototype.

Consider, for example, the indealised model and prototype systems shown in figs. 4.2A and 4.2B respectively. The model represents a uniform sequence of thick, competent sedimentary units alternating with thin, incompetent interbeds. In order to simplify the discussion it is assumed that (i) the plane of layering in both model and prototype is horizontal, (ii) the vertical (σ_{yy}) and horizontal (σ_{xx}) components of stress and principal stresses throughout the two systems and (iii) deformation is plane strain in the vertical plane. In this simple example, the model and prototype are viewed at equivalent stages of deformation before the initiation of fold instabilities within the multilayer sequences.

It is possible to demonstrate the derivation of Hubbert's scaling equations by considering the relationship between the state of stress in locally equivalent elements of the model and prototype systems illustrated in fig.4.2. For the purpose of this discussion, these equivalent elements are assumed to represent the local response of equivalent competent units to layer parallel shortening.

The state of stress within the model and prototype can be conveniently separated into a body stress field associated with the variation

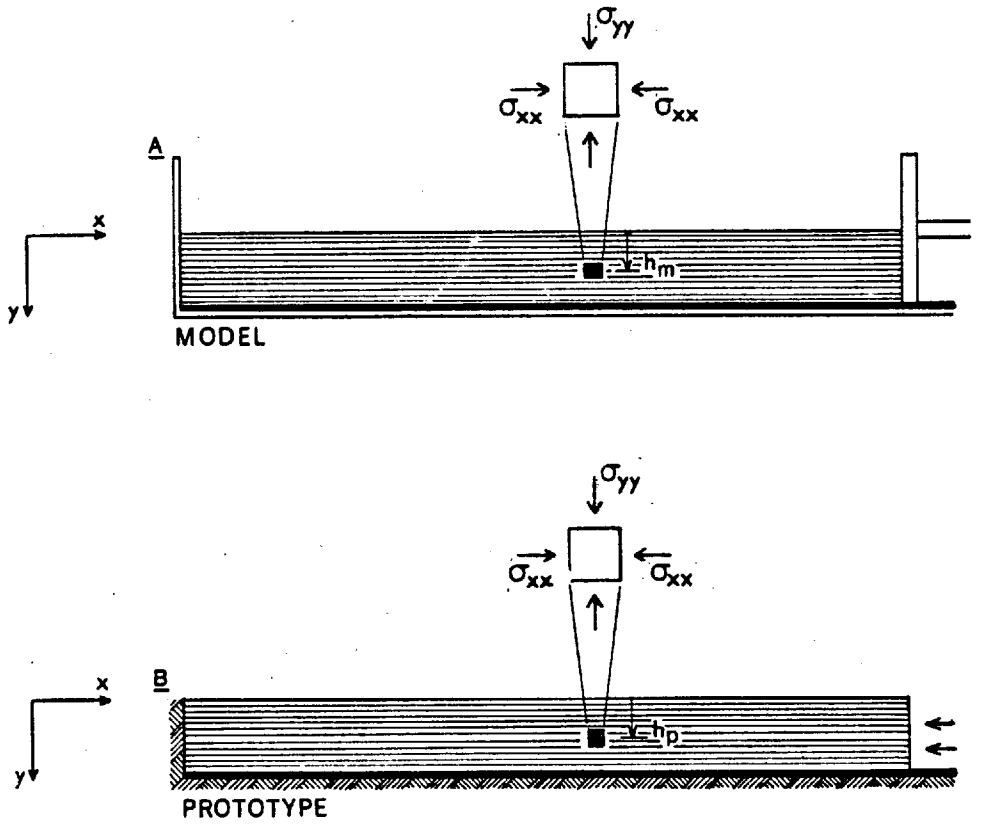


Figure 4.2 See text for discussion.

in gravitational potential and a superimposed "tectonic" stress field resulting from the resistance of the model and prototype to the applied boundary displacements. The magnitude of these induced stresses will obviously be a function of the rheological properties of the components of model and prototype and the state of finite strain and incremental strain rate within each.

During an equivalent increment of deformation of the model and the prototype elements identified in fig. 4.2, the gravitational stress acting on these elements can be represented by the vertical stress components $(\sigma_{yy})_m$ and $(\sigma_{yy})_p$ (subscripts m and p representing model and prototype respectively). The induced tectonic stresses can be represented by the horizontal differential stresses $(\sigma_{xx}-\sigma_{yy})_m$ and $(\sigma_{xx}-\sigma_{yy})_p$. If the principle of scale modelling is applied to the relationship between equivalent components of stress in the model and in the prototype then it can be stated, for example, that the ratio between vertical stress, σ_{yy}, and horizontal differential stress must be the same in equivalent elements of model and prototype. Thus, for the elements shown in fig. 4.2:

$$\frac{(\sigma_{yy})_m}{(\sigma_{xx}-\sigma_{yy})_m} = \frac{(\sigma_{yy})_p}{(\sigma_{xx}-\sigma_{yy})_p} \qquad \ldots\ldots 4.1$$

Rearranging this equation:

$$\frac{(\sigma_{xx}-\sigma_{yy})_m}{(\sigma_{xx}-\sigma_{yy})_p} = \frac{(\sigma_{yy})_m}{(\sigma_{yy})_p} \qquad \ldots\ldots 4.2$$

This simple relationship expressed in this equation can be extended to any other set of equivalent stress components in model and prototype. The relationship implies that the ratio between any two locally equivalent stresses in model and prototype must be equal to the ratio between gravitational body stresses at equivalent depths within model and prototype. This condition has important consequences since it can be

shown that the stress ratio is determined principally by the choice of length scaling which is applied in the design of an experiment. The magnitude of the vertical component of gravitational stress is given by the product of depth h, specific gravity ρ (assumed constant with depth) and g, the acceleration constant associated with body stress field.

Thus: $$(\sigma_{yy})_m = \rho_m h_m g_m$$

$$(\sigma_{yy})_p = \rho_p h_p g_p$$

and: $$\frac{(\sigma_{yy})_p}{(\sigma_{yy})_p} = \frac{\rho_m h_m g_m}{\rho_p h_p g_p} = \rho_r L_r$$

.... - where ρ_r = model ratio of (equivalent) specific gravities, L_r ($= h_m/h_p$) = model ratio of (equivalent) lengths, and, since both model and prototype are deformed in the gravitational field of the earth g_r($= g_m/g_p$) = 1.

Combining equations 4.2 and 4.3:

$$\simeq \quad \frac{\sigma_m}{\sigma_p} = \frac{(\sigma_{xx} - \sigma_{yy})_m}{(\sigma_{xx} - \sigma_{yy})_p} = \frac{(\sigma_{yy})_m}{(\sigma_{yy})_p} = \rho_r L_r \qquad \ldots\ldots 4.3$$

Thus the ratio between any two equivalent stress components in the model (σ_m) and the prototype (σ_p) is equal to the product of the model ratios of length and specific gravity. This relationship is illustrated graphically in fig. 4.3 for a model ratio of specific gravity of 0.5 and for $L_r = 10^{-4}$ and 10^{-5}. It can be seen from this figure that a range in prototype stress of 10 bars to 1 kb. corresponds to an equivalent range in model differential stress of 0.05 gm cm^{-2} to 5.0 gm.cm^{-2} at $L_r = 10^{-4}$. If the horizontal differential stress, induced locally with the prototype, is 100 bars and the reduction in length scale applied in the design of a model of this prototype is 10^{-5}, then the equivalent local differential stress

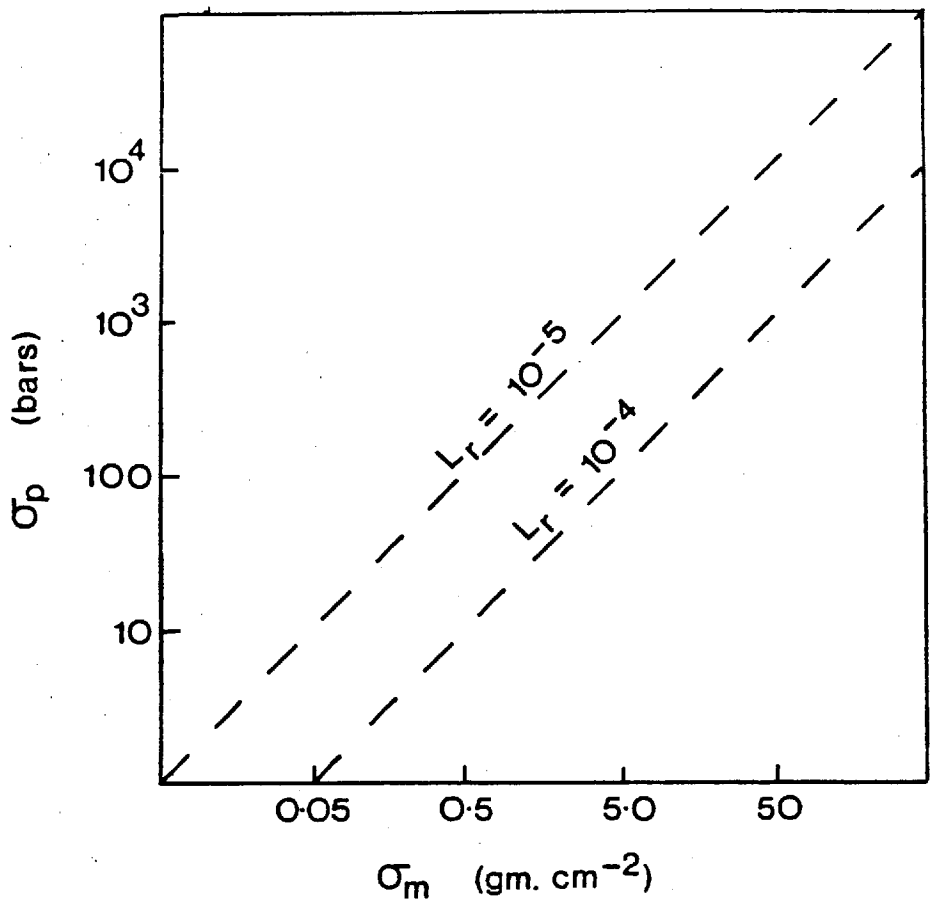


Figure 4.3 Relationship between equivalent components of stress in model (σ_m) and protoype (σ_p) calculated for a model ratio of specific gravity of $\rho_r = 0.5$ and for model ratios of length, $L_r = 10^{-4}$ and 10^{-5}.

within the model is 0.5 gm. cm^{-2}

The variation in gravitational body stress through a tectonic prototype is automatically simulated in a geometrically equivalent model by the natural gravitational field of the earth. All other stress components present in model and prototype must then be scaled in accord with the reduction in gravitational body stress. However, although similarity in stress and stress variation at a particular stage in deformation of a model and prototype is a necessary condition for similarity of finite deformation, the nature of locally equivalent stresses in model and prototype must be the same, i.e. equivalent components of model and prototype must have equivalent rheological properties. Hubbert (1937) demonstrated that the condition of stress similarity contained in equation 4.3 can be used to define the reduction in magnitude of equivalent rheological moduli which must be incorporated in the design of an experiment. This can be demonstrated by examining the relationship between the state of finite strain or incremental strain rate and the local state of stress within equivalent elements of model and prototype.

Consider for example the idealised case in which the model and prototype illustrated in fig. 4.2. are made up of layer compoents with linear elastic properties. At an equivalent stage of deformation, the state of finite strain must be the same in equivalent elements of model and prototype. The locally induced horizontal differential stress will be proportional to the product of the local elastic modulus, G, and the local strain, e_{xx}. For equivalent increments of strain in model and prototype, $(e_{xx})_m = (e_{xx})_p$ and :

$$\frac{(\sigma_{xx} - \sigma_{yy})_m / (e_{xx})_m}{(\sigma_{xx} - \sigma_{yy})_p / (e_{xx})_p} \cdot \frac{(\sigma_{xx} - \sigma_{yy})}{(\sigma_{xx} - \sigma_{yy})} = \frac{G_m}{G_p} = G_r \qquad 4.4$$

... where G_r is the model ratio of elastic rigidity modulus.

Combining equations 4.4 and 4.3:

$$G_r = \rho_r L_r \qquad 4.5$$

The model ratio of specific gravity, ρ_r, can take on only a small range of values.

Thus the reduction in local elastic modulus, involved in the design of the experiment, is determined principally by the reduction in length scale, L_r.

A similar relationship can be obtained for the scaling of a prototype made up of layer components with linear viscous rheologies. In this case, it is necessary to consider equivalent increments of deformation in model and prototype. The local incremental strain associated with such a deformation increment will be the same in equivalent elements of the model and the prototype. However, the duration of this increment and, therefore, the strain rate associated with the deformation increment will not be the same. If the duration is given by t_m in the model and t_p in the prototype, then the horizontal strain rate, $\dot{e}_{xx}$, induced in equivalent elements of model and prototype is given by:

$$(\dot{e}_{xx})_m = e_{xx}/t_m$$

$$(\dot{e}_{xx})_p = e_{xx}/t_p$$

The local horizontal differential stress is proportional to the product of the local viscous modulus, μ, and the locally induced strain rate, $\dot{e}_{xx}$, and:

$$\frac{(\sigma_{xx} - \sigma_{yy})_m}{(\sigma_{xx} - \sigma_{yy})_p} = \frac{\mu_m . (\dot{e}_{xx})_m}{\mu_p . (\dot{e}_{xx})_p} = \frac{\mu_m . t_p}{\mu_p . t_m} \qquad \ldots\ldots 4.6$$

Combining equations 4.6 and 4.3:

$$\frac{\mu_m . (\dot{e}_{xx})_m}{\mu_p . (\dot{e}_{xx})_p} = \rho_r L_r \qquad \ldots\ldots 4.7$$

and $$\mu_r = \frac{\mu_m}{\mu_p} = \rho_r L_r t_r$$

... where t_r is the model ratio (equivalent) times and μ_r is the model ratio of (equivalent) viscosities.

It can be seen from equations 4.7 and 4.8 that the choice of length scaling involved in the design of an experiment does not determine, uniquely, the magnitude of model material viscosity required to simulate a particular prototype material viscosity. In order to do this, it is necessary to define the reduction in time scale involved in the model experiment by considering the relationship between strain rates induced in model and prototype. Similar methods to those described above can be applied to the scaling of more complex and non-linear rheological properties.

4.3 RHEOLOGICAL TESTS ON THE MODEL MATERIALS USED IN THE FOLD SIMULATION EXPERIMENTS.

There were a number of considerations which led to the choice of paraffin wax as a model material for use in the large scale fold simulation experiments. It has been demonstrated in section 4.2 that , in such experiments, it is necessary to use model materials which are capable of deforming, at experimentally reasonable strain rates, under very low differential stresses of the order of grammes or fractions of grammes per sq. cm. This immediately leads to the practical problem in constructing laminated models from such weak materials.

The grades of paraffin wax used in the experiments are strong at room temperature. Thus it was possible to handle very thin sheets of the material (1mm thickness or less) at room temperature and prepare and transport finely laminated models with very little difficulty. (The method of preparation of the model multilayers is outlined in appendix 4.1.) The strength of the paraffin wax could then be reduced to the levels required by the theory of scale modelling by raising the temperature of the model multilayers. This was achieved by running the experiments in the large, purpose-built oven which is described in appendix 4.3.

Once an experiment was completed the model was allowed to cool back to room temperature. The model could then be removed from the apparatus, sectioned if required, photographed and stored indefinitely.

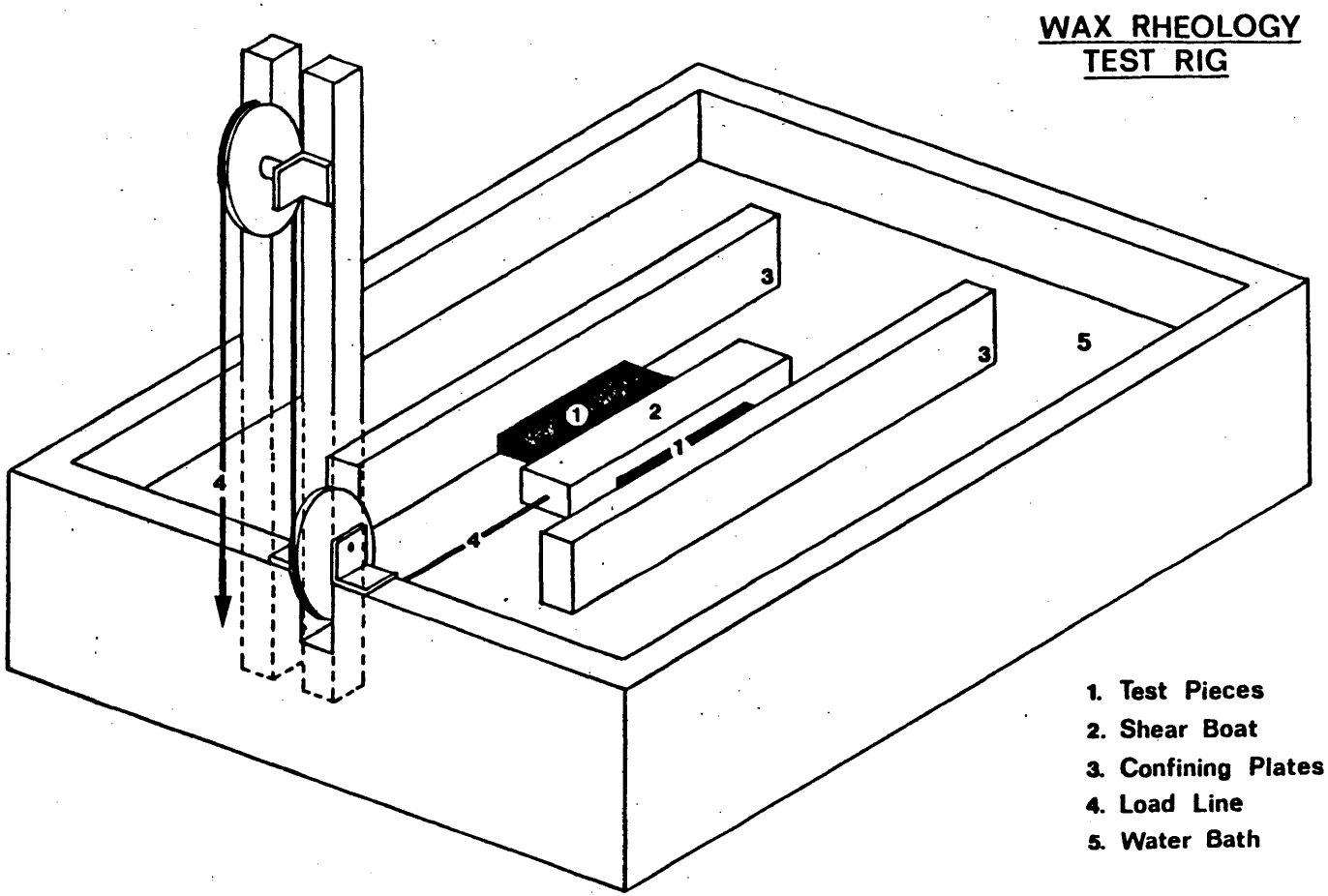


Figure 4.4 Test rig used in the study of the rheological properties of paraffin wax and paraffin wax multilayers.

A test rig, fig 4.4, was designed and built to test the rheological properties of the model materials. The apparatus was designed to study the behaviour of two rectangular wax blocks (approximately 1 cm. x 1 cm. x 5 cm.) deformed in simple shear under a constant shear stress. Two types of test blocks were used:

(a) uniform wax blocks

(b) representative multilayered wax blocks.

The procedure used in carrying out a test was as follows:

(i) Two identical test pieces (1) were machine prepared at room temperature and their initial dimensions measured with a Vernier screw gauge.

(ii) The test pieces were floated on the surface of a water bath which partly filled the apparatus.

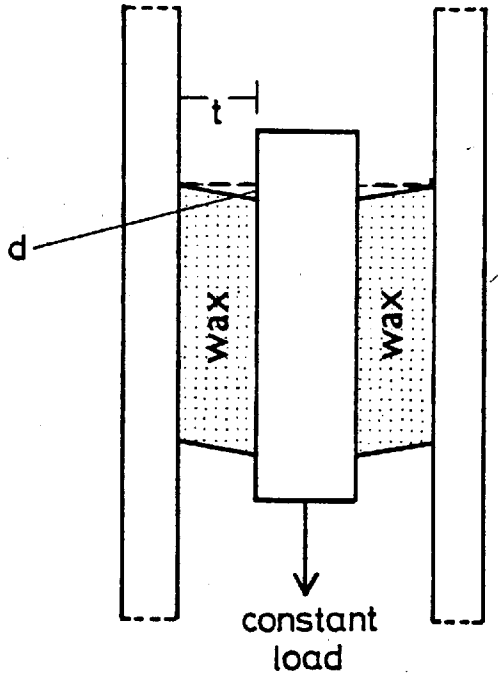
(iii) A buoyant boat (2) with vertical gridded sides was floated between the test pieces. The vertical sides plates (3) were then adjusted by a series of screws to clamp the test pieces firmly against the central floating boat.

(iv) Once the test pieces were clamped in position, the temperature of the water bath was raised to the required test temperature through a copper heat exchange pipe at the base of the water bath, (not shown in fig. 4.4). The temperature was stabilised by the use of a sensitive electronic thermostat which controlled the heating system (see: appendix 4.1). The temperature of the test pieces was measured indirectly by a thermocouple embedded in a dummy test piece floating next to the blocks under test.

(v) When the temperature of the test pieces had stabilised at the required test temperature the constant shear load was applied. This load was produced by a set of known weights attached to the load line (fig. 4.5). Tension in the load line induced a constant horizontal shear stress acting on the vertical faces of the test pieces through the central floating boat.

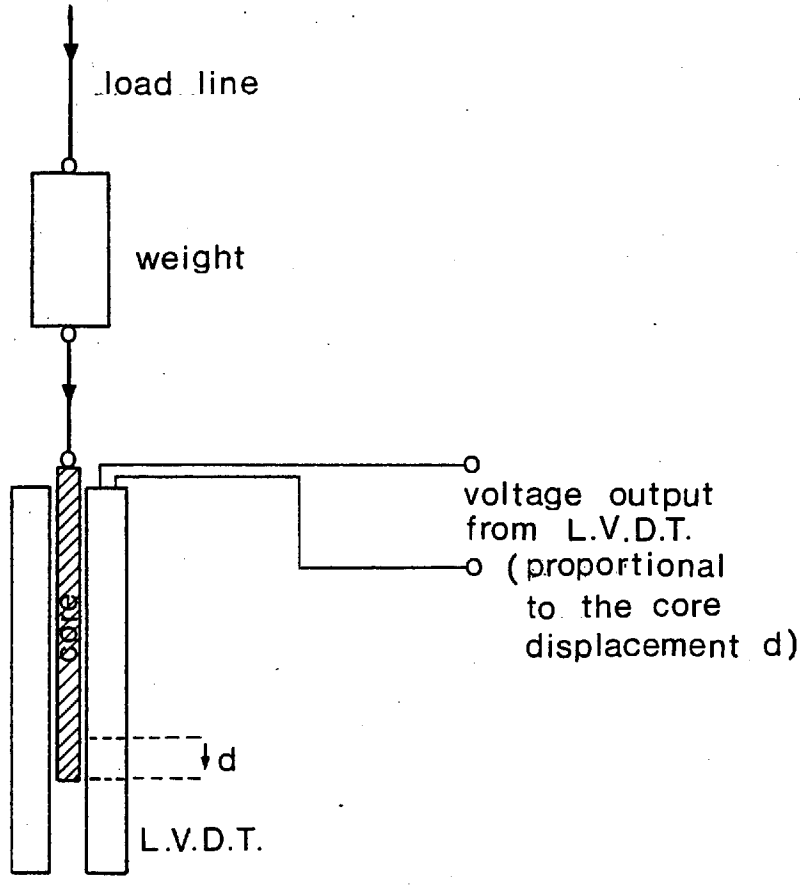
The horizontal displacement of the floating boat (d - fig.4.5) was measured by the movement of the core of a linear variable displacement transformer. The core was attached to the load line (fig. 4.6) and formed part of the known load. The voltage output of the L.V.D.T. produced a very sensitive measure of the shear displacement of the

Figure 4.5



shear strain = d/t

Figure 4.6



test pieces. The voltage signal was displayed on a multi-channel chart recorder and was easily converted into a graphical representation of shear strain against elapsed time by calibrating the L.V.D.T. voltage output to displacement (d) and expressing the finite displacement as shear strain within the test pieces (d/t). The chart recorder was also wired to display temperature data from a series of thermocouples monitoring the temperature of the dummy test piece and the water bath. Details of temperature stability of the apparatus and the sensitivity of the displacement and temperature calibrations are included in appendix 4.2.

The design of the apparatus resulted in a number of advantages in the testing of rheologically weak materials. In addition to providing a source of heat input and temperature stability, the use of the water bath and the floatation method employed in the tests ensured that no unwanted stresses acted on the test pieces. Because the boat and wax blocks were in buoyant equilibrium throughout a test the wax was subjected only to the known horizontal shear load. The vertical faces of the blocks maintained constant area during a test and were thus subjected to a constant and known shear stress. Friction in the pulley system was reduced to a minimum by the use of roller bearings and lubricant. The tests produced an accurate and sensitive measure of the response of the test pieces to stress.

4.3.1 Results of the tests

The typical form a shear stress - time creep curve produced in tests on uniform blocks of wax is shown in fig. 4.7. The curves show the classic stages of creep.

(i) An instantaneous elastic strain (oa).

(ii) A period of time dependent recoverable strain - primary or transient creep. (ab).

(iii) A period of steady state creep at constant shear strain rate (bc).

A feature of the tests on uniform wax blocks was that the shear strain rate, developed during steady state creep, was remarkably constant, at least up to approximately 0.3 shear strain. There was no tendency for strain hardening or strain softening to occur. Above

0.3 shear strain the deformation of the test pieces became somewhat heterogeneous because of end effects within individual test blocks.

The tests were carried out on the two grades of wax used in the model experiments (melting points 54°C and 45°C) and on multilayered specimens made up from stacks of uniform wax sheets separated by seams of silicone grease or liquid soap (corresponding to the two interlayer lubricants used in the majority of the fold simulation experiments). Preliminary tests indicated that 54°C m.pt. wax possesses a creep strength making it suitable for use in experiments simulating large scale tectonic processes ($L_r = 10^{-4}$, 10^{-5}) only at temperatures above approximately 35°C. The rheological tests were therefore concentrated on the temperature range 35 - 44°C, i.e. the temperature range used in the fold simulation experiments.

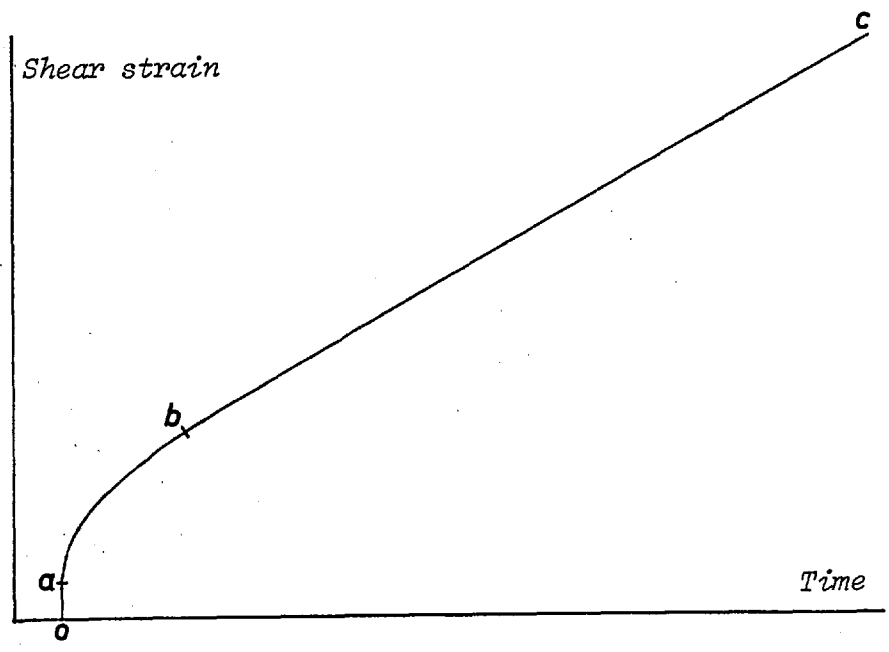


Fig. 4.7
Displacement/time creep curve reproduced directly from chart recorder output.

Figure 4.8

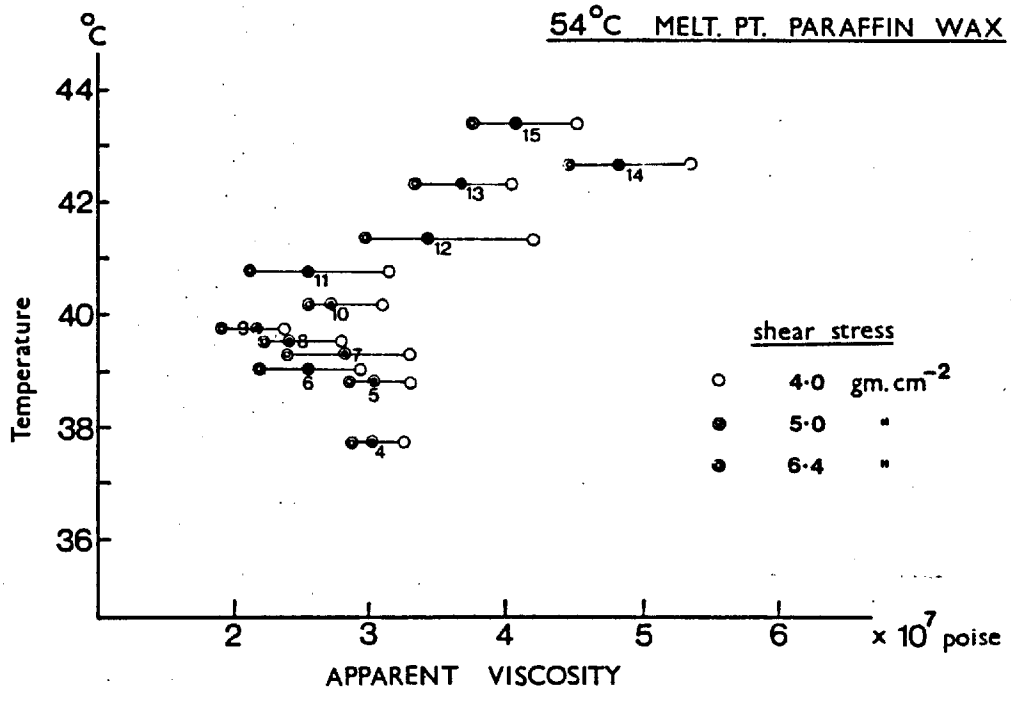
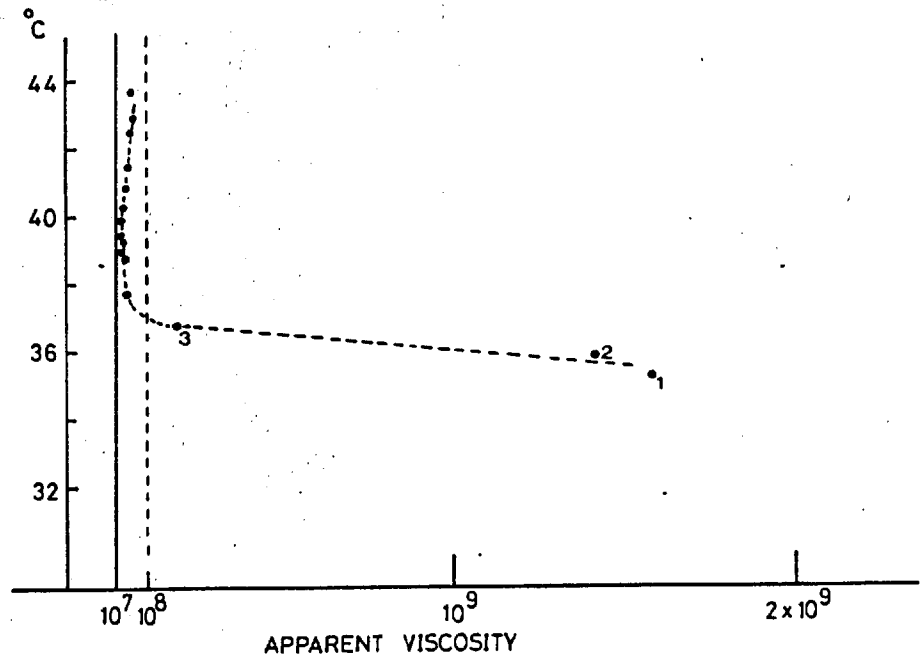


Figure 4.9



$54^{o}C$ Melting point paraffin wax

STEADY STATE CREEP

The strength of the uniform wax test blocks, during steady state creep, can be expressed by the apparent viscosity, μ, measured for a given value of applied shear stress. μ is obtained from the test results by calculating the ratio of applied shear stress (τ) to the associated, steady state, shear strain rate ($\dot{\gamma}$):

$$\mu = \tau/\dot{\gamma}$$

At each test temperature, three different levels of shear stress (τ = 4.0, 5.0, 6.4 $gm.cm^{-2}$) were applied to the tests blocks to investigate the relationship between applied stress and strain rate, during steady state creep. The results of these tests are illustrated in fig.4.8 in which the calculated apparent viscosity, μ, is plotted as a function of the test temperature for each of the three applied stress levels. The data for the intermediate value of constant shear stress (τ = 5.0 $gm.cm^{-2}$) are reproduced in fig. 4.9 , using a graph with expanded viscosity and temperature axes in order to include data (tests 1, 2 and 3) from three tests carried out at relatively low temperatures. The results of this investigation into the behaviour of the $54^{o}C$ m.pt. wax grade during steady state creep show the following features:

(i) The measured apparent viscosity is a function of the applied shear stress and, therefore, the relationship between shear stress and shear strain rate is non-linear. It is clearly difficult to specify the nature of the stress-strain rate relationship on the basis of results obtained using a limited range of applied stress. An attempt has been made, however, to see how closely the test results fit a power law stress-strain rate relationship of the form:

$$\dot{\gamma} = K \tau^n$$

The type of relationship leads to a linear relationship between the logarithm of stress and strain rate.

$$\log_{10} (\dot{\gamma}) = C + n \log_{10} (\tau)$$

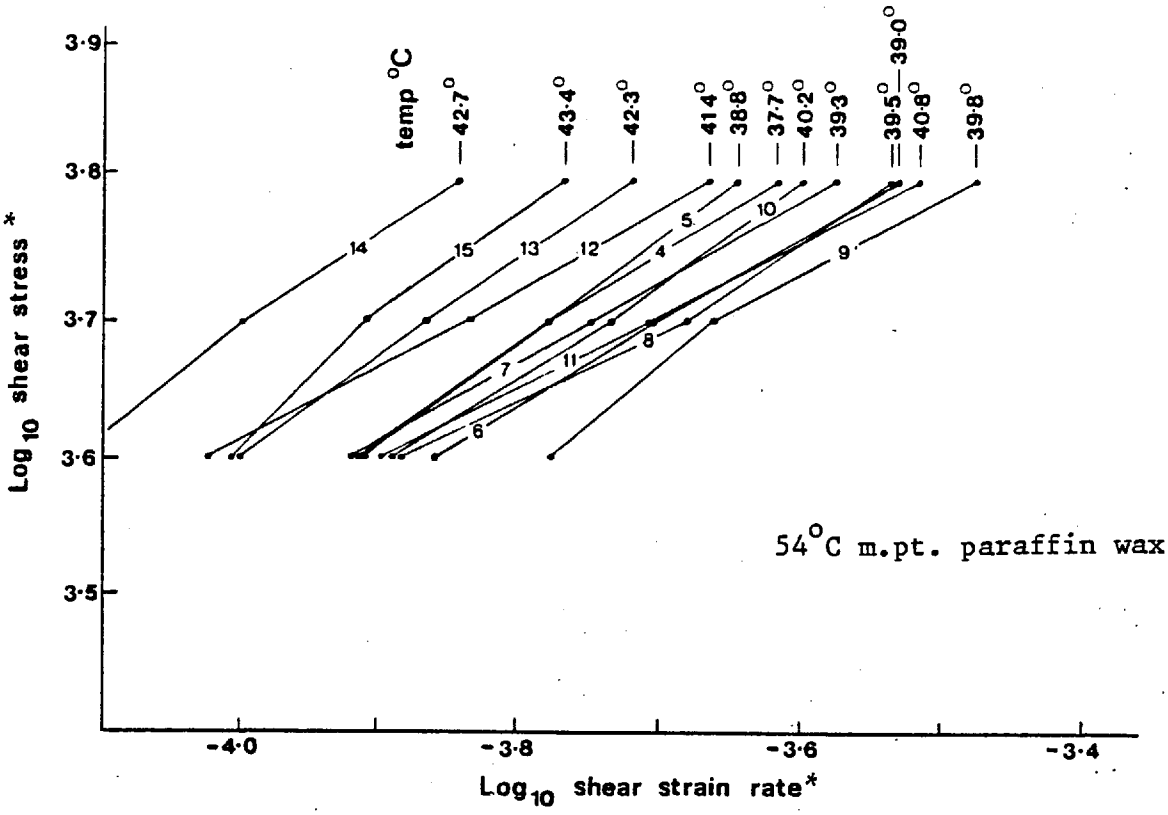
where: C (= $\log_{10}$ K) is a constant under specific conditions of deformation

The magnitude of the stress exponent, n, can be calculated from the slope of the straight line plot of $\log_{10}(\dot{\gamma})$ against $\log_{10}(\tau)$.

$$\frac{d (\log_{10} (\dot{\gamma}))}{d (\log_{10} (\tau))} = n$$

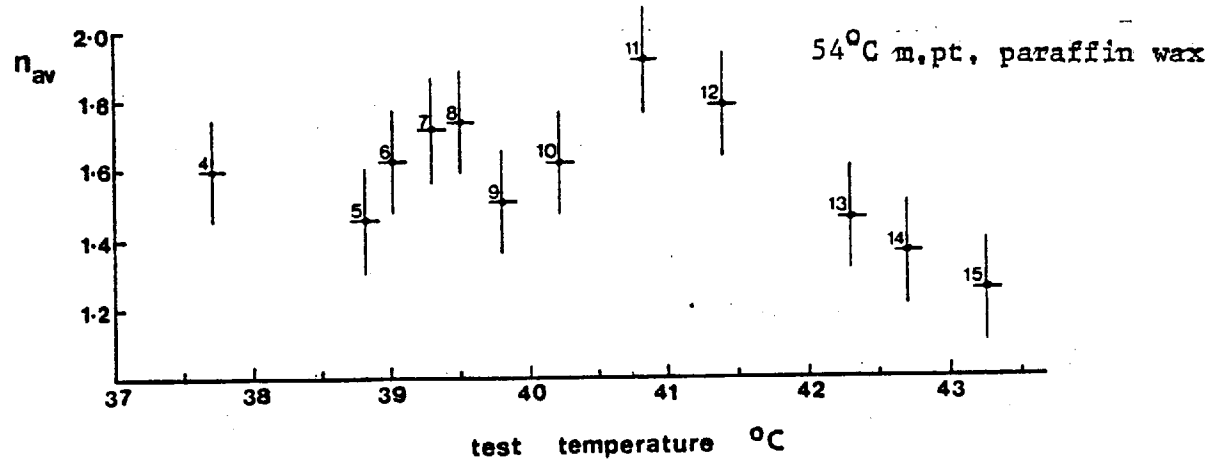
Data from twelve tests carried out in the temperature range 37°C to 44°C are shown in the form of a plot of $\log_{10}(\dot{\gamma})$ against $\log_{10}(\tau)$ in fig. 4.10 for the three stress levels used at each test temperature. Within the limits of experimental error, the data produces a reasonable fit to a straight line relationship between $\log_{10}(\dot{\gamma})$ and $\log_{10}(\tau)$ (exceptions are tests 8, 9 and 15). It is suggested that the relationship between stress and strain rate during steady state creep can be approximated by a power law relationship, at least over the restricted range of applied stress used in the creep tests. The magnitude of the slope of the logarithmic relationship shown in fig. 4.10 has been calculated for the two straight line intervals shown in this figure, for each test temperature. The average of these two values of slope has been used to estimate the magnitude of the stress exponent, n, at each test temperature. The resulting variation in the calculated value of n with temperature is illustrated in fig.4.11. There is no consistent relationship between n and temperature over the temperature range

Figure 4.10



(Stress - $gm.cm^{-2}$ x 10^{-3} , strain - per sec)

Figure 4.11



covered in fig. 4.11, n lies in the range 1.0 to 2.0 over the temperature range with an average value of approximately n = 1.6. Although the stress-strain rate relationship calculated for this wax grade is non-linear, the degree of non-linearity is substantially less than certain other materials which have been used in tectonic simulation experiments (McClay (1972) for example has indicated, on the basis of a series of rheological tests, that standard grade "plasticene" obeys a power law stress-strain rate relationship with a stress exponent of n = 7 - 9).

(ii) The variation in the steady state creep strength of 54°C m.pt. paraffin wax with temperature (figs. 4.8 and 4.9, shows the following features:

(a) There is a very significant decrease in strength, as expressed by apparent viscosity μ, over a small range in temperature (approximately 36.5°C - 37.5°C). It is possible that this temperature softening is due to the melting of a small fraction of low melting point material surrounding the grains of higher melting point (54°C) wax, which make up the bulk of the material. Such a process would greatly facilitate the development of grain boundary sliding as the dominant deformation mechanisms above the temperature range over which "softening" occurs. There is a decrease in apparent viscosity over the small range of temperature 36.5°C - 37.5°C of approximately two orders of magnitude. (This strength reduction is clearly reflected in the results of fold simulation experiments carried out below and above the "softening" temperature — see section 4.5).

(b) At temperatures above approximately 38.5°C there is relatively small but definite increase in apparent viscosity with increase in temperature up to the maximum temperature investigated in the rheological tests. This anomalous behaviour is clearly shown by the test results illustrated in fig. 4.8 (tests carried out at a specific, constant temperature) and was also observed in tests in which the test temperature was allowed to increase or decrease during steady state creep. The cause of this behaviour is not understood.

Instantaneous and time dependent elastic properties

Because of the low magnitude of the initial, instantaneous elastic shear strain induced in the uniform wax test blocks at the stress levels used in the tests ($\gamma < 0.005$) it was difficult to obtain an accurate value for the elastic rigidity modulus (G) associated with instantaneous elastic deformation. This problem was complicated by the difficulting in separating elastic strain induced within the test blocks from elastic strain induced within the apparatus itself. However, an order of magnitude estimate of the elastic rigidity modulus of the 54°C m.pt. made from the available data indicated a value for G in the range $10^5 - 10^6$ gm.cm.$^{-2}$.

Time dependent elastic creep was investigated by unloading test blocks during steady state creep and measuring the shear strain recovered over different intervals of time. The results of this process of alternating a constant applied load with periods of strain relaxation are reproduced from one test carried out at 38.8°C in fig. 4.12. Recovered transcient creep (shear strain) is plotted as a function of the recovery time in fig. 4.13. This type of test was used to estimate the level of stored elastic strain in the competent wax layers used in the multilayer experiments.

45°C Melting point paraffin wax

This second wax grade was investigated as a potential low strength material for use in the fold simulation experiments. The material is used in only one experiment reported in section 4.5 and the results of the rheological tests on this material are reported only for the properties measured during steady state creep.

Steady state creep

The relationship between apparent viscosity and test temperature is shown in fig. 4.14 for one level of applied stress (τ = 5.0 gm.cm.$^{-2}$). The 45°C m.pt. wax undergoes a steady decrease in apparent viscosity with increase in temperature, up to a temperature of approximately 41°C. Above this temperature there appears to be a rapid decrease in apparent viscosity as the test temperature approaches the nominal melting point of the material. A comparison of figs. 4.8 and 4.14 indicates that the 54°C m. pt. wax grade has an apparent viscosity

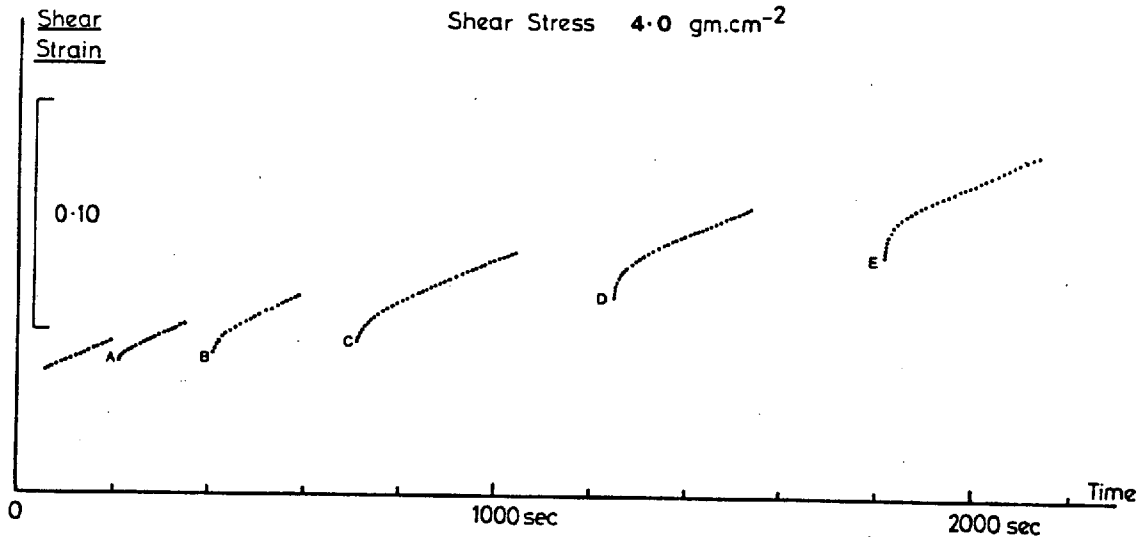


Figure 4.12 Results of cycling the application of a shear load. (54°C m.pt. paraffin wax, test temperature 38.8°C)

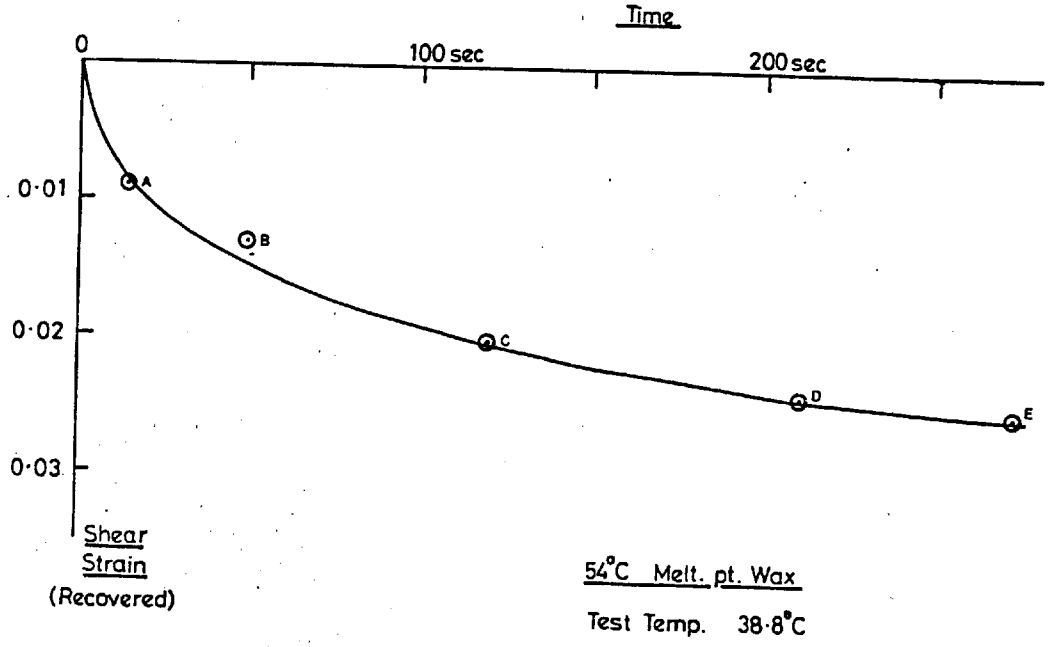


Figure 4.13 Plot of recovered transient elastic strain vs. recovery time. Data calculated from the test results shown in fig. 4.12

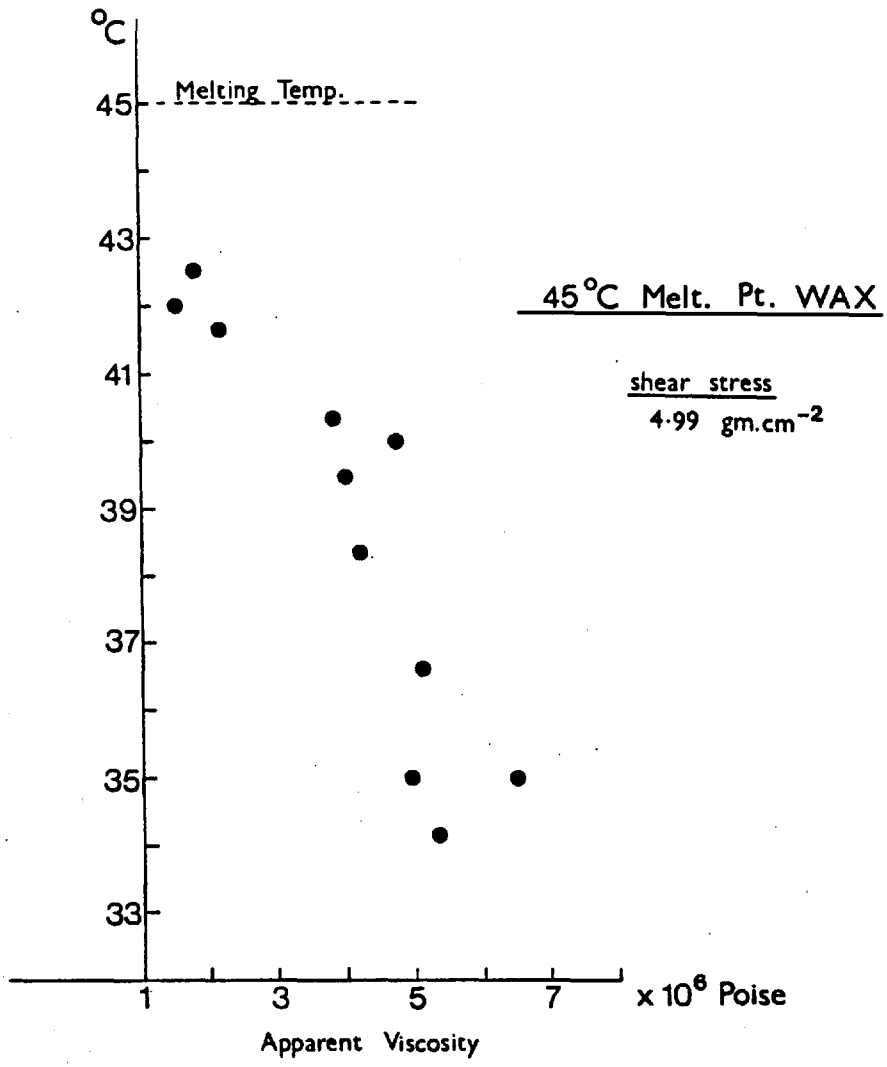

°C
Melting Temp.
45
43
41
39
37
35
33
45°C Melt. Pt. WAX
shear stress
4·99 gm.cm⁻²
1
3
5
7
x 10⁶ Poise
Apparent Viscosity

Figure 4.14

which is approximately an order of magnitude greater than that of the 45°C m.pt. grade, at the same applied stress level, over the temperature range 38° - 41°C.

Multilayered test blocks

A series of constant shear stress creep tests were carried out to investigate the response of representative multilayered test blocks to layer parallel shear. The configuration of these test blocks with respect to the applied shear stress is illustrated, schematically, in fig. 4.15 A. The test pieces were made up of a stack of eight uniform sheets of 54°C m.pt. wax separated by thin seams of lubricant. They represent the multilayers used in the majority of the fold simulation experiments described in section 4.5 and the shear tests were designed to investigate the bulk properties of these multilayers with respect to layer parallel shear. Two interlayer lubricants were employed in these tests and also used to serve as thin, low strength interbeds in the model experiments - (a) silicone grease (manufactured by the Dow Corning Co.), (b) liquid soap (manufactured under the brand name 'Zalpon'). These lubricants were chosen partly because they do not react with paraffin wax or weaken this material by solution.

A standard thickness for the individual wax layers of 1.65 ± 0.05 mm. was used both in the rheological tests and the model experiments. Individual sheets of wax of constant thickness were prepared by floating a thin layer of molten wax on hot water and allowing the wax to cool and solidify. This method of preparation is discussed in appendix 4.3. Interlayer lubricant was applied by hand and the average thickness of the lubricant seams was calculated by measuring the total thickness of a multilayered test block, using a micrometer screw gauge and subtracting the measured thickness of the wax layers from the total. The average thickness of the lubricant seams, calculated by this method, was in the range 0.02 - 0.06 mm.

The results of the creep tests for multilayers lubricated by silicone grease are shown in fig. 4.15. The strength of the multilayered test blocks under layer parallel shear is shown by the calculated apparent viscosity (bulk shear viscosity of the test block) for three different applied stress levels (τ = 4.0, 5.0 and 6.4 gm.cm^{-2}). Fig. 4.15 illustrates the variation in apparent shear

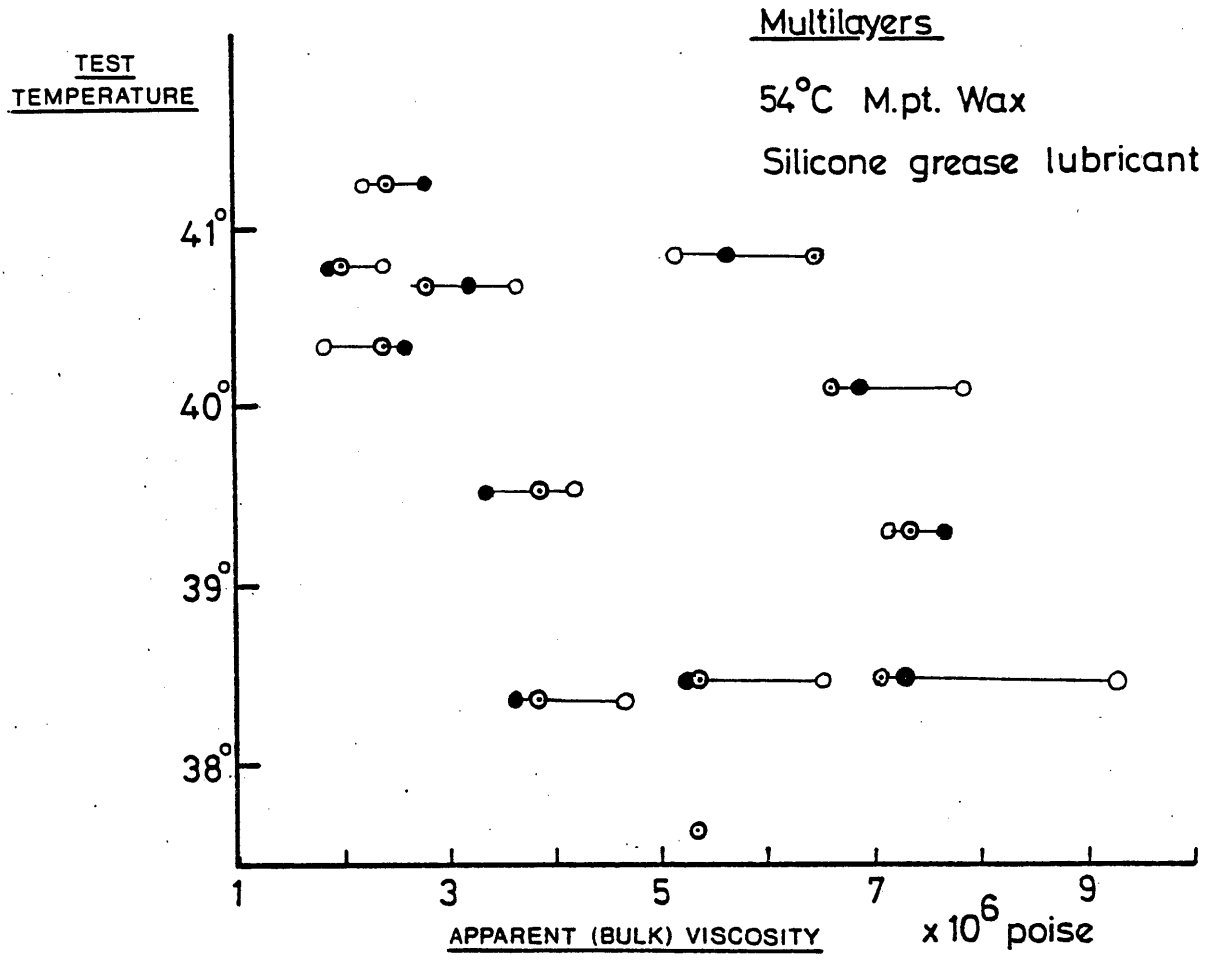
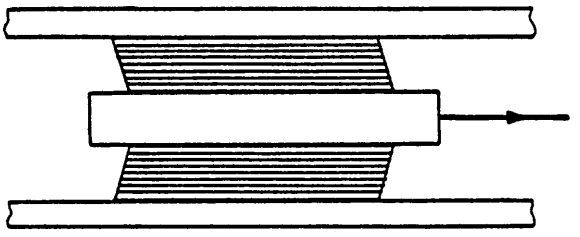


Figure 4.15 ● - 4.0 gm.cm^{-2} ○ - 6.4 gm.cm^{-2}
⊙ - 5.0 gm.cm^{-2}



Plan View

Figure 4.15 A

viscosity with temperature over the temperature range 37°C - 42°C. There appears to be no consistent relationship between strength in layer parallel shear and temperature over this range and there is a wider scatter of points than is the case for the tests carried out on unlaminated blocks. (This may be due to the difficulty of ensuring that the thickness of silicone grease lubricant seams was constant for each test).

It is difficult to determine, precisely, the nature of the relationship between applied stress and induced bulk strain rate from the test results shown in fig. 4.15. However, over the restricted range of applied stress used in these experiments it appears that the relationship is approximately linear. The calculated bulk shear viscosity of the multilayered test blocks with respect to layer parallel shear can be seen to lie in the range 2×10^6 to 8×10^6 poise.

An approximate estimate of the viscosity of the silicone grease lubricant seams can be made by calculating the relative contribution of shear within these seams and shear within the competent wax laminae to the bulk shear response of a multilayered test block. Biot (1965a) has demonstrated that the bulk viscosity (μ_t) of a uniform multilayer sequence with respect to layer parallel shear is given by:

$$\mu_t = \frac{\mu_1 \mu_2}{\alpha_1 \mu_2 + \alpha_2 \mu_1} \qquad \ldots\ldots 4.8$$

.. where, in the case of the lubricated wax multilayers:

μ_1 = viscosity of the competent wax layers

μ_2 = viscosity of the incompetent silicone grease seams

α_1 = fractional thickness of the competent layers within a competent/incompetent layer pair

α_2 = fractional thickness of the incompetent layers within a competent/incompetent layer pair.

Using an average value of 0.04 mm. for the thickness (t_2) of silicone grease lubricant seams and a value of 1.65 mm. for the thickness (t_1) of the uniform wax layers:

$$\alpha_1 = \frac{t_1}{t_1 + t_2} = 0.98$$

$$\alpha_2 = \frac{t_2}{t_1 + t_2} = 0.02$$

The viscosity of the competent wax layers can be estimated by taking an average value for the apparent viscosity of an unlaminated test block, measured at 38°C:

$$\mu_1 \simeq 3 \times 10^7 \text{ poise}$$

The average value of the bulk shear viscosity of the laminated blocks at 38°C is given, approximately, by:

$$\mu_t = 5 \times 10^6 \text{ poise}$$

Equation 4.8 can now be solved to obtain an order of magnitude estimate for the silicone grease lubricant seam viscosity :

$$\mu_2 = \frac{\mu_1\mu_2 - \alpha_2\mu_1\mu_t}{\alpha_1\mu_t}$$

$$\mu_2 \simeq 1.2 \times 10^5 \text{ poise}$$

This very approximate calculation indicates an estimated value for the viscosity of the silicone grease seams of the order of 10^5 poise.

The contrast in strength between the competent wax layers (54^0C m.pt.) and the silicone grease lubricant seams is of the order of 100 1000 : 1 for experiments carried out over the temperature range 38 - 44 C. - 44 C.

A number of tests were carried out using multilayered test blocks incorporating liquid soap as an interlayer lubricant (the second type of interlayer lubricant used in the fold simulation experiments). However, it proved impossible to get consistent results from this type of test due to the problem of draining of the fluid lubricant during the initial clamping of a test block with the test apparatus.

4.4 Relationship between the significant properties of paraffin wax multilayers and the equivalent properties of scaled tectonic prototypes

The purpose of this section is to estimate the properties of large scale tectonic prototypes whose deformational behaviour would be equivalent to the deformation of the paraffin wax multilayers used in the large scale fold simulation experiments. This can be done by using the theory of scale modelling (Section 4.2) and the results of the rheological tests (Section 4.3) to scale the rheological properties of particular wax multilayers to the dimensions of an equivalent, large scale tectonic prototype. Calculations of this type can be used to test the suitability of the model materials used in the experiments for the simulation of large scale fold development in simple, sedimentary sequences.

The scale calculations described in this section are based on the properties of the model experiment described later in this chapter (Section 4.5) as experiment F. The model is made up of a simple

stack of uniform wax layers (54^0C m.pt. paraffin wax), separated by seams of silicone grease lubricant. This multilayer rested on a thin décollement zone of liquid soap. The experiment was run at a constant temperature of $38.0^0 \pm 0.5^0$C.

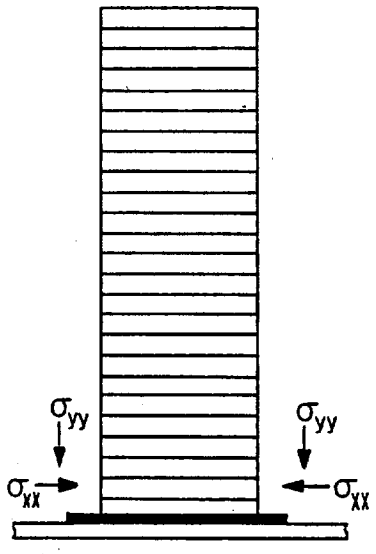
The properties of the model are listed in fig. 4.16. This list includes the significant physical parameters which are likely to influence the development of fold structures in the experiment, including the initial geometric properties of the model (thickness of layer components, etc.) and the rheological properties of the multilayer components calculated, for the temperature of the experiment, from the results of the rheological tests.

In figs. 4.17 and 4.18, a list of equivalent scaled properties are shown for two equivalent tectonic prototypes. These properties have been calculated for increases in length scale by a factor of 10^4 (tectonic prototype A - fig. 4.17 ($L_r = 10^{-4}$)) and 10^5 (tectonic prototype B - fig. 4.18 ($L_r = 10^{-5}$)).

Geometric properties of model and equivalent tectonic prototypes

The uniform model multilayer represents an alternating sequence of thick, competent beds and thin, incompetent interbeds resting on a décollement cushion above a rigid basement. For a range of model length scaling of $L_r = 10^{-4}$ to 10^{-5}, the total model thickness of 42mm is equivalent to a range of total prototype multilayer thickness of 420m (tectonic prototype A) to 4.2 km (tectonic prototype B). The thickness of the individual competent wax layers used in the model (1.6 - 1.7 mm) is equivalent to a prototype competent bed thickness of 16 - 17m (tectonic prototype A) or 160 - 170m (tectonic prototype B). It should be noted that the latter value for competent bed thickness is too large to represent a reasonable average bed thickness of sedimentary units within a typical sedimentary sequence. There is a problem in scaling, accurately, by bed thicknesses of the order of 10 metres or less in all model experiments simulating large scale deformations ($L_r \leq 10^{-5}$) due to the practical difficulties of producing very thin laminae within a laboratory model. If the results of the model experiments are to be

MODEL



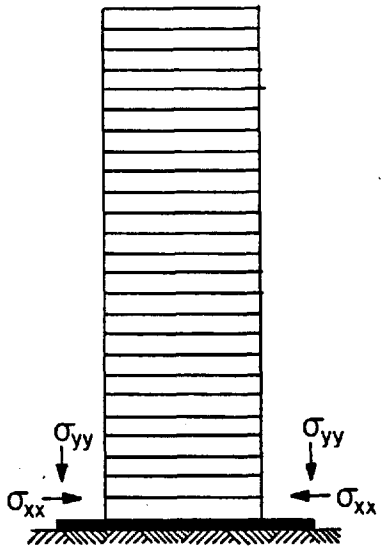
TOTAL MULTILAYER THICKNESS	42 mm.
NUMBER OF COMPETENT LAYER	25
COMPETENT LAYER THICKNESS	1.6 - 1.7 mm.
INCOMPETENT LAYER THICKNESS	0.02 - 0.06 mm.
DECOLLEMENT LAYER THICKNESS	c2 mm.
ELASTIC RIGIDITY MODULUS *	10^2 - 10^3 gm.cm^{-2}.
APPARENT VISCOSITY *	3.8 . 10^7 poise.
ESTIMATED MAXIMUM STORED ELASTIC STRAIN *	1.5 %
HORIZONTAL STRAIN RATE	3.4 . 10^{-5} per sec.

STRESSES AT BASE *(gm. cm^{-2})	
VERTICAL STRESS	3.8 gm.cm^{-2}.
HORIZONTAL STRESS	9.0 gm.cm^{-2}.
HORIZONTAL DIFFERENTIAL STRESS	5.2 gm.cm^{-2}.

*estimated for competent layers

Figure 4.16

TECTONIC PROTOTYPE A ($L_r = 10^{-4}$)



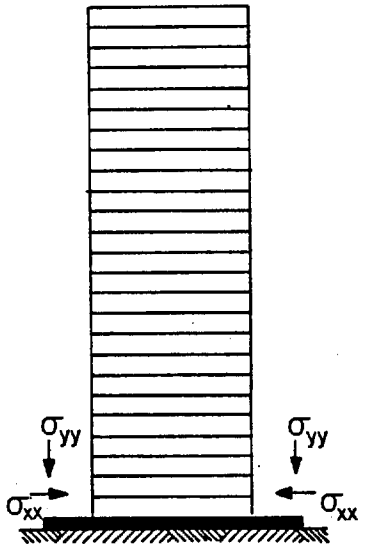
TOTAL MULTILAYER THICKNESS	420 m.
NUMBER OF COMPETENT LAYER	25
COMPETENT LAYER THICKNESS	16 - 17 m.
INCOMPETENT LAYER THICKNESS	20 - 60 cm.
DECOLLEMENT LAYER THICKNESS	c 20 m.
ELASTIC RIGIDITY MODULUS *	3.10^4 - 3.10^5 bars
APPARENT VISCOSITY *	$1.1 . 10^{21}$ poise
ESTIMATED MAXIMUM STORED ELASTIC STRAIN *	1.5 %
HORIZONTAL STRAIN RATE	$3.4 . 10^{-14}$ per sec.

STRESSES AT BASE *	
VERTICAL STRESS	114 bars
HORIZONTAL STRESS	269 bars
HORIZONTAL DIFFERENTIAL STRESS	155 bars

* estimated for competent layers

Figure 4.17

TECTONIC PROTOTYPE B ($L_r = 10^{-5}$)



TOTAL MULTILAYER THICKNESS	4.2 km.
NUMBER OF COMPETENT LAYER	25
COMPETENT LAYER THICKNESS	160 - 170 m.
INCOMPETENT LAYER THICKNESS	2 - 6 m.
DECOLLEMENT LAYER THICKNESS	c 200 m.
ELASTIC RIGIDITY MODULUS *	3.10^5 - 3.10^6 bars
APPARENT VISCOSITY *	$1.1 . 10^{22}$ poise
ESTIMATED MAXIMUM STORED ELASTIC STRAIN *	1.5 %
HORIZONTAL STRAIN RATE	$3.4 . 10^{-14}$ per sec.

STRESSES AT BASE *	
VERTICAL STRESS	1.14 Kb.
HORIZONTAL STRESS	2.69 Kb.
HORIZONTAL DIFFERENTIAL STRESS	1.55 Kb.

* estimated for competent layers

Figure 4.18

compared with fold development in sedimentary sequences with a total thickness of the order of kilometres, then the fact that the model simulates a massive bed thickness of the order of hundreds of metres should be borne in mind.

Boundary displacements

In each of the model experiments, a constant rate of piston movement of 3.7cm per hr. was applied to the models. This displacement rate corresponds to an initial horizontal strain rate of 3.4×10^{-5} per sec. for a model with a total length of 30cm.

Rheological properties

Competent layers

(i) Recoverable strain - The elastic rigidity modulus, G, of the competent wax layers has been estimated to lie in the range 10^5 to 10^6 gm cm^{-2}. This rigidity modulus can be scaled to the dimensions of the two tectonic prototypes by using equation 4.5.

$$G_p = G_m/\rho_r L_r$$

The model ratio of specific gravity ρ_r is taken to be 0.33 (ρ_{wax} = 0.9, $\rho_{prototype}$ = 2.7). Using this value, the range in wax rigidity modulus is equivalent to a range in prototype competent bed elastic rigidity of:

Tectonic prototype A ($L_r = 10^{-4}$)

$$G_p = 3 \times 10^4 - 3 \times 10^5 \text{ bars}$$

Tectonic prototype B ($L_r = 10^{-5}$)

$$G_p = 3 \times 10^5 - 3 \times 10^6 \text{ bars}$$

These scaled elastic rigidites can be compared with the range of 2 to 8 x 10^5 bars quoted, for the measured elastic rigidity of a variety of indurate sandstones and cemented limestones, by Jaeger and Cook (1969). It is suggested that the instantaneous elastic properties of the competent wax layers used are a reasonable analogue of the equivalent properties of indurate sedimentary rocks for a length scale reduction of 10^{-5}. For a length scale reduction of 10^{-4} the rigidity of the model material is probably too low by a factor of ten.

It is not possible to specify, exactly, the magnitude of recoverable elastic strain induced within the wax layers during the initial stages of layer parallel shortening from the results of the constant shear stress creep tests. (This could be done if the tests had been carried out at constant shear strain rate.) However, since the measured relaxation time of the 54^0 m.pt. wax grade is approximately 60 secs (see fig. 4.13) and the models were subjected to a relatively slow horizontal strain rate of 3.4 x 10^{-5} per sec., it is probable that the magnitude of the total recoverable elastic strain, induced during the initial phase of shortening, is less than 1.5%.

(ii) Permanent strain - The most direct method of scaling the strength of the competent wax layers, to the dimensions of the tectonic prototypes, is to express the creep strength of the wax, during steady state creep, as an apparent viscosity, $(\mu_a)_m$. This viscosity can then be scaled according to equation 4.7 :

$$(\mu_a)_p = (\mu_a)_m \,/\, \rho_r \, L_r \, t_r^{-1}$$

As has been indicated in the discussion of model scaling in section 4.2, however, this equation cannot be used to specify a unique value for the prototype viscosity, for a given model length ratio, L_r. In order to make this possible, it is necessary to specify a value for the reduction in time scale applied to the experimental deformation, given the model ratio of time, t_r. This

can be done, for example, by adopting a geologically reasonable value for the initial horizontal strain rate induced within a tectonic prototype and obtaining a value for t_r from the relationship:

$$\frac{\dot{e}_m}{\dot{e}_p} = \frac{t_p}{t_m} = \frac{1}{t_p}$$

. . . . where $\dot{e}_m$ and $\dot{e}_p$ are equivalent strain rates induced in model and prototype respectively.

However, the physical significance of the choice of model ratio of time and the implications of this choice in terms of the rheological properties which are simulated in a given experiment can be explained more clearly by first considering the relationship between various components of stress induced in model and prototype.

It has been shown that the paraffin wax used in experiment F (54^{0}C m.pt.; experimental temperature 38.0 ± 0.5^{0}C) has a slightly non-linear stress-strain rate relationship which can be approximated by a power law relationship with a stress exponent n in the range 1.0 - 2.0. In order to estimate the level of induced stress associated with the accumulation of permanent stress within the model material the same simplifying assumptions will be adopted as were used in the discussion of "tectonic" stresses in section 4.2. The stresses are referred to the initial stages of layer parallel shortening of the competent wax units, prior to the initiation of folding. Deformation is assumed to be plane strain in the vertical plane (x,y plane of fig. 4.2) and the vertical and horizontal stress components are assumed to be principal stresses ($\sigma_{xx} = \sigma_1$; $\sigma_{yy} = \sigma_3$). The horizontal differential stress, $\sigma_1 - \sigma_3$, is related to the horizontal strain rate by:

$$\sigma_1 - \sigma_3 = 4 \mu_a \dot{e}$$

In a non-linear material, the apparent shear viscosity, μ_a, is a function of strain rate and it is not possible to obtain a value for μ_a directly from the results of the rheological tests on the 54^{0}C m.pt. wax. This can be done, however, by obtaining a value for μ_a at

at a specific level of stress, and corresponding strain rate, from the rheological test results (eg. tests 4 and 5 in fig. 4.8, for an experimental temperature of 38^0C) and using this data to estimate the apparent viscosity of the wax under the horizontal strain rate applied during the initial stage of layer parallel compression in the fold simulation experiment. In carrying out this calculation it is necessary to convert the values of shear stress and shear strain rate measured in the constant shear stress creep tests to equivalent differential stresses and direct strain rates. The variation in apparent viscosity, μ_a, with strain rate has been calculated on this basis assuming a value of n = 1.6 for the stress exponent in the power law stress-strain rate relationship. Calculations based on the test results obtained for tests 4 and 5 indicate the following values for apparent viscosity and horizontal differential stress during the initial prefolding phase of deformation of the model multilayer discussed as experiment in section 4.5.

$$\mu_a = 3.8 \times 10^7 \text{ poise}$$

$$\sigma_1 - \sigma_3 = 5.2 \text{ gm.cm}^{-2}$$

calculated for $\dot{e} = 3.4 \cdot 10^{-5}$ per sec.

The significance of this level of differential stress can be illustrated by estimating the ratio of vertical gravitational stress ($= \sigma_3$) to horizontal differential stress at the base of the model multilayer. At this point, σ_3 is given by:

$$\sigma_3 = \sigma_{yy} = \rho_m g_m g_m$$

$$= 3.8 \text{ gm. cm.}^{-2}$$

Therefore $\sigma_3 / (\sigma_1 - \sigma_3) = 3.8/5.2 = 0.74$

It has been demonstrated in section 4.2 that, for dynamic simularity, the ratio of σ_3 to $\sigma_1 - \sigma_3$ must therefore be 0.74 at the base of any equivalent tectonic prototype. The vertical stresses at the base of the two prototype systems outlined in figs. 4.17 and 4.18 are given by:

Tectonic prototype A ($L_r = 10^{-4}$)

$$\sigma_3 = \sigma_{yy} = 114 \text{ bars}$$

Tectonic prototype B ($L_r = 10^{-5}$)

$$\sigma_3 = \sigma_{yy} = 1.14 \text{ Kb}$$

From the necessary scale relationship:

$$\left(\frac{\sigma_3}{\sigma_1 - \sigma_3}\right)_m = \left(\frac{\sigma_3}{\sigma_1 - \sigma_3}\right)_p = 0.74$$

. . . . values can be obtained for the prototype horizontal differential stresses which are dynamically equivalent, in their relationship with gravitational body stresses, to the stress components present in the model multilayer.

Tectonic prototype A ($L_r = 10^{-4}$)

$$\sigma_1 - \sigma_3 = 114/0.74 = 155 \text{ bars}$$

Tectonic prototype B ($L_r = 10^{-5}$)

$$\sigma_1 - \sigma_3 = 1.14/0.74 = 1.55 \text{ Kb}$$

As in the model multilayer, these "tectonically" induced horizontal differential stresses must be associated with a pseudo-viscous layer parallel shortening of competent laminae at a constant strain rate. It is possible to specify a series of combinations of apparent viscosity, μ_a, and horizontal strain rate, $\dot{e}$, which would give rise to the necessary levels of differential stress according the relationship (plane strain deformation of an isotropic material at constant volume):

Examples of viscosity-strain rate combinations which satisfy the conditions of dynamic similarity at the length scaling applied to prototypes A and B are listed in table 4.I .

It should be noted that, since both prototype and model materials must have equivalent rheological properties, total dynamic similarity will be satisfied only if the prototype competent bed rheology has the same form of stress-strain relationship during steady state creep as has been calculated for the competent wax layers. This implies that the paraffin wax simulates, at the experimental temperatures, a competent bed lithology with a slightly non-linear (power law?) stress-strain rate relationship with a low n value in the range 1.0 - 2.0. In addition, the apparent viscosity of these prototype beds must approximate to the values indicated in table 4.I at the corresponding strain rates.

It can be seen from table 4. I that the model experiment under consideration does not simulate the deformation of a prototype system with specific creep properties. In simple terms the model simulates either a fast deformation of a geologically "weak" bedded system (eg. $\mu_a = 1.2 \times 10^{18}$ poise at $\dot{e} = 3.4 \times 10^{-10}$ per sec - $L_r = 10^{-5}$) or a slow deformation of a geologically "strong" system (eg. $\mu_a = 1.2 \times 10^{24}$ at $\dot{e} = 3.4 \times 10^{-16}$ per sec - $L_r = 10^{-5}$). It can be suggested, however, from published estimates, that the "average" initial horizontal strain rate induced in a bedded sedimentary sequence, undergoing décollement tectonics, will lie in the range 10^{-13} to 10^{-14} per sec (see Price, 1975). Such estimates are obviously subject to question and locally strain rates may increase substantially above this range once fold initiation and amplification takes place. However, if this range in initial, horizontal strain rate is accepted then it can be used to limit the type of prototype system which is simulated. A prototype strain rate of 3.4×10^{-14} per sec indicates a corresponding apparent viscosity of 1.3×10^{21} ($L_r = 10^{-4}$ - tectonic prototype A) and 1.3×10^{22} ($L_r = 10^{-5}$ - tectonic prototype B). The model time ratio for this prototype strain rate is given by:

$$t_r = \dot{e}_p / \dot{e}_m = 10^{-9}$$

TABLE 4.I

	Differential Stress (bars)	Apparent Viscosity (poise)	Strain Rate (per sec)	Model Time Ratio (t_r)
PROTOTYPE A ($L_r = 10^{-4}$)	155	1.1×10^{23}	3.4×10^{-16}	10^{-11}
	155	1.1×10^{21}	3.4×10^{-14}	10^{-9}
	155	1.1×10^{19}	3.4×10^{-12}	10^{-7}
	155	1.1×10^{17}	3.4×10^{-10}	10^{-5}
PROTOTYPE B ($L_r = 10^{-5}$)	1550	1.1×10^{24}	3.4×10^{-16}	10^{-11}
	1550	1.1×10^{22}	3.4×10^{-14}	10^{-9}
	1550	1.1×10^{20}	3.4×10^{-12}	10^{-7}
	1550	1.1×10^{18}	3.4×10^{-10}	10^{-5}

4.5 RESULTS OF THE MODEL EXPERIMENTS

4.5.1 Effect of boundary shear stresses on the development of structures

An important consideration in the experiments was the influence of friction along contacts between the *perspex* apparatus and the model itself. Friction between the vertical walls of the apparatus and the model was reduced, as far as possible, by lubricating these contacts with liquid soap. Tests carried out by Cobbold (1973) indicate that this material is a particularly effective lubricant in experiments using paraffin wax as a model material. Efficient lubrication of the side walls of the apparatus was essential since shear stresses on these vertical contacts could play an unknown and geologically unrealistic role in the development of structures.

Shear stresses developed at the base of the model are, however, geologically realistic in the sense that equivalent stresses would be present at the base of an equivalent sedimentary sequence due to the shear resistance of the décollement horizon. A series of preliminary experiments were carried out using a relatively stiff lubricant - *vaseline* grease - as a décollement zone. The shear resistance of this material was sufficiently high, relative to the strength of the layered wax overburden, to produce a significant stress gradient, within a model, away from the piston face during the initial stages of compression. The resulting concentration of induced stress near the piston caused folds to initiate and amplify in this region. In experiment A (fig. 4.19) this resulted in the serial development of a train of folds in the direction of applied compression. The numbered fold sequence 1 - 4 shown in fig. 4.19 corresponds to the time sequence of development of these structures. (The arrow symbol superimposed on this and other figures in this section indicates the position and direction of movement of the piston face.)

The tendency for initial fold development to occur at or near the piston face as a result of stress concentration in this region was even more marked in preliminary experiments using a finer competent

A



FIGURE 4.19

B



FIGURE 4.20

layer thickness and a larger number of individual layers. In experiment B (fig. 4.20), for example, deformation is confined to the development of localised folds immediately adjacent to the piston face.

There is obviously a problem of interpretation of these types of structure due to the geologically unrealistic shear stress and displacement conditions present at the piston face. In order to resolve this problem, liquid soap was adopted as a décollement lubricant in the remainder of the fold simulation experiments. This material has a flow strength which is significantly lower than that of the *vaseline* grease lubricant used in the experiments illustrated in figs. 4.19 and 4.20. Consequently the shear resistance of the décollement zone was sufficiently low in comparison with the strength of the competent wax layers in the multilayer sequence to ensure that the initial displacement of the piston produced an almost immediate, homogeneous loading of the whole length of a model. No rheological tests were carried out to determine the strength and flow properties of this décollement material. However, it is probable that the strength of the liquid soap décollement layer and consequently the stresses developed within this layer were at least four orders of magnitude lower than the flow strength of, and the stresses induced within, the competent wax layers, over the range of temperatures used in the experiments. This obviously implies an equally significant contrast between the flow strength of competent units and décollement zone in an equivalent tectonic prototype.

4.5.2 The influence of the strength of competent units within the multilayer sequence on fold development

It is possible to recognise a relationship between the style of folding developed in particular experiments and the flow strength of the competent wax layers under the conditions of the experiment. This relationship is demonstrated by the contrasting fold styles produced in experiments C (fig. 4.21), D (fig. 4.22) and E (fig. 4.23). Each of these experiments was carried out using a uniform sequence of identical wax layers separated by liquid soap lubricant seams. The geological significance of these contrasting models can be demonstrated

by examining the strength of the competent wax layers under the conditions applied in the experiments.

The results of the rheological tests discussed in section 4.3 have been used to estimate an apparent shear viscosity for the uniform wax layers used in experiments C, D and E, at the experimental temperatures. This apparent viscosity is referred to the lateral strain rate of approximately 3.4×10^{-5} per sec which was applied during the initial stages of shortening of each of the models. The calculated viscosities are listed in table 4.II . In addition, an estimate has been made of the magnitude of the horizontal differential associated with this strain rate. This estimated stress level is a measure of the maximum differential stress induced within the models during initial layer parallel compression. Table 4.II also includes the equivalent differential stress which would be present at an equivalent stage of deformation of two tectonic prototypes corresponding to length scale reductions of 10^{-4} (tectonic prototype A) and 10^{-5} (tectonic prototype B). The methods used in these calculations have been discussed in sections 4.2 and 4.4. The prototype shear viscosities listed in table 4.II are based on an assumed model time ratio of $t_r = 10^{-9}$. This implies an equivalent initial lateral strain rate in the two tectonic prototypes of 3.4×10^{-14} per sec.

Experiment D, (fig. 4.22)

Multilayer	-	54^0C m.pt. wax/liquid soap
Décollement lubricant	-	liquid soap
Temperature	-	35.5^0C $\pm$ 0.5^0C

This experiment was carried out at a temperature below the "softening" temperature of the 54^0C m.pt. wax layers that has been recognised in the results of the rheological tests (see discussion of fig. 4.9). Deformation of the multilayer produced a single, large span fold. The competent wax layers retain constant orthogonal thickness throughout the structure and the fold mechanism was flexural slip on the lubricant interbeds. The void space seen at the core of the fold was occupied by décollement material during the course of the experiment.

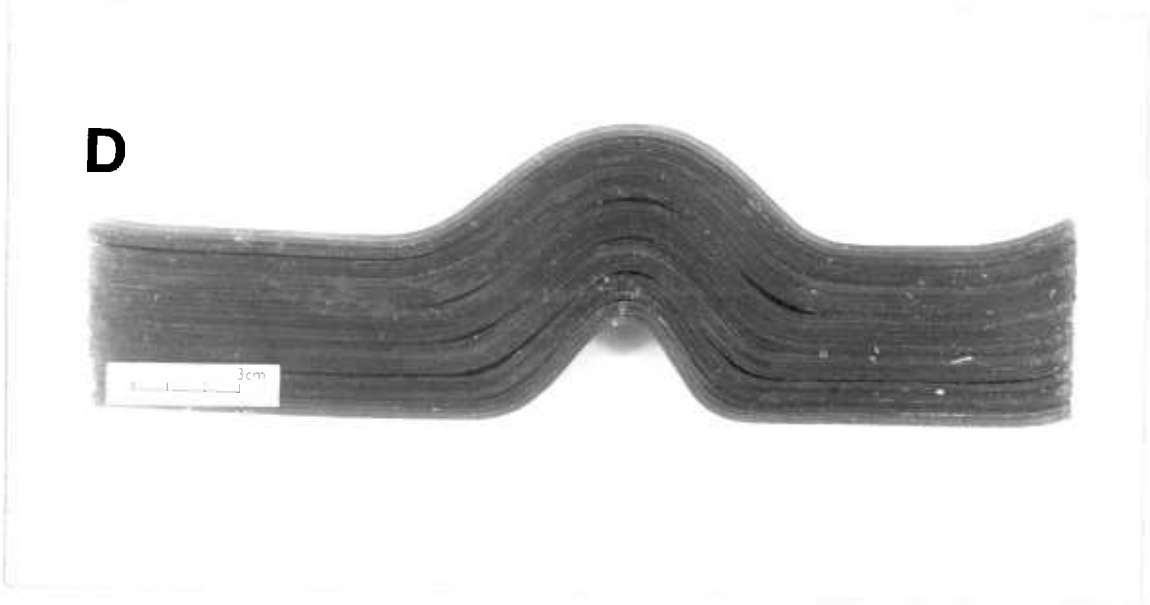


fig. 4.22

TABLE 4.II

Experiment		Total Thickness	Lateral Strain Rate per sec.	Shear Viscosity poise	Horizontal Diff. Stress bars	Vertical Stress bars
	Model	51 mm.	$3.4 \cdot 10^{-5}$	$2 \cdot 10^{9}$	0.27	0.0046
D	Prototype A	510 m.	$3.4 \cdot 10^{-14}$	$6 \cdot 10^{22}$	8100	138
	Prototype B	5.1 km.	$3.4 \cdot 10^{-14}$	$6 \cdot 10^{23}$	81000	1380
	Model	42 mm.	$3.4 \cdot 10^{-5}$	$4 \cdot 10^{7}$	0.0054	0.0038
C	Prototype A	420 m.	$3.4 \cdot 10^{-14}$	$1.2 \cdot 10^{21}$	162	114
	Prototype B	4.2 km.	$3.4 \cdot 10^{-14}$	$1.2 \cdot 10^{20}$	1620	1140
	Model	42 mm.	$3.4 \cdot 10^{-5}$	$4 \cdot 10^{6}$	0.00054	0.0038
E	Prototype A	420 m.	$3.4 \cdot 10^{-14}$	$1.2 \cdot 10^{20}$	16.2	114
	Prototype B	4.2 km.	$3.4 \cdot 10^{-14}$	$1.2 \cdot 10^{21}$	162	1140

The large span of this structure and the absence of layer thickening within the competent laminae reflects the relatively low constraint on fold amplification produced by gravitational body stress within the multilayer. The simple stress calculations reproduced in table 4.II demonstrate, for example, that the ratio between initially induced horizontal stress and the vertical component of gravitational body stress at the base of the model multilayer is of the order of 70 to 1. This ratio is obviously far too high to model, realistically, the equivalent stress ratio at the base of an equivalent sequence of indurate sedimentary beds. The point is emphasised by the levels of scaled prototype differential stresses indicated in table 4.II . This particular experiment effectively simulated the development of folding within a sedimentary sequence subjected to between 8 kb. and 80 kb. horizontal differential stress, assuming a total sedimentary thickness of 500 metres to 5km. Obviously such a system would fail by faulting at a stress level well below that required to produce a structure of the dimensions represented on a reduced scale by the fold developed in experiment D.

Experiment C (fig. 4.21)

Multilayer	-	54°C m.pt. wax/liquid soap
Décollement lubricant	-	liquid soap
Temperature	-	38.0°C ± 0.5°C

The same materials were used in the construction of this model as in the previous experiment. In this case, however, the experiment was run at a temperature above the critical range 36.5 - 37.5°C at which the 54°C m.pt. wax, used in the models, undergoes a marked temperature softening. The strength of the wax layers in this multilayer and a simple estimate of the induced layer parallel differential stress during initial lateral compression are indicated in table 4.II .

Gravitational body stresses played a significant role in inhibiting vertical deflections of the multilayer and in restricting the wavelength or span of folds in this experiment. The ratio of induced horizontal differential stress to vertical stress at the base

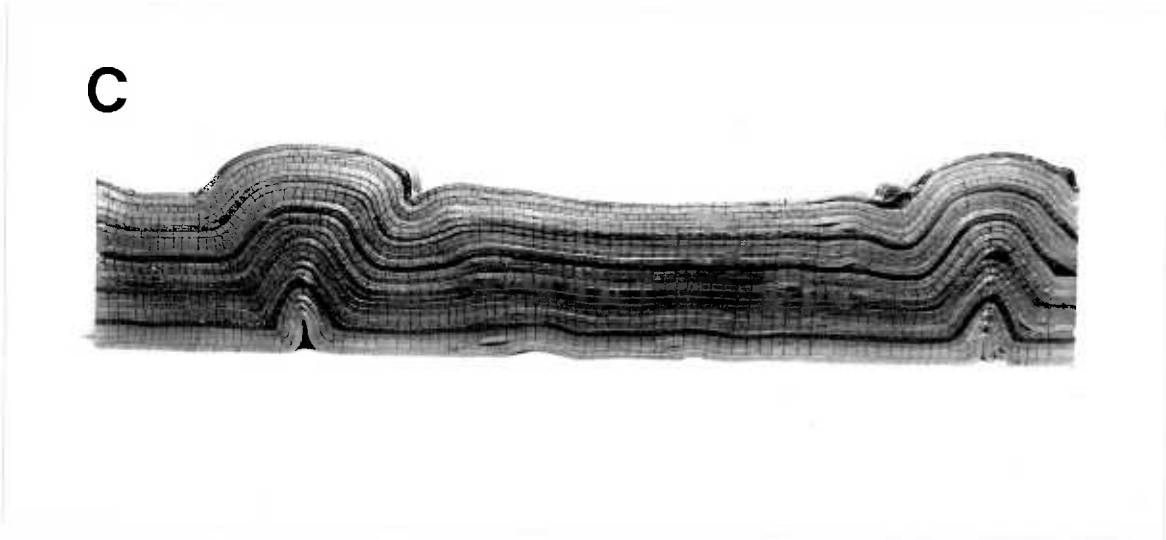


fig. 4. 21

of this model is approximately 1 : 1 and the scaled levels of prototype horizontal differential stress during initial layer parallel compression lie in the range 162 bars ($L_r = 10^{-4}$) to 1,6kb. ($L_r = 10^{-5}$) for a corresponding range in total prototype thickness of 420m to 4.2km. It can be argued that this range in differential stress is a reasonable analogue of the stress levels which would be induced within a uniform, indurate sedimentary sequence during initial layer parallel compression. Therefore, it can be suggested that the type of structures produced in model C were developed under experimental conditions which simulate, with reasonable accuracy, the relative roles of gravitational potential and induced flow stress within a highly anisotropic sequence of indurate sedimentary beds undergoing décollement tectonics.

Experiment E (fig. 4.23)

Multilayer	-	45^0C m.pt. wax/liquid soap
Décollement lubricant	-	liquid soap
Temperature	-	38^0C ± 0.5^oC

The initial geometry of this model was identical to that of the model used in experiment C. However, in this case the competent wax layers were constructed from 45^0C m.pt. wax, the weaker of the two wax grades, and the experiment run at 38^0C. Calculations based on the results of the rheological tests indicate a relative decrease in wax strength by a factor of approximately 10 in comparison with experiment C. The effect of this reduction in strength on the finite geometry of folds is clearly seen by comparison of figs. 4.22 and 4.23. There is a reduction in fold wavelength caused by the increased constraint produced by gravitational body stresses in this weak model. The structures are characterised by an increase in the amplitude of folds towards the surface of the multilayer and the local development of a "packet" of low wavelength internal buckles in the core of the major structure, adjacent to the piston. The ratio between induced horizontal differential stress during initial layer parallel compression and vertical gravitational stress at the base of the model is approximately 1 : 10 in this case. It can be seen from table 4.II that scale calculations of the

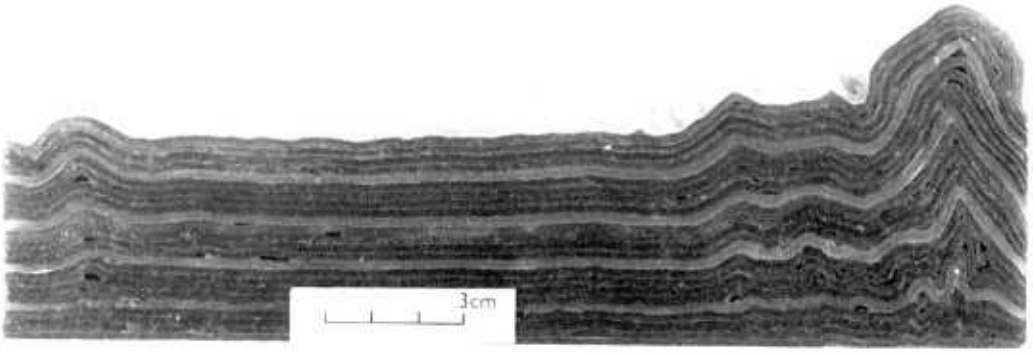


Figure 4.23 EXPERIMENT E

induced layer parallel differential stresses during initial compression indicate low prototype differential stresses in the range16.2 to 162 bars and correspondingly weak prototype rock materials for a geologically representative initial strain rate of 3.4×10^{-14} per sec.

The most significant effect of the increasing influence of gravitational body stresses on fold development seen in the sequence from models C to E, is the associated reduction in the span or wavelength of folding. The single fold developed in the high strength model, experiment ^{D}, has the general characteristics of Biot's second kind similar fold category (see chapter 1, section 1.2.1) with vertical displacements occurring at both the surface and base of the multilayer. In contrast, the structures developed in the weakest model, experiment E, are internal or semi-internal folds (Biot, 1965a), characterised by a variation in the amplitude of folding through the thickness of the multilayer. The transition in fold style observed in experiments C, D and E can be compared with the sequence of fold styles illustrated in fig. 1.11 of section 1.2. The idealised sequence illustrated in this figure is based on Biot's analyses of the development of fold instabilities in a multilayer resting on a semi-infinite, isotropic matrix and these analyses cannot be applied directly to decollement folding above a rigid basement. However, the decrease in fold span which accompanies an increase in the constraint on fold amplification due to the presence of gravitational body stress can be compared to the similar transition in fold span which accompanies an increase in constraint on fold amplification due to an increase in the stiffness of the matrix substrate in Biot's analyses. The author is not aware of any theoretical models of fold instability development which can be applied directly to the problem of large scale décollement folding in the presence of gravitational body stress.

DEVELOPMENT OF STRUCTURES IN INDIVIDUAL EXPERIMENTS

Experiment F, fig. 4.24

Multilayer	-	54^0C m.pt. wax/silicone grease
Décollement lubricant	-	liquid soap
Temperature	-	38^0C $\pm$ 0.5 C

The development of folds in this experiment showed the following features:

i) The fold A and the fold complex BC initiated and amplified separately and non-synchronously. This tendency for individual folds to develop in isolation, rather than as part of a continuous fold train, was typical of the décollement fold experiments. The phenomenon can also be seen in the results of similar experiments carried out by Willis (1891) and by Blay et al. (1977) using other types of model materials (see fig. 4.25). The finite development of individual folds in experiment F can be divided broadly into three stages:

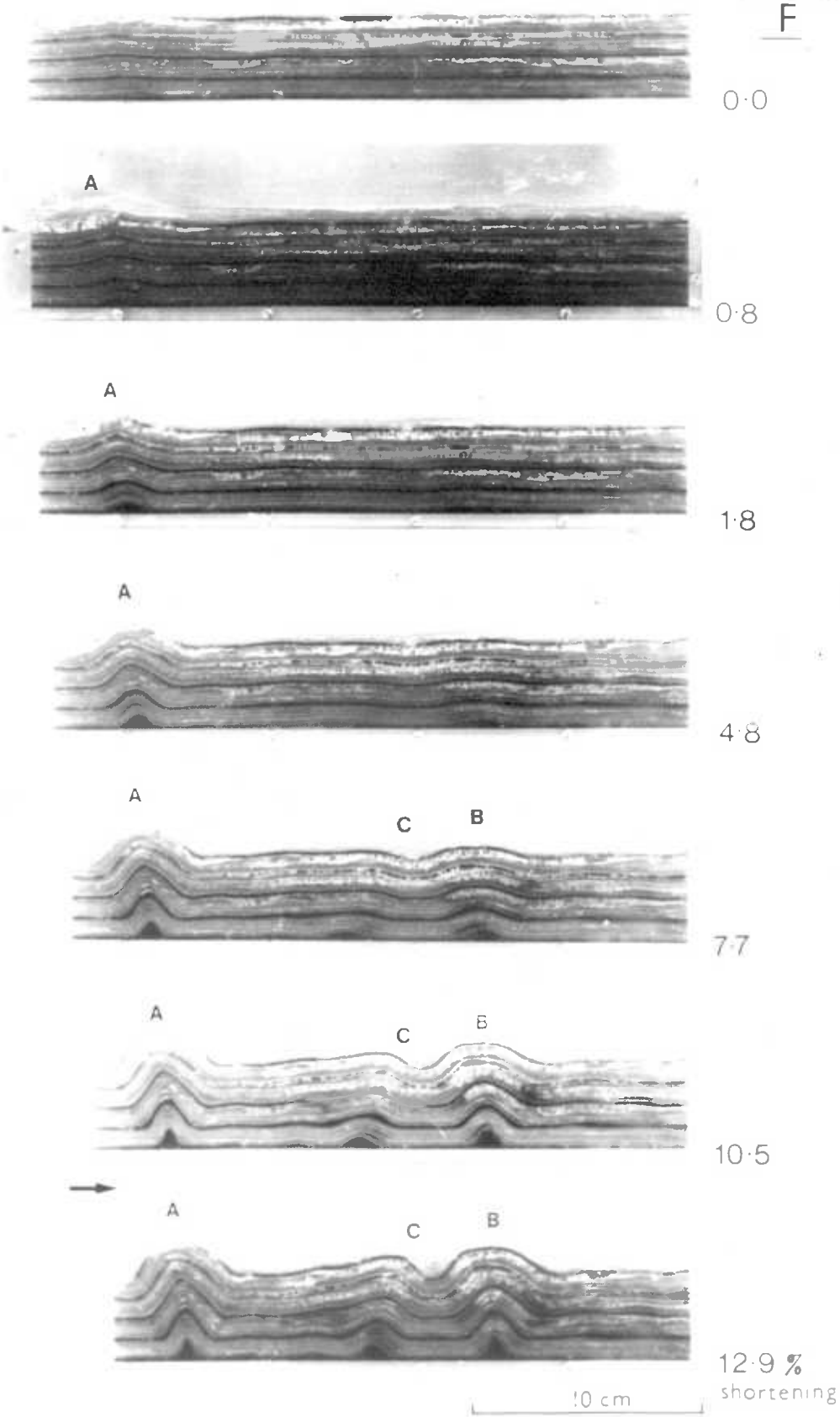
a) An initial, low amplitude phase associated with the development of a local buckling instability. This initial buckling phase probably involved the development and release of small transient elastic strains within the competent wax layers. In the case of fold A, for example, significant fold amplification was apparent after less than 1% total lateral shortening had been applied to the multilayer. It has been argued in section 4.4 that the role of transient elastic deformation during initial compression of the wax multilayers is a reasonable analogue of the equivalent elastic deformation in a series of indurate sedimentary beds at a length scale increased by a factor of 10^4 to 10^5.

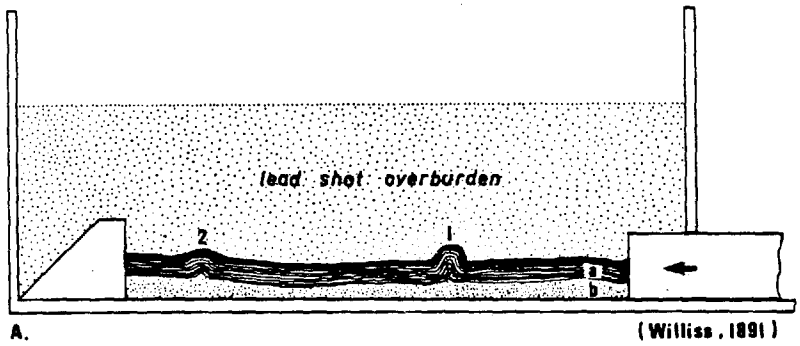
b) An intermediate phase of relatively rapid fold amplification. During this phase shortening of the whole length of the multilayer was concentrated within the limits of the growing fold.

c) A final phase in which the geometry and amplitude of the

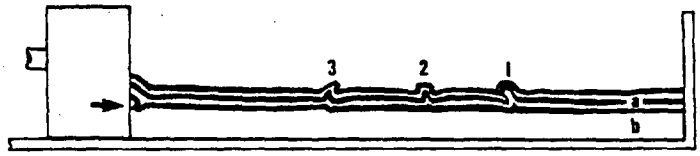
EXP. F

FIGURE 4.24





A. (Williss, 1891)



B. (Blay et al., 1977)

Figure 4.25 See text for details.

fold became stabilised or "locked". Once this had occurred, further shortening of the model multilayer was achieved by the initiation and subsequent amplification of other localised folds.

These three stages correspond to the stages recognised by Price (1975) in his discussion of the geological significance of fold development in weak gelatine multilayers. The rates of fold amplification observed in gelatine multilayer experiments (Blay, 1975) were, however, at least two orders of magnitude faster than the rates of amplification of equivalent localised fold structures in the paraffin wax experiments. This undoubtedly reflects the dominant role played by the rapid release of significant, and geologically unrepresentative, levels of stored elastic strains during the amplification of localised folds in weak gelatine multilayers.

ii) There are differences in detail between the finite geometries of the three folds, A, B and C, identified in fig. 4.24.

Fold A The location and finite geometry of this structure was influenced by an initial layer perturbation which was present in the wax multilayer before deformation. Initial perturbations in this, and other experiments, were caused by a small thermal expansion of the wax multilayers during the period of heating of the model, prior to the running of each experiment. In the case of experiment F, this expansion induced a low amplitude, cuspate layer perturbation. The amplitude and span of this perturbation were maximum towards the upper surface of the multilayer and the perturbation was characterised by a single, anticlinal hinge and a vertical, anticlinal axial plane. The finite geometry of fold A was, to a large extent, controlled by, and inherited from, the geometry of this localised initial layer disturbance. The structure remained single hinged throughout development and became increasingly angular with increase in amplitude. The finite structure was characterised by well defined zones of layer rotation, bounded by a vertical axial plane and flanking, synclinal axial surfaces which converged towards the base of the multilayer. The span of the structure, particularly in the higher levels of the multilayer, increased during the course of the experiment by the lateral migration of the synclinal axial planes.

Fold B The development and finite geometry of the structure was less influenced by the presence of a well defined initial layer disturbance than was the case in fold A. The development of this conjugate fold was typical of fold structures developed in lubricated multilayers made up of a uniform sequence of the stronger of the two wax grades (54^0C m.pt.) over the temperature range 38^0 - 44^0C (see experiments D and G). The structure developed through the amplification of a local, conjugate buckling instability that appeared to propagate from the décollement horizon to the upper surface of the multilayer. The low amplitude geometry of the fold was rounded in form and the structure became increasingly angular during the middle to late stages of fold amplification. The limbs of the initial conjugate fold were preferentially rotated in two, symmetrically opposed kink-like domains which became increasingly well defined. The point where the kink domains meet, at the base of the multilayer, was marked by the presence of an angular chevron fold, in the core of the conjugate box fold. There is evidence that this lower zone of chevron folding had begun to migrate upwards through the multilayer by the final stage in deformation seen in fig. 4.24. This process is achieved by the lateral migration of the conjugate planes defining the kinked limbs of the box folds, after the development of "locking" of these fold limbs.

The differences in detail between the two symmetric structures developed in experiment F (folds A and B) bring out an important point about the development of angular chevron folds in general. As is shown in this experiment the single axial plane which defines the plane of symmetry of a chevron fold may either:

a) develop at an early stage in the amplification of a symmetric fold, in which case the fold remains single hinged throughout its history.

or

b) develop by the progressive coalescence of the migrating boundaries of symmetrically opposed conjugate kinks.

These two mechanisms of chevron fold formation are not mutually exclusive; that is, both types of process can occur within a single model during the course of an experiment. Similar processes, occurring within the same experiment, have been observed to produce

chevron folds in model experiments simulating small scale fold development in uniform, confined multilayers (eg. Summers, 1970; Cobbold et al., 1971; Watkinson, 1976).

Fold C An important feature of experiment F was the development of the asymmetric fold, C, facing one limb of the adjacent box fold. In contrast to fold B, this asymmetric structure resulted from the development of only one of a potential conjugate pair of kink or rotation domains. The single kink domain forming the steep limb of the asymmetric fold C appeared to initiate by propagation from a zone of layer disturbance at the surface of the multilayer produced by rotation of the left hand limb of the box fold B. The phenomenon of reflection of a kink domain from the upper surface of the unconfined multilayer is similar to the reflection of kink domains which occurs at the rigid boundaries of a confined multilayer in experiments simulating small scale fold development (see Cobbold et al., 1971; Cobbold, 1973).

Experiment C*, fig 4.26

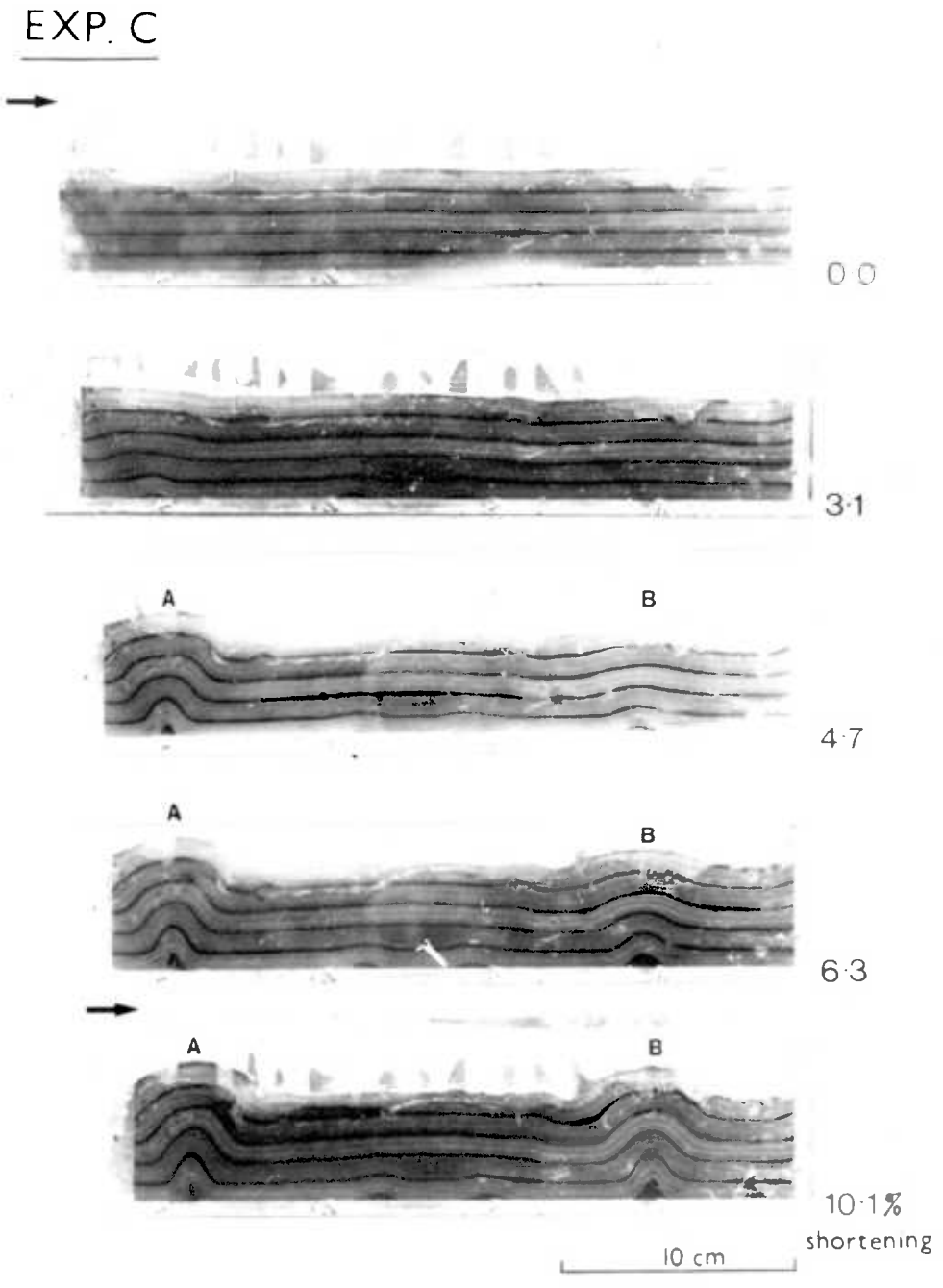
Multilayer	-	54^0C m.pt. wax/liquid soap
Décollement lubricant	-	liquid soap
Temperature	-	38^0C ± 0.5^0C

The multilayered model used in this experiment was geometrically identical to that used in experiment F and the experiment was run at the same temperature (38^0C). In this case, however, liquid soap was used as an incompetent interbed lubricant. The two conjugate box folds (A, B) developed in the experiment are similar to the conjugate fold B produced in experiment F and went through a similar process of development to that described for this structure.

In experiment C one side of the model was scored with a series of vertical passive marker lines. The rotation and relative displacements of these marker lines were used to compute the magnitude of the flexural slip and shear displacements involved in the development of the structures shown in fig. 4.26.

* also illustrated in fig. 4.21

Figure 4.26



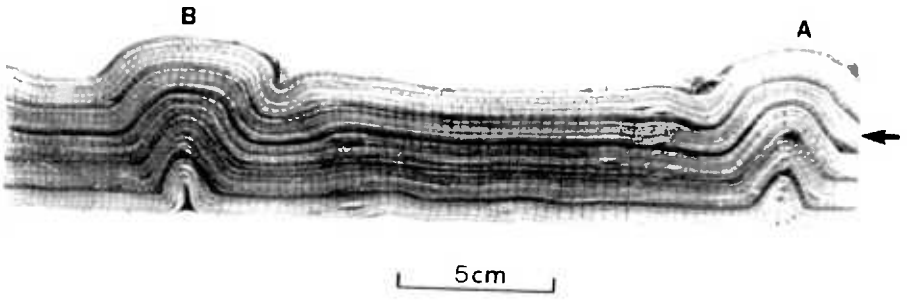


Figure 4.27 A

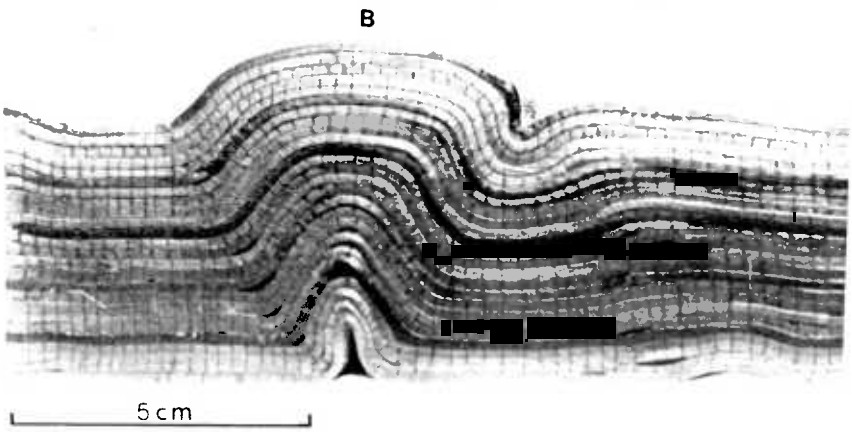
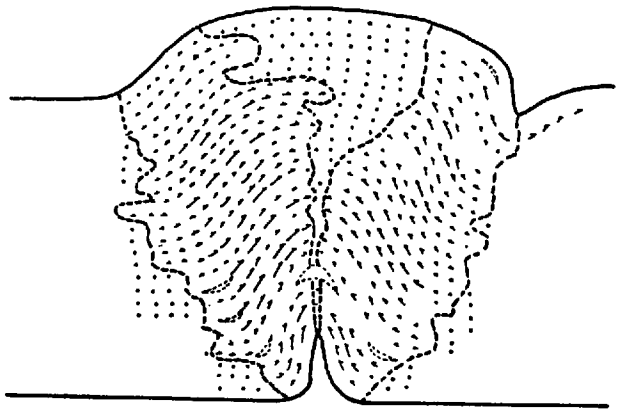


Figure 4.27 B



→ Slip Vector

· No Slip

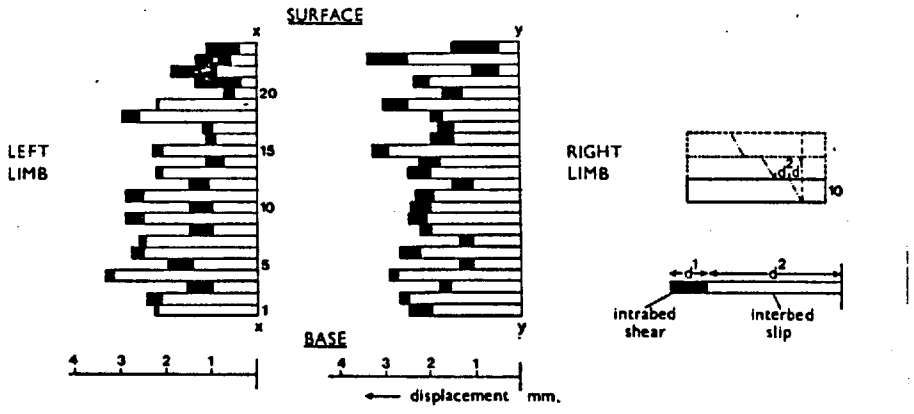


Figure 4.28 See text for details.

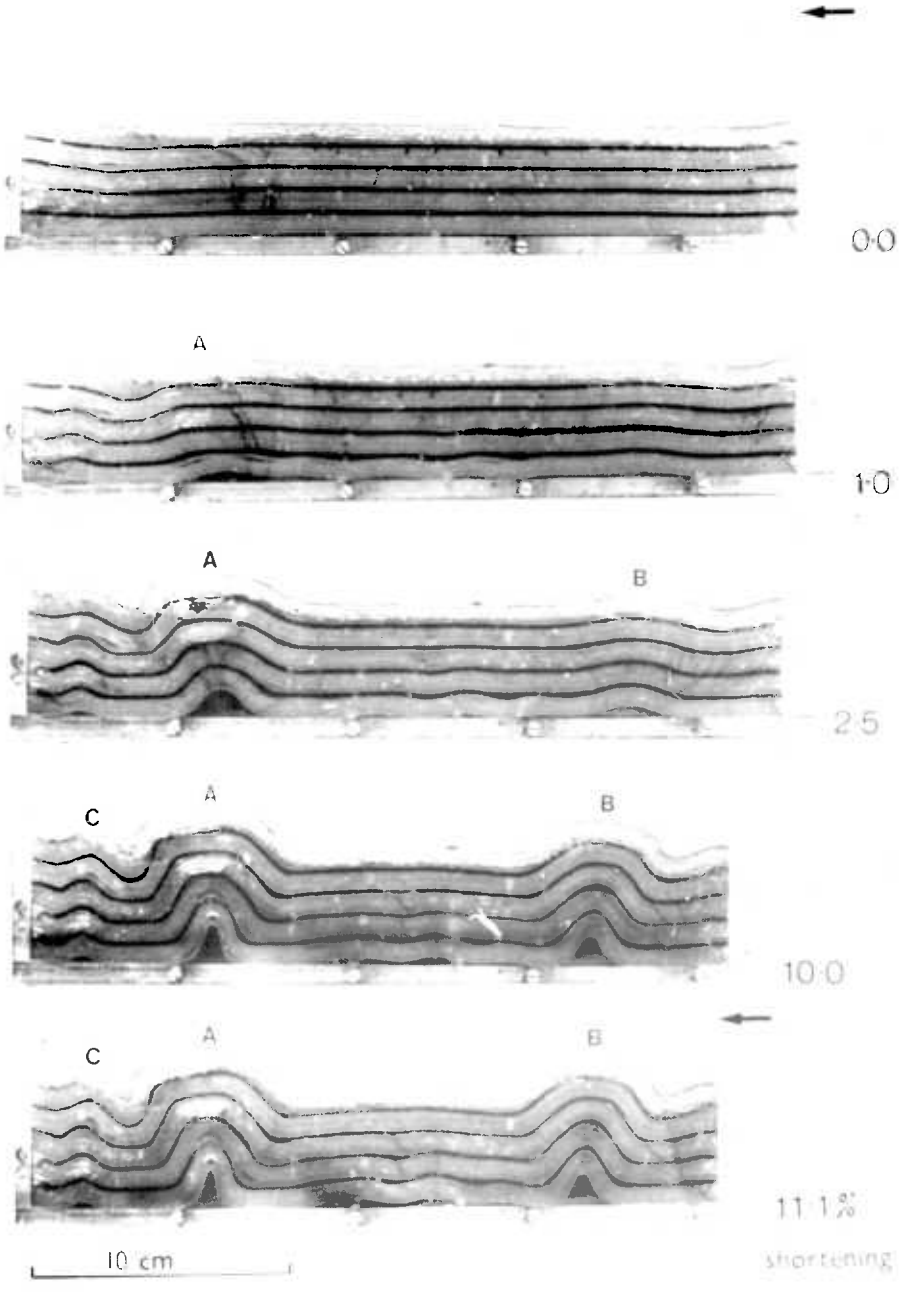
A photographic enlargement of fold B in experiment C is shown in fig. 4.27B to illustrate the movement and rotation of the passive marker lines in the region of this structure. A graphical method has been used to show the relative magnitudes of interbed slip and intra-bed, layer parallel shear displacement, measured from the displacement of the marker lines in this fold (fig. 4.28B). The magnitude of two layer parallel displacement components was measured along the mid-points of the fold limbs (along the lines XX and YY in fig. 4.28A). The results are shown in fig. 4.28B in the form of two graphs, corresponding to the opposing limbs. Each bar within these graphs is divided into two segments whose lengths indicate the magnitude of intra-bed shear displacement across one competent unit (d_1 - shaded) and the slip between this unit and the overlying competent unit (d_2 - unshaded). Successive bars correspond to successively higher competent/incompetent layer pairs. These graphs show that folding was achieved principally by discrete slip on the incompetent lubricant seams. Certain horizons within the structure, particularly in the left hand limb, show high slip values and alternate with interbeds along which relatively low amounts of inter-bed slip occurred. In this limb, interbeds showing high slip values tend to be associated with local saddle reef zones which became the sites of lubricant concentration during the course of the experiment.

Experiment G, fig. 4.29

Multilayer	-	54 C m.pt. wax/liquid soap
Décollement lubricant	-	liquid soap
Temperature	-	43^0C ± $0,5^0$C

This experiment was run with an identical model to that used in experiment C but at a temperature (43^0C) which was 5^0C higher than that of experiment C. The close similarities in the finite geometry of the conjugate folds developed in these two experiments reflects the similarity in model material strength indicated by the results of the rheological tests carried out over the temperature range 38^0 - 44^0C. Comparison of the structures developed in

Figure 4.29 EXP. G



identical multilayers at experimental temperatures of 35.5^{0}C (experiment D, fig 4.22), 38^{0}C (experiment C, fig. 4.21, fig.4.26) and 43°C (experiment G, fig 4.29) illustrates the effect of the substantial decrease in the strength of the 54^{0}C m.pt. paraffin wax which was identified over the temperature range 36^0 - 37^{0}C, from the results of the rheological tests.

It is not possible to apply the results of the mechanical analysis, given in chapters 2 and 3, directly to the results of the fold simulation experiments. The boundary conditions which are assumed in this analysis (eg. the assumption that structures extend indefinitely through a material of effectively infinite extent) certainly do not apply in the case of the experimental structures. The experimental structures themselves are more complex and involve more complex deformation histories than the type of simple tabular rotation domains that have been considered in the analysis and the rotation domain analysis does not incorporate a body force field variation.

Nevertheless, a number of the predictions of the mechanical analysis can be recognised in the results of the fold simulation experiments and reflect the role of layer anisotropy in the development of the experimental folds. In particular, there is a progressive increase in the angularity of individual folds which can be related to the type of processes which contribute to the development of structural angularity in the rotation domain analysis. The predicted development of stabilisation of fold amplitude during the later stages of fold amplification can also be seen in the model structures.

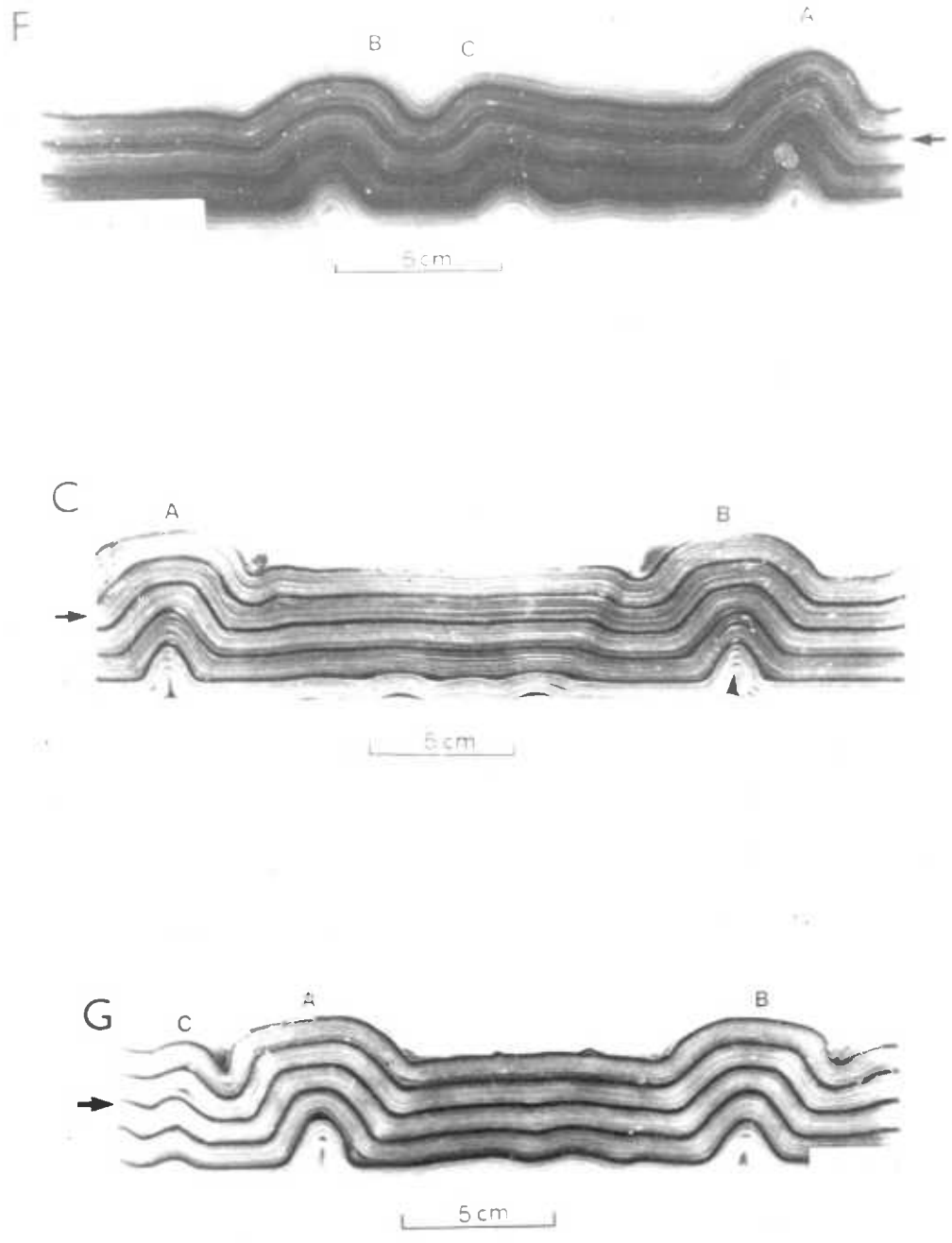


Figure 4.30 Experiments F, C and G shown removed from apparatus.

Table 4.III Details of the models discussed in section 4.5

Experiment	Competent Layers (wax m. pt.)	Incompetent Layers	Initial model thickness (mm.)	Number of competent layers	Decollement lubricant	TEMPERATURE	Figures
A	54°C	silicone grease	22	11	"vasilene"	38°C	4.19
B	54°C	silicone grease	31	19	vasilene	40°C	4.20
C	54°C	liquid soap	42	25	liquid soap	38°C	4.21,4.26 4.27,4.30
D	54°C	liquid soap	51	30	liquid soap	35.5°C	4.22
E	45°C	liquid soap	42	25	liquid soap	38°C	4.23
F	54°C	silicone grease	42	25	liquid soap	38°	4.24,4.30
G	54°C	liquid soap	42	25	liquid soap	43°	4.29,4.30

Appendix 2.1 Sign convention used in the rotation domain analysis

a) Stresses

Normal stresses acting on a plane are taken as positive when compressive, negative when tensile. Relatively positive mean stresses are, by this convention, relatively compressive.

Shear stresses are taken as positive if their sense of action is right lateral with respect to the plane on which they act.

b) Strains

A direct strain or strain rate is taken as negative if it is associated with a decrease in length along its line of resolution; positive if associated with an increase in length.

c) Angular parameters

The sign convention adopted for the angular parameters θ and ω used in the analysis can be referred to the orthogonal axes 1 and 2 oriented respectively parallel with and normal to the external foliation (fig. 2.1.1 A, B).

The angle of foliation rotation, ω, within the rotation band is measured from the axis 1. ω is positive if clockwise from 1 (fig. 2.1.1 A); negative if anticlockwise from 1 (fig. 2.1.1 B). (Note that the structures shown in these two figures correspond to a reverse kink (A) and a normal kink (B) in the terminology used by Dewey (1965).)

The angle, θ, which represents the orientation of the rotation domain with respect to the external foliation is measured from the axis 2. θ is positive if clockwise from 2; negative if anticlockwise.

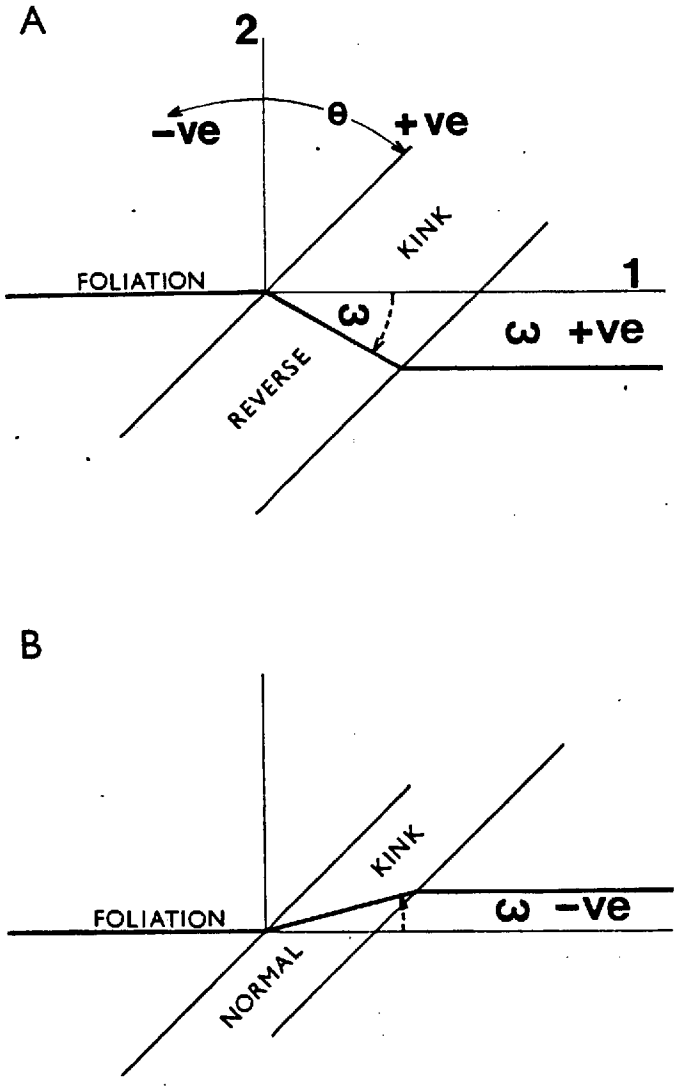

A
2
-ve
θ
+ve
KINK
FOLIATION
1
ω
ω +ve
REVERSE
B
KINK
FOLIATION
ω -ve
NORMAL

Figure 2.1.1

Appendix 4.1 Construction of layered models from paraffin wax.

A simple method of preparation of wax in the form of thin sheets, for use in multilayer experiments, was developed. This technique made use of the low specific gravity of wax by floating and cooling a thin sheet of molten wax on the surface of a water bath (fig. 4.1.1).

i) A known quantity of granular wax was floated on the surface of water contained within a 5 litre beaker. The contents of the beaker were heated to a temperature approximately 15^0C above the melting temperature of the wax to produce a surface layer of molten wax of known volume. A dye was added to the wax at this stage (fig 4.1.1A).

ii) While the wax was melting, a large quantity of water was heated separately in a water bath to a temperature approximately 25^0 - 30^0C above the melting temperature of the wax (fig. 4.1.1B).

iii) When the water bath had reached the required temperature, the water was transferred to a shallow plastic tank measuring approximately 200 cm x 75cm x 5cm. The hot wax was then poured on the water surface to form a thin sheet of floating liquid wax (fig. 4.1.1C). The thickness of this sheet was controlled by the volume of wax used. The contents of the tank were then allowed to cool to room temperature producing a thin sheet of solidified wax of constant thickness. By using this method it is possible to obtain, in a short time, a large quantity of sheet wax with a controlled thickness which varies by less than 5% over the total area of the sheet. Because of surface tension effects in the molten wax, it proved difficult to control the local thickness of the sheet below thickness of approximately 1mm.

iv) The floating, solidified sheet could be cut to convenient size and then machined to the dimensions required in a particular experiment. Sheets with a thickness as low as 1mm could be handled easily because of the high strength of the material at room temperature. It is possible to store wax in sheet form indefinitely.

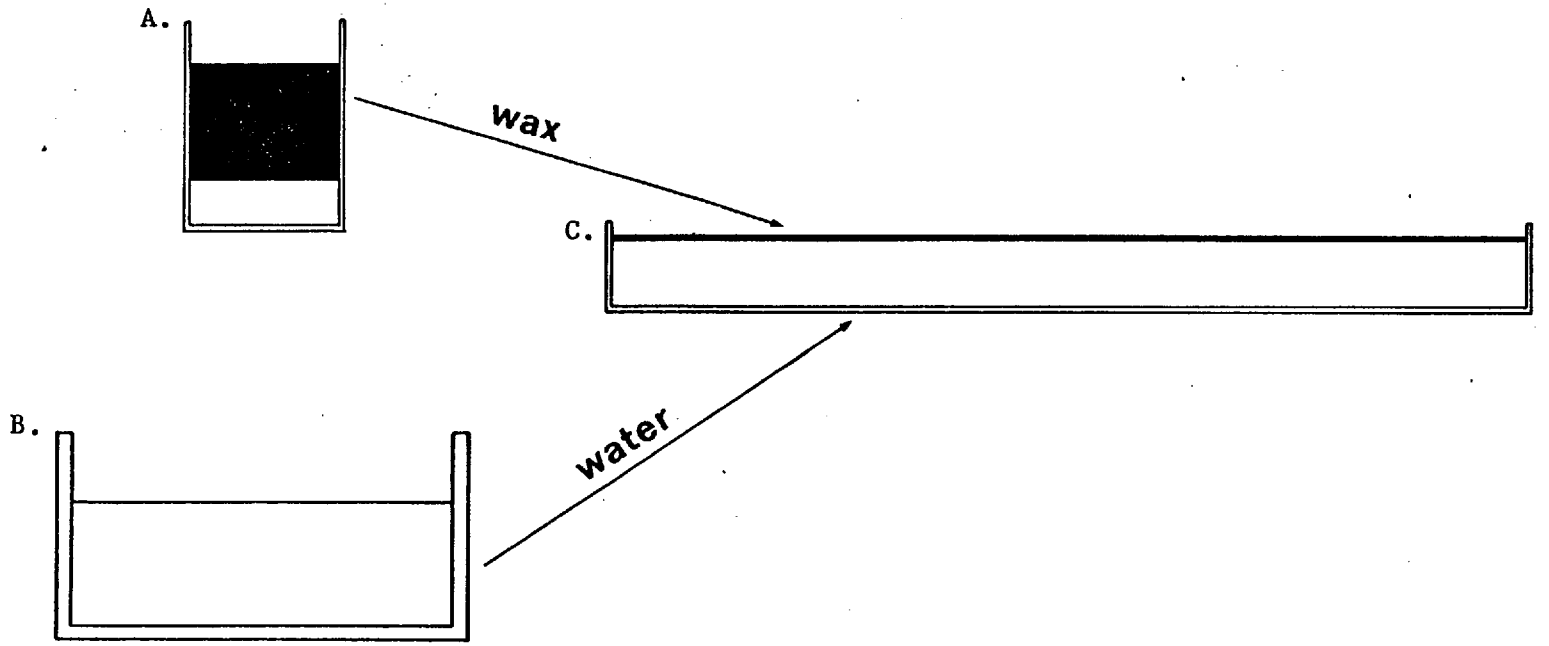
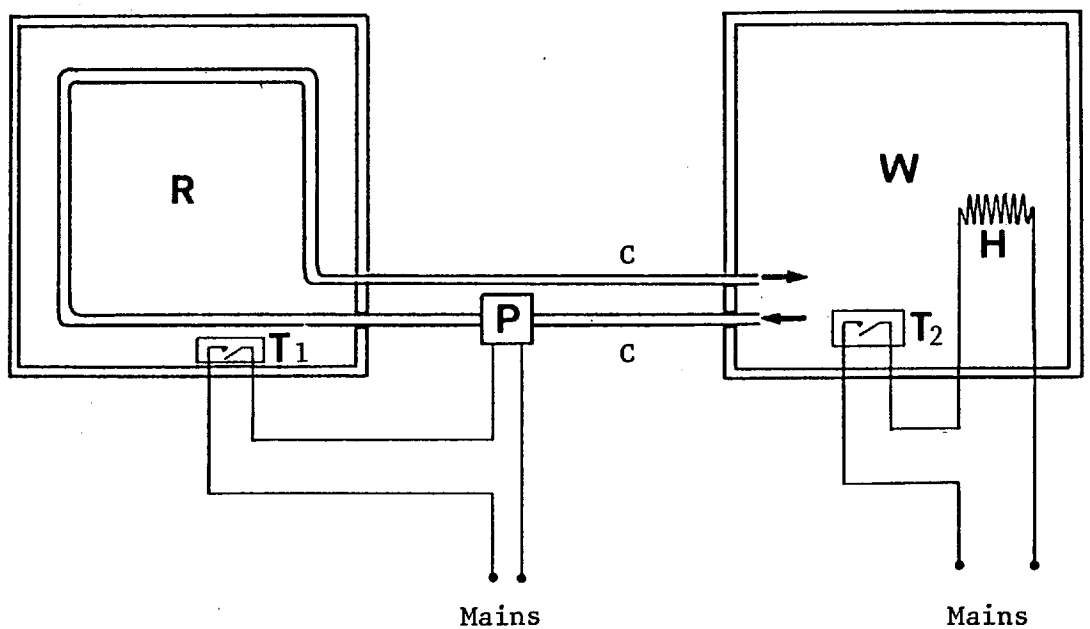


Figure 4.1.1 Method of preparation of thin wax sheet.

Appendix 4.2 Temperature control system used in the wax rheology test rig

The main features of the temperature control system are illustrated schematically in fig. 4.2.1. The rig contains a water bath (R) which was heated via a copper heat (C) exchange pipe at the base of the rig. Water was circulated through the copper pipes from a second water bath (W) which included an inbuilt thermostatic control (T2) The water temperature in this second bath was set 1^0C higher than the rig itself. A second thermostatic control, based on a Fi-monitor thermostat with a sensor head attached to a thermometer (T1) fixed within the rig water bath, was used to control the action of the pump (P) driving the heat exchange circuit. Using this system it was possible to control the temperature of the rig water bath and the wax test pieces to within ± 0.2 C of the required test temperature. Temperature could be held within these limits indefinitely.



R - RHEOLOGY TEST RIG WATER BATH

T - "FI-MONITOR" THERMOSTAT

P - PUMP

W - HEAT SUPPLY WATER BATH

H - HEATING COIL

T - THERMOSTAT

Figure 4.2.1 Temperature control system used in the wax rheology tests. (schematic)

Appendix 4.3 Details of the oven used in the wax experiment

A line diagram of the basic features of the oven used in the wax experiments is shown in fig. 4.3.1. The oven was constructed from a large metal cabinet (G) and all metal surfaces were insulated by a cladding of 3cm thick "rock wool" insulation (E). Two ½" thick perspex panels (F) were fitted to the sides of the working area of the oven. One panel was hinged to allow access to the working area.

The source of heat was provided by a two kilowatt domestic electric fire (D) and heat was transferred to the working area and circulated around the oven by a ducted fan (not shown in fig. 4.3.1). The apparatus (A) containing the model under test was fixed to a rigid base within the working area. Lateral movement of the compression piston was controlled by an electric motor, outside the oven, geared to transfer rotary motion of the motor to a constant rate of horizontal displacement in the drive shaft (B) and the piston. A constant horizontal piston velocity of 3.7cm per hour was used in all experiments.

Temperature control

The temperature control of the oven was based on the use of a Fi-monitor thermostat. This equipment acts essentially as a switch in the heating circuit. The switching action of the thermostat was controlled by a sensor head which was clamped to the barrel of a mercury thermometer (C). The position of the sensor head on the thermometer was adjusted to match the temperature required for the experiment. Activation or cut off of supply to the heating circuit was controlled by movement of the thermometer mercury thread through the sensor head.

The thermometer/sensor were positioned in the working area in the oven close to the experimental apparatus. Using this arrangement it was possible to control the temperature in the vicinity of the thermometer to $\pm$ 0.25^{0}C. Tests were carried out using a series of thermocouples located in different positions within the working area of the oven to examine temperature variation within the apparatus. It was found that temperature variation amounted to less than $\pm$ 0.25^{0}C about the nominal temperature of the

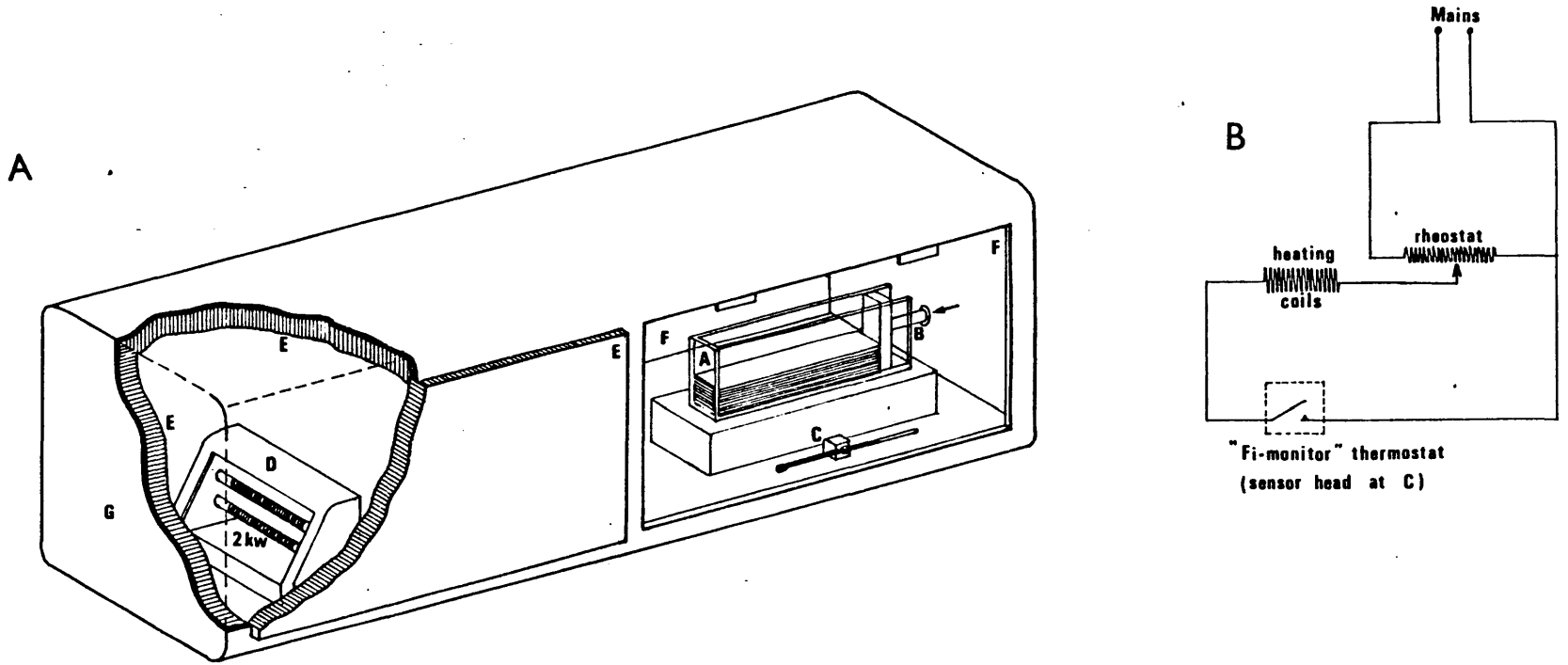


Figure 4.3.1 A) Oven and apparatus used in the fold simulation experiments.
B) Temperature control system.

BIBLIOGRAPHY

ANDERSON, T.B., 1968. The geometry of a natural orthorhombic system of kink bands. In: A. J. Baer and D. K. Norris (editors) Proc. Conference on Research in Tectonics, Geol. Survey Canada, paper 68-52.

BAYLY, M.B., 1974. An energy calculation concerning the roundness of folds. Tectonophysics, 26, pp. 291-316.

BIOT, M.A., 1957. Folding instability of a layered visco-elastic medium under compression. Roy. Soc. London Proc., Ser. A., 242, pp. 444-454.

BIOT, M.A., 1961. Theory of folding of stratified visco-elastic media and its implications in tectonics and orogenesis. Geol. Soc. Am. Bull., 72, pp. 1595-1620.

BIOT, M.A., 1963. Internal buckling under initial stress in finite elasticity. Royal.Soc. London Proc., Ser. A, 273, pp. 306 -326.

BIOT, M.A., 1964. Theory of internal buckling of a confined multi-layered structure. Geol. Soc. Am. Bull., 75, pp. 563-568.

BIOT, M.A., 1965a. Mechanics of incremental deformations. Wiley, New York, 504 p.

BIOT, M.A., 1965b. Theory of viscous buckling and gravity instability in multilayers with large deformation. Geol. Soc. Am. Bull., 76, pp. 371-378.

BIOT, M.A., 1965c. Further development of the theory of internal buckling of multilayers. Geol. Soc. Am. Bull., 76, pp. 833 -840.

BIOT, M.A., 1965d. Theory of similar folding of the first and second kind. Geol. Soc. Am. Bull., 76, pp. 251-258.

BIOT, M.A., 1966. Reheological stability with couple stresses and application to geological folding. Proc. Roy. Soc., Ser. A, 298, pp. 402-421.

BLAY, P., 1975. Unpublished Ph.D. Thesis, University of London.

```
      PROGRAM JULIE(INPUT=131B,OUTPUT=131B,TAPE6=131B,TAPE64=131B,
     +         TAPE61=131B,TAPE66=131B,TAPE5=INPUT)
      DIMENSION W(110)
      CALL START(2)
      CALL SWITCH(9HHARDCPYON)
   48 CALL NEWPAGE
      J=1
      CALL PROMPT(18HFOR HARDCPY TYPE 1,18)
      READ,MM
      DS=0.005
      CALL PROMPT(20HHOW MANY LAYERS REQD,20)
      READ,NL
      CALL PROMPT(35HENETR INITIAL BAND ANGLE IN DEGREES,35)
      READ,TS
      CALL PROMPT(25HENTER CONSTANT ANISOTROPY,25)
      READ,ANR
      CALL PROMPT(23HENTER INITIAL AMPLITUDE,23)
      READ,AMPL
      CALL PROMPT(33HENTER DIFFERENTIAL STRESS IN BARS,33)
      READ,SB
      CALL PROMPT(36HENTER EXPONENT OF VISCOSITY IN POISE,36)
      READ,IV
      SD=(SB*10.**6)/2.
      VP=10.**IV
      DT=DS*2.*VP/SD
      VV=FLOAT(IV)
      T1=TS/(180./3.14159)
      T=T1
      DO 200 I=1,100
      W(I)=ATAN(AMPL*(3.14159/100.)*SIN(3.14159*FLOAT(I-1)/100.))
  200 CONTINUE
   89 TM=FLOAT(J-1)*DT
      CALL FORMK(W,J,T,DT,SB,NL,VV,ANR,TS)
      IF(MM.EQ.1)CALL HARDCPY
   10 J=J+1
      DO 400 I=1,100
      RA=1.+1./ANR
      RB=1.-1./ANR
      SA=SIN(2.*(T-W(I)))*COS(2.*T)
      BA=4.*SIN(2.*T)-2.*RB*SIN(4.*(T-W(I)))*COS(2.*T)
      BB=RA-RB*COS(4.*(T-W(I)))
      SSB=COS(T-W(I))**2*BA/BB
      SC=SIN(2.*T)
      WMGA=-SA+SSB-SC
      DW=WMGA*DS
      W(I)=W(I)+DW
      T=ATAN(TAN(T1)*EXP(-2.*FLOAT(J-1)*DS))
  400 CONTINUE
      DO 334 JJ=21,101,20
      IF(J.EQ.JJ)CALL FORMK(W,J,T,DT,SB,NL,VV,ANR,TS)
  334 CONTINUE
      IF(J.LT.102) GO TO 10
      CALL PROMPT(28HTO ENABLE FURTHER RUN TYPE 1,28)
      READ,MJ
      IF(MJ.EQ.1)GO TO 48
      CALL BUFFEM
      STOP
      END
      SUBROUTINE FORMK(W,J,T,DT,SB,NL,VV,ANR,TS)
      DIMENSION XARRAY(110),YARRAY(110),W(110)
```

BLAY, P., COSGROVE, J.W. and SUMMERS, J.M., 1977. An experimental investigation of the development of structures in multi-layers under the influence of gravity. Jl. geol. Soc. Lond., 133, pp. 329-342.

BUXTORF, A., 1909. Ueber den Gebirgsbau der Clos du Doubs und der Vellerat-Kette im Berna Jura. Ber. Versamml. Oberrheinische Geol. Ver., 42, pp. 74-86.

BUXTORF, A., 1916. Prognosen und Befunde beim Haunsteinbasis und Grenchenberg-tunnel und die Bedeutung der letzteren fur die Geologie des Juragebirges. Verh. Naturforsch. Ges. Basel, 27, pp. 185-254.

CADELL, H.M., 1889. Experimental researches in mountain building. Trans. Roy. Soc. Edinburgh, Pt. 1, pp. 339-343.

CASEY, M., 1976. Unpublished Ph.D. thesis, University of London.

COBBOLD, P.R., 1973. Unpublished Ph.D.thesis, University of London.

COBBOLD, P.R., 1976. Mechanical effects of anisotropy during large finite deformations. Bulletin de la Societé Geologique de la France, 18, pp. 1497-1510.

COBBOLD, P.R., COSGROVE, J.W. and SUMMERS, J.M., 1971. Development of internal structures in deformed anisotropic rocks. Tectonophysics, 12, pp. 23-53.

COSGROVE, J.W., 1972. Unpublished Ph.D. thesis, University of London.

DEWEY, J.F., 1965. Nature and origin of kink bands. Tectonophysics, 1, pp. 459-494.

DONATH, F.A., 1968. Experimental study of kink band development in Martinsburg slate. In: A.J. Baer and D.K. Norris (editors), Proc. Conf. on Research in Tectonics, Geol. Survey Canada Paper, 68-52.

DIETRICH, J.H. and CARTER, N.L., 1969. Stress history of folding. Am. J. Sci., 267, pp. 129-154.

FAILL, R.T., 1969. Kink band structures in the Valley and Ridge Province, central Pennsylvania. Geol. Soc. Am. Bull., 80, pp. 2539-2550.

```
      TM=FLOAT(J-1)*DT
      XARRAY(1)=0.
      YARRAY(1)=0.
      XARRAY(2)=100.
      YARRAY(2)=0.
      DO 500 I=3,101
      XARRAY(I)=XARRAY(I-1)+1.
      YARRAY(I)=YARRAY(I-1)+TAN(W(I-1))
  500 CONTINUE
      XARRAY(102)=XARRAY(101)+250.
      YARRAY(102)=YARRAY(101)
      XMAG=EXP(-FLOAT(J-1)*0.005)
      CALL DRAWK(XARRAY,YARRAY,T,XMAG,J,TM,SB,NL,VV,ANR,TS,W)
      RETURN
      END
      SUBROUTINE DRAWK(X,Y,T,XM,J,TM,SB,NL,VV,ANR,TS,W)
      DIMENSION X(110),Y(110),W(110)
      TTT=T*180./3.14159
      CALL PROMPT(18HTYPE 1 TO CONTINUE,18)
      READ,IGO
      IF(IGO.EQ.1)CALL NEWPAGE
      CALL PLOT(1.,10.5,-3)
      DO 600 N=1,NL
      IF(N.EQ.1)YY=0.
      IF(N.EQ.1)SCALE=0.04
      IF(N.NE.1)SCALE=1.
      IF(N.NE.1)XMAG=1.
      IF(N.EQ.1)XMAG=XM
      YY=-0.2*1./XM
      X(1)=X(1)*SCALE*XMAG
      Y(1)=Y(1)*SCALE*XMAG
      X(2)=X(2)*SCALE*XMAG-YY*TAN(T)
      Y(2)=Y(2)*SCALE*XMAG
      DO 800 I=3,101
      X(I)=X(I)*SCALE*XMAG-YY*TAN(T)
      Y(I)=Y(I)*SCALE*XMAG
  800 CONTINUE
      X(102)=X(102)*SCALE*XMAG
      Y(102)=Y(102)*SCALE*XMAG
      DO 900 I=1,102
      CALL PLOT(X(I),Y(I),2)
  900 CONTINUE
      YY=-0.2*1./XM
      CALL PLOT(0.,YY,-3)
  600 CONTINUE
      YXY=FLOAT(NL)*YY
      CALL PLOT(0.,-YXY,-3)
      SHT=100.*(1.-XM)
      CALL PLOT(0.,YXY,-3)
      CALL PLOT(0.,-YY,-3)
      XD1=X(2)-(FLOAT(NL-1)*(-YY)+4.*(-YY))*TAN(T)
      YD1=FLOAT(NL-1)*(-YY)+4.*(-YY)
      XD2=X(2)+(4.*(-YY)*TAN(T))
      YD2=4.*YY
      XD3=XD1+X(101)-X(2)
      YD3=YD1+Y(101)-Y(2)
      XD4=XD2+X(101)-X(2)
      YD4=YD2+Y(102)-Y(2)
      CALL PLOT(XD1,YD1,3)
      CALL PLOT(XD2,YD2,2)
      CALL PLOT(XD3,YD3,3)
      CALL PLOT(XD4,YD4,2)
      RETURN
      END
```

GHOSH, S.K., 1968. Experiments of buckling of multilayers which permit interlaying gliding. Tectonophysics, 6, pp. 207-250.

HALL, J., 1815. On the vertical position and convolutions of certain strata. Trans. Roy. Soc. Edinburgh, 7, pp. 85-86.

HOBBS, B.E., MEANS, W.D. and WILLIAMS, P.F., 1977. An outline of structural geology. John Wiley and Sons Inc., 571 p.

HONEA, E., 1976. A theory of concentric, kink and sinusoidal folding and of monoclinic flexuring of compressible, elastic multilayers. IV. Development of sinusoidal and kink folds in multilayers confined by rigid boundaries. Tectonophysics, 30, pp. 197-239.

HUBBERT, M.K., 1937. Theory of scale models as applied to the study of geological structures. Geol. Soc. Am. Bull., 48, pp. 1459-1513.

HUDDLESTON, P.F., 1973. An analysis of "single-layer" folds developed experimentally in viscous media. Tectonophysics, 16, pp. 189-214.

HUDDLESTON, P.F. and STEPHANSSON, O., 1973. Layer shortening and fold shape development in the buckling of single layers. Tectonophysics, 17, pp. 299-321.

JAEGER, J.C. and COOK, N.G.W., 1976. Fundamentals of rock mechanics. Chapman and Hall, London, 585 p.

JOHNSON, A.M., 1970. Physical processes in geology. Freeman, Cooper and Company.

JOHNSON, A.M., 1976. Styles of Folding. Elsevier Publishing Co., Amsterdam.

LATHAM, J.-P. Experimentally developed folds in a material with a planar mineral fabric. (Tectonophysics - in press).

LAUBSCHER, H.P., 1973. Jura Mountains. In: K.A. de Jong and R. Scholten (editors), Gravity and Tectonics. Wiley, New York, pp. 217-227.

LAUBSCHER, H.P., 1975. Viscous components in Jura folding. Tectonophysics, 27, pp. 239-254.

LAUBSCHER, H.P., 1976a. Geometrical adjustments during the rotation of a Jura fold limb. Tectonophysics, 37, pp. 347-365.

LAUBSCHER, H.P., 1976b. Fold development in the Jura. Tectonophysics, 37, pp. 337-362.

NYE, J.F., 1957. Physical properties of crystals. Clarendon Press, Oxford.

PARRISH, D.R., 1973. A non-linear finite element fold model. Am. J. Sci., 273, pp. 318-334.

PATERSON, M.S. and L.E. Weiss, 1966. Experimental deformation and folding in phyllite. Geol. Soc. Am. Bull., 77, pp. 343-374.

PRICE, N.J., 1975. Rates of deformation. Jl. Geol. Soc. Lond., 131, pp. 553-576.

RAMBERG, H., 1959. Evolution of ptygmatic folding. Norsk Geol. Tidsskr., 39, pp. 99-151.

RAMBERG, H., 1961. Contact strain and folding instability in a multilayered body under compression. Geol. Rund., 51, pp. 405-439.

RAMBERG, H., 1967. Gravity, deformation and the earth's crust as studied by centrifuged models. Academic Press, New York, 241 p.

RAMBERG, I. and JOHNSON, A.M., 1976. Asymmetric folding in interbedded chert and shale of the Franciscan Complex, San Francisco Bay Area, California. Tectonophysics, 32, 295-320.

RAMSAY, J.G., 1967. Folding and fracturing of rocks. McGraw-Hill Book Co., New York, 568 p.

SUMMERS, J.M., 1970. Unpublished M.Sc. thesis, University of London.

TIMOSCHENKO, S. and GERE, J.M., 1961. Theory of elastic stability. 2nd edn., McGraw-Hill, New York.

VERBEEK, E.R., 1978. Kink bands in the Somport slates, west central Pyrenees, France and Spain. Geol. Soc. Am. Bull., 89, pp. 814-824.

WEISS, L.E., 1968. Flexural slip folding of foliated model materials. In: Proc. Conference on Research in Tectonics, A.J. Baer and D.K. Morris (editors). Canada Geol. Survey, Ottawa, paper 68-52.

WILLIS, B., 1891. The mechanics of Appalachian structure. U.S. Geol. Survey 13th Annual Rept., pp. 217-281.